Synthetic, Structural, Spectroscopic and Electrochemical Studies of Dinuclear bis μ-Oxo-Bridged Molybdenum(*IV*) and Tungsten(*IV*) Half-Sandwich Complexes

Dissertation

zur Erlangung des akademischen Grades Doktor der
Naturwissenschaften (Dr. rer. nat.)

am Institut für Anorganische und Angewandte
Chemie, Universität Hamburg

vorgelegt von

Yan Yu

2013, Hamburg

Diese Arbeit entstand in der Zeit von Oktober 2008 bis Dezember 2013 in der Arbeitsgruppe von Prof. Dr. P. Burger am Institut für Anorganische und Angewandte Chemie, Fakultät für Chemie, Universität Hamburg.

Gutachter:
Prof. Dr. Peter Burger
PD. habil. Dr. Michael Steiger

Tag der Disputation: 24.01.2014

DEDICATION

To my dear family
In memory of my father...

Yan

Acknowledgements

First and foremost, I would like to thank my PhD thesis supervisor Prof. Dr. Peter Burger for giving me this opportunity to work on this interesting and challenging project. I deeply appreciate the guidance and encouragement he gave me over the years, especially at the beginning of the research when I went through a frustrate time as a international chemical engineering student. I admire his broad knowledge and great scientific attitude towards chemistry which strove me always for the best. The enthusiasm he showed when I achieved nice results really cheered me up. Furthermore, I thank him for for carrying out many DFT calculations. Great thanks also go to PD Dr. Michael Steiger for evaluating my dissertation.

Secondly I want to thank all the former and current members of Burger work group, Dr. Daniel Sieh, Tabea Buban, Mandy Schlimm, Natascha Junker, Marlies Heffter, Friedrich Angersbach-Bludau, Nils Lindenmayer, Bernhard Bugenhagen, Matthias Schreyer, Christian Modrzynski, Sven Schierenbeck, Dr. Jan-Philipp Werner and Dr. Andrey Rogachev for the nice working atmosphere they created and the constant willingness to help. Thank you also for all the intense discussions during our Monday group meetings through the years. In particular, great thanks go to Dr. Daniel Sieh for teaching me all the lab techniques from the beginning of my PhD study. In addition, I want to thank the research student Kristina Rossow for the bachelor work dinuclear bis-μ-oxo-bridged molybdenum complexes.

Also, I want to thank all members of the technical service teams in chemistry department at Hamburg University, ie. the NMR spectroscopy, X-ray single crystal, elemental analysis, mass spectroscopy teams etc. Many thanks go to Prof. Dr. Ulrich Behrens for helping me solve complicated crystallographic problems.

Furthermore, I am truly grateful to China Scholarship Council (CSC) for the financial assistance to study abroad. The cooperative graduate program, Key Technologies for Sustainable Energy Systems in Smart Grids, is gratefully acknowledged for the financial support for the last 15 month.

Finally, I would like to give all my thanks to my family and friends. My special thanks go to my dear husband Rongyu Ju for being a rock in my life. Maybe you are not the most romantic guy in the world, but you are the steadiest guy in my life. You may not always be a great boyfriend, but you are a wonderful husband

and I know you will be an amazing father in the future. Thank you for the epic love since high school. Of course, my great thanks go to my parents, parents-in-law for the endless love and encouragements. And many thanks to family Ju in hamburg, our uncle, aunt and cousins for making hamburg our second hometown. Well, to family Li, Dr. Hongmei Li, Dr. Chao Li, little princess Helen, you are technically our family too, thank you for being such wonderful friends and it is a joy for us being Helen's Gan'ma and Gan'ba. And last, thanks to all our dear friends currently or once lived in hamburg, Dr. Yuna Huang, Yuan Li, Xiaojun Wu, Dr. Wei Shen, Dr. Junyu Lai, Dr. Xiuhua Zhu, Dr. Weiqiang Wang and many others for ski trips, vacations, home cooked meals, coffees, cocktails, swims, badminton plays, fun games and other activities we had together.

Abbreviation

δ	Chemical shift (NMR)
ϵ	Extinction Coefficient
η	Hapticity, attached to a metal center through more than one atome
μ	Bridging, attached to two metal centers
^{t}Bu	*tert*-Butyl
^{t}Bu$_2$bpy	4,4′-di-tert-butyl-2,2′-dipyridyl
^{t}Bu$_2$bpy-Mo^{IV}Mo^{IV}	$[(\mathrm{Cp}^*\mathrm{Mo}(^t\mathrm{Bu}_2\mathrm{bpy})(\mu{-}\mathrm{O}))_2]^{2+}$
(COOH)$_2$bpy	4,4′-dicarboxy-2,2′-bipyridine
(COOMe)$_2$bpy	4,4′-dimethoxycarbonyl-2,2′-bipyridine
CH_3CN	Acetonitrile
Et_2O	Diethylether
Li[Al(pftb)$_4$]	Lithium tetrakis(perfluoro-tert-butoxy)aluminate
A	Acceptor
ATP	Adenosine Triphosphate
BE	Bulk Electrolysis
Bu	Butyl
C	Chromophore
CCSD	Cambridge Crystallographic Structural Database
CE	Counter Electrode
COSY	Correlation Spectroscopy (NMR)
Cp*	Pentamethylcyclopentadienyl
CV	Cyclic Voltammetry
D	Donor

d	Doublet
dd	Doublet of Doublets
DEPT	Distortionless Enhancement by Polarisation Transfer (NMR)
DFT	Density Functional Theory
dpphen	4,7-diphenyl-1,10-phenanthroline
dpphen-$W^{IV}W^{IV}$	$[(Cp^{*}W(dpphen)(\mu{-}O))_2]^{2+}$
dpq	dipyrido[3,2-a:2′,3′-h]quinoxoline
dpq-$Mo^{IV}Mo^{IV}$	$[(Cp^{*}Mo(dpq)(\mu{-}O))_2]^{2+}$
dpq-$W^{III}W^{III}$	$[(Cp^{*}W(dpq)(\mu{-}O))_2]$
dpq-$W^{IV}W^{III}$	$[(Cp^{*}W(dpq)(\mu{-}O))_2]^{+}$
dpq-$W^{IV}W^{IV}$	$[(Cp^{*}W(dpq)(\mu{-}O))_2]^{2+}$
EI	Electron Ionization
eq	Equivalent
ES	Excited State
ESR	Electron Spin Resonance
Et	Ethyl
EXAFS	Extended X-ray Absorption Fine Structure
FAB	Fast Atom Bombardment
fac-	Facial
GS	Ground State
h	Hour(s)
HMBC	Heteronuclear Multiple Bond Correlation (NMR)
HOMO	Highest Occupied Molecular Orbital
HSQC	Heteronuclear Single Quantum Coherence (NMR)
IR	Infrared
L	Ligand
LMCT	Ligand to Metal Charge Transfer

LUMO	Lowest Unoccupied Molecular Orbital
m	Multiplet
m.p.	Melting Point
Me	Methyl
mer-	Meridional
min	Minute
MLCT	Metal to Ligand Charge Transfer
MS	Mass Spectrometry
NADP	Nicotinamide Adenine Dinucleotide Phosphate
NMR	Nuclear Magnetic Resonance
OEC	Oxygen Evolving Complex
OTf	Triflate, Trifluoromethanesulfonate
ox	Oxidation
PC	photo-catalyst
Ph	Phenyl
phd	1,10-Phenantroline-5,6-dione
PPNCl	bis-(triphenylphosphoranylidene)ammonium chloride
PS	Photosystem
q	Quartet
RE	Reference Electrode
red	Reduction
rxn	Reaction
s	Singlet
SCE	Saturated Calomel Electrode
SEC	Spectroelectrochemistry
sept	Septet
T	Temperature

t	Triplet
TDAE	Tetrakis(dimethylamino)ethylene
THF	Tetrahydrofuran
UV	Ultra-violet
WE	Working Electrode
XAS	X-ray Absorptionspectroscopy
XPS	X-ray Photoelectronspectroscopy
Z	Molecules per elementary cell
J	Coupling Constant (NMR)

Contents

Abbreviation VII

1. Introduction and Background 1

1.1. Natural and Artificial Photosynthesis 1

1.1.1. Water Splitting in Photosystem *II* 1

1.1.2. Molecular Approaches towards Solar Water Splitting 4

1.2. State of Research in the Work Group 8

1.3. The Aim and Structure of This Thesis 12

2. Mononuclear Half-Sandwich Tungsten(*IV*) and Molybdenum(*IV*) Halido Complexes 15

2.1. Starting Materials 15

2.1.1. Pentamethylcyclopentadienyl Tungsten(*V*) and Molybdenum(*V*) Chlorido Complexes 15

2.1.2. Dinuclear Chlorido Bridged Molybdenum(*IV*,*IV*) Complex 16

2.2. Anionic Tungsten(*IV*) and Molybdenum(*IV*) Complex 16

2.3. Bidentate N-donor Ligand Adducts of Tungsten(*IV*) and Molybdenum(*IV*) 18

2.3.1. Synthesis of dpq-W^{IV} (**2-a**) 18

2.3.2. Synthesis of dpphen-W^{IV} (**2-b**) 19

2.3.3. Synthesis of $(COOMe)_2$bpy-W^{IV} (**2-c**) 22

2.3.4. Synthesis of dpq-Mo^{IV} (**3-a**) 24

2.3.5. Synthesis of ^{t}Bu$_2$bpy-Mo^{IV} (**3-d**) 26

3. Dinuclear μ-Oxo-Bridged Tungsten Half-Sandwich Complexes 27

3.1. Synthesis of the Complexes dpq-$W^{IV}W^{IV}$ (**4-a**) and dpphen-$W^{IV}W^{IV}$ (**4-b**) 27

3.2. Attempted Chemical Oxidation of **4-a** 33

3.3. Chemical Reduction of **4-a** 37

3.4. Comproportionation Reaction between dpq-$W^{IV}W^{IV}$ and dpq-$W^{III}W^{III}$ 40

3.5. Spectral Properties 46

3.5.1. Electronic Absorption Spectroscopy of Complexes **4-a** and **4-b** 46

3.5.2. TD-DFT Calculations for Complex **4-a** 51

3.5.3. Raman Spectroscopy of Complex **4-a** 55

3.6. Electrochemical Properties of Complex **4-a** 57
  3.6.1. CV Measurement of **4-a** in ACN 57
  3.6.2. CV Measurement of **4-a** in ACN/THF Mixture 61
3.7. Distinctive Electrochemical Behavior of Complex **4-b** 64
  3.7.1. CV Measurement of **4-b** in ACN 64
  3.7.2. Current Dependence on Scan Rate 67
  3.7.3. Solvent Dependence of Reversibility 73
    3.7.3.1. CV Measurement in THF 73
    3.7.3.2. CV Measurement in THF upon addition of ACN . 76
    3.7.3.3. CV Measurement in ACN upon Addition of THF . 77
3.8. Photocatalysis 81

4. Molybdenum Analogues of Dinuclear μ-Oxo-Bridged Half-Sandwich Complexes 85
4.1. Synthesis of dpq-Mo^{IV}Mo^{IV} (**8-a**) 85
4.2. Spectral and Electrochemical Properties of Complex **8-a** 87
  4.2.1. Electronic Absorption Spectroscopy 87
  4.2.2. Cyclic Voltammetry 88
4.3. Synthesis of ^{t}Bu$_2$bpy-Mo^{IV}Mo^{IV} (**8-d**) 90
4.4. Spectral and Electrochemical Properties of Complex **8-d** 92
  4.4.1. Electronic Absorption Spectroscopy 92
  4.4.2. Cyclic Voltammetry 93

5. Summary 101

6. Experiment Section 109
6.1. General Methods 109
6.2. Characterization Methods 109
6.3. Synthetic Details 113
  6.3.1. Synthesis According to Literature 113
  6.3.2. Synthesis for Chapter 2 117
    6.3.2.1. [Cp*MoCl$_3$]$_2$ (**1-1**) 117
    6.3.2.2. PPN[Cp*WCl$_4$] (**1-2**) 117
    6.3.2.3. PPN[Cp*MoCl$_4$] (**1-3**) 118
    6.3.2.4. Cp*W(dpq)Cl$_3$ (**2-a**) 118
    6.3.2.5. Cp*W(dpphen)Cl$_3$ (**2-b**) 119
    6.3.2.6. Cp*W(COOMe$_2$bpy)Cl$_3$ (**2-c**) 119
    6.3.2.7. Cp*Mo(dpq)Cl$_3$ (**3-a**) 120

6.3.2.8. $Cp^*Mo(^tBu_2bpy)Cl_3$ (**3-d**) 120
6.3.3. Sythesis for Chapter 3 121
6.3.3.1. $[(Cp^*W(dpq)(\mu{-}O))_2][PF_6]_2$ (**4-a**) 121
6.3.3.2. $[(Cp^*W(dpq)(\mu{-}O))_2][PF_6][Al(pftb)_4]$ (**4-a1**) 122
6.3.3.3. $[(Cp^*W(dpq)(\mu{-}O))_2][Al(pftb)_4]_2$ (**4-a2**) 123
6.3.3.4. $[Cp^*W(dpq)(NCCH_3)_2(OH)][PF_6]_2$ (**5-a**) 124
6.3.3.5. $[(Cp^*W(dpq)(\mu{-}O))_2]$ (**6-a**) 124
6.3.3.6. $[(Cp^*W(dpphen)(\mu{-}O))_2][PF_6]_2$ (**4-b**) 125
6.3.4. Synthesis for Chapter 4 126
6.3.4.1. $[(Cp^*Mo(dpq)(\mu{-}O))_2][PF_6]_2$ (**8-a**) 126
6.3.4.2. $[(Cp^*Mo(^tBu_2bpy)(\mu{-}O))_2][PF_6]_2$ (**8-d**) 127

Bibliography **129**

I. Appendix **139**
I.I. Synthetic compounds directory 140
I.II. X-ray structural data 141
I.II.I. $Cp^*W(dpphen)Cl_3$ (**2-b**) 142
I.II.II. $Cp^*W(bpy{-}COOMe)Cl_3$ (**2-c**) 143
I.II.III. $[(Cp^*W(dpq)(\mu{-}O))_2][PF_6]_2$ (**4-a**) 144
I.II.IV. $[(Cp^*W(dpq)(NCCH_3)_2(OH)][PF_6]_2$ (**5-a**) 146
I.II.V. $[(Cp^*W(dpq)(\mu{-}O))_2]$ (**6-a**) 147
I.II.VI. $[(Cp^*W(dpq)(\mu{-}O))_2][PF_6]$ (**7-a1**) 148
I.II.VII.$[(Cp^*W(dpphen)(\mu{-}O))_2][PF_6]_2$ (**4-b**) 149
I.II.VIII$[(Cp^*Mo(dpq)(\mu{-}O))_2][PF_6]_2$ (**8-a**) 150
I.II.IX. $[(Cp^*Mo(^tbu_2bpy)(\mu{-}O))_2][PF_6]_2$ (**8-d**) 151
I.III. NMR spectroscopic data 152
I.IV. Chemicals categorized according to GHS 158

1. Introduction and Background

The energy consumption of today's society depends to a large degree (about 85%)[1] on fossil fuels, which soon meet their limitation of availability. In addition, green-house gases released upon burning of fossil fuels create a significant threat to our current living conditions. This makes the development of alternative renewable energy sources one of the central challenges of 21*st* century.[2–5] Solar energy is one of the most promising alternatives as it is available in almost unlimited extent.[3] The harvest of less than 0.02% of the incident sunlight on the earth would be enough to fulfill the world's energy requirements.[6] The most efficient system for the conversion of solar energy into stored chemical energy is natural photosynthesis, which displays a theoretical maximum efficiency of approximately 13%.[7] It provides a model for the development of a variety of artificial systems for energy conversion of solar energy. This is known as artificial photosynthesis.

1.1. Natural and Artificial Photosynthesis

1.1.1. Water Splitting in Photosystem *II*

Photosynthesis is the process by which autotrophic organisms like plants, algae, and cyanobacteria use light energy to make carbohydrates and oxygen gas from carbon dioxide and water.

$$6\,CO_2 \quad + \quad 6\,H_2O \xrightarrow{h\nu} C_6H_{12}O_6 \quad + \quad 6\,O_2$$

The remarkable light-driven chemistry of water splitting in Photosystem *II* (PS*II*) happens in the thylakoid membrane of the chloroplasts. A chlorophyll-a molecule in chloroplast, which is known as P680, absorbs red light of wavelength 680 nm to excite electrons from the reaction center. This electron then pass through a series of molecular intermediates called an electron transport chain into Photosystem *I* (PS*I*). (see Figure 1.1) The strong oxidant $P680^{\bullet+}$ generated by PS*II* drives water oxidation by means of a catalyst, known as oxygen evolving complex (OEC), to produce O_2 and H^+. The H^+ produced by the oxidation of water powered by chemiosmosis is used by ATP (Adenosine Triphosphate) synthase to generate ATP. At the meantime, another chlorophyll molecule called P700 in

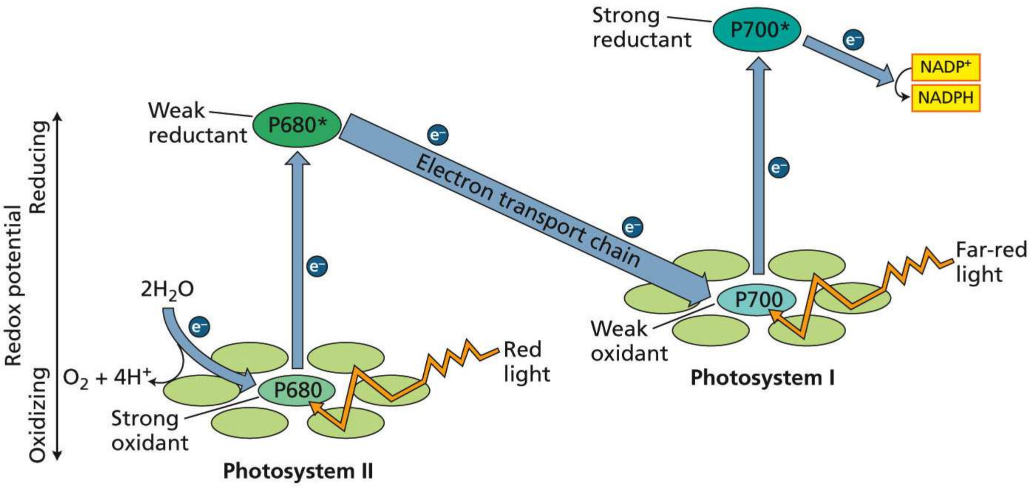

Figure 1.1.: Z scheme of photosynthesis. Red light absorbed by photosystem *II* produces a strong oxidant and a weak reductant. Far-red light absorbed by photosystem *I* (PS*I*) produces a weak oxidant and a strong reductant. The strong oxidant generated by PSII oxidizes water, while the strong reductant produced by PSI reduces NADP$^+$. [adopted from reference[8]]

PS *I* captures far-red light of wavelengths greater than 680 nm to form a strong reductant, which is able to reduce NADP$^+$ (Nicotinamide Adenine Dinucleotide Phosphate). PS *I* regains electrons from the electron transport chain (see Figure 1.1). This is called the Z (for zigzag) scheme of photosynthesis.[8] In total, through the light reactions in two connected photosystems, light energy was successfully transferred into active chemical energy stored in ATP and NADPH (reduced form of NADP$^+$). The ATP and NADPH produced by the light reactions provides the energy and the electrons necessary respectively for the reduction of carbon dioxide to glucose through the Calvin cycle (dark reactions).

The water oxidation catalyst OEC contains a cluster of four manganese ions (in oxidation states of +2, +3, +4 and +4), a tyrosine (Y_z) and Ca^{2+}, Cl^- co-factors.[9–11] The tyrosine reduces $P680^{\bullet+}$ to form a tyrosine radical that together with the manganese cluster extracts electrons from water to generate molecular oxygen.

Substantial information about oxygen production in PS*II* have been provided by flash experiments, electron spin resonance (ESR), and X-ray spectroscopy, but the chemical mechanism of photosynthetic water oxidation on the molecular level has remained obscure.[9,11–14] Based on a classic hypothesis in photosynthesis research proposed by Kok,[15] namely the S-cycle model, the Mn_4Ca-cluster undergos five intermediate oxidation states which are labeled as S_0, S_1, S_2, S_3, and S_4(the subscripts indicate the number of electrons extracted from S). The full S-state model presented in Figure 1.2 gives the basic understanding for oxygen evolution at the catalytically active center. Through each photon absorption and charge separation process in P680, the oxidizing equivalents accumulate step by step from S_0 to S_4. Only when the most oxidized S_4 state is reached, photooxidation of water occurs and brings the S_4 state back to the most reduced S_0 state. Y_z functions as an intermediate electron carrier between the Mn_4Ca-cluster and $P680^{\bullet+}$.[16]

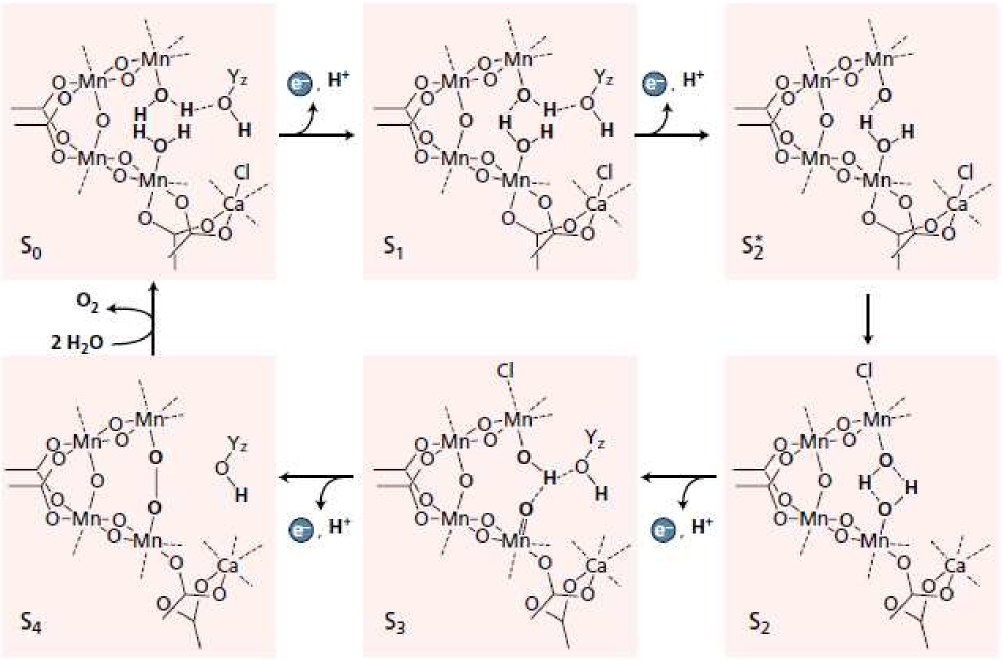

Figure 1.2.: Model of the S state cycle of oxygen evolution in PS*II*(after Tommos and Babcock 1998). [adopted from reference[8]]

This Mn_4Ca-cluster contains two active sites, Mn(*II*) and Mn(*III*) centers in S_0 state, which undergo proton coupled electron transfer to its S_4 state. Different arrangements of the Mn_4Ca-cluster OEC were revealed by EXAFS (Extended X-ray Absorption Fine Structure). The model proposed by Ferreira et al.[12] for OEC suggest a cubane-like Mn_3CaO_4 cluster linked to a forth Mn center by a mono-μ-oxo bridge. The Mn outside the Mn_3CaO_4-cubane is the reactive Mn ion, which is in S_4 state as a highly electron-deficient intermediate, either a Mn(*V*) oxo suggested by Brudvig[17] or a Mn(*IV*) oxyl radical proposed by Siegbahn.[18] The exact mechanism for oxygen bond formation is not yet fully understood. The model contains a Mn(*V*) oxo active site which undergoes nucleophilic attack by a water molecule ligated to Ca^{2+}. Based on DFT (Density Functional Theory) calculations, an alternative mechanism involves the formation of a Mn(*IV*) oxyl radical, which is a oxyl radical attack on the oxo-ligand of the Mn_3CaO_4-cubane. Although an article[19] reported later presented another organisation for the Mn_4Ca-cluster. There is common agreement that the four Mn ions are grouped in a 3 + 1 manner. The metal-to metal distances are 2.7 Å for the Mn-Mn centers within the grouped three Mn ions and 3.3 Å for the forth Mn ion to the group of three Mn ions, 3.4 Å for the Ca-Mn distance. Radiation damage caused by X-ray diffraction method has been considered as the reason for the inconsistencies between published models.[1]

1.1.2. Molecular Approaches towards Solar Water Splitting

The goal of artificial photosynthesis is to replicate the energy fixation process from sunlight to stored chemical energy conducted by green plants.[20–24] Among various alternatives, hydrogen is particularly attractive because it has very high calorific value, ie. upon combustion it releases 56.7 kcal/mol energy and leaves no carbon footprint behind. It is essentially very difficult to decompose water since it is thermodynamically unfavorable and involves multiple proton coupled electron transfers.[25,26] A highly effective photo-catalyst (PC) is urgently sought to lower the activation barrier of the four-electron reaction. The molecular approach offers one of the best solutions to mimic the natural energy conversion.

The water splitting reaction is given in Figure 1.3. This is a highly endothermic process and requires substantial amounts of input energy. The overall reaction of water splitting can be divided into two half-reactions, namely, hydrogen evolving and dioxygen producing. Between the two half-reactions, the oxidation of water to liberate oxygen gas faces the greatest challenge. In an electrochemical cell, the standard potential for the dioxygen producing reaction is 1.23 - (0.059 * pH) V vs the NHE reference electrode, that is 0.82 V under neutral condition (thermodynamic factor). As a rule of thumb, an overpotential of approximately 0.6 V is required to drive the oxidation reaction to take place at observable rate.[27] As in

$$
\begin{array}{cl}
4\,H^{+} + 4\,e^{-} \longrightarrow 2\,H_2 & E_{\mathrm{cathodic}} = 0\ \mathrm{V} - 0.059(\mathrm{pH})\ \mathrm{V} \\
O_2 + 4\,H^{+} + 4\,e^{-} \longrightarrow 2\,H_2O & E_{\mathrm{anodic}} = 1.23\ \mathrm{V} - 0.059(\mathrm{pH})\ \mathrm{V} \\
\hline
2\,H_2O \xrightarrow[PC]{h\nu} 2\,H_2 + O_2 & E_{\mathrm{rxn}} = -\,1.23\ \mathrm{V}
\end{array}
$$

Figure 1.3.: Nernstian potentials for the two half-reactions of water splitting vs Normal Hydrogen Electrode (NHE).

natural photosynthesis of green plants, the two half-reactions can be addressed separately and combined at a later stage into a single device.

With the inspiration of natural photosynthesis, the model for photochemical water splitting should at least consist of the following two components to successfully achieve a real working molecular system for the targeted reaction:[20,23,28]

1) A photosensitizing chromophore capable of directly absorbing light and performing light-induced charge separation events

The phtosensitizer converts sunlight energy into spatially separated electron/hole pairs and followed by excited-state electron transfer quenching. As a photoreaction center, the model at least consists of an electron donor (or acceptor) chromophore and an additional electron acceptor (or donor), i.e. C-A or D-C. In order to access a spatially charge separated state and hence a longer time scale before charge recombination, the molecular device has to compliant with a Donor-Chromophore-Acceptor (D-C-A) structure to have a better chance to achieve real functional model. The excited chromophore is either oxidatively quenched by the electron acceptor, D-C*-A $\rightarrow$ D-C$^+$-A$^-$, or reductively quenched by the electron donor, D-C*-A $\rightarrow$ D$^+$-C$^-$-A. In organometallic complexes, the incident light triggers metal to ligand charge transfer (MLCT) transitions. Further electron transfer derived by free-energy gradient, D-C$^+$-A$^-$ $\rightarrow$ D$^+$-C-A$^-$ or D$^+$-C$^-$-A $\rightarrow$ D$^+$-C-A$^-$, results in relatively long-lived charge separated oxidative and reductive equivalents.

2) Electron relay catalysts for water oxidation and proton reduction

Electron transfer from A$^-$ to a catalyst for reduction (Cat$_{red}$) and from a second catalyst for oxidation (Cat$_{ox}$) to D$^+$(as depicted in Figure 1.4) must happen before charge recombination. The repetition of the light absorption-electron transfer sequence is needed to provide the required number of redox equivalents for water

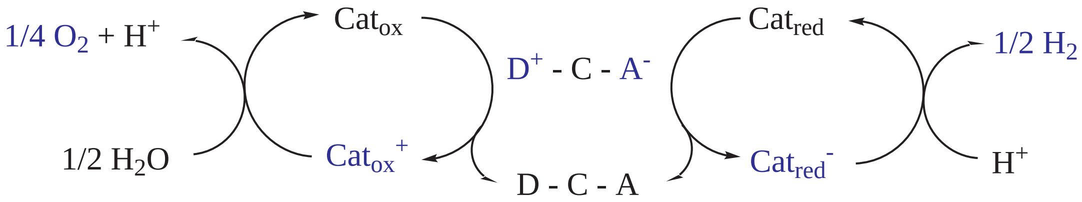

Figure 1.4.: Schematic diagram for electron relay in D-C-A unit.

splitting. Finally, the targeted two half reactions deactivate the proton reduction catalyst ($\mathrm{Cat}_{red}{}^{-}$) and oxygen evolving catalyst ($\mathrm{Cat}_{ox}{}^{+}$) to their original state.

The aforementioned two requirements should be used as a guideline for searching new artificial photosensitizers and active redox catalysts towards solar water splitting.

The success of PS*II* to convert sunlight energy into stored chemical energy prompts research of light harvest molecular devices. This is dominated by several approaches.

The first of them is based on porphyrins and metalloporphyrins as chromophores and their incorporation into molecular assemblies.[21,23,29–31] For example, molecular pentads (C-P-P-Q-Q) with two covalently liked porphyrin centers (P-P) that are attached to a carotenoid polyene (C) and a rigid diquinone (Q-Q) were studied by Gust et. al.[23] (see Figure 1.5). Photo-excitation of such pentads is based on $\pi \rightarrow \pi^*$ transitions of P-P followed by electron transfer results in the charge separated state $\mathrm{C}^{\bullet +}$-P-P-Q-$\mathrm{Q}^{\bullet -}$ with a lifetime approaching 0.5 ms.

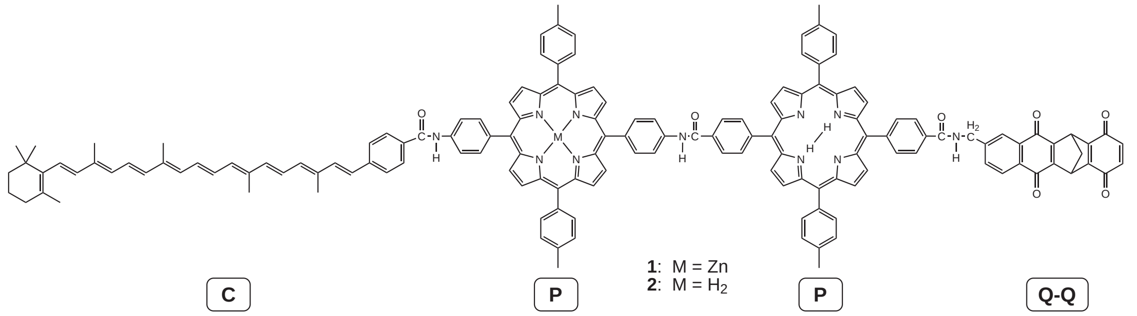

Figure 1.5.: Molecular pentads which mimic photosynthetic energy and electron transfer. (simplified from reference[23])

The second approach to light-induced charge separation is based on MLCT excited states of polypyridyl ruthenium and platinum complexes.[20,28,32–34] The absorption of light promotes an electron from a metal-based dπ orbital to a low-lying polypyridyl ligand-based π^* orbital. As illustrated in Figure 1.6, the oxidizing and reducing abilities of $[\mathrm{Ru(bpy)_3}]^{2+}$ are enhanced by 2.1 eV ($\Delta G_{ES}{}^{o}$) due to excitation from the ground state (GS) to the excited state (ES).[28] Excited-state redox potentials are calculated from ground-state redox potentials by correction with free-energy difference between two states, i.e. $\mathrm{E}^o(\mathrm{ES}^{+/0})$ = $\mathrm{E}^o(\mathrm{GS}^{+/0})$ - $\Delta G_{ES}{}^{o}/\mathrm{F}$ and $\mathrm{E}^o(\mathrm{ES}^{0/-})$ = $\mathrm{E}^o(\mathrm{GS}^{0/-})$ + $\Delta G_{ES}{}^{o}/\mathrm{F}$. The MLCT exited state of

$[Ru(bpy)_3]^{2+}$ and its derivatives displayed a lifetime in the 1-10 μs time scale.[35–37]

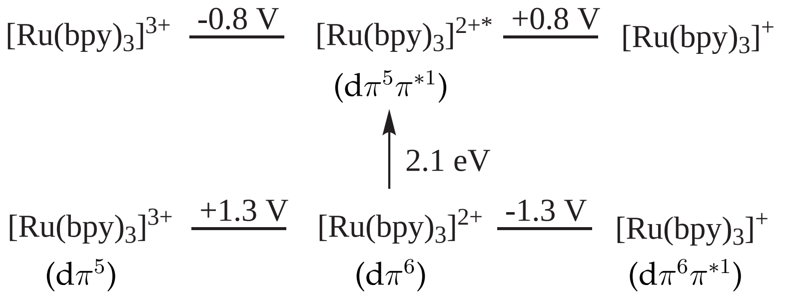

Figure 1.6.: Excited- and ground-state redox potentials (vs SCE in CH_3CN) for $[Ru(bpy)_3]^{2+}$ at 25 °C.[28]

Both approaches utilize the same underlying physical principles and both employ systematic molecular assembly strategies.

There are different types of catalysts for water oxidation explored by scientists worldwide. The first functional designed molecule for catalytic chemical oxidation of water is reported by Meyer and co-workers in 1982.[38] That is the so-called "blue dimer", $[(bpy)_2(H_2O)Ru^{III}ORu^{III}(H_2O)(bpy)_2]^{4+}$, which was primarily oxidized by 4 equivalents of Ce^{4+}.

The water oxidation catalysts were recently reviewed.[39–41] The most extensively studied homogeneous transition metal catalysts are based on ruthenium (T. J. Meyer,[28,38,42–44] C. P. Berlinguette[45,46]). Homogeneous systems based on iridium,[47–49] platinum[34,50] and heterogeneous systems based on cobalt phosphates[51–53] also received much attention.

The OEC of PS*II* is known to consist of a tetranuclear manganese cluster with two active catalytic sites (vide supra). For a long time, it was considered that two metal sites are required for effective water oxidation, but a few mononuclear catalysts were also found to be active in catalytic water splitting.[54] The first organometallic mononuclear ruthenium catalyst, $[Ru(bnp)(MePy)_2(OH_2)]^{2+}$, which showed catalytic activity in water oxidation was reported in 2005 (bnp = 4-tert-Butyl-2,6-di([1′,8′]-naphthyride-2′-yl)pyridine, Py = pyridine).[55] Since then several polypyridyl ligands were employed and the ruthenium complex, $[Ru(tpy)(bpy)(OH_2)]^{2+}$, has become the most extensively studied mononuclear catalyst.[45,56–58]

The metal complexes that catalyze the oxidation of water generally require sacrificial electron donors. The design of molecular catalysts for photogeneration of hydrogen and oxygen without utilizing sacrificial oxidants and reductants remains a major challenge. Therefore, only few heterogeneous photocatalytic system based on metal oxides[59–63] have been reported to decompose water in a non-sacrificial manner. A distinct approach of consecutive thermal hydrogen liberation and light-induced oxygen evolution by a Ru(*II*) hydrido-hydroxo pincer complex was presented by Milstein et al. in 2009,[64] which drew a lot of attentions.[27,65–69] They revealed that the light-induced oxygen-oxygen bond formation is an intramolecular process and has highlighted as reductive elimination of hydrogen peroxide. This evidenced that the oxygen bond formation does not necessarily involve metal oxo intermediates.

With regard to the photocatalytic hydrogen productions, early examples of multi-component photosystems incorporating light absorber, electron relays and hydrogen reduction catalysts were developed.[70–72] More recently, various Ir-, Pt-based phtosensitizers were employed in cooperation with Rh or Co catalyst to effectively reduce protons.[73–75] The single-component supramolecular photocatalysts, mainly Ru-Pt,[76] Ru/Ir-Co[77,78] and Ru-Ru[79] bimetallics as well as Ru-Rh-Ru trimetallics,[80] were also developed to combine the role of a photosensitizer and a catalyst for hydrogen reduction. However, there is another promising approach to hydrogen production, which is based on mixed-valence dinuclear transition metal complexes.[5,81] For instance, Nocera and co-workers have shown that Rh^0Rh^{II}-based complexes with fine-tuned ligand systems are efficient catalysts for hydrogen production from acidic solution.[81]

The dinuclear tungsten systems are also potential photocatalysts, initiating the research efforts in our group.

1.2. State of Research in the Work Group

The chemistry of half-sandwich complexes of tungsten in medium oxidation states was previously established in our group by Dr. Christian Cremer.[82–84] The previous research are summarized below.

The bipyridyl substituted half-sandwich tungsten (*IV*) complexes of the type $Cp^*W(R_2bpy)Cl_3$ (R = Me, NMe_2, ^{t}Bu) were obtained in good yields through one electron reduction of the versatile starting material Cp^*WCl_4 with TDAE (Tetrakis(dimethylamino)ethylene) in the presence of bipyridyl donors[82] (see Figure 1.7). The neutral W^{IV} complexes were shown to have C_s symmetry (facial isomer) by ^{1}H-NMR spectroscopy, with reduced steric repulsion between the Cp^* and one of the bipyridyl rings than in the meridional isomer. Susceptibility measurements showed that these 18-electron d^2-configured complexes are weakly paramagnetic with magnetic moments of 0.5 to 0.8 μ_B at room temperature.

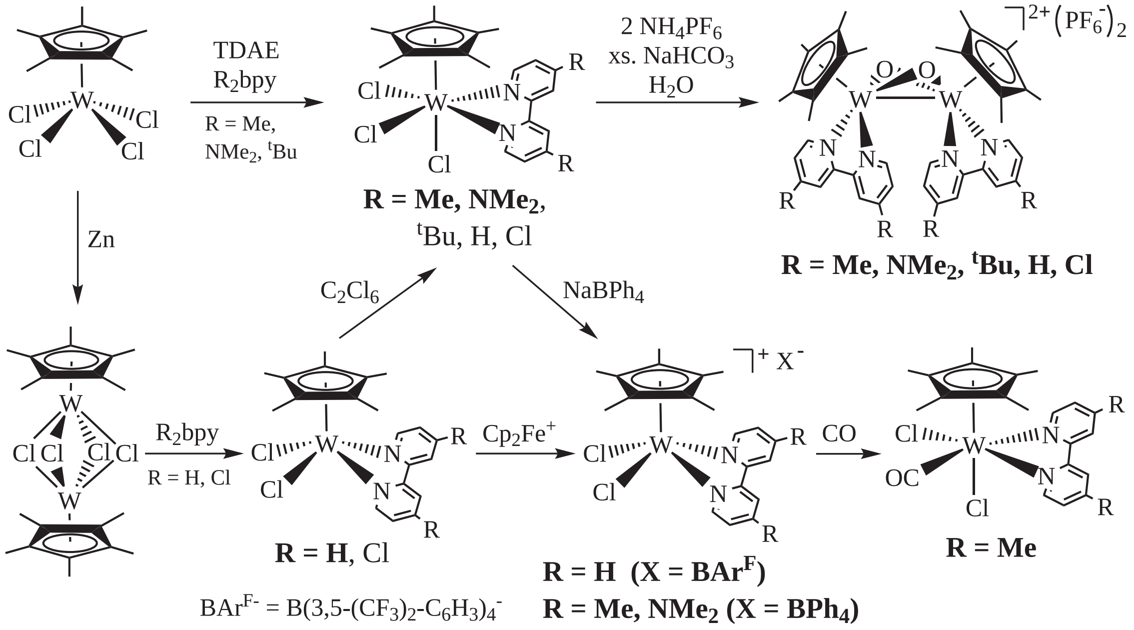

Figure 1.7.: Sythetic pathway for bipyridyl substituted half-sandwich W^{IV}, cationic W^{IV} and dinuclear $W^{IV}W^{IV}$ μ-oxo-bridged complexes.[82–84]

Facile ionization of one chlorido ligand in this electron rich complexes enables the isolation of corresponding cationic tungsten (*IV*) complexes $[Cp^*W(R_2bpy)Cl_2]^+$ (for R = Me, NMe_2). Due to the very low solubility of the trichlorido complexes $Cp^*W(R_2bpy)Cl_3$ for the unsubstitutied and more electron withdrawing Cl substituted bipyridines, another synthetic pathway was sought. The related W^{III} complexes of $Cp^*W(R_2bpy)Cl_2$ (for R = H, Cl) have been successfully obtained by using Zn powder to reduce the starting material to give $[Cp^*WCl_2]_2$ followed by bipyridyl coordination.[84] Further oxidation of neutral $Cp^*W(bpy)Cl_2$ complex by ferrocenium leads to the corresponding catioic W^{IV} complex of $[Cp^*W(bpy)Cl_2]^+$. It should be noted that the magnetic behavior of these cationic tungsten (*IV*) compounds can be also tuned by variation of the nature of the bipyridyl ligands.[84] 1/T-dependence of ^{1}H NMR resonance of $[Cp^*W(R_2bpy)Cl_2]^+$ complexes showed linear behavior for R = H (pure triplet state) and deviation from Curie-Weiss behavior for R = Me, NMe_2 (singlet-triplet spin equilibrium). The more electron donating the substituent, the bigger the HOMO-LUMO energy gap, hence the lower preference for the triplet states.

The half-sandwich trichlorido mononuclear complexes of tungsten(*IV*) can be cleanly converted to the dinuclear bis μ-oxo-bridged tungsten(*IV*,*IV*) complexes, $[(Cp^*W(R_2bpy)(\mu{-}O))_2]^{2+}$ (R = Me, NMe_2, ^{t}Bu, H, Cl), which are both water soluble and stable. These compounds display remarkable spectro- and electrochemical properties.[83] Moreover, the redox potentials of these oxo-complexes can be tuned over a wide range by using different R_2bipy ligands and display an excellent correlation with the σ Hammett-parameter of the R substituents (Figure 1.8). Therefore, in combination with the strong absorptions in the visible and NIR range (up to $\epsilon = 10^4\ M^{-1}cm^{-1}$), these systems were deemed to have a high potential as photochemical redox catalysts and might combine the role of a redox catalyst and a photosensitizer.

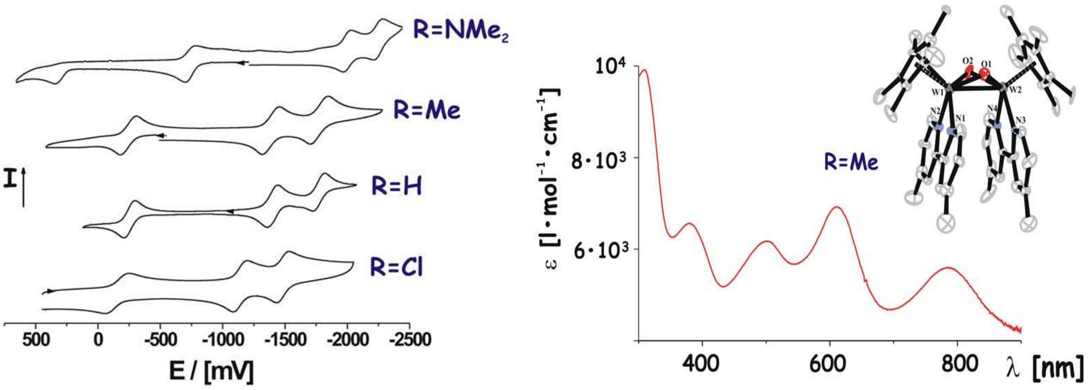

Figure 1.8.: Dependence of electrochemical properties of complexes on the substituents R in bipyridine ligands and absorbance spectrum of complex $[(Cp^*W(R_2bpy)(\mu{-}O))_2]^{2+}$ representative.[83]

In order to access the electrochemically generated redox couples of $W^{IV}W^{IV}$ oxo-complexes, the chemical oxidation and reduction reactions were carried out. The tricationic paramagnetic tungsten(*IV*,*V*) complex $[(Cp^*W(Me_2bpy)(\mu{-}O))_2]^{3+}$ was isolated by one-electron oxidation with ferrocenium. (see Figure 1.9) In contrast to previously investigated Ru complexes, protonation of the novel tungsten(*IV*,*IV*) complexes is possible, which is an important step in the hydrogen reduction process. Two equivalents of sodium naphthalenide were used to achieve the diamagnetic tungsten(*III*,*III*) complexes of $[(Cp^*W(R_2bpy)(\mu{-}O))_2]$ (R = Me,

^{t}Bu). The X-ray crystal structure of this tungsten(*III,III*) complex (R = Me) differs from all other structures and displays a *trans* arrangement of the Cp* ligands with a flat W_2O_2 ring. Although, the *cis* geometry is maintained on the time scale of cyclic voltammetry (CV) measurement, which is the reason why the process of redox couple $W^{IV}W^{III}/W^{III}W^{III}$ still is electrochemically reversible. The mixed valence mono cationic complex $[(Cp^*W(Me_2bpy)(\mu{-}O))_2]^+$ was isolated as a side product which showed structural resemblance of *cis* tungsten(*IV,IV*) compounds. The lower valent $W^{III}W^{III}$ complex of $[(Cp^*W(^tBu_2bpy)(\mu{-}O))_2]$ is capable of reducing protons to dihydrogen under acidic condition.

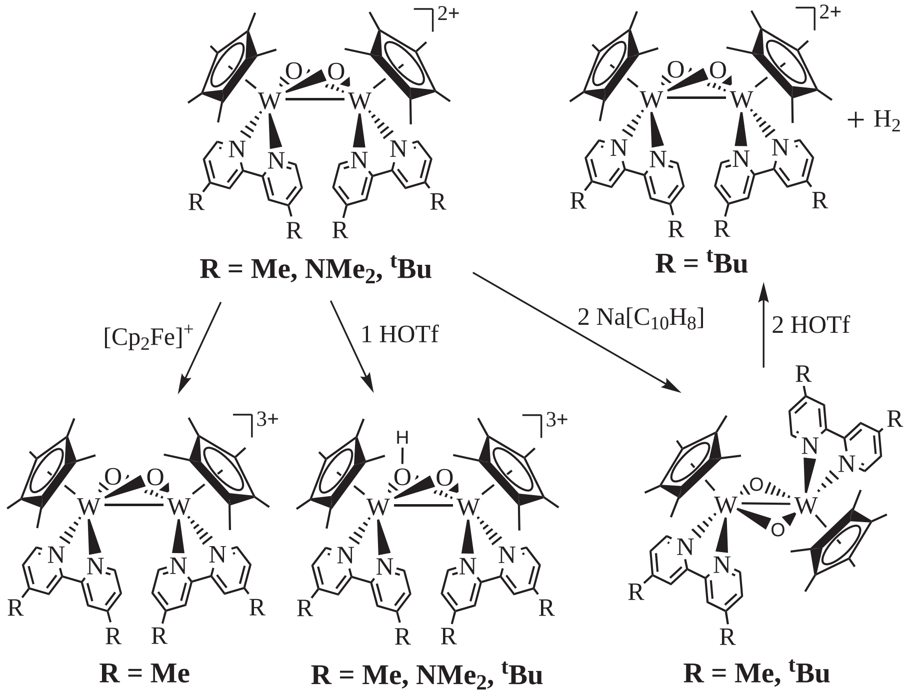

Figure 1.9.: Reactivity of dinuclear $W^{IV}W^{IV}$ μ-oxo-bridged complexes.[83]

Despite all advantages of the novel dinuclear bis μ-oxo-bridged tungsten(*IV,IV*) half-sandwich complexes, H_2 has not yet been released from neutral to acidic solutions in preliminary irradiation experiments. This might be caused by the short lived excited state, which decays to the ground state before the electron is transferred to the proton.

1.3. The Aim and Structure of This Thesis

This dissertational work is aimed to design and synthesize dinuclear group 6 transition metal complexes with improved electrochemical and photophysical properties towards water splitting. In pursuing this goal, the diimine ligands as well as the metal center are to be modified.

Previous work on $W^{IV}W^{IV}$ systems established a strong dependence of the redox potentials on the electron-withdrawing/donating properties of the substituents R of the bipy ligands. The potential for oxidation can be increased by 0.62 V going from NMe_2 to Cl substituents of the 4.4-disubstituted bipy ligand. Even more electron-withdrawing substituents like R = COOMe are to be used in bipy ligand supposedly leading to even more positive redox potentials. Two new electron-withdrawing 1,10-phenanthroline based ligands, dpphen (4,7-diphenyl-1,10-phenanthroline) and dpq (dipyrido[3,2-*f*:2′,3′-*h*]quinoxoline), will be applied (Figure 1.10). These ligands are well-recognized as photosensitive ligands due to low lying LUMOs with strong π^* characters.[85,86] In combination with their electron-acceptor properties, a significant increase of efficiency for light absorbance as well as charge separation is anticipated. Consequently, extended excited state life times of the aforementioned tungsten(*IV*) and molybdenum(*IV*) complexes are deemed accessible.

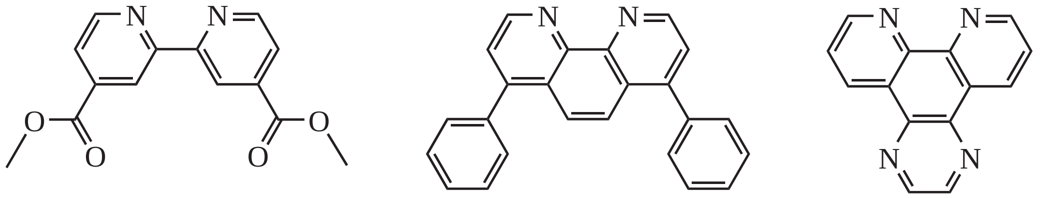

(COOMe)$_2$bpy **dpphen** **dpq**

Figure 1.10.: New electron-withdrawing ligands used in this thesis.

The redox potentials of molybdenum complexes are supposed to increase with regard to the tungsten complexes,[87] which offer a better chance to oxidize water. Therefore, the molybdenum(*IV*) analogues of the dinuclear tungsten(IV) complexes were also to be explored.

In these tungsten(*IV*) and molybdenum(*IV*) organometallic architecture, the Cp* ligands will be employed as donor components and the diimine ligands will perform as acceptors.

The synthesis of various mononuclear half-sandwich tungsten(IV) and molybdenum(IV) complexes will be described in Chapter 2. The synthetic routes, spectroscopic and electrochemical studies of dinuclear μ-oxo-bridged tungsten and molybdenum complexes will be presented in chapter 3 and 4 respectively. In chapter 5, a summary of the thesis will be given. The experimental details will be specified in Chapter 6.

2. Mononuclear Half-Sandwich Tungsten(*IV*) and Molybdenum(*IV*) Halido Complexes

The organometallic chemistry of the cyclopentadiene ligand is generally well developed. The monocyclopentadienyl halido complexes of d- and f-block transition metals have been reviewed by Poli in 1991.[88] The monocyclopentadienyl halido compounds of tungsten and molybdenum in oxidation state *II*,[89–91] *III*,[91,92] *IV*,[93–98] *V*,[99–104] *VI*[105,106] were extensively studied by Poli, Schrock and Green. In the original work of Cremer,[82] a new series of Cp* ($\eta^5 - C_5Me_5$) tungsten(*IV*) complexes with an additional bipyridyl ligand, [Cp*W(R_2bpy)Cl_3] (R = Me, NMe_2, ^{t}Bu), was prepared by one-electron reduction of the versatile starting material [Cp*WCl_4]. The synthesis and characterization of dpq, dpphen, $(COOMe)_2$bpy and $({}^t Bu)_2$bpy substituted half-sandwich W^{IV} and Mo^{IV} halido complexes are presented herein.

2.1. Starting Materials

2.1.1. Pentamethylcyclopentadienyl Tungsten(*V*) and Molybdenum(*V*) Chlorido Complexes

The starting materials [Cp*MCl_4] (M = W, Mo) were prepared in three reaction steps from the commercially available metal hexacarbonyls (see Reaction Scheme 2.1). Tungsten/molybdenum hexacarbonyl was refluxed with with butyronitrile to give fac-$M(CO)_3(NCPr)_3$,[107] followed by reaction with Cp*H to generate Cp*$M(CO)_3H$,[108] which was oxidized with PCl_5 to Cp*MCl_4 (M = W, Mo).[99,109]

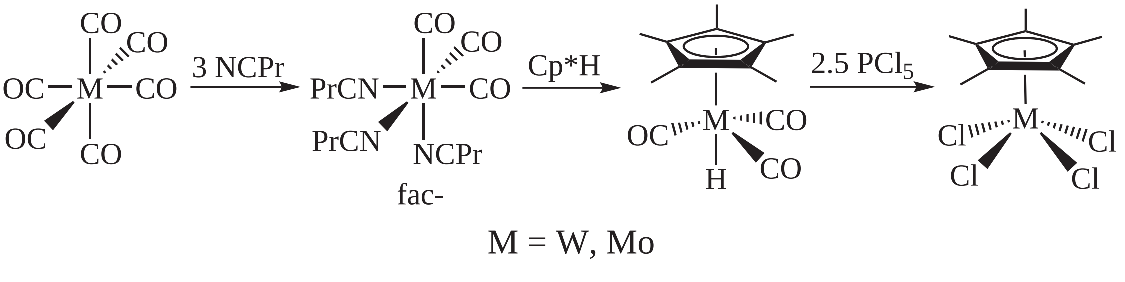

Reaction Scheme 2.1: Synthetic pathway of pentamethylcyclopentadienyl tungsten and molybdenum tetra-chlorido starting materials.

The C_{3v} symmetry of facial W(CO)$_3$(NCPr)$_3$ compound was verified by infrared spectroscopy, which showed two v(C-O) vibrational bands at 1913 and 1796 cm^{-1} in dichloromethane solution. The crystalline compounds Cp*M(CO)$_3$H (M = W, Mo) can be easily purified by sublimation. The orange Cp*WCl$_4$ and purple Cp*MoCl$_4$ complexes are barely soluble in organic solvents.

2.1.2. Dinuclear Chlorido Bridged Molybdenum(*IV*,*IV*) Complex

The chlorido bridged molybdenum(*IV*,*IV*) complex [Cp*MoCl$_3$]$_2$ (**1-1**) was obtained by one-electron reduction of Cp*MoCl$_4$ with amalgamated sodium as described by Poli.[94] (see Reaction Scheme 2.2)

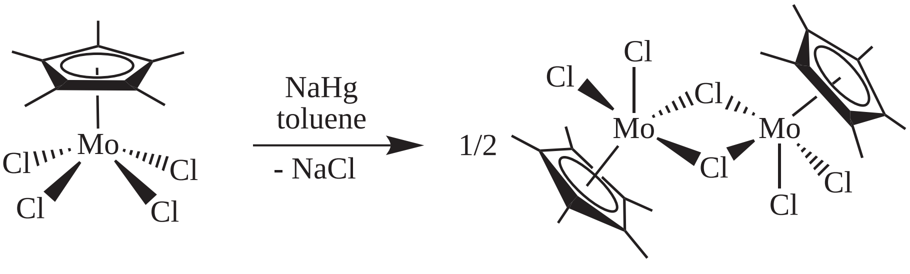

1-1 (79%)

Reaction Scheme 2.2: Synthesis of dinuclear chlorido-bridged molybdenum(*IV*,*IV*) complex.

To avoid formation of [(Cp*MoCl$_2$)$_2$], the addition of NaHg to Cp*MoCl$_4$ has to be carefully controlled. The olive green chlorido bridged molybdenum(*IV*,*IV*) complex **1-1** is extremely air sensitive and insoluble in innocent solvents, such as toluene. The ^{1}H NMR spectrum of the obtained paramagnetic compound **1-1** in CD$_2$Cl$_2$ shows a broad signal at δ = - 4.19 ppm ($\omega_{1/2}$ = 42.3 Hz).

2.2. Anionic Tungsten(*IV*) and Molybdenum(*IV*) Complex

To improve the solubility of the starting material, Cp*WCl$_4$ was reduced with half equivalent of TDAE in the presence of bis(triphenylphosphoranylidene)-ammonium chloride (PPNCl). The chemical structure of PPNCl is shown in Figure 2.1.

PPN$^+$ assists the isolation of the reduced anion and forms a crystalline salt which is otherwise difficult to crystallize. The brown anionic tungsten(*IV*) compound PPN[Cp*WCl$_4$] (**1-2**) is obtained in good yield of 83% (see Reaction Scheme 2.3). This paramagnetic compound is well soluble in polar organic solvents. A broad singlet is observed by proton NMR spectroscopy at 6.84 ppm in CD$_2$Cl$_2$ attributed to the Cp* ligand at room temperature.

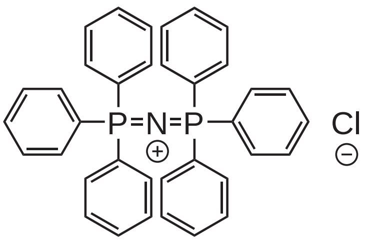

Figure 2.1.: Structure of PPNCl.

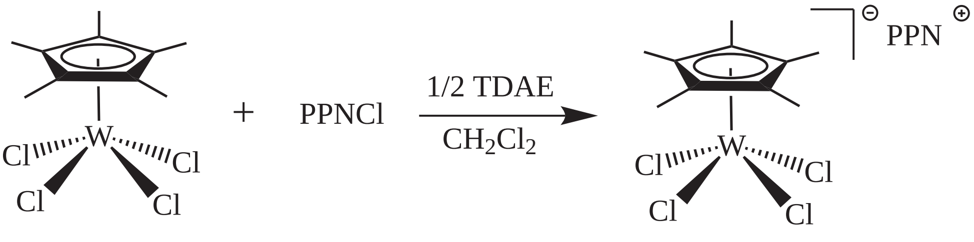

1-2 (83%)

Reaction Scheme 2.3: Synthesis of the half-sandwich tungstate(*IV*) complex **1-2**.

The synthesis of Complex PPN[Cp*MoCl$_4$] was adopted from the procedure described by Poli.[94] The dinuclear chlorido bridged molybdenum(*IV,IV*) complex was mixed with PPNCl to give the green paramagnetic molybdate(*IV*) compound PPN[Cp*MoCl$_4$] (**1-3**) with a yield of 89% (see Reaction Scheme 2.4). The ^{1}H-NMR spectrum of complex **1-3** showed a broad singlet at - 13.96 ppm in CD$_2$Cl$_2$ at room temperature.

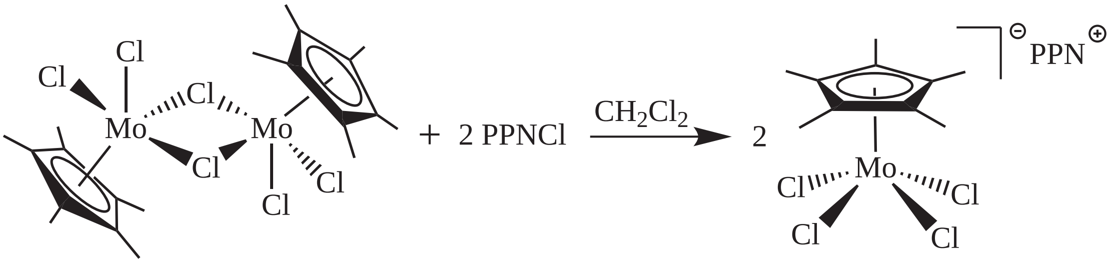

1-1 **1-3** (89%)

Reaction Scheme 2.4: Synthesis of the half-sandwich molybdate(*IV*) complex **1-3**.

2.3. Bidentate N-donor Ligand Adducts of Tungsten(*IV*) and Molybdenum(*IV*)

2.3.1. Synthesis of dpq-W^{IV} (2-a)

The bidentate dpq ligand was employed to synthesize the monomeric chlorido half-sandwich tungsten complex [Cp*W(dpq)Cl$_3$] (**2-a**). The dpq substituted half-sandwich tungsten(*IV*) complex **2-a** was obtained in good yield (89%) from reaction of PPN[Cp*WCl$_4$] with the dpq ligand as shown in Reaction Scheme 2.5.

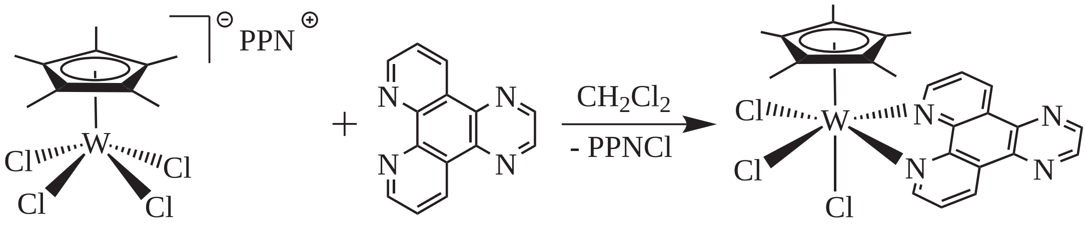

1-2 **dpq** **2-a** (89%)

Reaction Scheme 2.5: Synthesis of the dpq substituted half-sandwich tungsten(*IV*) trichlorido complex [Cp*W(dpq)Cl$_3$] (**2-a**).

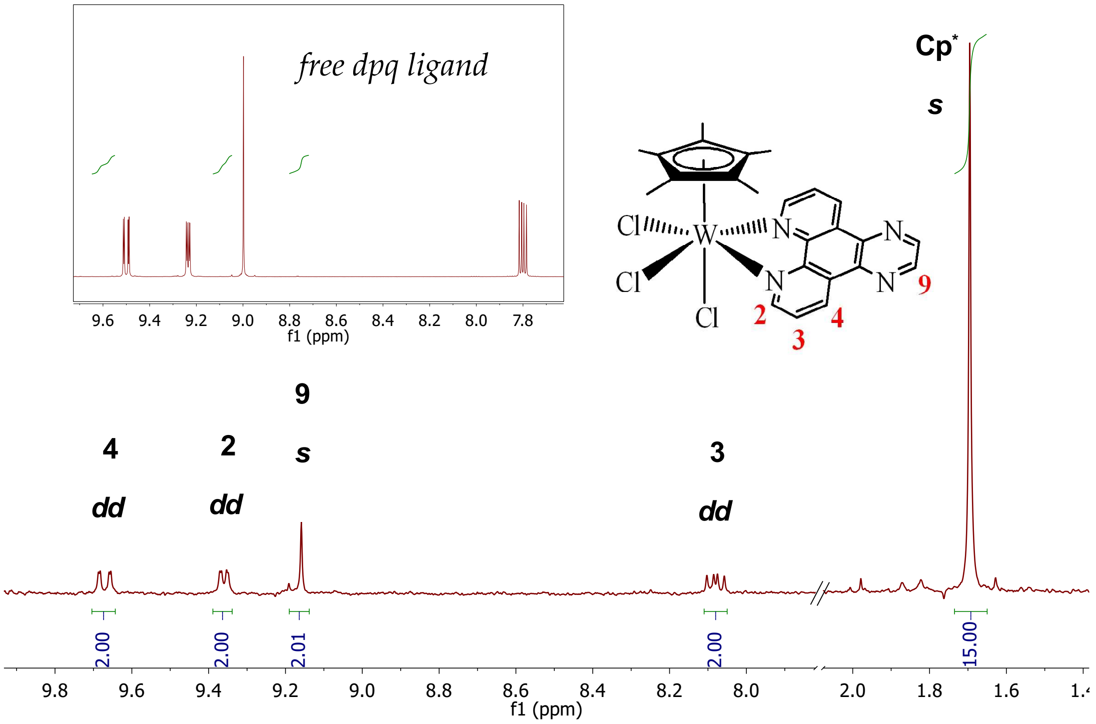

Figure 2.2.: ^{1}H-NMR Spectrum of complex [Cp*W(dpq)Cl$_3$] (**2-a**) in CD$_2$Cl$_2$ at 300 MHz. The inlay shows the ^{1}H-NMR Spectrum of the free dpq ligand in CD$_2$Cl$_2$.

The mononuclear half-sandwich dpq-W^{IV} complex **2-a** has a blueish purple color and is highly insoluble in organic solvents. The proton NMR spectrum of **2-a** presented in Figure 2.2 shows a downfield shift of the attached dpq ligand compared to the free ligand. The ^{1}H-NMR spectrum revealed three doublets of doublets (***dd***) at 9.67, 9.36 and 8.08 ppm for the protons in para, ortho and meta positions respectively, consistent with the C_s symmetry of **2-a** as a facial isomer. The electron impact ionization mass spectrum of **2-a** showed the highest mass of m/z = 656 for the molecular ion [2-a]$^{+}$. The purity of product **2-a** was evidenced by elemental analysis.

2.3.2. Synthesis of dpphen-W^{IV} (2-b)

The diphenyl substituted phenanthroline ligand, 4,4′-diphenyl phenanthroline (dpphen), was used to increase the donor ability and extend the conjugated system of the N-donor type molecule. The desired dpphen substituted tungsten(*IV*) tri-chlorido complex [Cp*W(dpphen)Cl$_3$] (**2-b**) was synthesized in a good yield of 84% (see Reaction Scheme 2.6). The structure was confirmed by the proton NMR spectroscopy, mass spectrometry, elemental analysis and X-ray crystallography (see below).

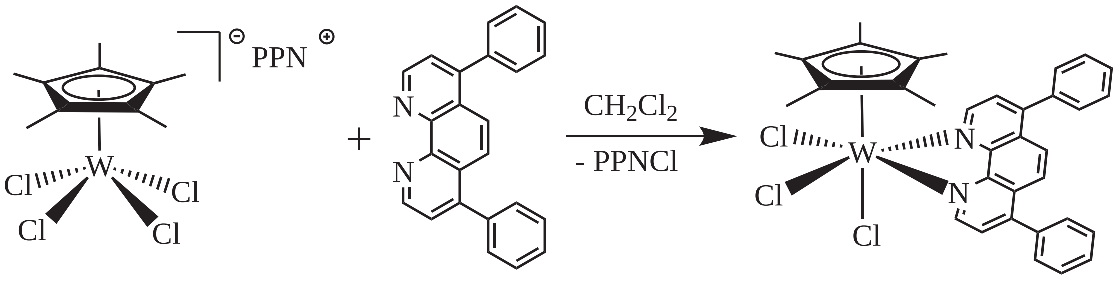

1-2 **dpphen** **2-b** (84%)

Reaction Scheme 2.6: Synthesis of dpphen half-sandwich tungsten(*IV*) tri-chlorido complex [Cp*W(dpphen)Cl$_3$] (**2-b**).

The green compound dpphen-W^{IV} (**2-b**) is moderately soluble in polar organic solvents. Slightly broadened signals were observed in the ^{1}H-NMR spectrum for this 18 electron d^2-configured compound (Figure 2.3). The ^{1}H-NMR spectrum of complex **2-b** showed a singlet at 8.08 ppm for protons in position 7 and two sets of doublets at 9.31 and 7.88 ppm for the protons in the ortho and meta positions (position 2 and 3) respectively.[*] This provided evidence for a C_s symmetrical

---

[*] The labeling scheme is explained in Figure 2.3.

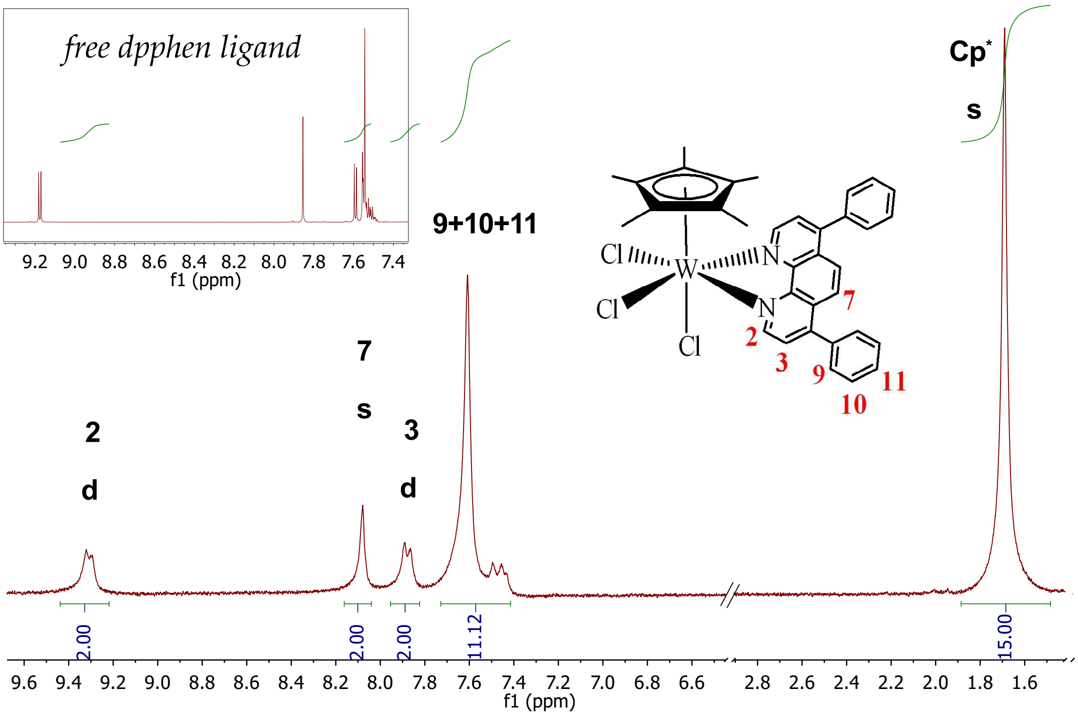

Figure 2.3.: ^{1}H-NMR Spectrum of complex [Cp*W(dpphen)Cl$_3$] (**2-b**) in CD_2Cl_2 at 200 MHz. The inlay shows the ^{1}H-NMR Spectrum of the free dpphen ligand in CD_2Cl_2.

structure and the existence of a facial isomer. The aromatic proton resonances of the coordinated dpphen ligand were shifted to downfield with regard to the free ligand.

X-ray crystal structure of 2-b

Single crystals of complex **2-b** suitable for X-ray crystal structural analysis were obtained from Et_2O/DCM solution and unambiguously confirmed the structure of the facial isomer. (see Figure 2.4) Selected bond lengths and angles of complex dpphen-W^{IV} are given in Table 2.1. The data collection parameters are listed in the Appendix.

The structure of this tungsten(*IV*) tri-chlorido complex can be described as a pseudo-octahedral geometry with the Cp* ligand occupying one co-ordination site. The equatorial plane, which includes two nitrogen atoms of the ligand dpphen (N1, N2) and two Cl ligands, Cl2 and Cl3, bends towards Cl1 in the trans position of the Cp* ligand. The Cl1-W1-Z1 angle amounts to 176.20°.* The W1-Z1

---

* Z1 is the centroid of the Cp ring.

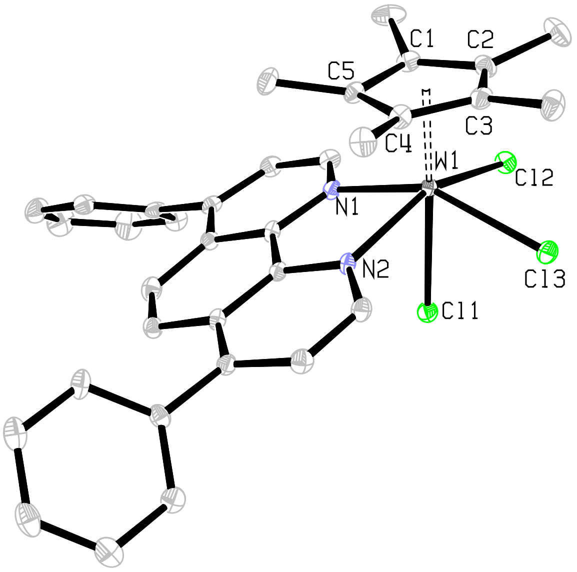

Figure 2.4.: Crystal structure of complex 2-b (Ortep-representation; 50%). For reasons of clarity, hydrogen atoms and the co-crystallized dichloromethane solvent molecule are not shown.

Table 2.1.: Selected bond lengths [Å] and angles [°] of complex 2-b.[a]

W1-N1	2.163(2)	W1-N2	2.169(6)
W1-Cl1	2.5449(7)	W1-Cl2	2.4728(7)
W1-Cl3	2.4579(7)	W1-C1	2.238(3)
W1-C2	2.351(3)	W1-C3	2.497(3)
W1-C4	2.415(3)	W1-C5	2.265(3)
W1-Z1[b]	2.016		
N1-W1-N2	75.52(9)	N1-W1-Cl1	72.35(7)
N1-W1-Cl2	89.30(7)	N1-W1-Cl3	150.28(7)
N2-W1-Cl1	72.34(7)	N2-W1-Cl2	149.16(7)
N2-W1-Cl3	94.64(7)	Cl1-W1-Cl2	77.55(2)
Cl1-W1-Cl3	77.95(2)	Cl2-W1-Cl3	85.36(2)
N1-W1-Z1	107.17	N2-W1-Z1	103.87
Cl1-W1-Z1	176.20	Cl2-W1-Z1	106.24
Cl3-W1-Z1	102.39		

[a] estimated standard deviations in parentheses

[b] Z1 is the ring centroid of carbon atoms C1-C5.

distance (2.016 Å) in this half-sandwich tri-chlorido W^{IV} complex is significantly shorter than in Me_2bpy substituted complex $[(\eta^5\text{-}C_5Me_4Et)W(Me_2bpy)Cl_3]$ (2.20 Å). A slight distortion of the Cp* ring towards a η^3 ligand coordination was noticed. The η^3-hapticity motif incorporating carbon atoms C1, C2 and C5 is notable from short W-C bonds of 2.24 - 2.35 Å while long W-C distances of 2.42 - 2.50 Å are observed for the ring atoms C3 and C4. The methyl groups of the Cp* ligand are bending out of the Cp-ring plane opposite to the equatorial plane. It is noteworthy that the bond length of Cl1-W1 (2.5449 Å) is significantly longer than the Cl2-W1 (2.4728 Å) and Cl3-W1 (2.4579 Å) distances. The phenyl substituents of the dpphen ligand are twisted out of the penantroline plane by + 42.6° and - 51.4° respectively. Slightly bigger torsion angles (55.1° and 50.2°) were found in iridium complex $[Ir(epqc)_2(dip)]^+$.[110]

2.3.3. Synthesis of $(COOMe)_2$bpy-W^{IV} (2-c)

The previously established Hammett correlation for the redox potentials of the bipy substituted complexes $[(Cp^*W(R_2bpy)(\mu{-}O))_2]^{2+}$ (R=NMe$_2$, Me, H, Cl) revealed that more electron withdrawing R substituents lead to higher oxidation potentials of the ditungsten complexes. For the even more electron deficient R$_2$bpy ligand with R = COOMe substituents, a potential of +0.68 V (vs. NHE) should be accessible, hence a higher potential as a water oxidation catalyst is anticipated. There is evidence that rhenium bipyridyl CO_2 reduction catalysts covalently attached to a TiO_2 surface through carboxylate groups display increased photocatalytic reductive ability.[111] A carboxylate functionalized dinuclear tungsten oxo-bridged complex bonded to a TiO_2 semiconductor surface could serve as the reaction center by acting as a trap for excited electrons.

Synthetic access to the desired complex was achieved by reaction of the corresponding 4,4'-dicarboxylate bipy ligand with PPN[Cp*WCl$_4$]. At room temperature, an unknown paramagnetic product along with unseparated side products was obtained. Due to the carboxylate group, the solubility of the obtained complexes were high in both polar and non-polar solvents, which hampered the isolation of the desired pure compound. In the product, unshifted v(CO) band compared to the free ligand (1732 cm^{-1}) was observed in the infrared (IR) spectrum.

In order to access complex Cp*W(COOMe$_2$bpy)Cl$_3$ (**2-c**), the reaction temperature was risen to 100 °C for two days (Reaction Scheme 2.7). A further color change was observed: in acetonitrile from brown to dark purple and in dichloromethane from brown to dark blue. The ^{1}H-NMR spectroscopy proved that the two differently colored compounds are identical. The IR spectrum of this product displays

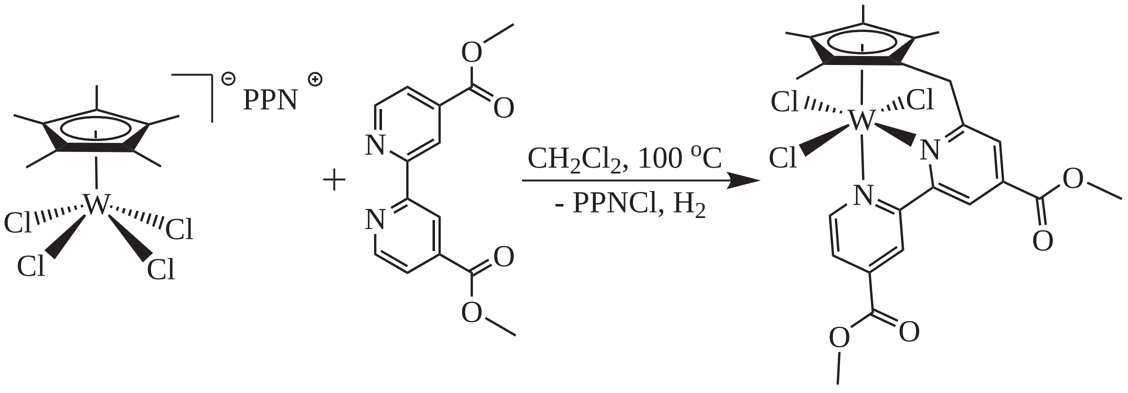

1-2 **(COOMe)$_2$bpy** **2-c**

Reaction Scheme 2.7: Synthesis of (COOMe)$_2$bpy substituted half-sandwich tungsten(*IV*) tri-chlorido complex **2-c** in elevated temperature.

two v(CO) bands of strong intensity at wavenumbers 1713 and 1731 cm^{-1}. The ^{1}H-NMR spectrum was hard to interpret, suggesting a low symmetrical structure. This was confirmed by X-ray diffraction. Apparently hydrogen elimination from a Cp* methyl group and the ortho-position of the bpy ligand is enforced by the high temperatures.

X-ray crystal structure of 2-c

Suitable single crystals of complex **2-c** for X-ray diffraction were obtained from a diluted filtered solution of acetonitrile after high temperature reaction. The refined crystal structure presented in Figure 2.5 contains an ester group, which is rotationally disordered over two split positions. Selected bond lengths and angles are listed in Table 2.2.

The crystal structure of complex (COOMe)$_2$bpy-W^{IV} displays a pseudo-octahedral geometry. It is a meridional isomer with three Cl and one N occupying the equatorial plane. It is noteworthy that dihydrogen was apparently eliminated between Cp* and (COOMe)$_2$bpy ligands. Bond C1-C6 is bent towards the (COOMe)$_2$bpy ligand (C6 atom is 0.1329 Å below the Cp plane), while the other four methyl groups of Cp* ligand are pointing away from the equatorial plane. The centroid of the Cp ring, Z1, and W1, N2 is forming an angle of 172.87° which is 3.33° smaller than the facial isomer. The three W-Cl bond lengths are essentially identical and in the narrow range of 2.4392 to 2.4538 Å. The W1-N1 bond in the equatorial plane is rather short (2.1108 Å) while the W1-N2 bond in the trans position of Cp* is elongated to 2.2358 Å.

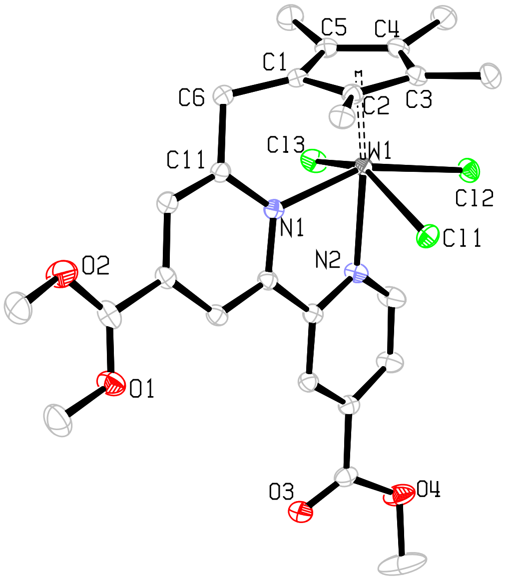

Figure 2.5.: Crystal structure of complex 2-c (Ortep-representation; 50%). For reasons of clarity, hydrogen atoms are not shown.

Table 2.2.: Selected bond lengths [Å] and -angles [°] of 2-c.[a]

W1-N1	2.1108(13)	W1-N2	2.2358(13)
W1-Cl1	2.4538(4)	W1-Cl2	2.4392(4)
W1-Cl3	2.4406(4)	W1-C1	2.2297(15)
W1-C2	2.2884(15)	W1-C3	2.3355(15)
W1-C4	2.4396(16)	W1-C5	2.4767(16)
W1-Z1[b]	2.040		
N1-W1-N2	72.59(5)	N1-W1-Cl1	85.42(4)
N1-W1-Cl2	155.07(4)	N1-W1-Cl3	92.79(4)
N2-W1-Cl1	74.11(4)	N2-W1-Cl2	83.02(4)
N2-W1-Cl3	75.24(4)	Cl1-W1-Cl2	83.012(13)
Cl1-W1-Cl3	148.365(14)	Cl2-W1-Cl3	85.724(15)
N1-W1-Z1	100.38	N2-W1-Z1	172.87
Cl1-W1-Z1	106.96	Cl2-W1-Z1	104.09
Cl3-W1-Z1	104.43	C1-C6-C11	107.14(13)

[a] estimated standard deviations in parentheses

[b] Z1 is the ring centroid of carbon atoms C1-C5.

2.3.4. Synthesis of dpq-Mo^{IV} (3-a)

The molybdenum analogue of the half-sandwich tungsten(*IV*) tri-chlorido complex [Cp*Mo(dpq)Cl$_3$] (**3-a**) was synthesized in a similar manner by reaction of half-sandwich molybdate(*IV*) complex **1-3** with dpq ligand in DCM solution (see Reaction Scheme 2.8).

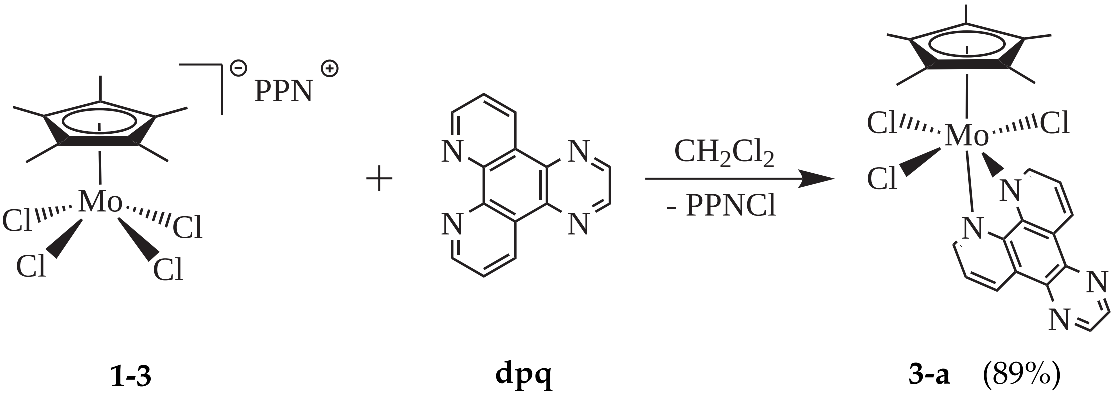

Reaction Scheme 2.8: Synthesis of the molybdenum(*IV*) half-sandwich tri-chlorido complex Cp*Mo(dpq)Cl_3 (**3-a**).

The purple product **3-a** is obtained in a good yield of 89% and is also rather insoluble in organic solvents. For a very low concentrated solution of complex [Cp*Mo(dpq)Cl_3] in CD_3CN, an ^{1}H-NMR spectrum was recorded, Figure 2.6.

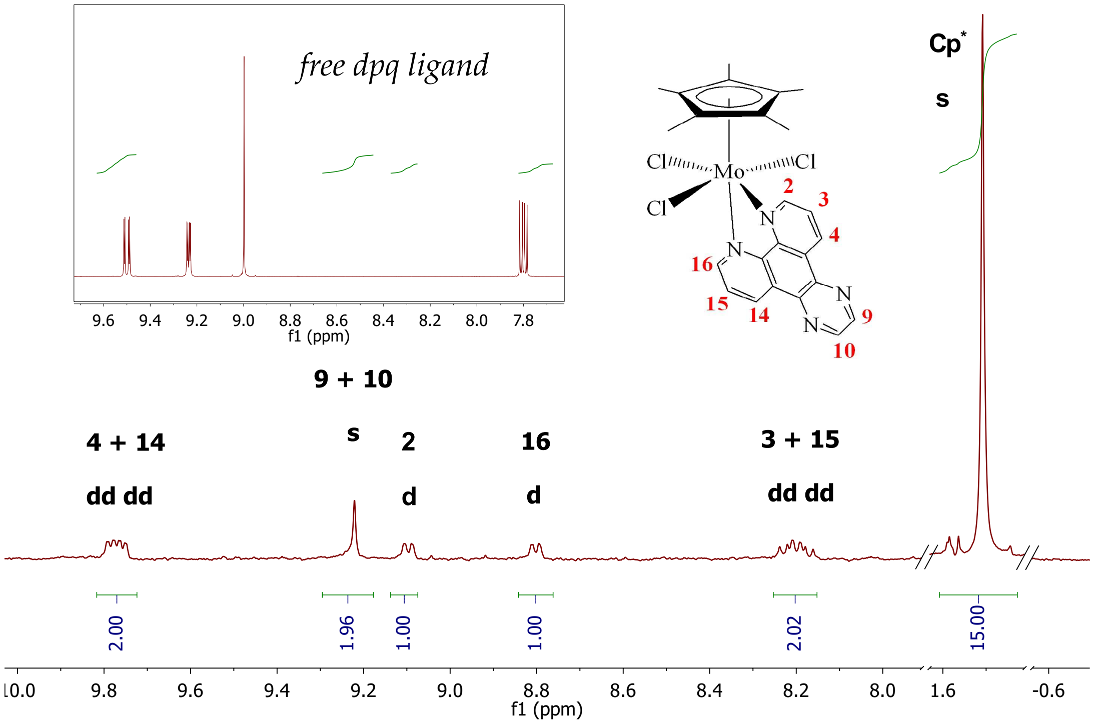

Figure 2.6.: ^{1}H-NMR Spectrum of complex [Cp*Mo(dpq)Cl_3] (**3-a**) in CD_3CN at 300 MHz. The inlay corresponds to the ^{1}H-NMR Spectrum of the free dpq ligand in CD_2Cl_2.

Comparison of the ^{1}H-NMR spectra of the fac-tungsten analogue [Cp*W(dpq)Cl_3] (**2-a**) and compound **3-a** revealed that the tri-chlorido Mo^{IV} complex has apparently a meridional structure. The protons $H_{[2]}$ and $H_{[16]}$ of the dpq ligand are diastereotopic and appear as doublets at δ = 9.10 and 8.80 ppm in the ^{1}H-NMR spectrum. The protons $H_{[3]}$ and $H_{[15]}$ are overlapping (two ***dd*** close to 8.20 ppm). Peaks for protons $H_{[4]}$ and $H_{[14]}$ are very close in chemical shift, while the peaks for protons $H_{[9]}$ and $H_{[10]}$ has the same chemical shifts.

2.3.5. Synthesis of ^{t}Bu$_2$bpy-Mo^{IV} (3-d)

The molybdenum tri-bromido analogue of the bpy substituted half-sandwich tungsten(*IV*) complex CpMo(bipy)Br_3 was published in 1966.[112] The related half-sandwich tri-chlorido complex Cp*Mo(R_2bpy)Cl_3 were obtained by reaction of dinuclear chlorido bridged molybdenum(*IV*,*IV*) complex **1-1** with the R_2bpy ligand (R = Me, NMe_2, ^{t}Bu). The resulting complexes Cp*Mo(Me_2bpy)Cl_3 (brown) and Cp*Mo(NMe_2bpy)Cl_3 (red) are barely soluble in any solvents tested. Only the ^{t}Bu$_2$bpy substituted complex Cp*Mo(^{t}Bu$_2$bpy)Cl_3 (**3-d**), which is brown in color, is slightly soluble in dichloromethane. (see Reaction Scheme 2.9)

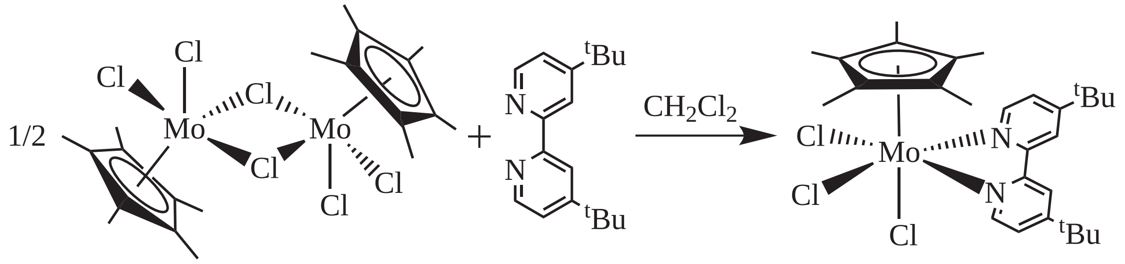

1-1 **^{t}Bu$_2$bpy** **3-d** (76%)

Reaction Scheme 2.9: Synthesis of molybdenum(*IV*) half-sandwich tri-chlorido complex Cp*Mo(^{t}Bu$_2$bpy)Cl_3 (**3-d**).

The ^{1}H-NMR spectrum of complex **3-d** in CD_2Cl_2reveals a strongly paramagnetic behaviour (δ = 2.24 ppm for Cp* protons at RT). A down-field shift of the three aromatic bipyridine protons over the free ligand and a broad signal for the Cp* protons at δ = 2.24 ppm ($\omega_{1/2}$ = 184 Hz) were detected. Tungsten (*IV*) and molybdenum (*IV*) complexes have a d^2-configuration, thus can be present as low-spin or high-spin compounds. Based on the broad signals observed in the ^{1}H-NMR spectrum, complex ^{t}Bu$_2$bpy-Mo^{IV} (**3-d**) is considered as a high-spin paramagnetic (S = 1) compound.

3. Dinuclear μ-Oxo-Bridged Tungsten Half-Sandwich Complexes

The chemistry of novel dinuclear μ-oxo-bridged tungsten(*IV*,*IV*) half-sandwich complexes with substituted bipyridyl ligands was developed by Cremer.[83] To create more significant charge separation as well as photosensitizing metal centers, the bidentate N-donor ligands dpq and dpphen were employed to synthesize the dimeric tungsten(*IV*,*IV*) complexes. The synthetic, spectral and electrochemical study of dinuclear μ-oxo-bridged tungsten(*IV*,*IV*) half-sandwich complexes $[(Cp^*W(dpq)(\mu{-}O))_2][PF_6]_2$ (**4-a**) and $[(Cp^*W(dpphen)(\mu{-}O))_2][PF_6]_2$ (**4-b**) is described in this chapter.

3.1. Synthesis of the Complexes dpq-W^{IV}W^{IV} (4-a) and dpphen-W^{IV}W^{IV} (4-b)

The dpq and dpphen substituted half-sandwich ditungsten(*IV*,*IV*) oxo-complexes of $[(Cp^*W(dpq)(\mu{-}O))_2][PF_6]_2$ (**4-a**) and $[(Cp^*W(dpphen)(\mu{-}O))_2][PF_6]_2$ (**4-b**) were obtained in 67% and 76% yield respectively by hydrolysis of the mononuclear half-sandwich tungsten (*IV*) halido complexes. After neutralizing with $NaHCO_3$ in solid state, the products were precipitated by addition of NH_4PF_6 (see Reaction Scheme 3.1). The raw products were then extracted with DCM and recrystallized from Et_2O/DCM.

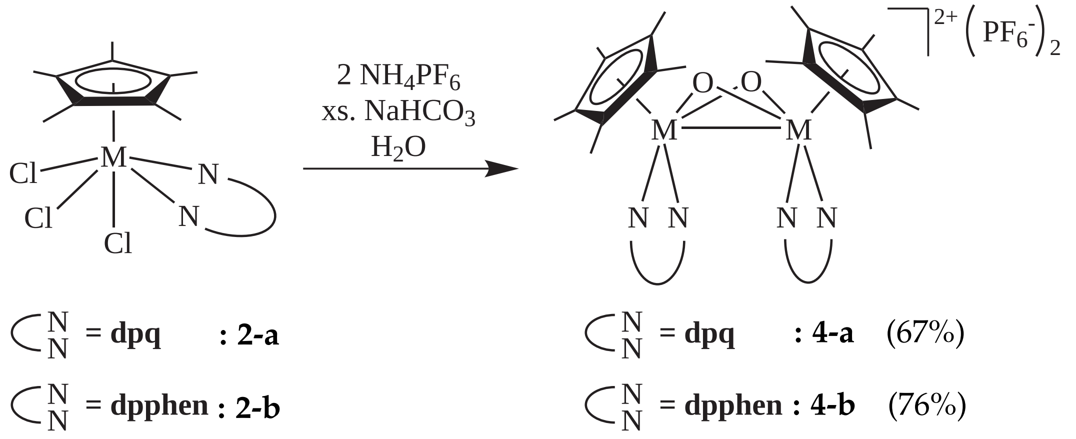

Reaction Scheme 3.1: Synthesis of μ-oxo-bridged tungsten(*IV*,*IV*) half-sandwich complexes of $[(Cp^*W(dpq)(\mu{-}O))_2][PF_6]_2$ (**4-a**) and $[(Cp^*W(dpphen)(\mu{-}O))_2][PF_6]_2$ (**4-b**).

The reddish purple complex **4-a** is well soluble in polar solvent like DCM and ACN, sparingly soluble in THF and nonpolar organic solvents. The ^{1}H-NMR spectrum of the dpq-W^{IV}W^{IV} compound is consistent with the C_{2v}-symmetry of **4-a** and shows high-field shifts for all protons with regard to the mononuclear reactant **2-a**. Two dimensional ^{13}C-^{1}H-NMR methods such as HSQC and HMBC techniques were employed to assign the observed signals. The desired compound **4-a** was verified by FAB$^+$ mass spectrometry, in which the major peak was found at m/z = 567.1 for the doubly charged cation $[(Cp^*W(dpq)(\mu{-}O))_2]^{2+}$ with the expected isotopic pattern, and elemental analysis (data presented in Experimental detail section). The dimeric structure was unambiguously confirmed by X-ray crystal structure analysis (see below).

The salt $Li[Al(pftb)_4]$ is a useful precursor for introducing the weakly coordinating $[Al(pftb)_4]^-$ anion into various other salts by metathesis (Reaction Scheme 3.2). For example, complex $[(Cp^*W(dpq)(\mu{-}O))_2][PF_6][Al(pftb)_4]$ (**4-a1**) was obtained

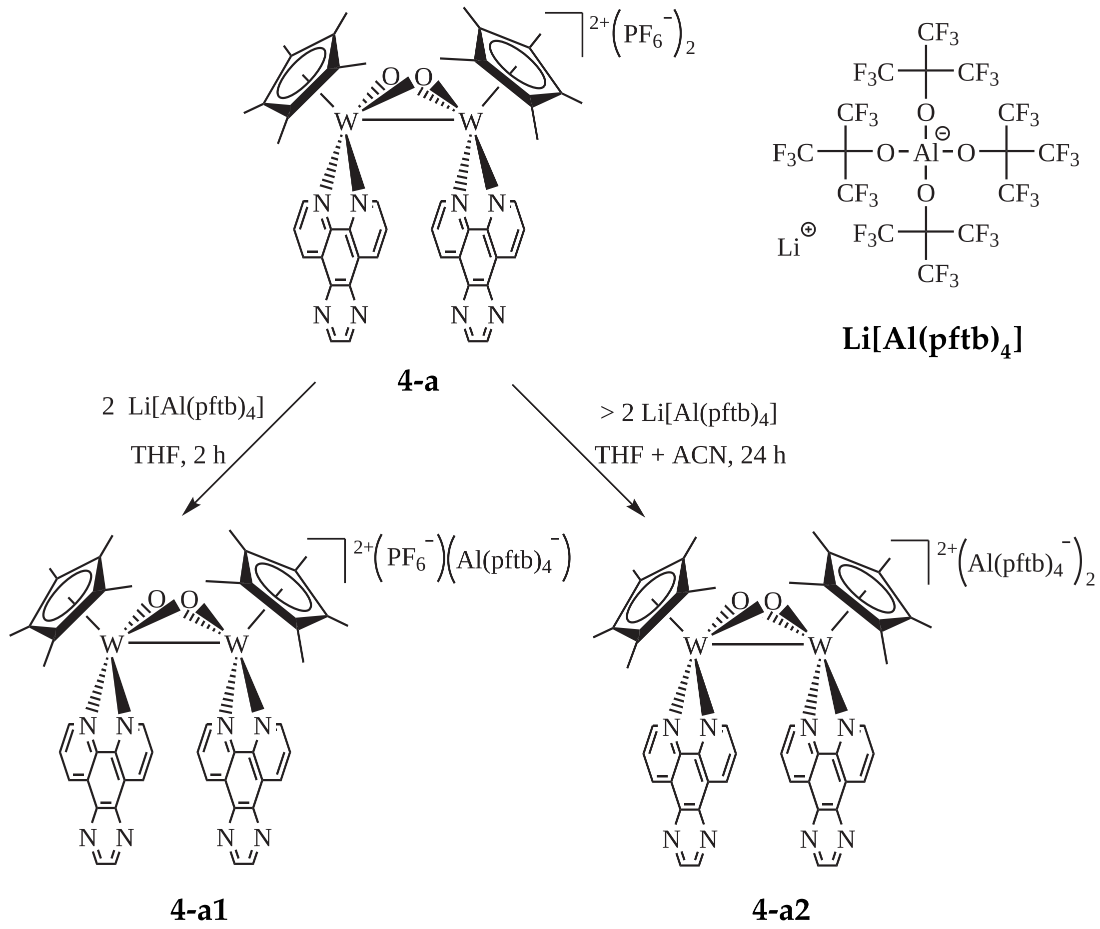

Reaction Scheme 3.2: Metathesis reaction of complex $[(Cp^*W(dpq)(\mu{-}O))_2][PF_6]_2$ (**4-a**) with $Li[Al(pftb)_4]$.

by stirring of complex **4-a** with two equivalents of Li[Al(pftb)$_4$] in THF for two hours. The ^{19}F resonance of the anionic moieties consist of a doublet for [PF$_6$]$^-$ at -72.87 ppm ($^1J_{FP}$ = 707 Hz) and a singlet for [Al(pftb)$_4$]$^-$ at - 75.98 ppm in CD$_3$CN, and the integration fits to 6 : 36 for [PF$_6$]$^-$: [Al(pftb)$_4$]$^-$. In order to obtain complex with only [Al(pftb)$_4$]$^-$ counter anions, i.e. [(Cp*W(dpq)(μ−O))$_2$][Al(pftb)$_4$]$_2$ (**4-a2**), a small amount of acetonitrile was added to dissolve the reactant **4-a**. A singlet attributed to the [Al(pftb)$_4$]$^-$ anion was detected in ^{19}F-NMR spectrum at - 77.77 ppm. Complex **4-a2** with the weakly coordinating [Al(pftb)$_4$]$^-$ counter anions is more soluble in less polar THF solvent.

X-ray crystal structure of 4-a

Single crystals suitable for X-ray diffraction were obtained by diffusion of Et$_2$O into a DCM solution of complex **4-a**. Figure 3.1 depicts the molecular structure of **4-a**. The most important bond lengths and angles are listed in Table 3.1.

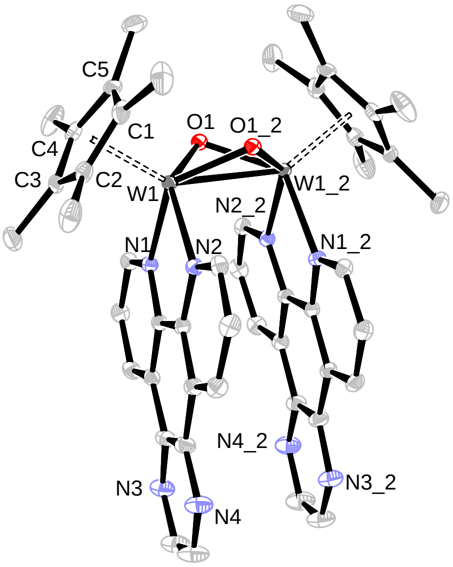

Figure 3.1.: Crystal structure of complex **4-a** (Ortep-representation; 50%). For reasons of clarity, hydrogen atoms and two [PF$_6$]$^-$ anions are not shown here.

The molecule is located on a special position. One half of the molecule, which consists of a Cp*W(O)(dpq) unit, was refined. The dinuclear complex **4-a** displays a *cis* geometry for the two Cp* ligands. Each tungsten metal center adopts a square pyramidal coordination sphere, in which the Cp* ligand occupies one coordination site, which is located in apical position of the pyramidal structure,

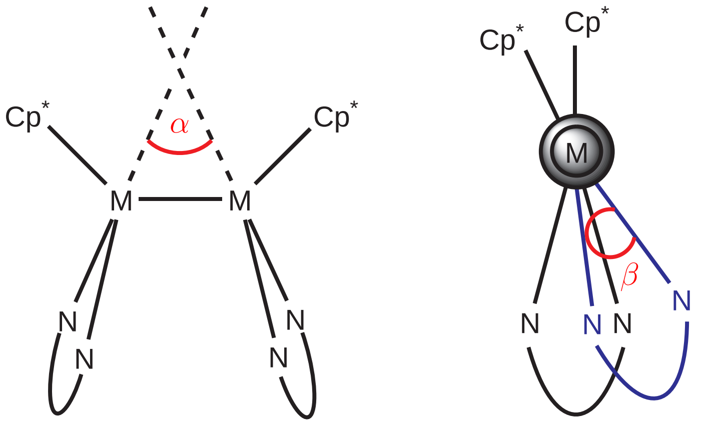

Figure 3.2.: The definitions of angles α and β: α is the angle between two bidentate N-donor ligand planes, β is the torsion angle between two bidentate N-donor ligands.

Table 3.1.: Selected bond lengths [Å] and -angles [°] of **4-a**.[a]

W1-O1	1.9554(15)	W1-O1_2	1.9454(15)
W1-N1	2.1529(18)	W1-N2	2.1835(18)
W1-W1_2	2.73622(16)	W1-C1	2.374(2)
W1-C2	2.431(2)	W1-C3	2.383(2)
W1-C4	2.312(2)	W1-C5	2.311(2)
W1-Z1[b]	2.026		
N1-W1-N2	74.63(7)	O1-W1-O1_2	76.91(7)
W1-O1-W1_2	89.09(6)	N1-W1-W1_2	90.82(5)
O1-W1-W1_2	45.31(4)	N2-W1-W1_2	97.26(5)
O1_2-W1-W1_2	45.61(4)	O1-W1-N1	88.12(6)
O1_2-W1-N1	129.83(6)	O1-W1-N2	139.713(6)
O1_2-W1-N2	86.16(6)	W1_2-W1-Z1	147.05
N1-W1-Z1	114.16	N2-W1-Z1	109.50
O1-W1-Z1	111.35	O1_2-W1-Z1	115.91
α[c]	11	β[d]	8.8

[a] estimated standard deviations in parentheses

[b] Z1 is the ring centroid of carbon atoms C1-C5.

[c] α is the angle between two dpq ligand planes.

[d] β is the torsion angle between two dpq ligands.

four atoms (N1, N2, O1, O1_2) are placed at the corners of the square base and the tungsten center is above the basal plane of the pyramidal. The distance between the two tungsten centers amounts to 2.736 Å, the bond is bridged by two oxygen atoms forming a puckered W_2O_2 ring. The distance from W1 to the carbon atoms of the Cp ring are in a narrower range of 2.311 to 2.431 Å compared to the monomeric complexes (2.238 to 2.497 Å for **2-b** and 2.223 to 2.477 Å for **2-c**), the α and β angles are defined in Figure 3.2. Two dpq ligand planes are nearly coplanar with a small α angle of 11° (see footnote of Table 3.1), which is much smaller than the values in R_2bpy substituted dinuclear complexes $[(Cp^*W(R_2bpy)(\mu{-}O))_2]^{2+}$ (α = 17.8° for R = Me, α = 35.6° for R = ^{t}Bu).[83] The rings are slightly eclipsed, the torsion angle of 8.8° between the two planes of the dpq ligands is also observed. The N1-W1-W1_2 angle is close to 90° (90.82°) while the N2-W1-W1_2 angle are lager by 6.44°. The square pyramidal geometry of complex **4-a** is slightly distorted as can be seen by inspection of various axial site -metal - basal site angles, which amount to 109.50° for Z1-W1-N2, 111.35° for Z1-W1-O1, 114.16° for Z1-W1-N1 and 115.91° for Z1-W1-O1_2.

The blue complex **4-b** is well soluble in DCM and ACN, slightly soluble in THF and insoluble in nonpolar organic solvents. Structure characterization of complex **4-b** by ^{1}H-NMR spectroscopy was performed in CD_2Cl_2, which showed high-field shifts for all proton signals with regard to the monomer complex **2-b**. Two-dimensional NMR measurements (COSY, HSQC and HMBC) were also performed to assist the peak assignment. The structure of the desired bimetallic complex was unambiguously confirmed by mass spectrometry, elemental and X-ray crystal analysis.

X-ray crystal structure of 4-b

A single crystal suitable for X-ray diffraction was obtained by diffusion of diethyl ether into a DCM solution of complex **4-b**. The crystal structure of the complex dication and anions were well resolved (see Figure 3.3), the co-crystallized solvent molecules were refined as 0.33 DCM, 0.45 and 0.22 of two independent Et_2O molecules. Important structure information of complex **4-b** is listed in Table 3.2.

The geometry around the tungsten centers are essentially square pyramidal and the two dpphen ligands are arranged in a *cis* orientation. The observed W1-N1, W1-N2 bond lengths (2.1507, 2.1545 Å) for **4-b** are smaller than the values for the mononuclear complex **2-b**, while the distance for the W2 center (W2-N3 2.1636, W2-N4 2.1669) are comparable with the distance in **2-b**. The distance for the two tungsten centers (2.736 Å) in dpphen-$W^{IV}W^{IV}$ equals to the distance in the corresponding tungsten centroids distance in complex dpq-$W^{IV}W^{IV}$ (**4-a**). The angle formed by the planes of the phenanthroline unit of the dpphen ligand (α) is

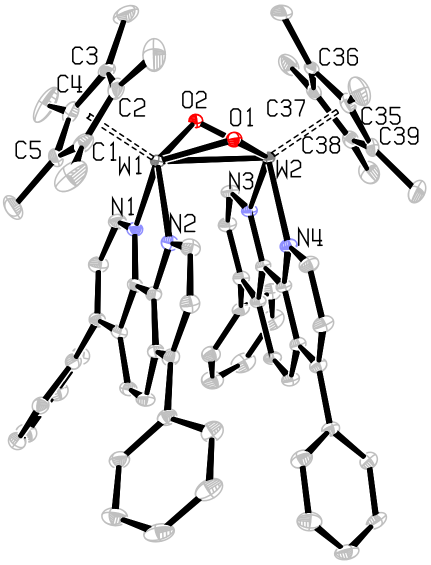

Figure 3.3.: Crystal structure of complex **4-b** (Ortep-representation; 50%). For reasons of clarity, two $[PF_6]^-$ anions, the hydrogen atoms and the co-crystallized solvent molecules are not shown.

quite large (16.46°), presumably due to steric repulsion between the phenyl substituents. The torsion angle between the two dpphen ligands is 11.6°, which is also larger than the torsion angle between the dpq ligands in complex **4-a**. The angle between the phenanthroline unit and the phenyl substituents of the dpphen ligand coordinated to W1 are only + 36.7° and - 36.8°, while larger angles of + 53.8° and + 58.6° are observed between the phenyl substituents and the phenanthroline unit of the dpphen ligand coordinated to the tungsten metal center W2.

Table 3.2.: Selected bond lengths [Å] and -angles [°] of **4-b**.[a]

W1-W2	2.73622(13)		
W1-O1	1.9454(14)	W2-O1	1.9624(14)
W1-O2	1.9572(14)	W2-O2	1.9481(14)
W1-N1	2.1507(17)	W2-N3	2.1636(16)
W1-N2	2.1545(17)	W2-N4	2.1669(16)
W1-C1	2.400(2)	W2-C35	2.365(2)
W1-C2	2.393(2)	W2-C36	2.2972(19)
W1-C3	2.357(2)	W2-C37	2.318(2)
W1-C4	2.322(2)	W2-C38	2.383(2)
W1-C5	2.343(2)	W2-C39	2.422(2)
W1-Z1[b]	2.030	W2-Z2[c]	2.020
N1-W1-N2	74.27(6)	N3-W2-N4	74.40(6)
O1-W1-O2	76.92(6)	O1-W2-O2	76.83(6)
W1-O1-W2	88.77(6)	W1-O2-W2	88.96(6)
N1-W1-W2	92.17(5)	N3-W2-W1	95.66(5)
N2-W1-W2	94.77(5)	N4-W2-W1	93.44(5)
O1-W1-W2	45.81(4)	O1-W2-W1	45.42(4)
O2-W1-W2	45.39(4)	O2-W2-W1	45.66(4)
O1-W1-N1	130.74(6)	O1-W2-N3	138.18(6)
O2-W1-N1	90.11(6)	O2-W2-N3	84.40(6)
O1-W1-N2	83.79(6)	O1-W2-N4	90.88(6)
O2-W1-N2	137.27(6)	O2-W2-N4	131.84(6)
W2-W1-Z1	147.08	W1-W2-Z2	146.54
N1-W1-Z1	113.78	N3-W2-Z2	111.15
N2-W1-Z1	111.05	N4-W2-Z2	112.37
O1-W1-Z1	115.19	O1-W2-Z2	110.66
O2-W1-Z1	111.65	O2-W2-Z2	115.56
α[d]	16.46	β[e]	11.6

[a] estimated standard deviations in parentheses

[b] Z1 is the ring centroid of carbon atoms C1-C5.

[c] Z2 is the ring centroid of carbon atoms C35-C39.

[d] α is the angle formed by planes of phen moiety in dpphen ligand.

[e] β is the torsion angle between two dpphen ligands.

3.2. Attempted Chemical Oxidation of 4-a

The oxidation of bis-μ-oxo ditungsten(IV/IV) complex **4-a** was carried out by adding a stoichiometric amount of oxidant $[Cp_2Fe][PF_6]$, $Ag[PF_6]$ or $[NO][PF_6]$ which have formal potentials 0 V, 0.87 V in ACN, 0.65 V in DCM respectively vs the $[Cp_2Fe]^+/[Cp_2Fe]$ couple.[113] The oxidized compound could only be isolated for the reaction with the stronger oxidant [NO][PF_6] in acetonitrile (see Reaction Scheme 3.3).

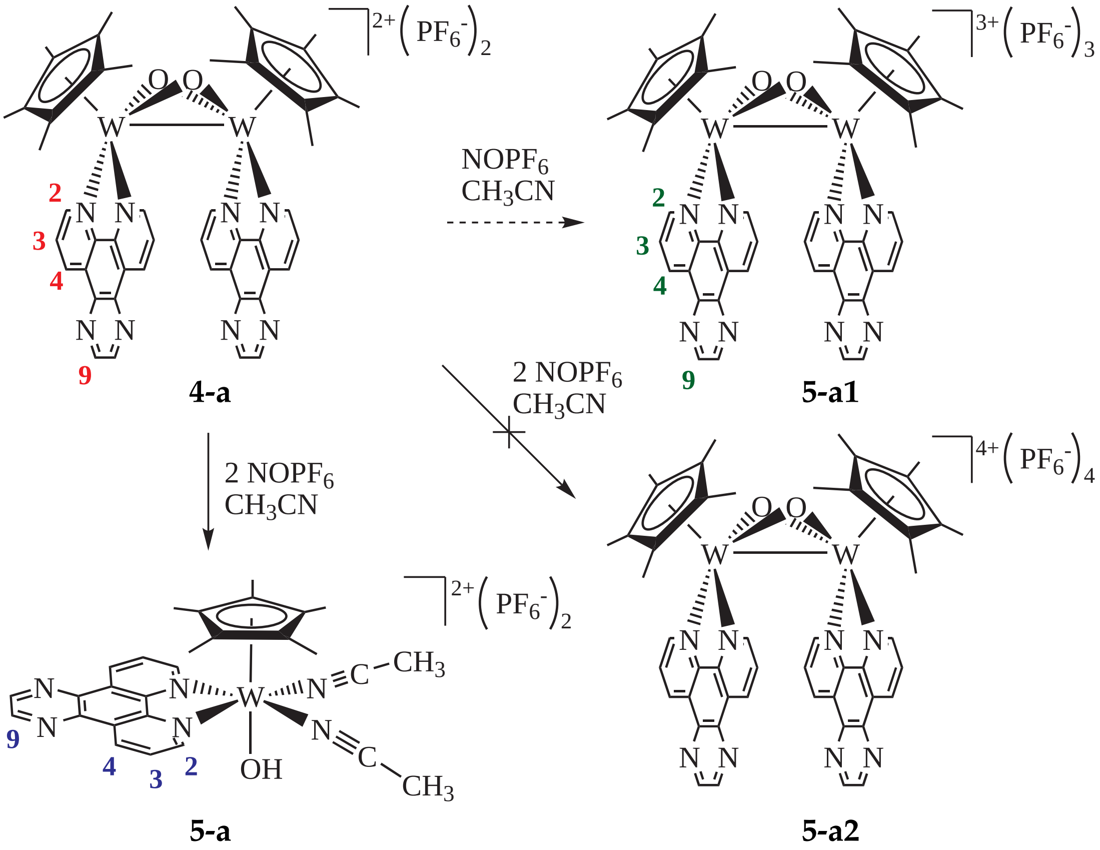

Reaction Scheme 3.3: Attempted chemical oxidation of complex **4-a** with one and two equivalents of nitrosonium salt in acetonitrile.

Through oxidation of the purple complex dpq-$W^{IV}W^{IV}$ (**4-a**) with one equivalent of [NO][PF_6] in acetonitrile, the yellow bis-μ-oxo ditungsten(*IV*/*V*) complex [(Cp*W(dpq)(μ–O))$_2$][PF_6]$_3$ (**5-a1**) was obtained and verified by ^{1}H-NMR spectroscopy (see Figure 3.4). By comparison of the ^{1}H-NMR spectra for **5-a1** and the reactant **4-a**, the proton resonance for Cp* is shifted from 1.61 ppm to 1.58 ppm and all proton peaks for the attached dpq ligand (9.90 ppm for $H_{[4]}$, 9.27 ppm for $H_{[9]}$ + $H_{[2]}$, 8.34 ppm for $H_{[3]}$) are strongly shifted down-field*. It can be seen that all peaks are slightly broadened indicating paramagnetism of the ditungsten(*IV*/*V*) complex **5-a1**.

Through oxidation with two equivalents [NO][PF_6] in acetonitrile, the dimeric structure of complex **4-a** breaks down to the mononuclear complex and acetonitrile is coordinated to the metal center. A single crystal structure verified the brown product as [(Cp*W(dpq)($NCCH_3$)$_2$(OH)][PF_6]$_2$ (**5-a**). Comparison of the

---

* The numbering scheme of the protons used in Figure 3.4 is specified in Reaction Scheme 3.3.

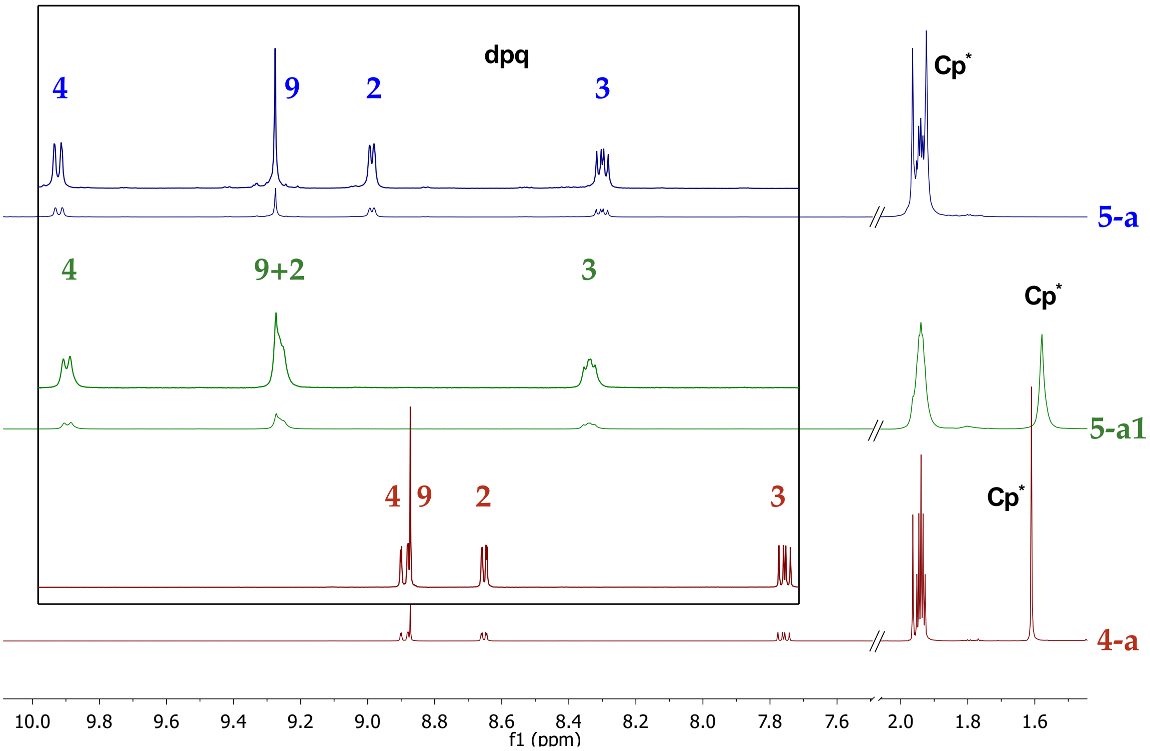

Figure 3.4.: ^{1}H-NMR Spectrum of complex **4-a** (brickred), **5-a1** (green) and **5-a** (blue) in CD_3CN at 400 MHz. The inlay is scaled up view of the attached dpq ligand.

^{1}H-NMR spectra for the dimeric complex **4-a** and the monomeric compound **5-a** reveals that the proton resonance for the Cp* ligand is shifted from 1.61 ppm to 1.92 ppm, furthermore, a down-field shift of the proton resonances for the dpq ligand was also detected. The proton attached to the oxygen atom was not detected by proton NMR spectrum, presumably due to H/D exchange with the deuterated solvent. To avoid solvent coordination at the final product, the polar solvent nitromethane was employed for this reaction, but the desired ditungsten(V/V) complex (**5-a2**) could not be obtained by the solvent variation.

X-ray crystal structure of 5-a

Single crystals of complex $[(Cp^*W(dpq)(NCCH_3)_2(OH)][PF_6]_2$ (**5-a**) were easily obtained by crystallization from Et_2O/CH_3CN solution. Figure 3.5 depicts the X-ray crystal structure of **5-a**. The molecular cation is well refined, while the $[PF_6]^-$ anions are disordered over two positions. The cavity between molecules is filled with solvent molecules, which could not be well resolved. Selected bond lengths and angles of the dication are listed in Table 3.3.

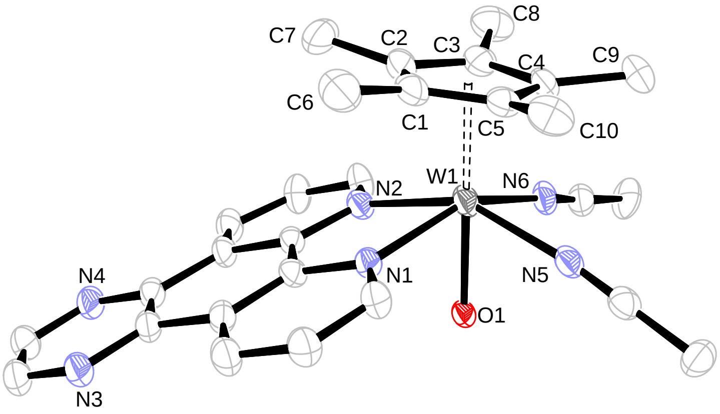

Figure 3.5.: Crystal structure of complex **5-a** (Ortep-representation; 50%). For reasons of clarity, hydrogen atoms, two $[PF_6]^-$ anions and the co-crystallized solvent molecule are not shown.

Table 3.3.: Selected bond lengths [Å] and angles [°] of complex **5-a**.[a]

W1-N1	2.169(4)	W1-N2	2.176(4)
W1-N5	2.129(5)	W1-N6	2.130(5)
W1-O1	1.948(3)	W1-C1	2.443(6)
W1-C2	2.398(6)	W1-C3	2.315(6)
W1-C4	2.278(5)	W1-C5	2.361(5)
W1-Z1[b]	2.025		
N1-W1-N2	76.64(17)	N1-W1-N5	92.70(17)
N1-W1-N6	152.39(17)	N1-W1-O1	76.33(15)
N2-W1-N5	152.07(17)	N2-W1-N6	91.53(16)
N2-W1-O1	75.99(15)	N5-W1-N6	86.27(17)
N5-W1-O1	76.41(15)	N6-W1-O1	76.62(16)
N1-W1-Z1	103.18	N2-W1-Z1	104.31
N5-W1-Z1	103.25	N6-W1-Z1	103.89
O1-W1-Z1	179.36		

[a] estimated standard deviations in parentheses

[b] Z1 is the ring centroid of carbon atoms C1-C5.

The six-coordinate W^{IV} is centered in a distorted octahedral configuration with Z1-W1-equatorial ligand atom angles between 103.18° to 104.31° and a Z1-W1-O1 angle of 179.36° (Z1 is the ring centroid of the Cp* ligand). The bond lengths of W1-N5 (2.129 Å) and W1-N6 (2.130 Å) for the coordinated acetonitrile ligands are shorter than the W1-N1 (2.169 Å) and W1-N2 (2.176 Å) distances for the attached dpq ligand. The W1-O1 bond length of 1.948 Å is substantially longer than typical W=O double bonds, which display an average distance of 1.74 Å.[114,115] Therefore, the oxygen atom O1 in complex **5-a** is a hydroxyl group rather than a terminal oxo ligand. The W-O bond length falls into typical range of W-O single bond, which is consistent with the observed diamagnetic behavior. The W-O bond lengths of hydroxyl groups in other complexes were found to be 1.829 Å (with stronger hydrogen bonding with ether), 1.858 Å (with weaker hydrogen bonding to OTf^-) in complex $[Cp^*W(OH)(\mu{-}S)_2RuH(PPh_3)_2]^+$,[115] 2.064 Å (no hydrogen bonding) in complex $[Cp^*W(OH)(NO)(\eta^2{-}HN{=}C(Me)CH{=}CPh)$[116,117] and 1.916 Å in complex *trans*-$[W(OH)(O)(dppe)_2]^+$.[118]

3.3. Chemical Reduction of 4-a

Due to the extremely high air-sensitivity of the reduced form of bis-μ-oxo ditungsten(*IV*/*IV*) complexes, several efforts to prepare the reduced bis-μ-oxo ditungsten(*III*/*III*) complex $[(Cp^*W(dpq)(\mu{-}O))_2]$ (**6-a**) failed. By carefully handling the solvent purity and removing co-crystallized dichloromethane of the crystalline complex dpq-$W^{IV}W^{IV}$ (**4-a**), the reduced complex dpq-$W^{III}W^{III}$ (**6-a**) was obtained by reaction with two equivalents of sodium naphthalenide. The latter was prepared in situ by stirring naphthalene with an excess amount of freshly cut sodium. (Reaction Scheme 3.4).

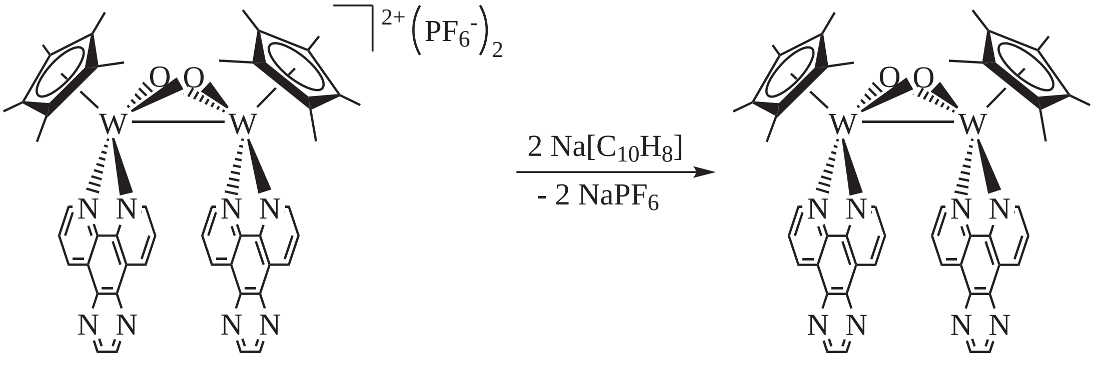

Reaction Scheme 3.4: Reduction of complex **4-a** with sodium naphthalenide to yield neutral complex $[(Cp^*W(dpq)(\mu{-}O))_2]$ (**6-a**).

The bluish purple product **6-a** was obtained in a good yield of 77% by extraction with pentane. The identification of complex **6-a** rests on the results from NMR spectroscopy, mass spectrometry and X-ray crystal structure analysis. The ^1H-NMR spectrum of complex **6-a** in C_6D_6 reveals diamagnetic behavior and exhibits four sets C-H units of the coordinated dpq ligand at 7.84, 7.35, 6.31 and 5.62 ppm with integrations of 4:4:4:4 ratio, the singlet at 1.63 ppm was assigned to the protons of the Cp^* ligand coupling pattern. The neutral complex **6-a** is soluble in less polar solvents, e.g. THF and even slightly soluble in pentane, but decomposes in polar solvent like DCM. The MALDI-TOF mass spectrum displays the exact isotopic pattern as calculated mass distribution for complex $[(Cp^*W(dpq)(\mu{-}O))_2]$ with the expected m/z at 1134.291.

X-ray crystal structure of 6-a

Single crystals of complex **6-a** suitable for X-ray diffraction were grown in pentane/THF solution at - 32 °C over long time. Figure 3.6 displays the molecular structure of the neutral complex **6-a**. The co-crystallized THF molecule and hydrogen atoms are omitted for clarification. Selected bond lengths and angles are presented in Table 3.4.

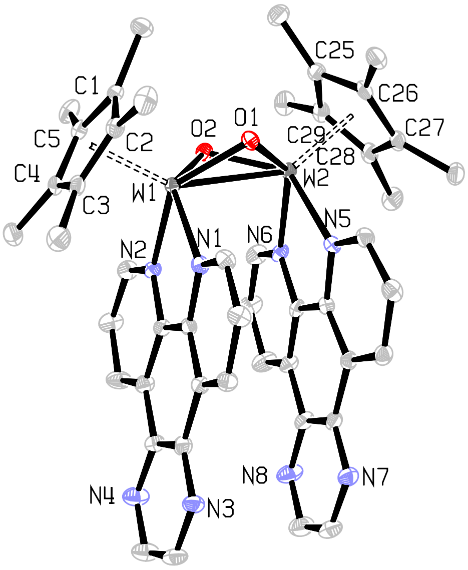

Figure 3.6.: Crystal structure of complex **6-a** (Ortep-representation; 50%). For reasons of clarity, hydrogen atoms and the co-crystallized THF solvent molecule are not shown.

In contrast to the crystal structure of the Me_2bpy substituted ditungsten(*IV*,*IV*) complex $[(Cp^*W(Me_2bpy)(\mu{-}O))_2]$, which has a *trans* arrangement of the Cp^* ligands with a flat W_2O_2 ring,[83] the molecular structure of the dpq substituted complex $[(Cp^*W(dpq)(\mu{-}O))_2]$ (**6-a**) displays a *cis* configuration with a puckered W_2O_2 ring. The main structure of the neutral complex **6-a** shows great resem-

Table 3.4.: Selected bond lengths [Å] and -angles [°] of **6-a**.[a]

W1-W2	2.71343(10)		
W1-O1	1.9602(13)	W2-O1	1.9633(14)
W1-O2	1.9617(14)	W2-O2	1.9582(13)
W1-N1	2.1423(18)	W2-N5	2.1411(17)
W1-N2	2.1426(18)	W2-N6	2.1292(19)
W1-C1	2.289(2)	W2-C25	2.303(2)
W1-C2	2.330(2)	W2-C26	2.367(2)
W1-C3	2.423(2)	W2-C27	2.441(2)
W1-C4	2.442(2)	W2-C28	2.410(2)
W1-C5	2.350(2)	W2-C29	2.329(2)
W1-Z1[b]	2.031	W2-Z2[c]	2.034
N1-W1-N2	73.91(7)	N5-W2-N6	74.28(7)
O1-W1-O2	78.53(6)	O1-W2-O2	78.54(6)
W1-O1-W2	87.51(6)	W1-O2-W2	87.61(5)
N1-W1-W2	94.33(5)	N5-W2-W1	93.75(4)
N2-W1-W2	95.08(5)	N6-W2-W1	92.97(5)
O1-W1-W2	46.29(4)	O1-W2-W1	46.20(4)
O2-W1-W2	46.14(4)	O2-W2-W1	46.25(4)
O1-W1-N1	87.45(6)	O1-W2-N5	86.02(6)
O2-W1-N1	134.84(6)	O2-W2-N5	134.99(6)
O1-W1-N2	136.18(6)	O1-W2-N6	133.67(6)
O2-W1-N2	87.09(6)	O2-W2-N6	86.47(6)
W2-W1-Z1	148.38	W1-W2-Z2	148.69
N1-W1-Z1	110.91	N5-W2-Z2	110.90
N2-W1-Z1	109.67	N6-W2-Z2	111.68
O1-W1-Z1	114.01	O1-W2-Z2	114.49
O2-W1-Z1	114.04	O2-W2-Z2	114.00
α[d]	8.7	β[e]	1.2

[a] estimated standard deviations in parentheses

[b] Z1 is the ring centroid of carbon atoms C1-C5.

[c] Z2 is the ring centroid of carbon atoms C25-C29.

[d] α is the angle between two dpq ligand planes.

[e] β is the torsion angle between two dpq ligands.

blance to the dication of complex **4-a** which adopts a square pyramidal coordination sphere for the tungsten centers. However, the W1-O1 (1.9602 Å), W1-O2 (1.9617 Å) and W2-O1 (1.9633 Å), W2-O2 (1.9582 Å) bonds are slightly longer than the W-O bond in complex **4-a** (1.9554 and 1.9454 Å), while the W1-W2 bond (2.71343 Å) is 0.02279 Å shorter in the reduced compound **6-a**. DFT calculations were performed for the dication complex **4-a** and the neutral complex **6-a**.

As illustrated in Figure 3.7, the HOMO of complex **4-a** is purely metal based while the HOMO of **6-a** has some bonding character between two dpq ligands, which explains the shorter W-W bond in the reduced compound **6-a**. The α angle between two dpq ligands is 2.3° smaller with regard to the cationic species and the torsion angle between the two dpq ligands (β) in bis-μ-oxo ditungsten(III/III) complex (1.2°) are remarkably smaller compared to those in bis-μ-oxo ditungsten(IV/IV) complexes (11°).

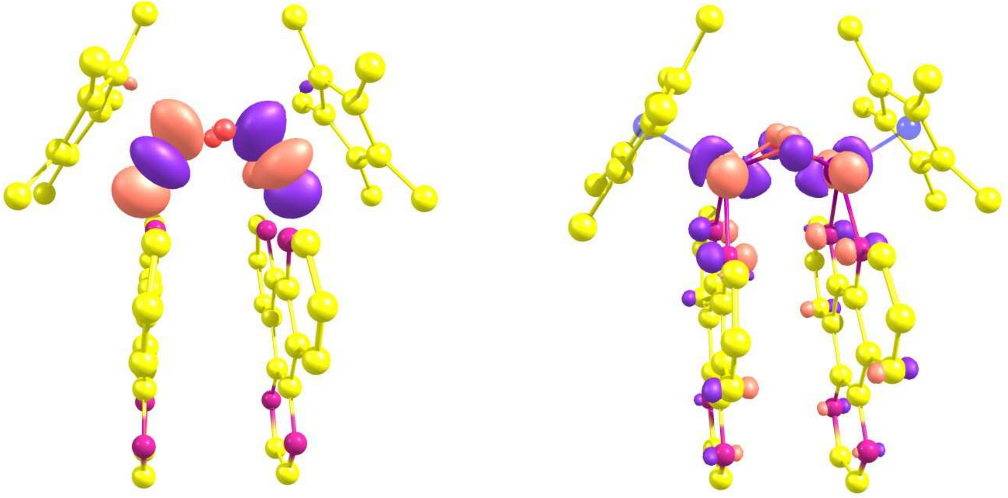
HOMO of 4-a **HOMO of 6-a**

Figure 3.7.: The HOMOs of complexes $[(Cp^*W(dpq)(\mu{-}O))_2][PF_6]_2$ (**4-a**) and $[(Cp^*W(dpq)(\mu{-}O))_2]$ (**6-a**).

3.4. Comproportionation Reaction between dpq-$W^{IV}W^{IV}$ and dpq-$W^{III}W^{III}$

The mixed valence complex dpq-$W^{IV}W^{III}$ (**7-a**) can be obtained by comproportionation reaction of dpq-$W^{IV}W^{IV}$ (**4-a**) and dpq-$W^{III}W^{III}$ (**6-a**) in THF (Reaction Scheme 3.5). The purple complex dpq-$W^{IV}W^{III}$ with the $[Al(pftb)_4]^-$ counter anion (**7-a2**) is paramagnetic and moderately soluble in THF. A broad signal at 10.6 ppm and a singlet at 8.8 ppm were observed in the ^1H-NMR spectrum in THF-d_8 at room temperature.

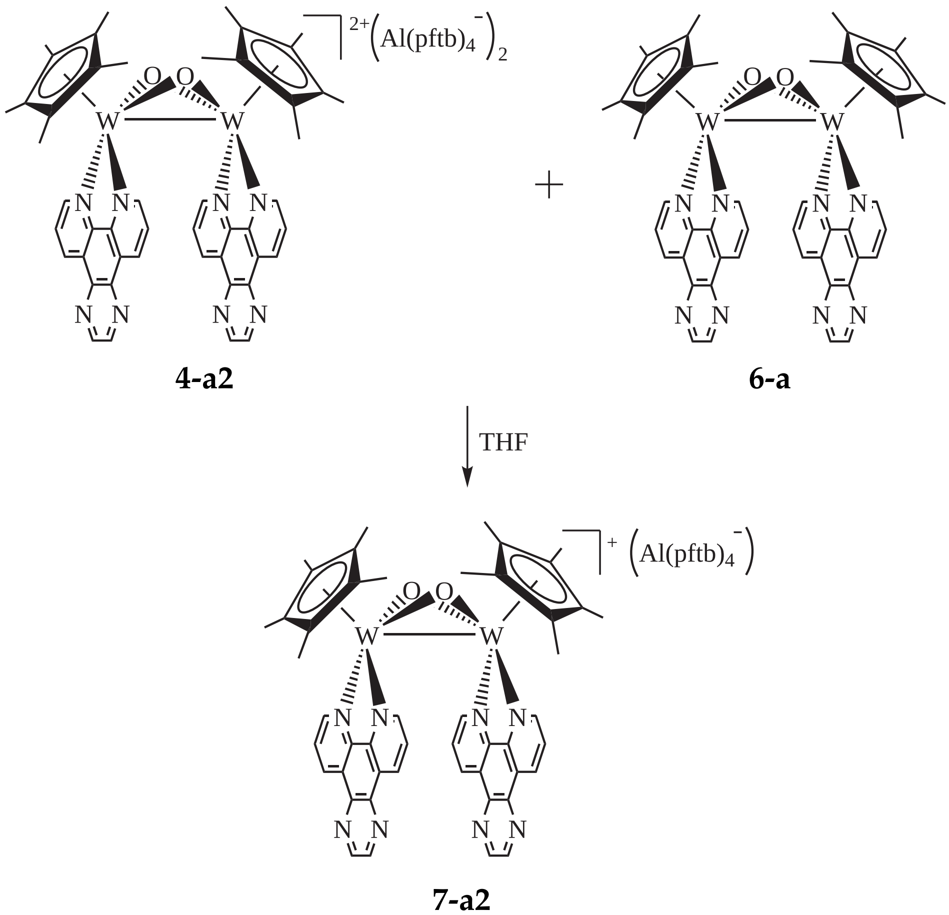

4-a2

6-a

7-a2

Reaction Scheme 3.5: Comproportionation reaction of complex dpq-$W^{IV}W^{IV}$ (**4-a2**) with dpq-$W^{III}W^{III}$ (**6-a**) to generate the paramagnetic complex dpq-$W^{III}W^{IV}$ (**7-a2**).

VT-NMR of Complex 7-a2

Figure 3.8 displays the variable temperature proton NMR spectra measured in THF-d_8 in the temperature range from 230 to 300 K. The broad peak shifted to the down-field and showed significant broadening when the temperature dropped, while the singlet shifted slightly and also broadened.

The temperature dependence of the paramagnetic shifts showed good agreement with Curie behavior, which confirmed the doublet state of complex dpq-$W^{III}W^{IV}$ (see Figure 3.9).

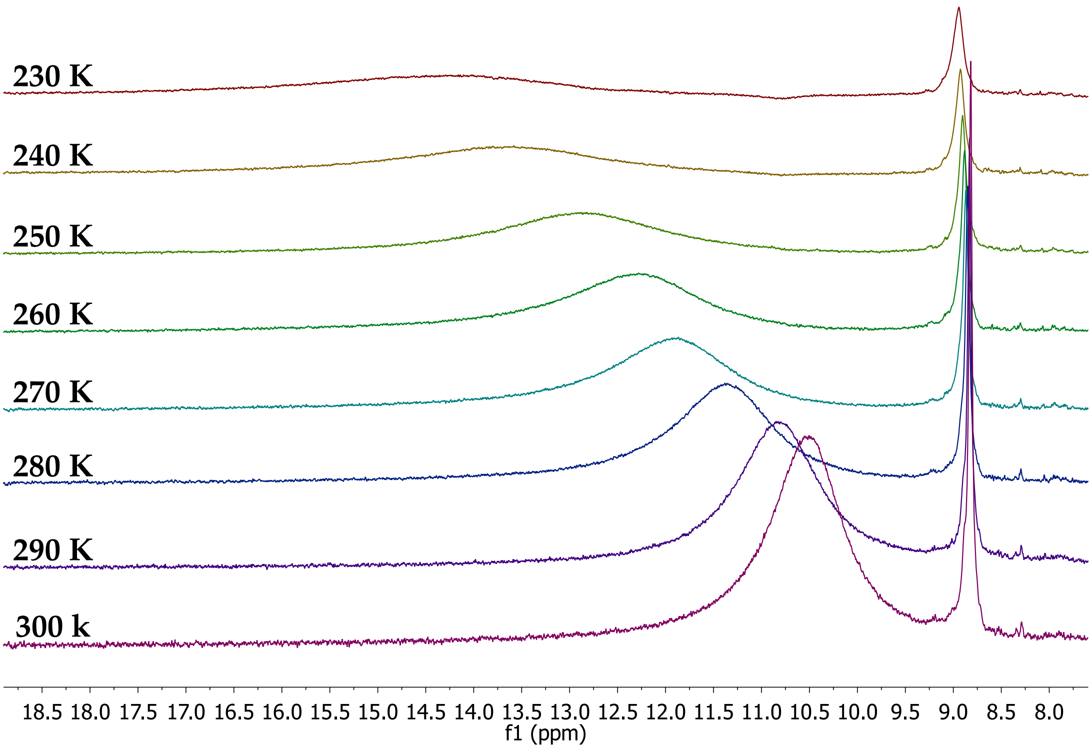

Figure 3.8.: Variable temperature ^{1}H-NMR Spectra of complex **7-a2** in THF-d_8 measured in the temperature range between 230 to 300 k.

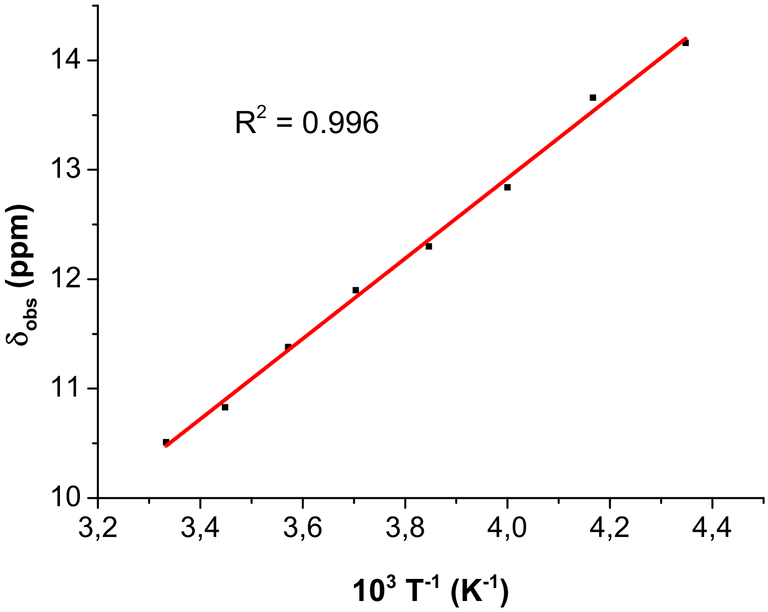

Figure 3.9.: Temperature dependence of NMR paramagnetic shift in Figure 3.8.

X-ray crystal structure of the mixed valence complex 7-a1

Single crystals suitable for X-ray diffraction are separated from the Et_2O/ACN solution of complex $[(Cp^*W(dpq)(\mu{-}O))_2][PF_6]$ (**7-a1**). Figure 3.10 presents the molecular structure of complex **7-a1**. Selected structural parameters of complex **7-a1** are summarized in Table 3.5.

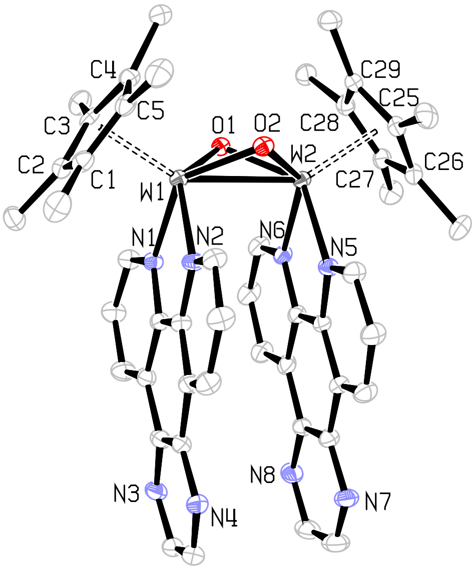

Figure 3.10.: Crystal structure of complex **7-a1** (Ortep-representation; 50%). For reasons of clarity, hydrogen atoms, one PF_6 anion and the co-crystallized solvent ACN molecule are omitted.

The geometry of complex $[(Cp^*W(dpq)(\mu{-}O))_2][PF_6]$ is essentially identical to complex $[(Cp^*W(dpq)(\mu{-}O))_2][PF_6]_2$ (**4-a**) and complex $[(Cp^*W(dpq)(\mu{-}O))_2]$ (**6-a**). Of these three complexes, the α angle (7.7°) for **7-a1** is the smallest and the β angle (6.1°) lies in between. The distance between the two tungsten centers is 2.73231 Å which is close to the distance in complex **4-a**.

Table 3.5.: Selected bond lengths [Å] and -angles [°] of **7-a1**.[a]

W1-W2	2.73231(17)		
W1-O1	1.956(2)	W2-O1	1.954(2)
W1-O2	1.957(2)	W2-O2	1.956(2)
W1-N1	2.141(3)	W2-N5	2.145(3)
W1-N2	2.164(2)	W2-N6	2.156(2)
W1-C1	2.418(3)	W2-C25	2.314(3)
W1-C2	2.410(3)	W2-C26	2.392(3)
W1-C3	2.348(3)	W2-C27	2.442(3)
W1-C4	2.303(3)	W2-C28	2.373(3)
W1-C5	2.356(3)	W2-C29	2.307(3)
W1-Z1[b]	2.030	W2-Z2[c]	2.028
N1-W1-N2	74.65(10)	N5-W2-N6	74.44(10)
O1-W1-O2	77.36(9)	O1-W2-O2	77.43(9)
W1-O1-W2	88.65(8)	W1-O2-W2	88.58(8)
N1-W1-W2	93.38(7)	N5-W2-W1	93.12(7)
N2-W1-W2	94.58(7)	N6-W2-W1	94.23(7)
O1-W1-W2	45.65(6)	O1-W2-W1	45.70(6)
O2-W1-W2	45.69(6)	O2-W2-W1	45.74(6)
O1-W1-N1	88.37(9)	O1-W2-N5	132.47(9)
O2-W1-N1	133.02(9)	O2-W2-N5	88.72(9)
O1-W1-N2	136.26(9)	O1-W2-N6	84.77(9)
O2-W1-N2	85.38(9)	O2-W2-N6	136.19(9)
W2-W1-Z1	148.48	W1-W2-Z2	147.83
N1-W1-Z1	110.80	N5-W2-Z2	112.54
N2-W1-Z1	110.75	N6-W2-Z2	110.68
O1-W1-Z1	112.95	O1-W2-Z2	114.73
O2-W1-Z1	116.02	O2-W2-Z2	113.13
α[d]	7.7	β[e]	6.1

[a] estimated standard deviations in parentheses

[b] Z1 is the ring centroid of carbon atoms C1-C5.

[c] Z2 is the ring centroid of carbon atoms C25-C29.

[d] α is the angle between two dpq ligand planes.

[e] β is the torsion angle between two dpq ligands.

EPR of Complex 7-a2

X-band ($\nu \sim 9.5$ GHz) electron paramagnetic resonance spectra of the mixed valence complex **7-a2** were collected using a Bruker Elexsys E500 CW spectrometer at liquid nitrogen temperature as a frozen glass and at room temperature in 2-methyl-tetrahydrofuran.

At a temperature of T = 97 K, a rhombic lineshape was observed (Figure 3.11). The g-factor of complex dpq-$W^{IV}W^{III}$ is anisotropic, the g-values are as follows: $g_x = 2.00$, $g_y = 1.98^*$, $g_z = 1.89$. No hyperfine structures to ^{183}W (I = 1/2, 14%) and ^{14}N (I = 1, long distance from unpaired electron) were observed.

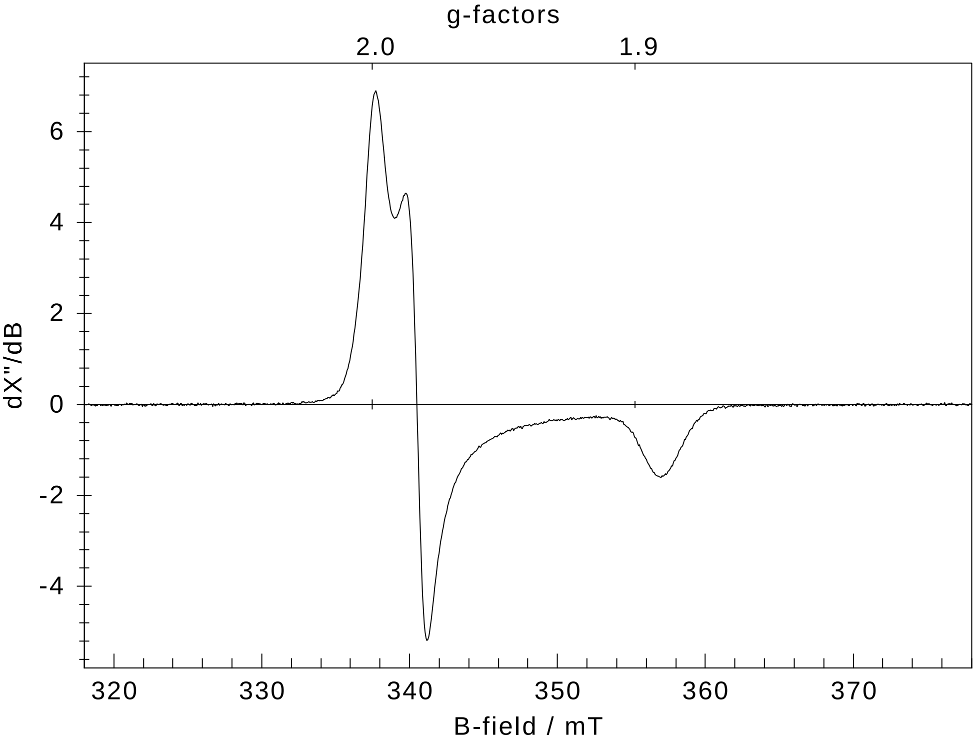

Figure 3.11.: EPR spectrum of complex 7-a2 in a frozen 2-Methyl-tetrahydrofuran glass.

At room temperature, the observed EPR line of the mixed valence complex **7-a2** becomes broader and weaker (Figure 3.12). The resulting spectra are motionally averaged, and show two peaks corresponding to the g-values of 1.95*, 1.89.

---

* The g-value is determined at the crossing point of the the EPR spectrum.

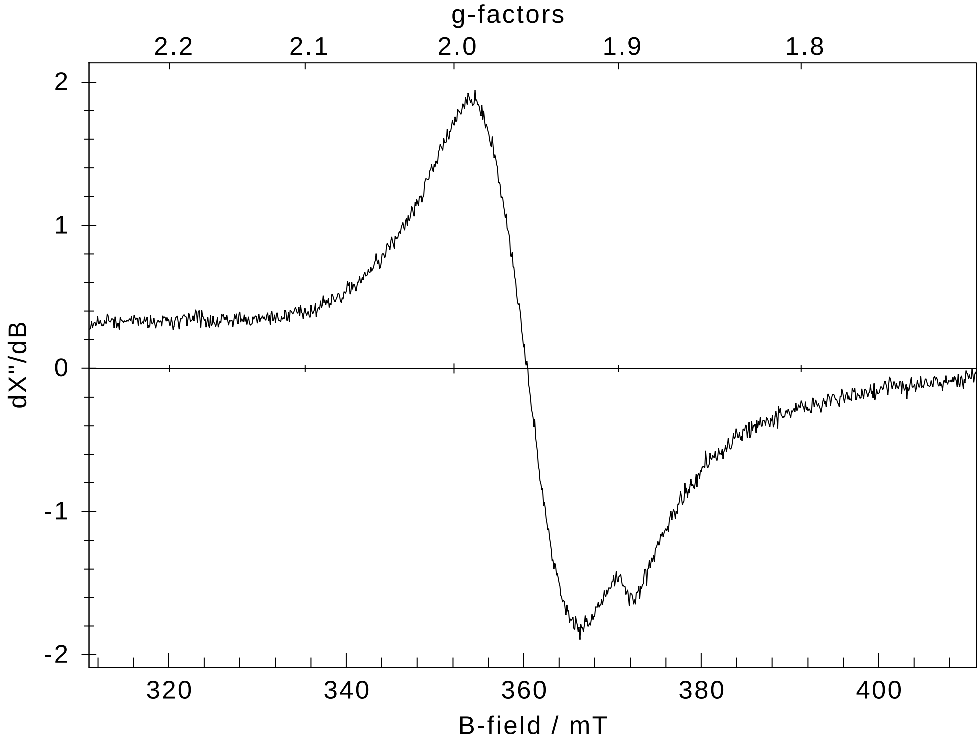

Figure 3.12.: EPR spectrum of complex 7-a2 in 2-Methyl-tetrahydrofuran at room temperature.

3.5. Spectral Properties

3.5.1. Electronic Absorption Spectroscopy of Complexes 4-a and 4-b

The electronic absorption spectrum of complex $[(Cp^*W(dpq)(\mu{-}O))_2][PF_6]_2$ (**4-a**) was recorded in the range of 400 - 1000 nm using a 0.82 mM solution in acetonitrile and dichloromethane (Figure 3.13). The strongest absorption band at 535 nm (ϵ = 11998 $M^{-1}\cdot cm^{-1}$) with a shoulder around 630 nm and the lowest-energy electronic transition at 790 nm (ϵ = 6570 $M^{-1}\cdot cm^{-1}$) in ACN are observed in the visible and NIR region respectively.

The observed large extinction coefficients (ϵ = 11998 and 6570 $M^{-1}\cdot cm^{-1}$) are typical for symmetry allowed charge transfer bands, which normally have large extinction coefficients between 1000 and 50000 $M^{-1}\cdot cm^{-1}$. This compares to the intensity of *d-d* transitions, which are typically small ($\epsilon \approx 250$ $M^{-1}\cdot cm^{-1}$ for *d-d*

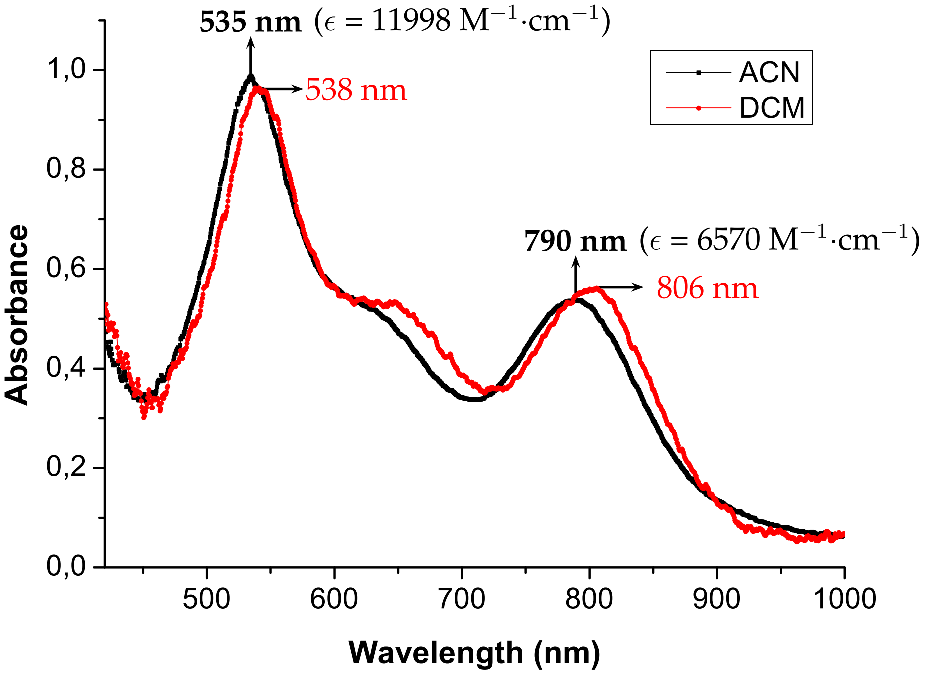

Figure 3.13.: Electronic absorption spectrum of complex **4-a** in ACN (C = 0.82 mM) and DCM. Cuvette light pass length is 0.1 cm.

transition in noncentrosymmetric complexes and $\epsilon \approx 1000$ $M^{-1}\cdot cm^{-1}$ for symmetry allowed transitions). LMCT bands are favored if the metal has low lying vacant orbitals i.e. metal in high oxidation states or if the ligands have lone pairs of relatively high energy e.g. sulphur atoms. The energy gap between the 5*d* orbitals of the tungsten center and the oxygen centered lone pairs is very large thus LMCT bands from the oxygen lone pairs to the tungsten centers should be in the UV region. In the molecules studied here, LMCT bands attributes to charge transfer from the Cp* π donor ligand to the W^{IV} metal centers. MLCT bands can be attributed to the electron transfer from the metal based orbital to the empty low lying π^* orbital (E_{LUMO} = - 2.759 eV vs $[Cp_2Fe]^{+/0}$, calculated from electrochemical data, see next section) of the dpq ligand.

In addition, complex **4-a** shows a slight red-shift of absorption bands in dichloromethane with respect to ACN. Such solvent-induced shifts are typically observed for charge transfer bands.[119–121] A change in solvent polarity will show different stabilization effect on the ground and excited states since the polarity of the excited state differs from the ground state.

Therefore, the absorption at 535 and 795 nm can be readily assigned to MLCT bands, which is charge transfer from tungsten *d* orbital to the π^* orbital of dpq ligand, and LMCT bands, corresponding to charge transfer from the π orbital of Cp* ligand to the π^* orbital of the tungsten center.

By comparison with the absorption spectra of complexes containing the same ligand set and metal center, for example, complex $[(Cp^*W(Me_2bpy)(\mu{-}O))_2][PF_6]_2$[83] and complex $[(Cp^*W(dpphen)(\mu{-}O))_2][PF_6]_2$ (see Figure 1.8 in Chapter 1 and Figure 3.16 in this section respectively), the assignment of the absorption band at 790 nm to LMCT transition (Cp* $\rightarrow$ W) was conjectured on the position of the absorption around 790 nm. Whether this tentative assignment has a real physical basis or not will be investigated later through TD-DFT calculations (vide infra).

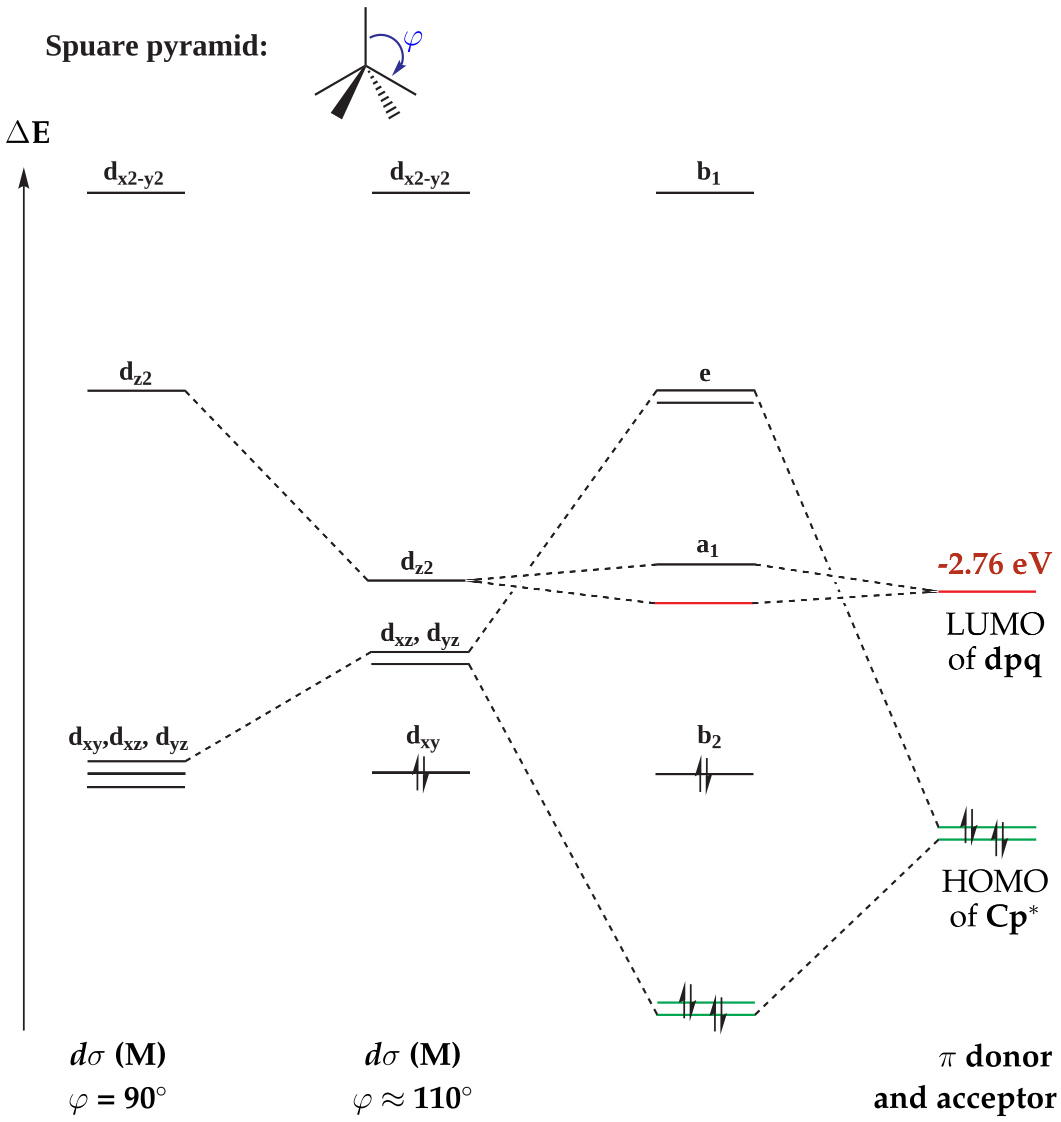

Figure 3.14.: Relative energy of frontier molecular orbital for square pyramidal molecule.

The energy scheme of the orbitals for square pyramidal complexes is presented in Figure 3.14. The metal based vacant orbital d$_{z^2}$ is perturbed by interaction with the low-lying π^* orbital of the dpq ligand. The metal based degenerate orbitals d$_{xz}$ and d$_{yz}$ are elevated by interaction with filled π orbitals of the Cp* ligand.

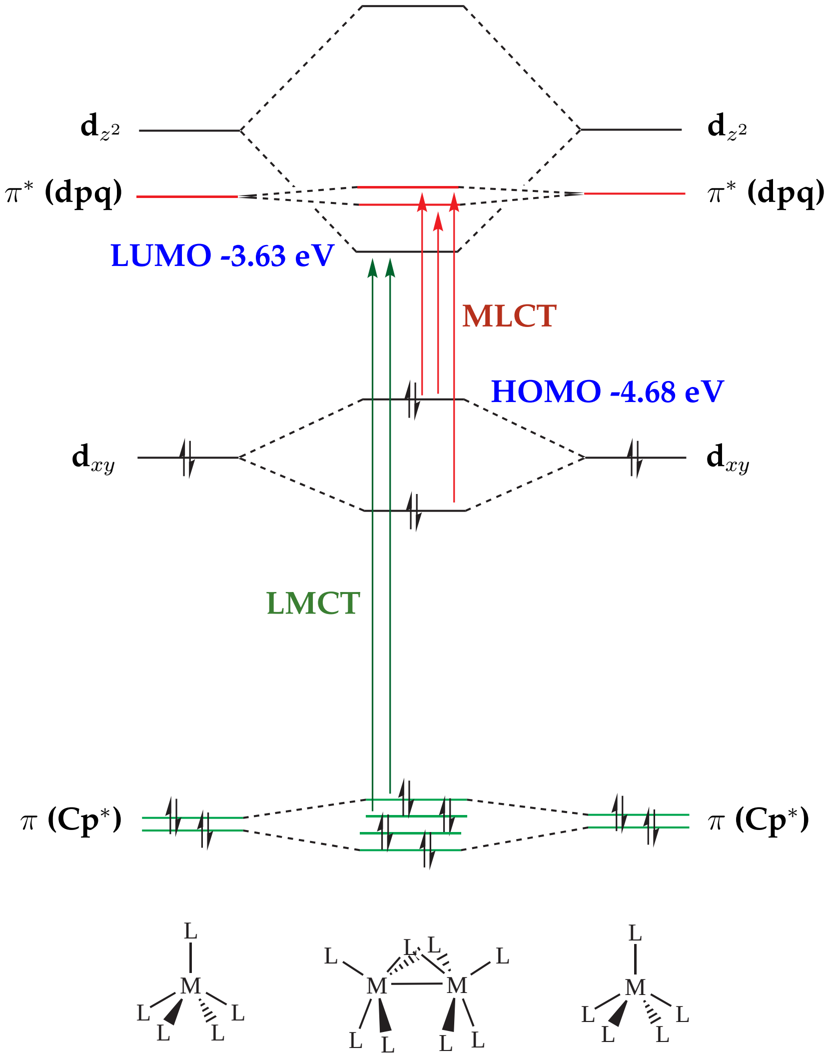

Figure 3.15.: Schematic interaction diagram for two weakly interacting square pyramidal d^2 complex. Potential low-energy one-electron excitations of ground state

The schematic interaction diagram for two strongly interacting square pyramidal d^2 configured complex is shown in Figure 3.15. The metal based molecular orbital d$_{xy}$, d$_{z^2}$ levels of the dimer split by the perturbation of the other metal atom. The high lying antibonding degenerate orbitals d$_{xz}$,d$_{yz}$ and orbital d$_{x^2-y^2}$ are not shown in Figure 3.15. The HOMO and LUMO energies of the dimer complex **4-a** are calculated from the CV data (cf. below). Based on the experimental data, the lowest energy transition (HOMO → LUMO) should be in the NIR region due to the small HOMO-LUMO energy gap (1.05 eV). As illustrated in Figure 3.15, several MLCT and LMCT bands are expected in the visible and NIR region. MLCT transitions occur due to the possession of several low-lying vacant orbitals of dpq ligand. The LMCT transitions are usually in the ultraviolet region, however, due to the donor ability of the Cp* ligand bind the relatively high oxidation state of the W^{IV} center, they are anticipated to occur in the visible region.

To investigate the photophysical properties of the dpphen substituted ditungsten(*IV*,*IV*) complex $[(Cp^*W(dpphen)(\mu{-}O))_2][PF_6]_2$ (**4-b**), the electronic absorption spectrum was measured in acetonitrile. The spectrum is shown in Figure 3.16.

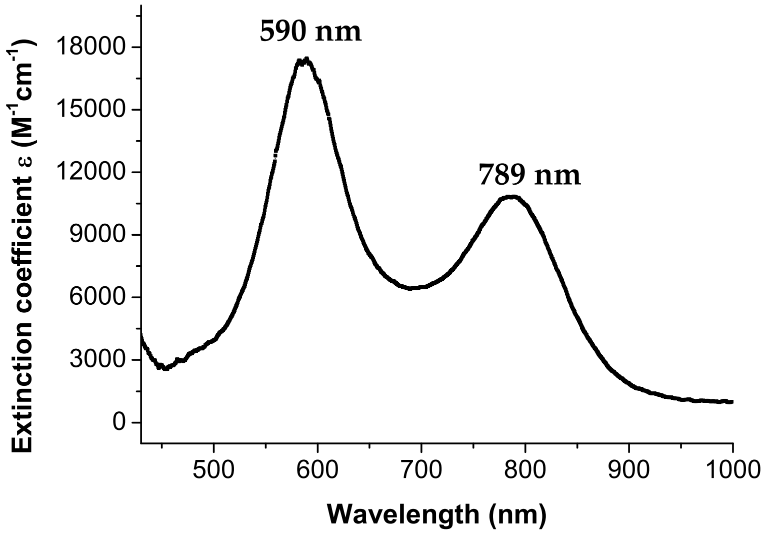

Figure 3.16.: Vis-NIR absorbance spectrum of complex **4-b** in acetonitrile (C = 0.80 mM).

The intense high-energy absorption bands in the UV region can be safely assigned to dpphen ligand based transitions, which are not shown here. The maximum absorption in the visible range is at λ = 590 nm (ϵ = 17469 $M^{-1}{\cdot}cm^{-1}$), which is red shifted due to the donor ability of the phenyl substituents as compared to the dpq substituted complex **4-a**. The lower-energy MLCT band at 789 nm has an extinction coefficient of 10841 $M^{-1}{\cdot}cm^{-1}$, found at a similar position for complex dpq-$W^{IV}W^{IV}$ (790 nm).

3.5.2. TD-DFT Calculations for Complex 4-a

DFT (density functional theory) calculations were applied with success as a theoretical approach to study the electronic transitions for the Ru,[122–124] Re[125–128] and Ir[129] polypyridyl complexes. Therefore, time-dependent DFT (TD-DFT) calculations were carried out also to interpret the photophysical properties of the μ-oxo-bridged tungsten(*IV*,*IV*) half-sandwich complex **4-a**.

Figure 3.17 compares the calculated electronic transitions* with the measured electronic absorptions for complex **4-a** in acetonitrile. The dielectric continuum model (COSMO) was applied for the TD-DFT calculations.

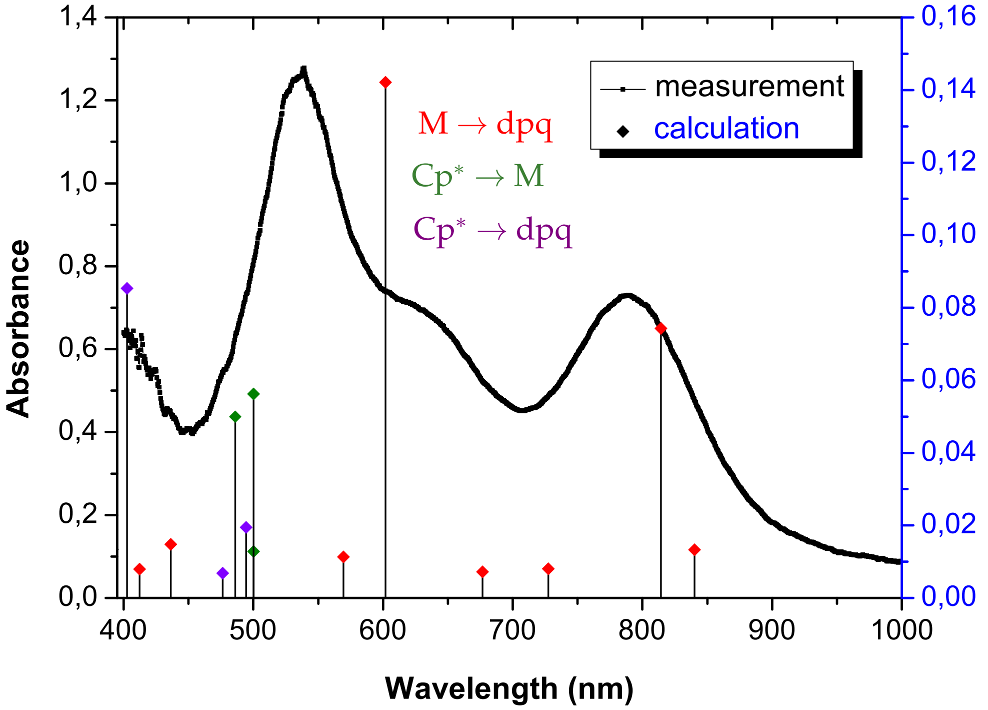

Figure 3.17.: The absorption spectrum measured in acetonitrile and the bar-spectrum simulated based on the TD-DFT calculation for complex dpq-W^{IV}W^{IV} (**4-a**) in acetonitrile.

According to the TD-DFT calculations, the absorption band at 535 nm has contributions from both LMCT and MLCT transitions while the absorption at 790 nm results purely from MLCT transition. The interligand transition of Cp* → dpq is mainly located in the near UV region.

---

[*] Turbomole;[130] Functional:B-P86;[131,132] Basis sets: def2-TZVP for W, def-SV(P) for O, N, C, H.

Table 3.6 shows the COSMO molecular orbitals with major contributions to the MLCT and LMCT transitions in the range from 400 to 1000 nm. The major MLCT transitions were calculated to emerge at 814, 602, 486 nm and the LMCT transitions were expected mainly at 500, 486 nm.

Detailed data for transitions with oscillator strengths larger than 0.0058 (the oscillator strength of the HOMO $\rightarrow$ LUMO transition) for complex **4-a** is listed in Table 3.7.

Table 3.6.: Major orbital contributions of the electronic transitions in complex dpq-W^{IV}W^{IV} (**4-a**) in the visible region calculated by TD-DFT.

Major contributions	λ (nm)	Occupied orbital	Vacant orbital	
MLCT transitions	814 nm	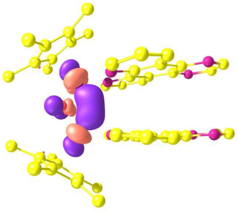	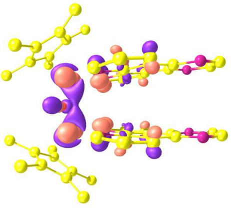	48%
		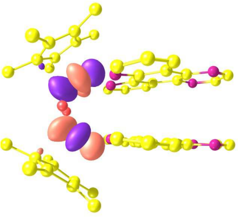	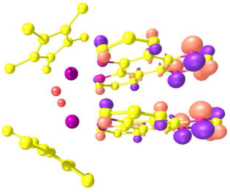	29%
	602 nm	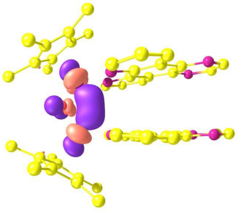	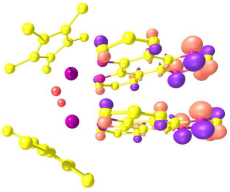	39%
			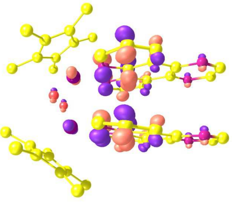	26%
	486 nm	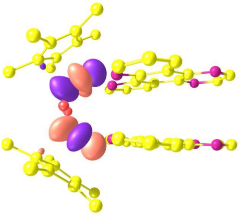	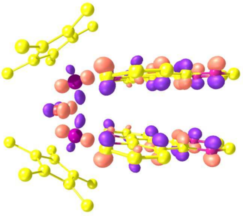	50%
LMCT transitions	500 nm	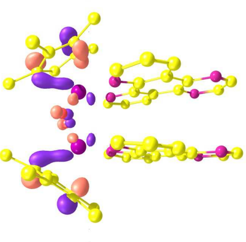	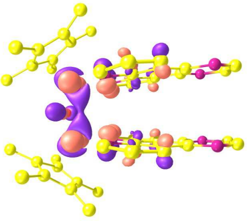	79%
	486 nm	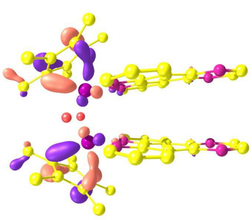	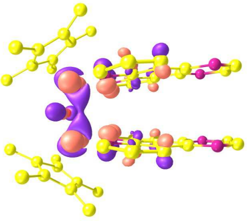	37%

Table 3.7.: Oscillator strengths for the electronic transitions of complex dpq-$W^{IV}W^{IV}$ (**4-a**) calculated by TD-DFT.

λ (nm)	f^a (≥ 0.0058)	Major contributions	Composition (≥ 0.2)
1922.17	0.0058	MO216a → MO217a (HOMO → LUMO)	0.815
840.19	0.0133	MO216a → MO222a (HOMO → LUMO+5)	0.862
814.38	0.0743	MO215a → MO217a (HOMO-1 → LUMO)	0.481
		MO216a → MO221a (HOMO → LUMO+4)	0.285
727.56	0.0081	MO215a → MO220a (HOMO-1 → LUMO+3)	0.624
		MO216a → MO223a (HOMO → LUMO+6)	0.321
676.67	0.0072	MO215a → MO221a (HOMO-1 → LUMO+4)	0.558
		MO216a → MO223a (HOMO → LUMO+6)	0.331
601.81	0.1422	MO215a → MO221a (HOMO-1 → LUMO+4)	0.385
		MO215a → MO220a (HOMO-1 → LUMO+3)	0.264
569.50	0.0113	MO215a → MO223a (HOMO-1 → LUMO+6)	0.928
500.26	0.0128	MO210a → MO217a (HOMO-6 → LUMO)	0.616
		MO216a → MO225a (HOMO → LUMO+6)	0.336
500.09	0.0562	MO212a → MO217a (HOMO-4 → LUMO)	0.789
494.31	0.0195	MO214a → MO218a (HOMO-2 → LUMO+1)	0.863
485.94	0.0499	MO216a → MO225a (HOMO → LUMO+8)	0.498
		MO210a → MO217a (HOMO-6 → LUMO)	0.366
476.23	0.0068	MO212a → MO218a (HOMO-4 → LUMO+1)	0.914
436.45	0.0148	MO216a → MO227a (HOMO → LUMO+10)	0.683
		MO215a → MO224a (HOMO-1 → LUMO+7)	0.267
412.15	0.0080	MO215a → MO225a (HOMO-1 → LUMO+8)	0.856
402.69	0.0853	MO210a → MO220a (HOMO-6 → LUMO+3)	0.866
391.26	0.0134	MO207a → MO219a (HOMO-9 → LUMO+2)	0.454
		MO212a → MO221a (HOMO-4 → LUMO+4)	0.306

[a] length representation of oscillator strength

The strong absorption of complex **4-a** in the visible spectrum makes it a potential photosensitizer for catalytic solar water splitting. The existence of both MLCT (W → dpq) and LMCT (Cp^* → W) transitions will create a charge separated state $[Cp^*]^+$-W-$[dpq]^-$ where the positive and negative charges are separated by some distance. As reported by Wasielewski et al.,[30,31,133–135] the electron transfer is distance-dependent in donor-bridge-acceptor systems. This charge separation might lead to a longer lived excited state due to the slower charge recombination over a longer distance.

3.5.3. Raman Spectroscopy of Complex 4-a

Resonant Raman spectroscopy was employed to shed a light on the character of the electronic transitions in the visible range. The Raman spectra of complex **4-a** was recorded on a Bruker Raman microscope spectrometer SENTERRA using laser excitation at 532, 633, 785 nm. The incident laser frequencies were chosen to be coincident with the charge transfer band energy (535 and 790 nm) and a third laser excitation (633 nm), where the absorption spectrum showed only weak absorptions, was employed for comparison.

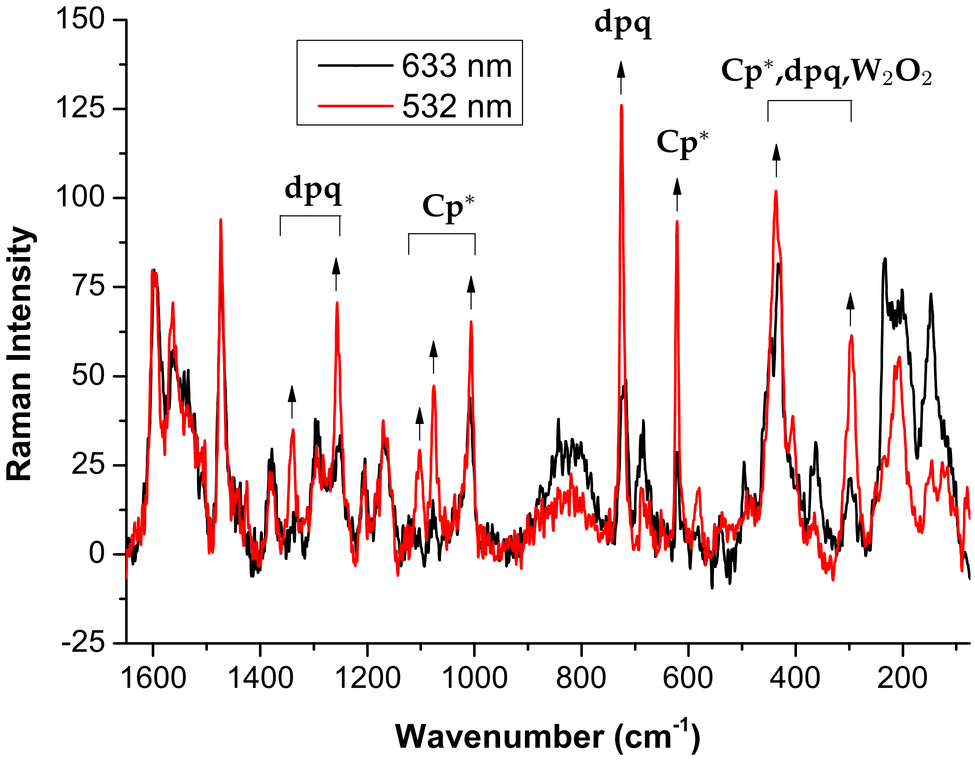

Figure 3.18.: Raman spectra of complex **4-a**, excitation wavelength: 532 nm (red line), 633 nm (black line).

Figure 3.18 compares the Raman spectra resonant at 532 nm with the spectra excited at 633 nm. The intensities of some of the Raman active vibrational modes are enhanced. Based on the results of DFT calculations (PBE functional, basis set: def2-TZVP), the enhanced vibrations at 1339, 1257 and 726 cm^{-1} are mainly vibration of the dpq ligand, while the vibrations of Cp* ligand has Raman active bands at 1103, 1076, 1006 and 622 cm^{-1}. This result confirms that the absorption at 535 nm of complex **4-a** (Figure 3.13) involves both Cp* and dpq ligands, i.e. the contribution from both LMCT and MLCT transitions.

Figure 3.19 shows the Raman spectra of complex **4-a** excited at 785 and 633 nm. Due to similar absorption at 633 and 785 nm (both of them are dpq → W charge transfer according to TD-DFT calculations, see Figure 3.17), the Raman spectra showed great resemblance except slightly more prominent low energy molecular vibrations at 404, 217 and 148 cm^{-1} when excited with the 785 nm NIR laser. This suggested that the same charge transfer transition is involved at both wavelengths of 633 and 785 nm, which is consistent with the assignment of the charge transfer bands at 630 and 790 nm to MLCT transitions.

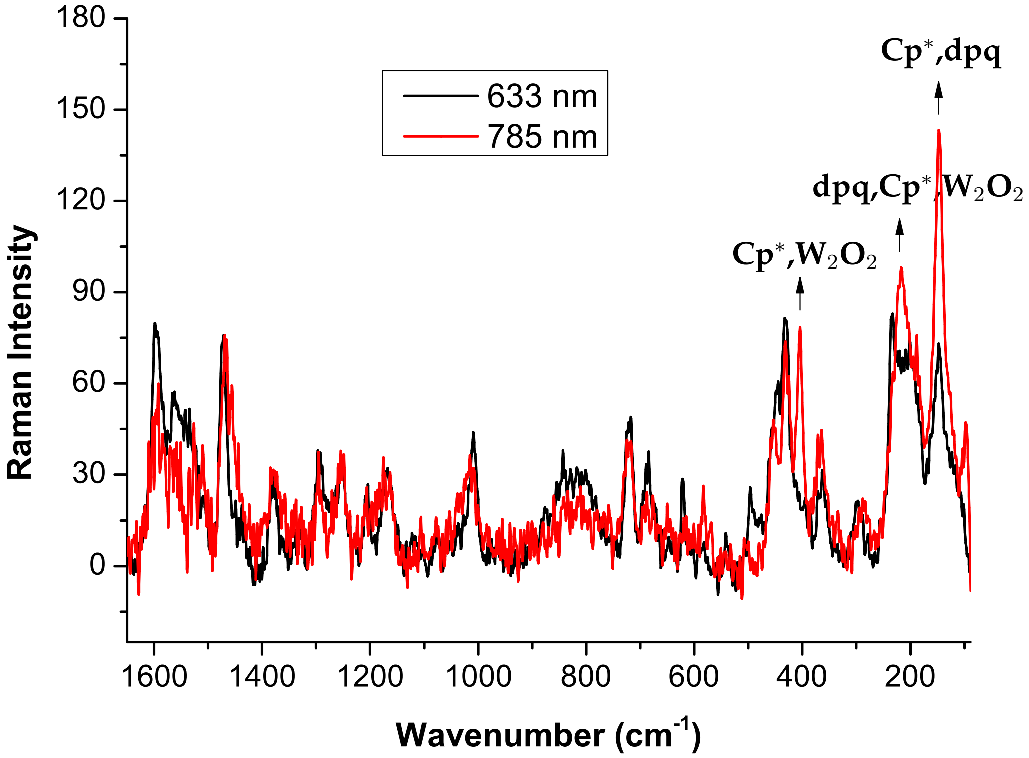

Figure 3.19.: Raman spectra of complex **4-a**, excitation wavelength: 785 nm (red line), 633 nm (black line).

3.6. Electrochemical Properties of Complex 4-a

Electrochemical experiments were carried out to study in detail the electron transfer processes of the μ-oxo ditungsten(*IV*/*IV*) complex $[(Cp^{*}W(dpq)(\mu{-}O))_2][PF_6]_2$ (**4-a**). The cyclic voltammetry (CV) method was performed using a Bioanalytical System (BAS) 100BW potentiostat with a three-electrode configuration in a glass cell in the glove box at RT. A 0.1 M solution of Bu_4NPF_6 supporting electrolyte in either acetonitrile or THF solvent was used. Ferrocene was employed as external reference due to its well behaved electrochemical reversibility. During each CV measurement, the solution remained quiescent. $E_{1/2}$ values for reversible processes were calculated from the middle position of cathodic and anodic redox peaks, which are used as formal redox potentials assuming that the differences in diffusion coefficients for oxidized and reduced species are negligible.

3.6.1. CV Measurement of 4-a in ACN

The potential-controlled electrochemical method CV was used to study the electron transfer property of complex **4-a**. The cyclic voltammogram of **4-a** in ACN is shown in Figure 3.20.

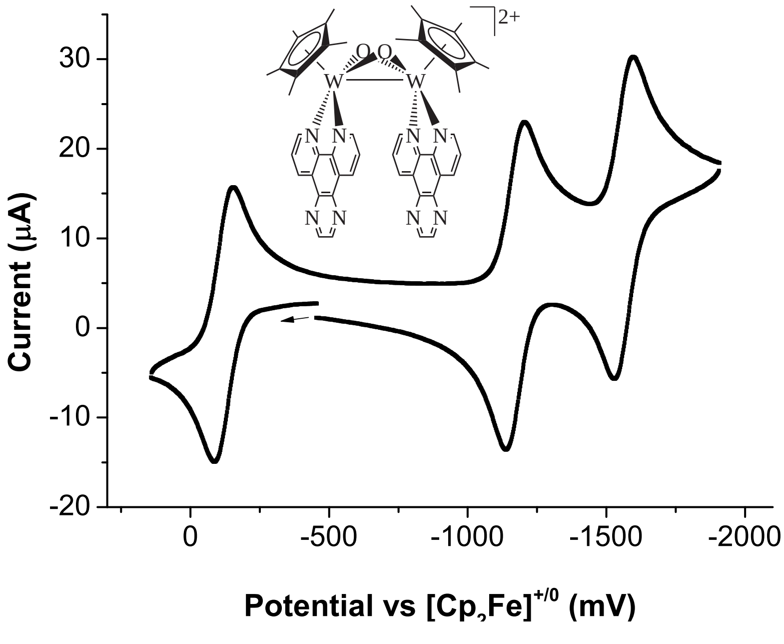

Figure 3.20.: Cyclic voltammogram for complex **4-a** [1 mM] in CH_3CN vs $[Cp_2Fe]^{+/0}$ at a scan rate of 100 mVs^{-1}, GC (Glassy Carbon) electrode (diameter = 3.0 mm) in 0.1 M NBu_4PF_6 acetonitrile solution.

The aforementioned DFT calculations showed that the HOMO and LUMO of complex **4-a** are both centered on the tungsten metal (see Table 3.6), therefore the observed redox waves can be readily assigned to the oxidation of the metal center. The cyclic voltammogram of complex **4-a** revealed three reversible electron transfer steps at - 120 mV (ΔE_p = 64 mV, I_{pc}/I_{pa} = 0.98), - 1171 mV (ΔE_p = 66 mV, I_{pc}/I_{pa} = 1.09) and - 1565 mV (ΔE_p = 66 mV, I_{pc}/I_{pa} = 0.99) vs. $[Cp_2Fe]/[Cp_2Fe^+]$, which can be assigned to redox couples $W^{V}W^{IV}/W^{IV}W^{IV}$, $W^{IV}W^{IV}/W^{IV}W^{III}$ and $W^{IV}W^{III}/W^{III}W^{III}$ respectively. The electrochemical data for complex **4-a** are summarized in Table 3.8.

Table 3.8.: Results of cyclic voltammetry experiment for complex **4-a** in CH_3CN (vs $[Cp_2Fe]^{+/0}$).

4-a	$W^{V}W^{IV}/W^{IV}W^{IV}$	$W^{IV}W^{IV}/W^{IV}W^{III}$	$W^{IV}W^{III}/W^{III}W^{III}$
$E_{1/2}$ [mV]	-120	-1171	-1565
ΔE_p [mV]	64	66	66
I_{pc}/I_{pa}	0.98	1.09	0.99

The difference in cathodic and anodic peak potentials (ΔE_p) at 25 °C is equal to $60/n$ mV for reversible multielectron transfer processes, which is derived from the relationship (eq. 3.1):

$$\Delta E_p = \frac{2.3 \cdot R \cdot T}{n \cdot F} \tag{3.1}$$

where n is the number of electron exchanged per molecule of species under study. In reality, a peak separation (ΔE_p) of 60 - 70 mV is often observed in CV experiments for reversible electron transfer due to the resistance of the solution.[136] Solution resistance causes a potential drop, called IR drop, therefore distorting the Faradaic response of reversible processes. The IR drop can be minimized by optimizing the electrolyte concentration, placing the working electrode and reference electrode as close as possible and using the feedback compensation method. For reversible electron transfer, the ratio between cathodic and anodic peak current with respect to their baselines (I_{pc}/I_{pa}) is 1. This current ratio allows to determine that the electrogenerated species is stable on the timescale of the CV experiment. According to the values for ΔE_p and I_{pc}/I_{pa} of complex **4-a**, the electrochemical mechanisms for the observed three redox couples can be described all as $\mathbf{E}_r$, which corresponds to fast one-electron transfers at the working electrode surface without geometrical reorganization in the redox steps.

Comproportionation constant

The comproportionation constant K_c can be measured electrochemically, since eq. 3.2

$$\Delta G^\circ = -RT(lnK_c) = -nF(\Delta E_{ox}) \tag{3.2}$$

relates ΔE_{ox} to the K_c of the chemical reaction (eq. 3.3)

$$W^{IV}W^{IV} + W^{III}W^{III} \rightleftharpoons 2\,W^{IV}W^{III} \tag{3.3}$$

where ΔE_{ox} corresponds to the separation between the two redox potentials for the successive oxidation processes.

The comproportionation equilibrium constant in the mixed-valence species dpq-$W^{IV}W^{III}$ (**7-a**) was determined by the difference between $E_{1/2}$ of the successive redox couples $W^{IV}W^{IV}/W^{IV}W^{III}$ and $W^{IV}W^{III}/W^{III}W^{III}$. The derived value of K_c = 4.6 x 10^6 is in the typical range (i.e. $10^6 \sim 10^{12}$) for delocalized valence electrons in the classification of Robin and Day.[137] The short distance between two tungsten metal centers (2.73 Å) allows the interaction by direct orbital overlap. The real electron configuration for the assigned formal oxidation state $W^{III}W^{IV}$ is therefore $d^{2.5}d^{2.5}$ rather than d^3d^2.

HOMO-LUMO energy gap

The redox potentials recorded in the cyclic voltammograms can be used to determine the LUMO and HOMO energy levels of the analyte, and the potential difference between the onset oxidation and reduction can be used to estimate the HOMO-LUMO gap.[138] The energy levels for complex **4-a** was calculated from the CV data (referenced to the $[Cp_2Fe]^{+/0}$ couple) using the expressions 3.4, 3.5 and 3.6:

$$E_{HOMO} = -(4.8eV + {E_{1/2}}^{ox}) \tag{3.4}$$

$$E_{LUMO} = -(4.8eV + {E_{1/2}}^{red}) \tag{3.5}$$

$$E_g = E_{LUMO} - E_{HOMO} \tag{3.6}$$

The HOMO and LUMO energy values of complex **4-a** were estimated to be - 4.68 eV and - 3.63 eV vs $[Cp_2Fe]^{+/0}$ respectively. The derived energy gap between the HOMO and LUMO amounts to 1.05 eV.

CV Measurement of the free dpq ligand in ACN

Based on the fact that the dpq ligand possesses a low-lying π^* orbital, it is an potentially non-innocent ligand, i.e. can also be reduced itself. In order to find out, whether the redox processes observed for complex **4-a** are based on the metal centers or the attached dpq ligand, further electrochemical studies were carried out for the free dpq ligand. The cyclic voltammogram for the free dpq ligand was recorded in acetonitrile (see Figure 3.21).

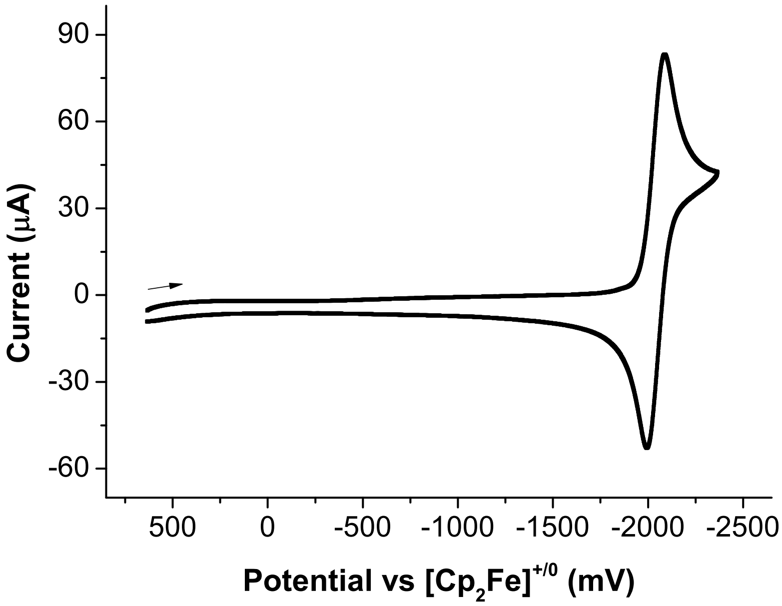

Figure 3.21.: Cyclic voltammogram for the free dpq ligand in CH_3CN vs $[Cp_2Fe]^{+/0}$, scan rate: 100 mVs^{-1}, GC electrode (diameter = 3.0 mm), 0.1 M NBu_4PF_6.)

A reversible redox wave at - 2042 mV (ΔE_p = 89 mV, I_{pc}/I_{pa} = 1.02) was observed for the free ligand dpq vs. $[Cp_2Fe]/[Cp_2Fe^+]$. The formal potential of the first reduction of the dpq free ligand was used to correlate the energy of its lowest unoccupied molecular orbital, which was found to be - 2.759 eV vs $[Cp_2Fe]^{+/0}$. This confirmed that the three reversible redox waves of complex **4-a** at - 120 mV, - 1171 mV and - 1565 mV are based on the redox processes of the two tungsten centers.

3.6.2. CV Measurement of 4-a in ACN/THF Mixture

In the potential window of acetonitrile, three reversible redox waves were observed. In order to find out whether further reductive processes could take place at potentials lower than - 2 V, THF was employed, which has a larger cathodic window. However, the solubility of complex **4-a** in THF is rather poor. A solvent mixture of CH_3CN/THF (1:1) was used to access more negative potentials and yet retain a reasonable solubility for complex **4-a**. The cyclic voltammogram of complex **4-a** in a CH_3CN/THF(1:1) solvent mixture is presented in Figure 3.22.

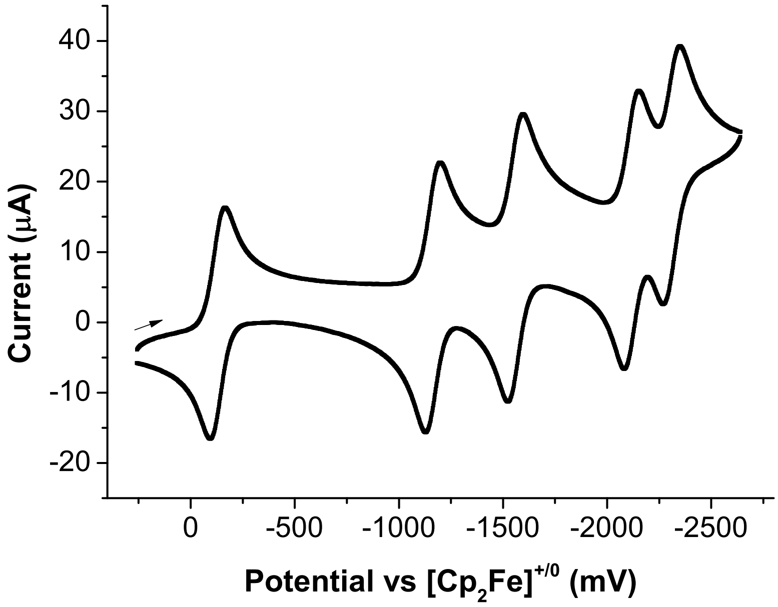

Figure 3.22.: Cyclic voltammogram for complex **4-a** [1 mM] in CH_3CN/THF (1:1) vs $[Cp_2Fe]^{+/0}$ at a scan rate of 100 mVs^{-1}, GC electrode (diameter = 3.0 mm) in 0.1 M NBu_4PF_6 solution.

The cyclic voltammogram of complex **4-a** measured in a CH_3CN/THF solvent mixture revealed also three tungsten based reversible redox couples at - 129 mV, - 1164 mV and - 1560 mV, furthermore, two additional redox couples at - 2116 mV (ΔE_p = 70 mV, I_{pc}/I_{pa} = 1.22) and - 2310 mV (ΔE_p = 78 mV, I_{pc}/I_{pa} = 0.72). Due to the small separation between the last two redox waves, the cathodic and anodic peak currents could not be accurately determined.

CV Measurement of the free dpq ligand in ACN/THF Mixture

The CV measurement was also performed for the free dpq ligand under the same condition in the CH_3CN/THF (1:1) solvent mixture. The cyclic voltammogram of the free dpq ligand (Figure 3.23) displays a reversible electron transfer at the potential of - 2087 mV (ΔE_p = 75 mV, I_{pc}/I_{pa} = 1.01). Scanning the potential more negative beyond this redox process revealed no additional waves before the limit of the solvent window was reached.

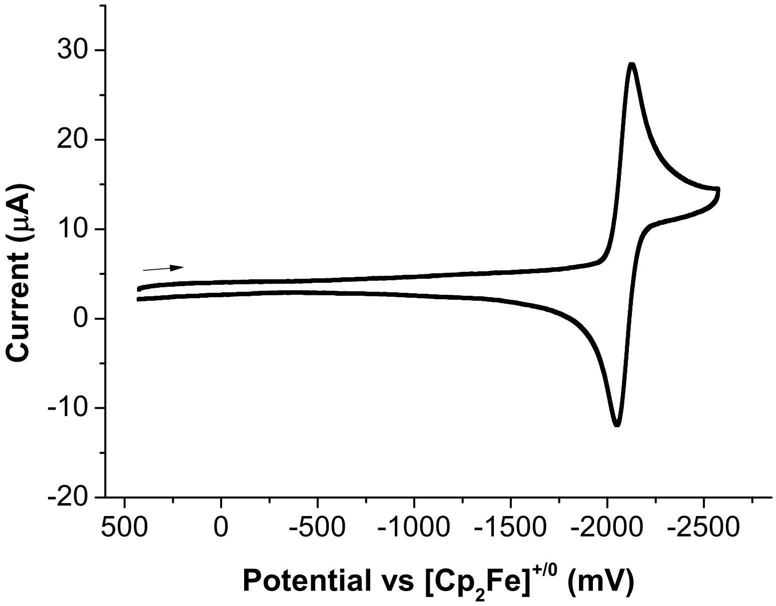

Figure 3.23.: Cyclic voltammograms for dpq ligand [1 mM] in CH_3CN/THF (1:1) vs $[Cp_2Fe]^{+/0}$ at a scan rate of 100 mVs^{-1}, GC electrode (diameter = 3.0 mm), 0.1 M NBu_4PF_6.

According to DFT calculations, the HOMO of dpq-$W^{III}W^{III}$ is mainly based on the metal center, while the LUMO is based on the dpq ligand (see Figure 3.24). Thus, the redox waves observed at - 2116 mV and - 2310 mV in Figure 3.22 are assigned to the dpq ligand rather than the tungsten centers. This is also in accordance with the redox waves for the free dpq ligand located at - 2087 mV (see Figure 3.23). The CV data for complex **4-a** in CH_3CN/THF is summarized in Table 3.9.

By comparison with the CV measured in pure acetonitrile for **4-a**, there is a notable shift of the $E_{1/2}$ values in the THF/ACN (vol:vol 1:1) solvent mixture. The oxidation potential for $[\mathbf{4\text{-}a}]^+/[\mathbf{4\text{-}a}]$ is less positive in THF/ACN (- 129 mV) than in pure ACN (- 120 mV) while the reduction potentials for $[\mathbf{4\text{-}a}]/[\mathbf{4\text{-}a}]^-$ and [**4-**

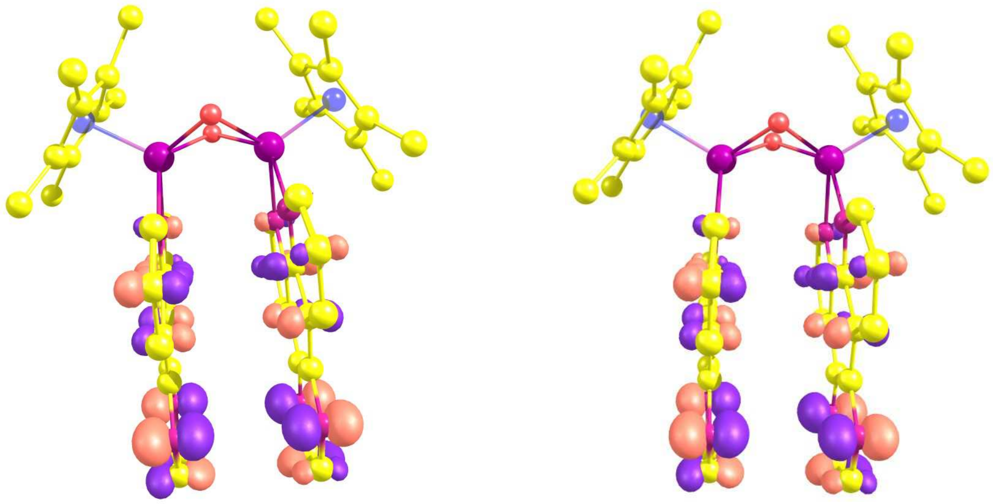

LUMO orbital **LUMO+1 orbital**

Figure 3.24.: The LUMO and LUMO+1 plots of [**4-a**]$^{2\ominus}$.

Table 3.9.: Results of cyclic voltammetry experiments for complex 4-a in CH_3CN/THF (vs $[Cp_2Fe]^{+/0}$).

4-a	$E_{1/2}$ [mV]	ΔE_p [mV]	I_{pc}/I_{pa}
$W^{V}W^{IV}/W^{IV}W^{IV}$	-129	68	1.00
$W^{IV}W^{IV}/W^{IV}W^{III}$	-1164	70	1.16
$W^{IV}W^{III}/W^{III}W^{III}$	-1560	70	0.96
$dpq^{0/-}$	-2116	70	1.22
$dpq^{0/-}$	-2310	78	0.72

a]$^-$/[**4-a**]$^{2-}$ are less negative in THF/ACN (- 1164 and -1560 mV) than in pure ACN (- 1171 and - 1565 mV), indicating that complex **4-a** is more stable in ACN than in THF. This can be readily rationalized by the stronger solubility of the ionic system in the more polar ACN solvent.

3.7. Distinctive Electrochemical Behavior of Complex 4-b

The electrochemical behavior of complex **4-b** was investigated by cyclic voltammetry in ACN, THF and a solvent mixture of ACN/THF. As will be detailed below, the electrochemical properties of the dpphen substituted μ-oxo-bridged complex **4-b** differ from the R_2bpy (R = NMe_2, Me, H, Cl) and dpq substituted analogues, which all showed simple E_r mechanism.

3.7.1. CV Measurement of 4-b in ACN

The cyclovoltammetric study was performed for complex **4-b** using a platinum disk working electrode in acetonitrile. As can be seen from the black line in Figure 3.25, two reversible redox couples were observed at - 209 mV (ΔE_p = 61 mV, I_{pc}/I_{pa} = 0.93) and - 1307 mV (ΔE_p = 61 mV, I_{pc}/I_{pa} = 1.06) vs $[Cp_2Fe]^{+/0}$ when the cyclic voltammograme was recorded in the range of + 70 to - 1580 mV, which can be assigned to the $W^VW^{IV}/W^{IV}W^{IV}$ and $W^{IV}W^{IV}/W^{IV}W^{III}$ redox couples respectively.

However, when the range was extended to -2030 mV, a further irreversible reduction peak at -1706 mV was observed. A huge anodic Gaussian shaped current at E_{pa2} = - 1237 mV (I_{pa2} = - 9.705$\times10^{-5}$ A) was detected upon sweeping back, instead of the previously observed reversible one-electron oxidation wave of E_{pa1} = - 1277 mV (see red line in Figure 3.25). The cathodic current at - 1336 mV for one-electron reduction is + 1.441$\times10^{-5}$ A (I_{pc1}), which leads to a current ration of I_{pa2}/I_{pc1} = 6.73.

The application of platinum and glassy carbon working electrodes both led to similar voltammograms, which are reproducible and did not change in repetitive scans.

The CV of the Me_2bpy substituted bis-μ-oxo bridged complex Me_2bpy-$W^{IV}W^{IV}$ ($[(Cp^*W(Me_2bpy)(\mu{-}O))_2][PF_6]_2$) presented in Chapter 1 Figure 1.8 revealed one reversible one-electron oxidation and two reversible one-electron reduction steps. The isolated complexes Me_2bpy-W^VW^{IV} and Me_2bpy-$W^{IV}W^{III}$ display essentially identical geometries to complex Me_2bpy-$W^{IV}W^{IV}$ with a *cis* orientation of the Cp^* rings. On the contrary, the crystal structure analysis of the independently pre-

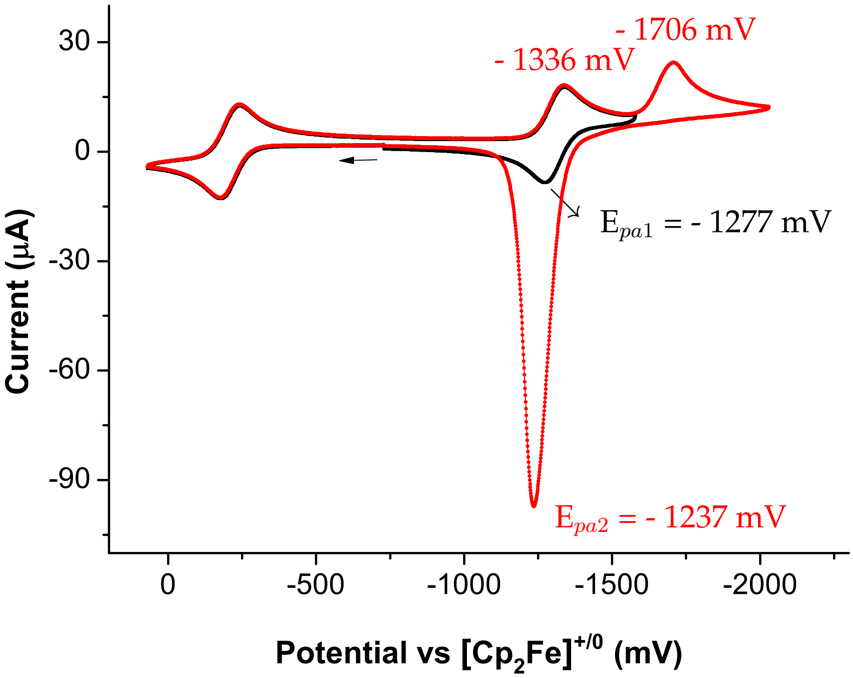

Figure 3.25.: Cyclic voltammograms for complex **4-b** [0.82 mM] in CH_3CN vs $[Cp_2Fe]^{+/0}$ at a scan rate of 200 mVs^{-1}, GC electrode (diameter = 3.0 mm), 0.1 M NBu_4PF_6 solution.

pared complex Me_2bpy-$W^{III}W^{III}$ evidenced a *trans* disposition of the Cp rings. At first glance, this is conflict with the reversible wave observed for the second reduction. It was deemed that the cis-geometry of complex Me_2bpy-$W^{III}W^{III}$ is maintained on the timescale of the electrochemical experiment.[83] Based on those previous results, we considered an ECE mechanism for the Gaussian shape anodic wave, where the chemical steps correspond to cis/trans isomerizations.

In the case of the dpphen substituted bis-μ-oxo bridged complex **4-b**, the cis-trans isomerization might be faster than in the Me_2bpy substituted complex Me_2bpy-$W^{IV}W^{IV}$. This is supported by the higher steric repulsion for the cis-isomer in the dpphen system . In the time domain of the CV experiments, the isomerization interferes with the electrochemical behavior. The reduction mechanisms for complex **4-b** can be ascribed as follows:

$$\mathbf{E:} \quad cis-W^{IV}W^{IV} + e \rightleftharpoons cis-W^{IV}W^{III} \tag{3.7}$$

$$\mathbf{E:} \quad cis-W^{IV}W^{III} + e \rightleftharpoons cis-W^{III}W^{III} \tag{3.8}$$

$$\mathbf{C:} \quad cis-W^{III}W^{III} \rightarrow trans-W^{III}W^{III} \tag{3.9}$$

$$\textbf{ECE:}\quad trans-W^{III}W^{III} \rightleftharpoons cis-W^{IV}W^{IV} + 2e \tag{3.10}$$

The first reduction wave at - 1336 mV corresponds to the one-electron reduction of *cis*-$W^{IV}W^{IV}$ to *cis*-$W^{IV}W^{III}$ (3.7). The second reduction wave at - 1706 mV can be described as EC mechanism, which is recognized by the lack of the reverse peak. The EC process consists of an one-electron reduction at the electrode surface to form *cis*-$W^{III}W^{III}$ and a consecutive chemical reaction in solution that converted *cis*-$W^{III}W^{III}$ to *trans*-$W^{III}W^{III}$ (see 3.8 and 3.9). The shape of the last reduction wave at - 1706 mV is quite sharp as compared with the other one-electron transfer peaks. This kind of peak shape typically corresponds to fast electrode kinetics and chemical kinetics.[136] Furthermore, the reverse peak is virtually absent due to the fast irreversible chemical reaction following the electrode reduction. As soon as the *cis*-$W^{III}W^{III}$ is generated, it is removed from the electrode surface by the isomerization reaction.

With regard to the Gaussian shaped anodic wave, it is possible that the active species was adsorbed on the electrode surface, which is excluded by analysis of current dependence on scan rate (vide infra). The chemically generated species *trans*-$W^{III}W^{III}$ has a different oxidation potential (E_p = - 1237 mV) as the *cis*-isomer. The huge anodic current I_{pa2} is ascribed to a simultaneous two-electron transfer step of *trans*-$W^{III}W^{III}$ accompanied with molecular reorganization (3.10). This process can be expressed in detail with the following equations:

$$\textbf{E:}\quad trans-W^{III}W^{III} \rightleftharpoons trans-W^{IV}W^{III} + e \qquad E_1^{o\prime} \tag{3.11}$$

$$\textbf{C:}\quad trans-W^{IV}W^{III} \rightarrow cis-W^{IV}W^{III} \tag{3.12}$$

$$\textbf{E:}\quad cis-W^{IV}W^{III} \rightleftharpoons cis-W^{IV}W^{IV} + e \qquad E_2^{o\prime} \tag{3.13}$$

In principle, the addition of the first electron must render the second electron addition electrostatically unfavorable and this is the reason why most electron transfers occur sequentially. Only in the case that some molecular reorganization at the microscopic level occurs within the original molecule, which rendering available a non-bonding molecular orbital, can allow the second electron to enter simultaneously or even more favorably than the first one.[139] Here, the formal electrode potential for one-electron oxidation of *trans*-$W^{III}W^{III}$, $E_1^{o\prime}$, is even more positive than the formal electrode potential for one-electron oxidation of *cis*-$W^{IV}W^{III}$ $E_2^{o\prime}$. That is to say that *cis*-$W^{IV}W^{III}$ is more easily oxidized than *trans*-$W^{III}W^{III}$. Therefore the two one-electron transfers 3.11 and 3.13 take place simultaneously. The evidence of ECE mechanism for the Gaussian shaped wave is provided by analysis of the current dependence on the scan rate (see below).

3.7.2. Current Dependence on Scan Rate

In order to gain further insight into the mechanism of the oxidation process of electrochemically generated neutral species **[4-a]**$^{2\ominus}$, cyclic voltammetry of complex **4-b** were analyzed at scan rates of 10, 50, 100, 200 and 500 mV/s in acetonitrile (Figure 3.26).

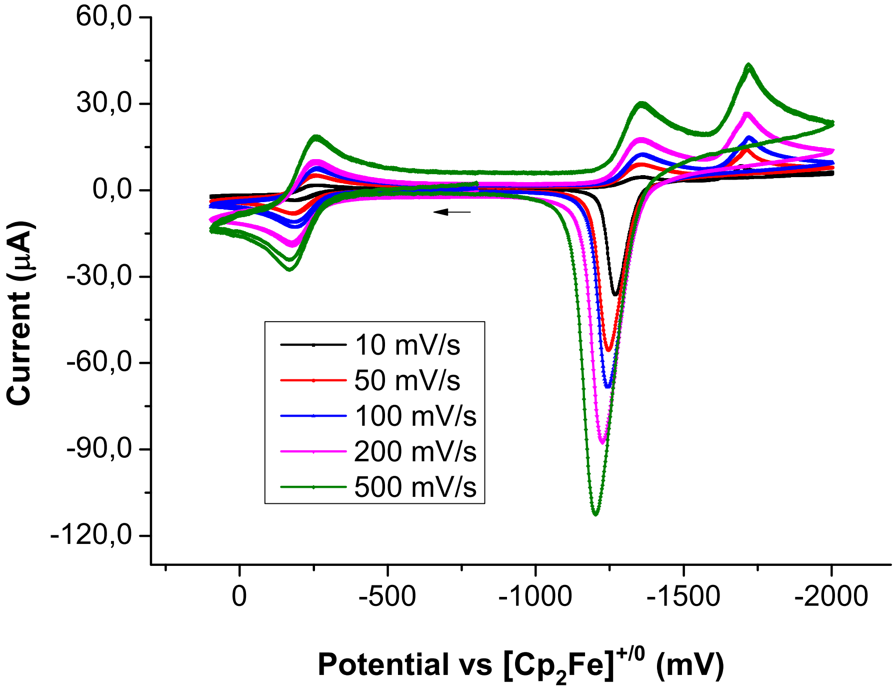

Figure 3.26.: Cyclic voltammograms for complex **4-b** [1.74 mM] in CH_3CN vs $[Cp_2Fe]^{+/0}$ at various scan rates, Pt electrode (diameter = 1.6 mm), 0.1 M NBu_4PF_6.

The effect of the scan rate (ν) on the CV can be described by the Randle-Sevcik equation[136] for an electrochemically reversible system (rapid electron transfer at the electrode surface) at 25 °C:

$$I_p = (2.69 \times 10^5) \cdot n^{3/2} \cdot A \cdot D^{1/2} \cdot C \cdot \nu^{1/2} \tag{3.14}$$

where

I_p is the peak current
n is the electron stoichiometry
A is the electrode area (cm^2)
D is the diffusion coefficient (cm^2/s)
C is the concentration (mol/cm^3)
ν is the scan rate (V/s)

Thus, I_p is proportional to C and $\nu^{1/2}$ for a reversible electrode reaction. From a plot of i_{pc} or i_{pa} versus $\nu^{1/2}$ the diffusion coefficient for the system can be derived. According to the onset anodic (oxidation) current of complex **4-b** presented in Figure 3.25, the diffusion coefficient of dpphen-W^{IV}W^{IV} complex in ACN solvent can be estimated as 8.0239 $\times 10^{-6}$ cm^2/s using the geometrical values for the surface of the disk electrode.

The linear dependence of the peak current for the reversible process on the square root of scan rate is most accurately determined for the initial sweep peak, which have the same initial concentration of the analyte. Figure 3.27 shows the plots of the peak current of the first oxidation and the first reduction of complex **4-b** as a function of the square root of scan rate, which clearly revealed diffusion controlled processes.

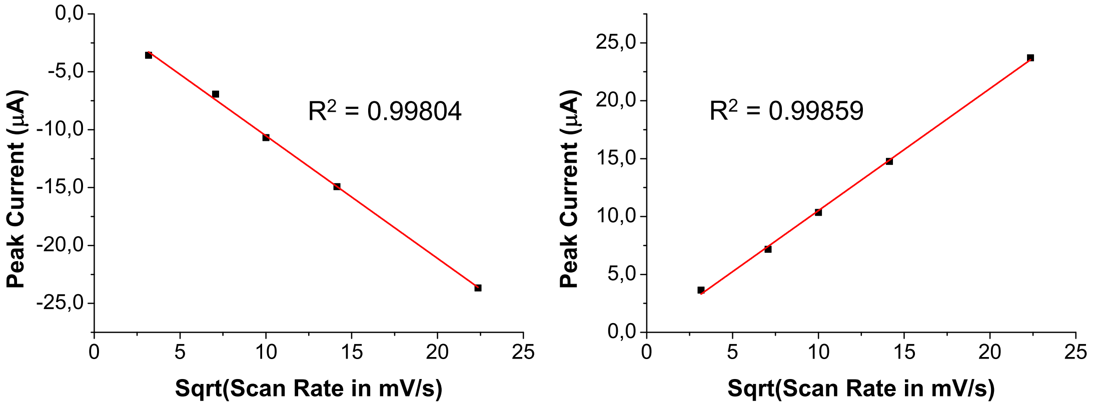

Figure 3.27.: Plots of the peak currents of the first oxidation (left) and the first reduction (right) waves of complex **4-b** in CH_3CN, as a function of the square root of the scan rate.

The huge anodic peak current was proportional to the square root of the scan rate at least up to 500 mV/s, which clearly showed a diffusion-controlled process rather than an adsorption process (see Figure 3.28 left).

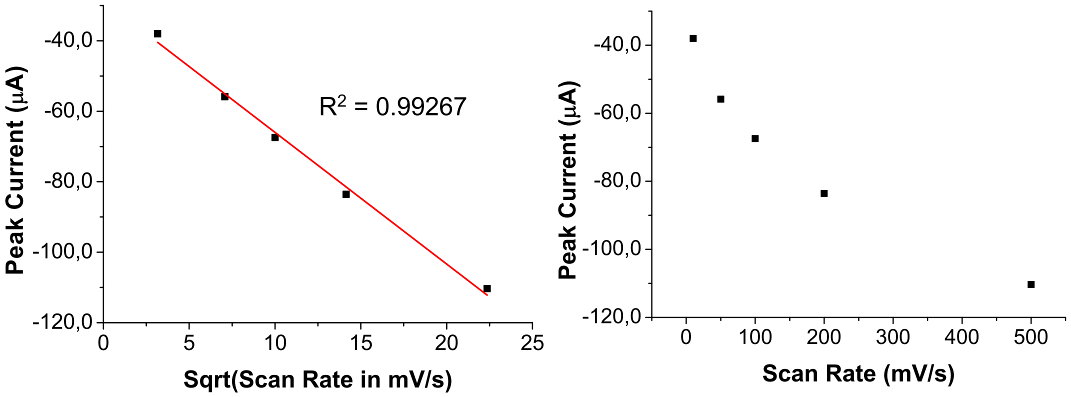

Figure 3.28.: Plots of the anodic peak current for the two-electron oxidation process of complex **4-b** upon sweeping back in CH_3CN as a function of the square root of scan rate (left) and as a function of scan rate (right).

The peak current i_p involving adsorption can be given by:

$$i_p = \frac{n^2 \cdot F^2}{4 \cdot R \cdot T} \cdot \nu \cdot A \cdot \Gamma_{ox} \tag{3.15}$$

where Γ_{ox} is the surface coverage(mol/cm^2). On increasing the scan rate, the intensity of the adsorption peak should linearly increase with ν, which is not this case for the Gaussian shaped current (Figure 3.28 right).

According to equation 3.1, the peak separation (ΔE_p) is independent of the scan rate for reversible processes. However, the values for ΔE_p derived from Figure 3.26 for the first reversible oxidation are 72, 74, 76 and 90 mV for scan rates of 50, 100, 200 and 500 mV/s, respectively. At higher scan rates, ΔE_p starts to increase. This may be due to slow electron transfer kinetics or an ohmic potential (*iR*) drop.

When the scan rate was extended to 10 V/s, the linear dependence of the Gaussian shaped current on the square root of the scan rate ($\nu^{1/2}$) was no longer observed (see Figure 3.29). At scan rates higher than 2 V/s, the corresponding anodic wave for the second reduction starts to appear. The current ratio I_{pr}/I_{pf} of the second reduction increases with the scan rate up to 1, which is the most significant evidence for a EC mechanism.

At a scan rate of 10 V/s, the chemical reaction rate is too slow to compete with the electrode reaction rate. Therefore, three reversible redox waves at - 211 mV (ΔE_p = 131 mV, I_{pc}/I_{pa} = 0.94), - 1308 mV (ΔE_p = 154 mV, I_{pc}/I_{pa} = 0.91) and - 1695 mV (ΔE_p = 134 mV, I_{pc}/I_{pa} = 1.18) vs $[Cp_2Fe]^{+/0}$ were observed, which can be confi-

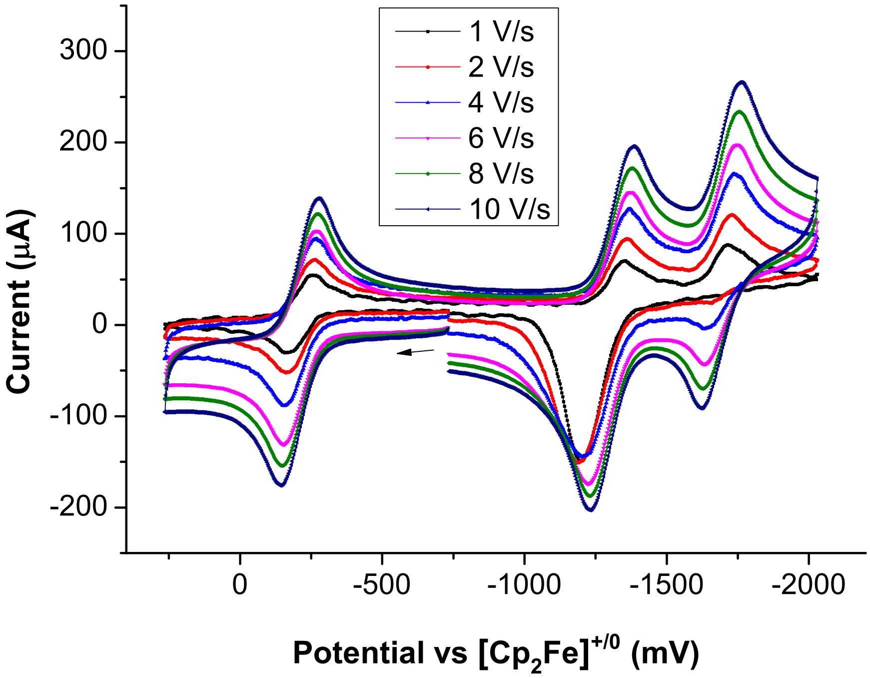

Figure 3.29.: Cyclic voltammograms for complex **4-b** [0.82 mM] in CH_3CN vs $[Cp_2Fe]^{+/0}$ at various scan rates, glassy carbon electrode (diameter = 3.0 mm), 0.1 M NBu_4PF_6.

dently assigned to $W^VW^{IV}/W^{IV}W^{IV}$, $W^{IV}W^{IV}/W^{IV}W^{III}$ and $W^{IV}W^{III}/W^{III}W^{III}$ redox couples respectively. The electrochemical data for complex **4-b** at a scan rate of 10 V/s in ACN is listed in Table 3.10.

Table 3.10.: Results of cyclic voltammetry experiments for complex **4-b** in ACN at a scan rate of 10 V/s (vs $[Cp_2Fe]^{+/0}$).

4-b	$W^VW^{IV}/W^{IV}W^{IV}$	$W^{IV}W^{IV}/W^{IV}W^{III}$	$W^{IV}W^{III}/W^{III}W^{III}$
$E_{1/2}$ [mV]	-211	-1308	-1695
ΔE_p [mV]	131	154	134
I_{pc}/I_{pa}	0.94	0.91	1.18

When the scan rate is beyond 10 V/s, the *iR* drop and charging current distortions become very significant. A cyclic voltammogram for complex **4-b** at a scan rate of 15 V/s in the full potential window of acetonitrile is provided in Figure 3.30.

Besides the previously assigned three redox waves, two additional redox waves at - 2304 mV (ΔE_p = 166 mV, I_{pc}/I_{pa} = 1.22) and - 2654 mV (ΔE_p = 189 mV, I_{pc}/I_{pa} =

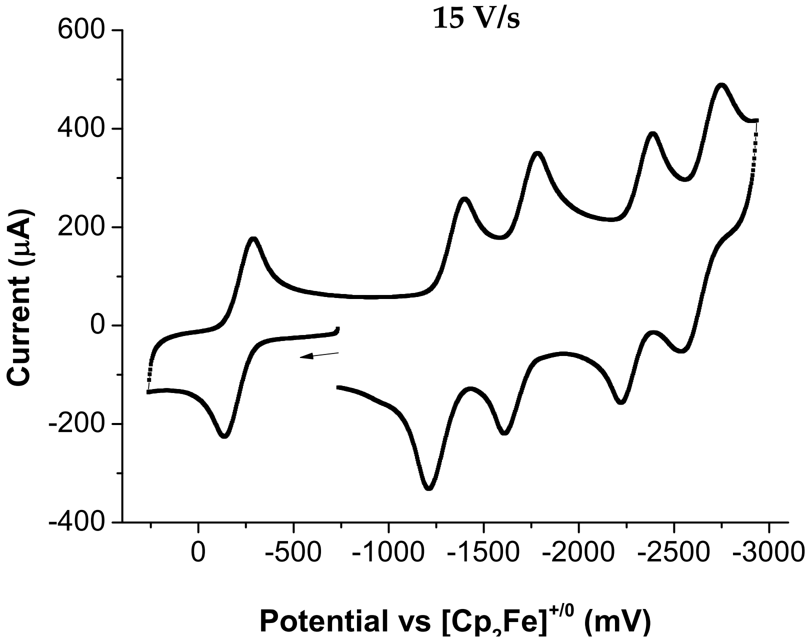

Figure 3.30.: Cyclic voltammograms for complex **4-b** [0.82 mM] in CH_3CN vs $[Cp_2Fe]^{+/0}$ at a scan rate of 15 V/s, glassy carbon electrode (diameter = 3.0 mm), 0.1 M NBu_4PF_6.

1.26) vs $[Cp_2Fe]^{+/0}$ were also observed. These redox waves have potentials comparable to those of the free dpphen ligand (- 2359 mV vs $[Cp_2Fe]^{+/0}$ at a scan rate of 100 mV/s, see Figure 3.32). It is therefore anticipated that these redox processes are also ligand based redox couples as the dpq substituted analogue **4-a**. All electrochemical data for complex **4-b** at a scan rate of 15 V/s are summarized in Table 3.11.

Table 3.11.: Results of cyclic voltammetry experiments for complex **4-b** in ACN at a scan rate of 15 V/s (vs $[Cp_2Fe]^{+/0}$).

4-b	$E_{1/2}$ [mV]	ΔE_p [mV]	I_{pc}/I_{pa}
$W^{V}W^{IV}/W^{IV}W^{IV}$	-213	150	0.92
$W^{IV}W^{IV}/W^{IV}W^{III}$	-1306	185	0.93
$W^{IV}W^{III}/W^{III}W^{III}$	-1696	172	1.10
$dpphen^{0/-}$	-2304	166	1.22
$dpphen^{0/-}$	-2654	189	1.26

When the negative window of ACN was explored at a low scan rate of 100 mV/s, decomposed complexes were observed (see Figure 3.31) instead of two ligand based reversible redox waves recorded at a scan rate of 15 V/s. From Figure 3.30 (scan rate of 15 V/s) and Figure 3.31 (scan rate of 100 mV/s), we can estimate that *cis*-$W^{III}W^{III}$ can undergo two reversible reduction but *trans*-$W^{III}W^{III}$ decomposes upon reduction. This further confirmed that the consecutive two reduction waves of *cis*-$W^{III}W^{III}$ is based on the ligand rather than the metal centers.

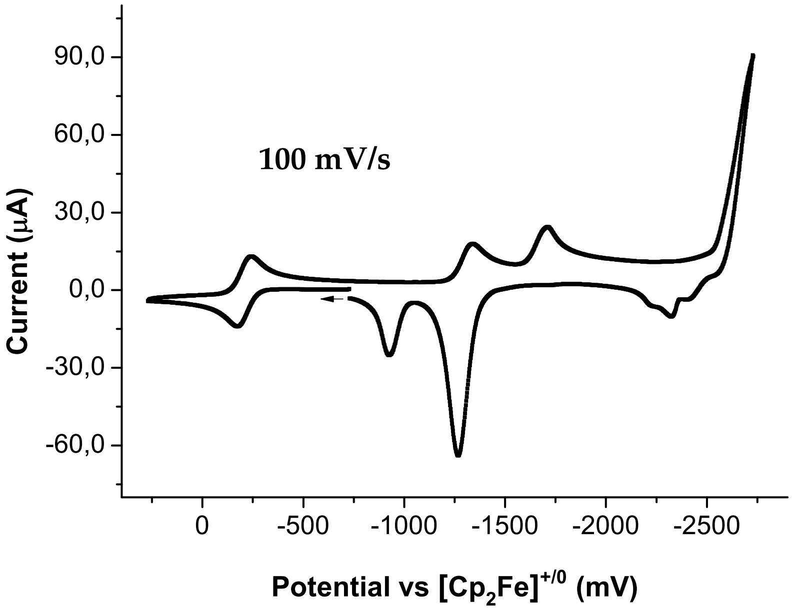

Figure 3.31.: Cyclic voltammograms for complex **4-b** [0.82 mM] in CH_3CN vs $[Cp_2Fe]^{+/0}$ at a scan rate of 100 mV/s, glassy carbon electrode (diameter = 3.0 mm), 0.1 M NBu_4PF_6.

CV Measurement of the Free dpphen Ligand in ACN

The electrochemical study was also performed for the free dpphen ligand under the same condition. Figure 3.32 shows a reversible redox process at - 2359 mV vs $[Cp_2Fe]^{+/0}$ with peak separation of 77 mV near the potential window of acetonitrile solvent.

Applying eq. 3.5, the LUMO energy of the dpphen free ligand can be derived as - 2.441 eV vs $[Cp_2Fe]^{+/0}$, which is 0.318 eV higher than the energy of the LUMO of the free dpq ligand.

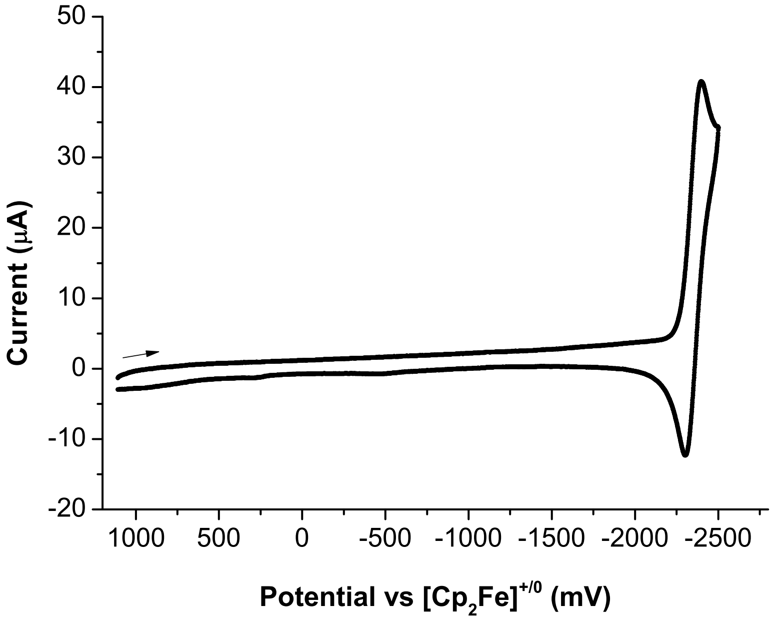

Figure 3.32.: Cyclic voltammogram for the free dpphen ligand in CH_3CN vs $[Cp_2Fe]^{+/0}$ at a scan rate of 100 mVs^{-1}, Pt electrode (diameter = 1.6 mm), 0.1 M NBu_4PF_6.

3.7.3. Solvent Dependence of Reversibility

In the course of the study, it was found that the reversibility of the electrochemical steps in the dpphen substituted μ-oxo-bridged ditungsten complex **4-b** is solvent dependent. This was systematically probed for different ratios of the ACN/THF mixture.

3.7.3.1. CV Measurement in THF

The electrochemical study of complex **4-b** was also performed in THF solvent. In THF, complex **4-b** is only slightly soluble and the concentration of the analyte in THF solvent is less than 1.74 mM. Normal reversible redox waves were observed in THF solvent, see Figure 3.33.

The cyclic voltammogram of complex **4-b** in THF illustrates one reversible oxidation wave at - 286 mV (ΔE_p = 126 mV, I_{pc}/I_{pa} = 0.97) for $W^{V}W^{IV}/W^{IV}W^{IV}$, two reversible reduction waves at - 1335 mV (ΔE_p = 128 mV, I_{pc}/I_{pa} = 1.18) and - 1656 mV (ΔE_p = 126 mV, I_{pc}/I_{pa} = 0.97) for $W^{IV}W^{IV}/W^{IV}W^{III}$ and $W^{IV}W^{III}/W^{III}W^{III}$

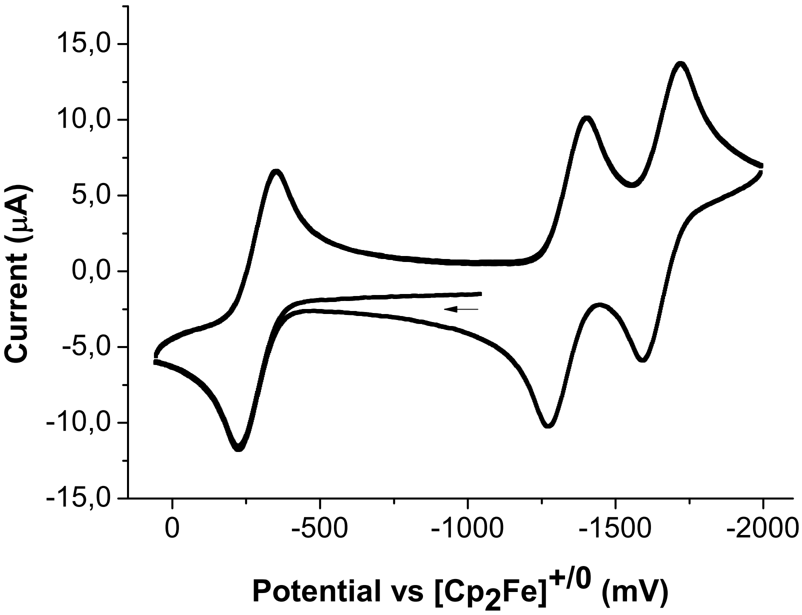

Figure 3.33.: Cyclic voltammograms for complex **4-b** [$\leq$ 1.74 mM] in THF vs $[Cp_2Fe]^{+/0}$ at a scan rate of 100 mVs^{-1}, GC electrode (diameter = 3.0 mm) in 0.1 M NBu_4PF_6 solution.

respectively. The CV data in THF for **4-b** are listed in Table 3.12.

Table 3.12.: Results of cyclic voltammetry experiments for complex **4-b** in THF (vs $[Cp_2Fe]^{+/0}$).

4-b	$W^{V}W^{IV}/W^{IV}W^{IV}$	$W^{IV}W^{IV}/W^{IV}W^{III}$	$W^{IV}W^{III}/W^{III}W^{III}$
$E_{1/2}$ [mV]	-286	-1335	-1656
ΔE_p [mV]	126	128	126
I_{pc}/I_{pa}	0.97	1.18	0.97

The effect of the scan rate on the voltammograms was also investigated using various scan rates: 50, 100, 200, 500 and 1000 mV/s. All peak currents are linearly dependent on the square root of scan rate, which proved that all redox process are diffusion controlled.

A CV of complex **4-b** at lower concentration ($\leq$ 0.88 mM) in THF was also recorded in a wider potential range in the presence of ferrocene (Figure 3.34).

This voltammogram showed a third reversible one-electron reduction wave at -2415 mV (ΔE_p = 108 mV, I_{pc}/I_{pa} = 1.09) which is assigned to the ligand based

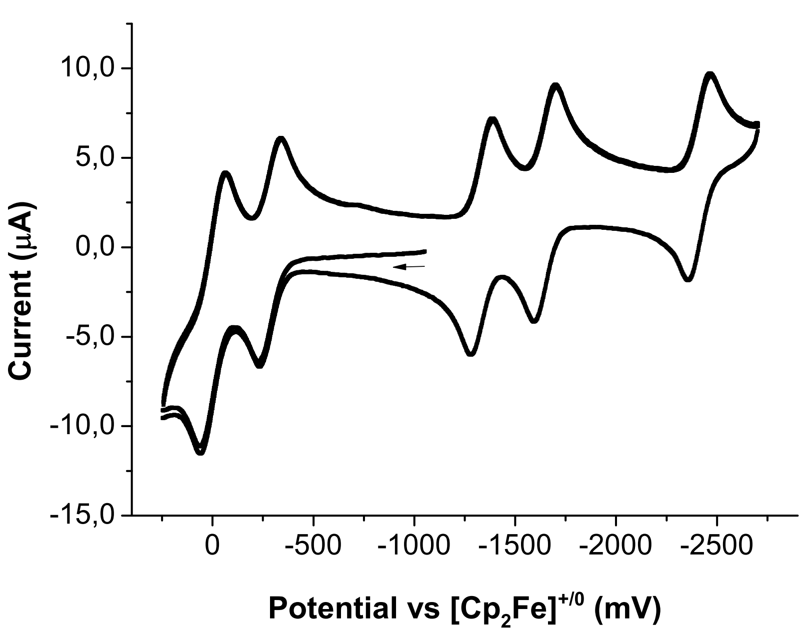

Figure 3.34.: Cyclic voltammograms for complex **4-b** [$\leq$ 0.88 mM] in THF at a scan rate of 100 mVs^{-1}in the presence of ferrocene, GC electrode (diameter = 3.0 mm) in 0.1 M NBu_4PF_6 solution. Potentials are referenced to the ferrocenium/ferrocene couple shown at 0 V.

redox couple dpphen$^{0/-}$. The detailed CV data are summarized in Table 3.13. It is noted that the peak separation ΔE_p is smaller for lower concentration of the analyte. Due to the narrow separation of the redox waves, the deviation of current ratio I_{pc}/I_{pa} from unit is not compromising the reversibility of the process.

Table 3.13.: Results of cyclic voltammetry experiments for complex **4-b** in THF (vs $[Cp_2Fe]^{+/0}$).

4-b	$E_{1/2}$ [mV]	ΔE_p [mV]	I_{pc}/I_{pa}
$[Cp_2Fe]^+/[Cp_2Fe]$	0	114	0.73
$W^VW^{IV}/W^{IV}W^{IV}$	-286	110	0.84
$W^{IV}W^{IV}/W^{IV}W^{III}$	-1335	108	1.25
$W^{IV}W^{III}/W^{III}W^{III}$	-1646	114	0.87
dpphen$^{0/-}$	-2415	108	1.09

3.7.3.2. CV Measurement in THF upon addition of ACN

The CV of complex **4-b** ($\leq$ 1.0 mM) in pure THF is shown in Figure 3.35 (black line) . Upon addition of acetonitrile to THF, the 4 reversible redox waves shifted slightly to more negative potential without dramatic change. During the measurements of all cyclic voltammograms, the overall concentration of the electrolyte NBu_4PF_6 was kept constant at 0.1 M.

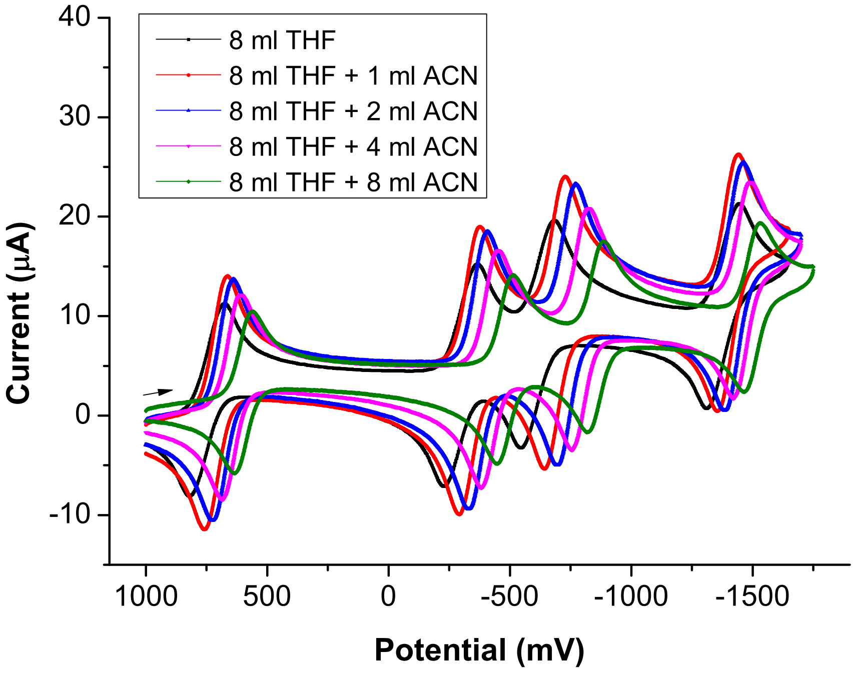

Figure 3.35.: Cyclic voltammograms for complex **4-b** in THF upon addition of ACN at a scan rate of 100 mV/s, GC electrode (diameter = 3.0 mm) in 0.1 M NBu_4PF_6 solution.

According to equation 3.14, the current raise after addition of first 1 ml ACN is likely due to higher concentration of active species*. The CV data for complex **4-b** (0.5 mM) referenced to $[Cp_2Fe]^{+/0}$ in the THF/ACN (1:1) solvent mixture is provided in Table 3.14.

---

* The THF solution might not have been homogeneous.

Table 3.14.: Results of cyclic voltammetry experiments for complex **4-b** (0.5 mM) in THF/ACN(1:1) solvent mixture (vs $[Cp_2Fe]^{+/0}$).

4-b	$E_{1/2}$ [mV]	ΔE_p [mV]	I_{pc}/I_{pa}
$W^{V}W^{IV}/W^{IV}W^{IV}$	-228	71	0.98
$W^{IV}W^{IV}/W^{IV}W^{III}$	-1307	64	1.15
$W^{IV}W^{III}/W^{III}W^{III}$	-1676	66	0.97
$dpphen^{0/-}$	-2324	61	1.09

3.7.3.3. CV Measurement in ACN upon Addition of THF

The CV of complex **4-b** in ACN (1.0 mM) shows an irreversible anodic diffusion-controlled wave, which displays a substantially huger current than the other one-electron redox waves (black line in Figure 3.36). Note that there is a baseline shift since the first scan in pure ACN was carried out with a sensitivity of 100 μA/V while the residual measurements were recorded with a sensitivity of 10 μA/V.

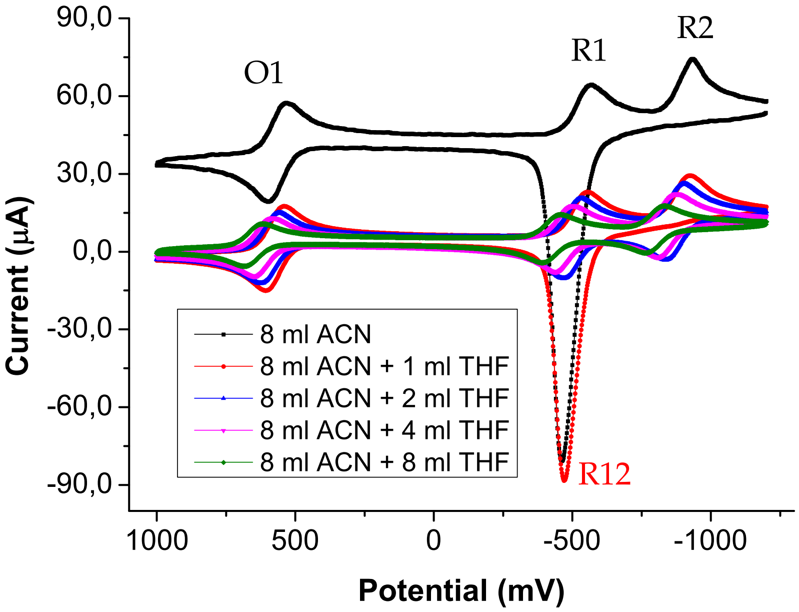

Figure 3.36.: Cyclic voltammograms for complex **4-b** in ACN upon addition of THF at a scan rate of 100 mVs^{-1}, GC electrode (diameter = 3.0 mm) in 0.1 M NBu_4PF_6 solution.

Upon addition of THF to the ACN solution of **4-b**, the anodic peak R12 decreased dramatically and disappeared (see Figure 3.36). The decrease of peak currents against the concentration of the analyte is summarized in Figure 3.37. The peak current for the reversible process decrease linearly with the concentration, neglecting small differences of the diffusion constants. The Gaussian shaped anodic current decreases sharply and the reverse peak of the second reduction appears upon addition of THF.

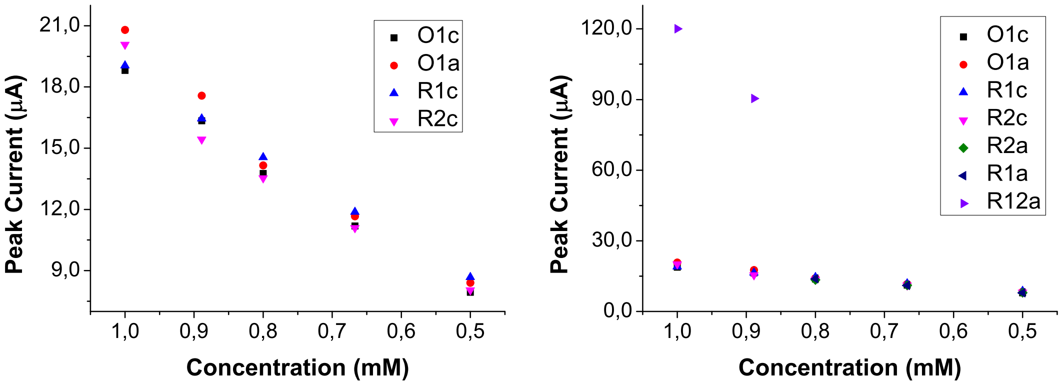

Figure 3.37.: Plots of the peak currents against concentration of complex **4-b** for O1c, O1a, R1c and R2c (left), for all peak currents (right).

The CV of complex **4-b** (0.5 mM) in ACN/THF (1:1) solvent mixture shows four reversible redox waves at -217 mV (ΔE_p = 64 mV, I_{pc}/I_{pa} = 0.94), -1292 mV (ΔE_p = 66 mV, I_{pc}/I_{pa} = 1.11), -1668 mV (ΔE_p = 66 mV, I_{pc}/I_{pa} = 0.95) for metal center based redox couples $W^{V}W^{IV}/W^{IV}W^{IV}$, $W^{IV}W^{IV}/W^{IV}W^{III}$, $W^{IV}W^{III}/W^{III}W^{III}$ respectively and -2321 mV (ΔE_p = 68 mV, I_{pc}/I_{pa} = 1.09) for the ligand based redox couple dpphen$^{0/-}$ vs $[Cp_2Fe]^{+/0}$ in the potential window of solvent mixture ACN/THF (1:1). (see Table 3.15 for CV data)

Table 3.15.: Results of cyclic voltammetry experiments for complex **4-b** (0.5 mM) in ACN/THF (1:1) solvent mixture (vs $[Cp_2Fe]^{+/0}$).

4-b	$E_{1/2}$ [mV]	ΔE_p [mV]	I_{pc}/I_{pa}
$W^{V}W^{IV}/W^{IV}W^{IV}$	-217	64	0.94
$W^{IV}W^{IV}/W^{IV}W^{III}$	-1292	66	1.11
$W^{IV}W^{III}/W^{III}W^{III}$	-1668	66	0.95
dpphen$^{0/-}$	-2321	68	1.09

The solvent dependence of the cyclic voltammetric measurements is interpreted in terms that the THF solvent is preventing the isomerization process, *cis*-$W^{III}W^{III}$ $\rightarrow$ *trans*-$W^{III}W^{III}$. Solvent effects on the rates of homogeneous chemical reactions are well known. In some extreme cases,[140] a change of solvent can alter the reaction rate by a factor up to *ca.* 10^9. According to transition-state theory, solvents can modify the Gibbs energy of activation by different solvation of the reactants and the activated complex.[141] The mechanism for the isomerization reaction has been proposed in Figure 3.38. The transition state involves a rotation around W-W bond which will rupture the W-O bond and π-bond of W-W to give a more polar activated complex. There are different stabilization effects between THF and ACN for the reactant as well as the activated complex. The THF solvent is stabilizing both the reactant *cis*-$W^{III}W^{III}$ and the product *trans*-$W^{III}W^{III}$ as they are preferentially solvated in less polar solvent THF than ACN. On the other hand, the dipolar transition state complex is preferentially solvated in the more polar solvent ACN. Therefore, it is anticipated that the activation barrier for isomerization is higher in THF than in ACN.

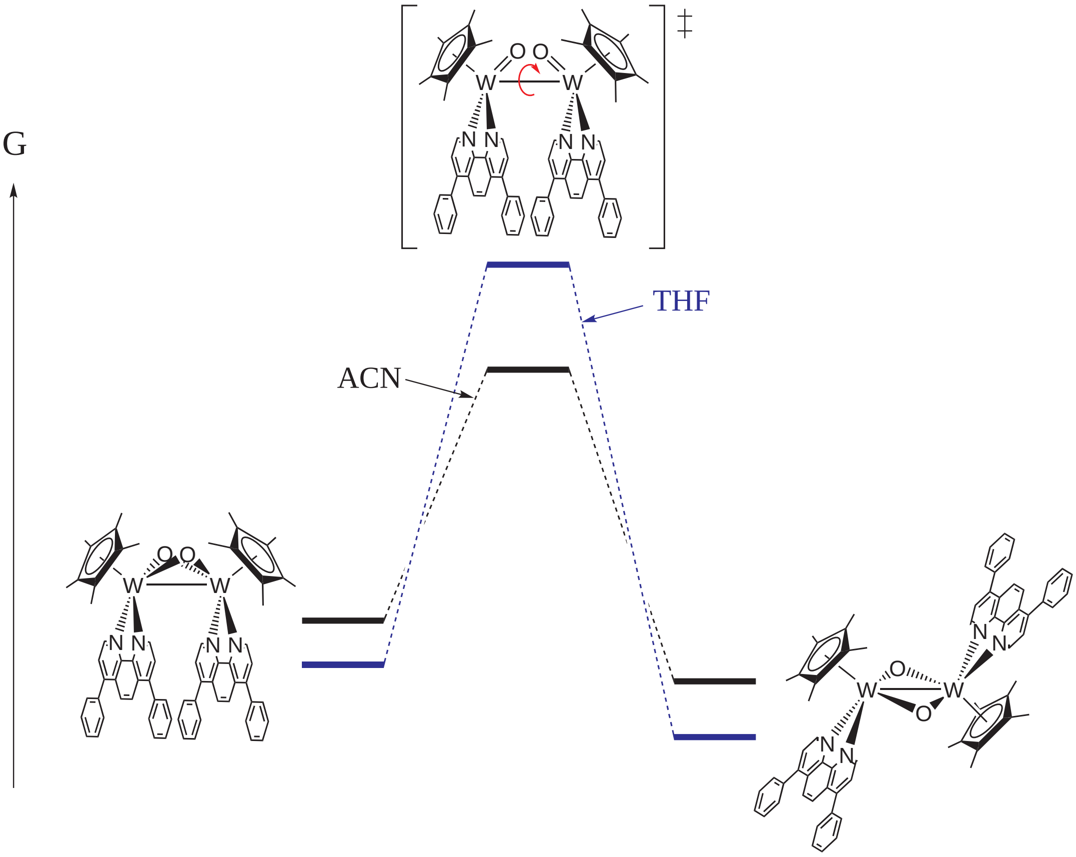

Figure 3.38.: One-dimensinal Gibbs energy diagram for cis-to-trans isomerization of dpq-$W^{III}W^{III}$ in two different solvents ACN and THF.

Reaction rates are very sensitive to the height of the activation barrier according to Arrhenius Equation (eq. 3.16):

$$k = A \cdot e^{-E_a/RT} \tag{3.16}$$

where k is the rate constant, A is the prefactor and E_a is the activation energy. For instance, a change of only 2 kcal/mol for the activation barrier can accelerate or decelerate the reaction rate by a factor of 31 at room temperature. Accordingly, the reaction rate of isomerization is assumed to be significantly slower in THF due to its higher activation barrier. This explains the retardation of isomerization upon addition of THF solvent.

3.8. Photocatalysis

Based on the spectroscopic and electrochemical properties of the half-sandwich transition metal complexes of **4-a** and **4-b**, they are anticipated to have great potential as both photosensitizers and redox catalysts. Due to their absorption in the visible and NIR range at 535 and 790 nm (LMCT and MLCT transitions), the oxidizing and reducing powers of **4-a** are enhanced from the ground state going to the excited state (see Figure 3.39).

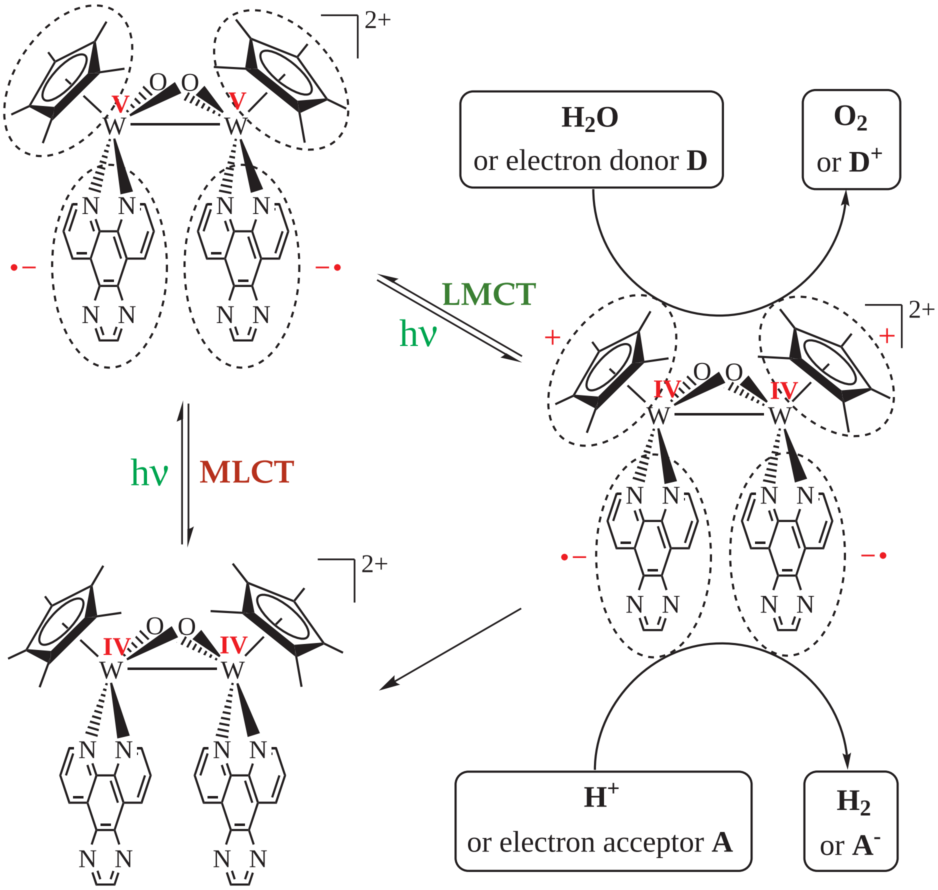

Figure 3.39.: Proposed photo-catalysis mechanism of complex **4-a** for solar water splitting.

The exited state of a photosensitizer is certainly a better electron donor and meanwhile a better electron acceptor than its ground state. According to the theoretical predictions of Rehm-Weller,[142] the excited state redox potentials of a photosensitizer can be estimated based on the redox potentials of the ground state applying corrections shown in the following equations (3.17, 3.18):

$$E^o(ES^{+/0}) = E^o(GS^{+/0}) - \Delta G_{ES}{}^o/F \tag{3.17}$$

$$E^o(ES^{0/-}) = E^o(GS^{0/-}) + \Delta G_{ES}{}^o/F \tag{3.18}$$

The exited state redox potentials of complex **4-a** was estimated from the ground state redox potentials obtained by cyclic voltammetry[28,143] and are presented in Figure 3.40.

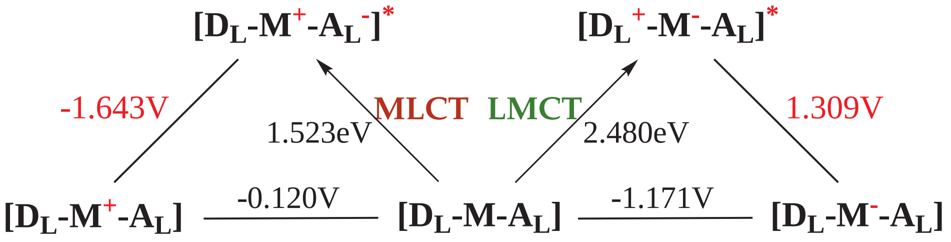

Figure 3.40.: Excited and ground state redox potentials for complex **4-a** (represented as D_L-M-A_L, in which D_L is the donor ligand, M is the metal center, A_L is the acceptor ligand) at 25 °C (vs $[Cp_2Fe]^{+/0}$ in ACN).

The excited state oxidizing potential was correlated with the optical transition energy 1.523 eV (814 nm) involving the HOMO, in which the electron transfer from metal based HOMO to acceptor ligand dpq based LUMO+4 (see Table 3.7). Meanwhile, the excited state potential for reduction was obtained by correction of the LMCT transition involve LUMO (2.480 eV, 500 nm), in which charge transfer occur from donor ligand Cp^* based HOMO-4 to metal based LUMO. The oxidation and reduction power of the excited state (- 1.643 V and 1.309 V) are both enhanced with regard to the ground state (- 1.171 V and - 0.120 V). Therefore, the excited state of the dinuclear tungsten(*IV*,*IV*) half-sandwich complex **[4-a]** thermodynamically should be capable of water oxidation and hydrogen reduction. It should be noted however that this kind of approximation for redox potential of excited state is inaccurate, often with the uncertainties of ±100 mV or more.

Photocatalysis experiments were performed using an aqueous methanol solution of complex **4-a** in a Young NMR tube under radiation with UV-light. Unfortunately no hydrogen was detected through NMR monitoring. The photocatalysis experiment was also tested in the presence of an extra electron donor N,N-Dimethylaniline, however, no hydrogen was released from the solution either. The measurements of emission spectra of complex **4-a** revealed no light emission in the the region of 600 - 1200 nm. It is likely that the emission lines are in the near infrared region, which are hard to detect. Therefore, it is unclear whether the lifetime of the excited state species is too short for water splitting. The measurements of the excited state absorption spectra will shed a light on this issue.

4. Molybdenum Analogues of Dinuclear μ-Oxo-Bridged Half-Sandwich Complexes

To improve the redox property of the potential catalyst, the molybdenum analogues of μ-oxo-bridged half-sandwich complexes $[(Cp^*Mo(dpq)(\mu{-}O))_2][PF_6]_2$ (**8-a**) and $[(Cp^*Mo(^tBu_2bpy)(\mu{-}O))_2][PF_6]_2$ (**8-d**) were synthesized and studied with spectroscopic and electrochemical methods.

4.1. Synthesis of dpq-Mo^{IV}Mo^{IV} (8-a)

The dpq substituted dinuclear Mo^{IV}Mo^{IV} complex **8-a** was synthesized from the monomeric complex **3-a** by hydrolysis in a yield of 77% (see Reaction Scheme 4.1). The meridional isomer of **3-a** was mixed with degassed water under nitrogen. After neutralization with solid $NaHCO_3$, the reddish purple product **8-a** was precipitated by addition of NH_4PF_6, extracted with DCM and recrystallized from Et_2O/CH_2Cl_2.

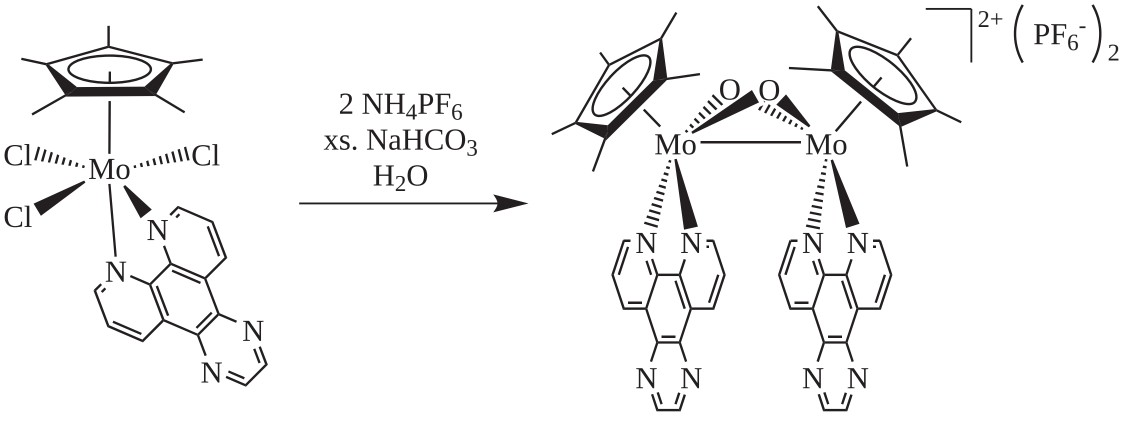

Reaction Scheme 4.1: Synthesis of μ-oxo-bridged molybdenum(*IV*,*IV*) half-sandwich complex $[(Cp^*Mo(dpq)(\mu{-}O))_2][PF_6]_2$ (**8-a**).

Evidence for the structure of **8-a** is provided by the ^{1}H-NMR, ^{13}C-NMR and two dimensional NMR (HH-COSY, HSQC, HMBC) spectroscopy, MALDI-TOF mass spectrometry, elemental analysis and X-ray single crystal structure analysis. The ^{1}H-NMR spectrum of **8-a** in CD_2Cl_2 revealed the expected 4 sets of aromatic protons of the coordinated dpq ligand at 9.12 ppm (dd, 4H), 8.95 ppm (dd, 4H), 8.86

ppm (s, 4H), 7.96 ppm (dd, 4H) and a singlet for the Cp* methyl groups at 1.51 ppm (s, 15H).

X-ray crystal structure of 8-a

Single crystals of **8-a** suitable for X-ray diffraction were obtained by slow diffusion of diethyl ether into dichloromethane solution of **8-a**. The Ortep view of the solid state structure of complex **8-a** is shown in Figure 4.1. Important bond lengths and angles are summarized in Table 4.1.

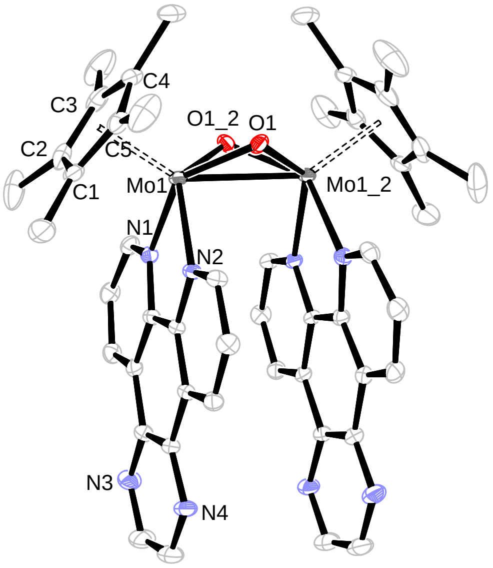

Figure 4.1.: Crystal structure of complex 8-a (Ortep-representation; 50%). For reasons of clarity, hydrogen atoms and the co-crystallized solvent molecule are not shown here.

The molybdenum centers in **8-a** display a square pyramidal structure similar to the tungsten analogue **4-a**. The distances from the molybdenum center to the four basal coordination sites (Mo1-O1 1.978 Å, Mo1-O1_2 1.964 Å, Mo1-N1 2.208 Å, Mo1-N2 2.179 Å) are ca. 0.02 Å longer than in the tungsten analogue and the averaged distance from Mo1 to the centroid of the Cp ring (2.036 Å) is 0.01 Å longer. The Mo1-Mo1_2 bond length amounts to 2.7469 Å, which is roughly 0.01 Å longer than the W-W bond in **4-a**. All bond angles show great resemblance with the tungsten analogue. The α angle formed by the two dpq ligand planes is 8.04° while the torsion angle between two dpq ligands is 9.3°.

Table 4.1.: Selected bond lengths [Å] and -angles [°] of 8-a.[a]

Mo1-O1	1.978(2)	Mo1-O1_2	1.964(2)
Mo1-N1	2.208(2)	Mo1-N2	2.179(2)
Mo1-Mo1_2	2.7469(5)	Mo1-C1	2.384(3)
Mo1-C2	2.429(3)	Mo1-C3	2.378(3)
Mo1-C4	2.323(3)	Mo1-C5	2.327(3)
Mo1-Z1[b]	2.036		
N1-Mo1-N2	74.22(8)	O1-Mo1-O1_2	77.90(11)
Mo1-O1-Mo1_2	88.36(10)	N1-Mo1-Mo1_2	97.80(6)
O1-Mo1-Mo1_2	45.61(6)	N2-Mo1-Mo1_2	90.88(6)
O1_2-Mo1-Mo1_2	46.03(6)	O1-Mo1-N1	139.68(8)
O1_2-Mo1-N1	86.19(8)	O1-Mo1-N2	88.02(8)
O1_2-Mo1-N2	129.88(9)	Mo1_2-Mo1-Z1	146.85
N1-Mo1-Z1	109.27	N2-Mo1-Z1	114.28
O1-Mo1-Z1	115.70	O1_2-Mo1-Z1	111.02
α[c]	8.04	β[d]	9.3

[a] estimated standard deviations in parentheses

[b] Z1 is the ring centroid of carbon atoms C1-C5.

[c] α is the angle formed by two dpq ligand planes.

[d] β is the torsion angle between two dpq ligands.

4.2. Spectral and Electrochemical Properties of Complex 8-a

4.2.1. Electronic Absorption Spectroscopy

The absorption spectroscopic behaviour of complex **8-a** was studied for a 0.80 mM acetonitrile solution in a 0.1 cm cuvette. The Vis-NIR spectrum of complex **8-a** is given in Figure 4.2.

In the visible and near IR range, complex **8-a** exhibits two strong absorption bands at 503 nm (ϵ = 8287 $M^{-1}\cdot cm^{-1}$) and 697 nm (ϵ = 3380 $M^{-1}\cdot cm^{-1}$) due to MLCT and LMCT transitions. As previously stated for the tungsten analogue **4-a**, the MLCT transition is due to charge transfer from the non-bonding filled *d* orbitals of the metal center to the low-lying empty π^* anti-bonding orbitals of the dpq ligand. The LMCT transition corresponds to the electron transfer from the filled bonding orbital of the Cp* ligand to an empty anti-bonding metal *d* orbital.

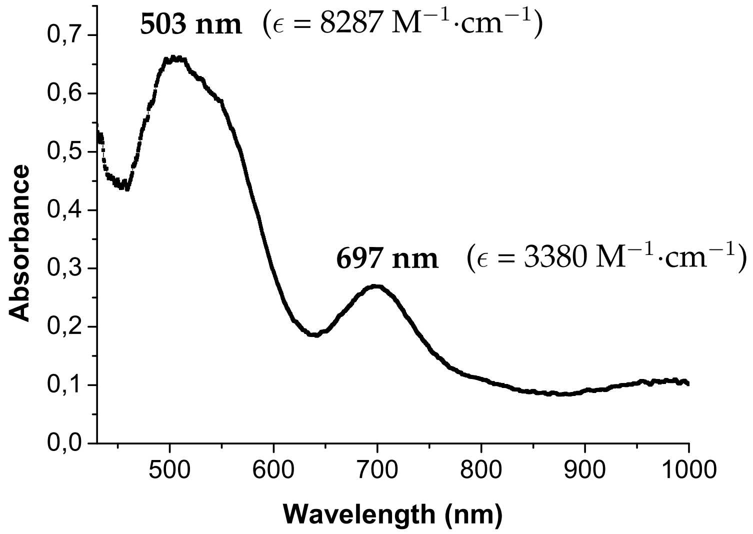

Figure 4.2.: Electronic absorbance spectrum of complex **8-a** in acetonitrile (C = 0.80 mM). Cuvette light pass length is 0.1 cm.

The orbitals of the molybdenum center are lower in energy than the tungsten analogue, thus the *d* orbitals of molybdenum are lower in energy, hence the charge transfer bands are blue-shifted from 535 nm (2.318 eV), 790 nm (1.570 eV) to 503 nm (2.465 eV), 697 nm (1.780 eV) in going from tungsten to molybdenum.

4.2.2. Cyclic Voltammetry

The dpq substituted dinuclear μ-oxo-bridged molybdenum(*IV*,*IV*) half-sandwich complex **8-a** was studied also electrochemically. The CV experiment was performed with the GC electrode for complex **8-a** as a 1 mM acetonitrile solution in the presence of 0.1 M NBu_4PF_6 supporting electrolyte. The cyclic voltammogram of complex **8-a** at a scan rate of 100 mV/s is shown in Figure 4.3.

Five reversible redox waves were observed for complex **8-a** in the potential window of acetonitrile at 166 mV (ΔE_p = 62 mV, I_{pc}/I_{pa} = 0.88), - 1201 mV (ΔE_p = 58 mV, I_{pc}/I_{pa} = 0.96) and - 1574 mV (ΔE_p = 70 mV, I_{pc}/I_{pa} = 1.08), which can be safely assigned to redox couples $Mo^{V}Mo^{IV}/Mo^{IV}Mo^{IV}$, $Mo^{IV}Mo^{IV}/Mo^{IV}Mo^{III}$ and $Mo^{IV}Mo^{III}/Mo^{III}Mo^{III}$ respectively, followed by two dpq ligand based reduction at - 2096 mV (ΔE_p = 70 mV, I_{pc}/I_{pa} = 1.10) and - 2359 mV (ΔE_p = 68 mV, I_{pc}/I_{pa} = 1.01). All CV data were referenced to $[Cp_2Fe]/[Cp_2Fe^+]$ couple and listed in Table 4.2.

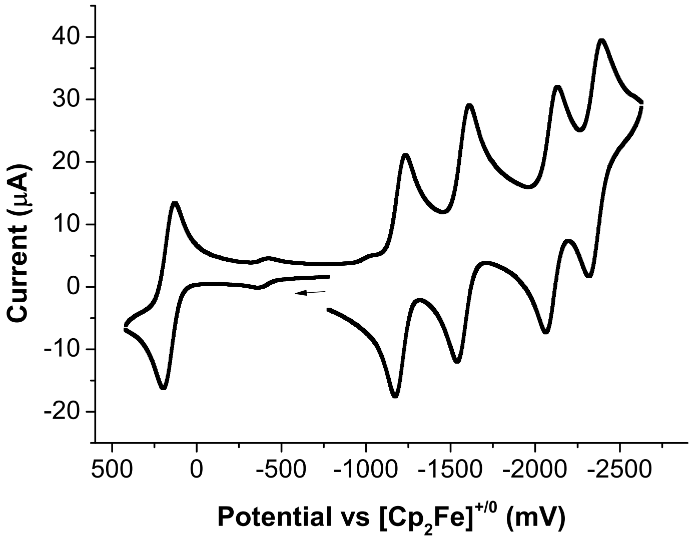

Figure 4.3.: Cyclic voltammogram for complex **8-a** (1 mM) in CH_3CN vs $[Cp_2Fe]^{+/0}$ at a scan rate of 100 mVs^{-1}, GC electrode, 0.1 M NBu_4PF_6.

Table 4.2.: Results of cyclic voltammetry experiment for complex **8-a** in CH_3CN.

8-a	$E_{1/2}$ [mV]	ΔE_p [mV]	I_{pc}/I_{pa}
$Mo^VMo^{IV}/Mo^{IV}Mo^{IV}$	+166	62	0.88
$Mo^{IV}Mo^{IV}/Mo^{IV}Mo^{III}$	-1201	58	0.96
$Mo^{IV}Mo^{III}/Mo^{III}Mo^{III}$	-1574	70	1.08
$dpq^{0/-}$	-2096	70	1.10
$dpq^{0/-}$	-2359	68	1.01

The HOMO and LUMO energy of complex **8-a** can be calculated by equations mentioned in Chapter 3 from the onset oxidation and reduction respectively. The values derived from equations 3.4, 3.5 for the HOMO and LUMO are: E_{HOMO} = -4.966 eV, E_{LUMO} = -3.599 eV vs. $[Cp_2Fe]/[Cp_2Fe^+]$ and the HOMO-LUMO energy gap E_g is 1.367 eV. The HOMO in the molybdenum complex is 0.285 eV lower than the tungsten analogue dpq-$W^{IV}W^{IV}$ (**4-a**) while the LUMO energy of dpq-$Mo^{IV}Mo^{IV}$ is 0.031 eV higher than **4-a**.

There is a tiny redox current at $E_{1/2}$ = - 395 mV due to a small amount of an unknown impurity in the analyte sample of **8-a**. Although complex **8-a** was recrystallized from Et_2O/DCM several times, unfortunately the small amount of impurity remains in the sample.

4.3. Synthesis of ^{t}Bu$_2$bpy-Mo^{IV}Mo^{IV} (8-d)

Complex $[(Cp^*Mo(^tBu_2bpy)(\mu{-}O))_2][PF_6]_2$ (**8-d**) was synthesized from mononuclear complex **3-d** by hydrolysis. After neutralization with solid $NaHCO_3$, the red product was precipitated with NH_4PF_6 (see Reaction Scheme 4.2). The analytical pure compound was obtained by extraction with DCM in a yield of 65%.

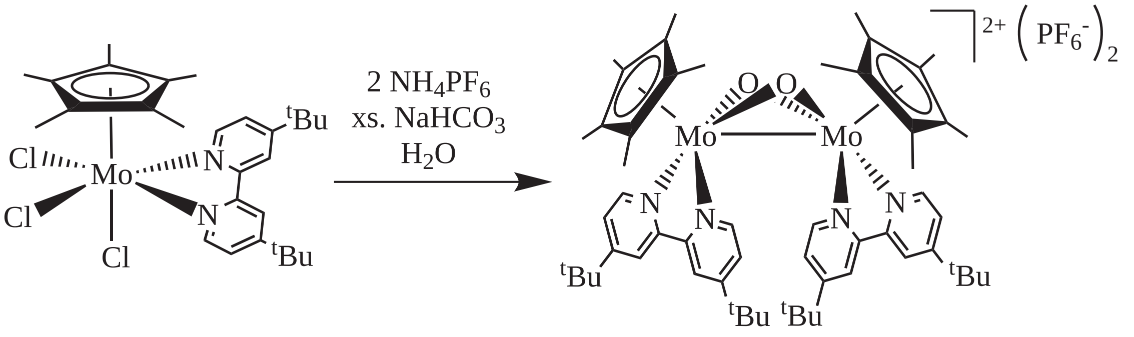

3-d

8-d (65%)

Reaction Scheme 4.2: Synthesis of the μ-oxo-bridged molybdenum(*IV*,*IV*) half-sandwich complex $[(Cp^*Mo(^tBu_2bpy)(\mu{-}O))_2][PF_6]_2$ (**8-d**).

The ^{1}H-NMR spectrum of complex **8-d** showed the expected two doublets (8.47, 7.91 ppm) and a doublet of doublet (7.42 ppm) for the aromatic protons of bpy unit, a singlet at 1.29 ppm for the ^{t}bu substituents and a singlet at 1.37 ppm for Cp* ligand. All signals showed high field shifts compared to the mononuclear complex **3-d**. ^{13}C-NMR and 2D-NMR techniques (HH-COSY, HSQC, HMBC) were employed to assign the observed signals. Further evidence for the structure of complex **8-d** was provided by mass spectrometry, elemental analysis and X-ray crystallography.

X-ray crystal structure of 8-d

Single crystals of **8-d** suitable for X-ray crystal structure analysis were grown by diffusion of diethyl ether into a dichloromethane solution. The Ortep representation of the dication **8-d** is shown in Figure 4.4 and relevant bond lengths and angles are presented in Table 4.3.

The two molybdenum(*IV*) centers both adopt a square pyramidal geometry employing five coordination sites and are bridged by two oxygen atoms. The axial

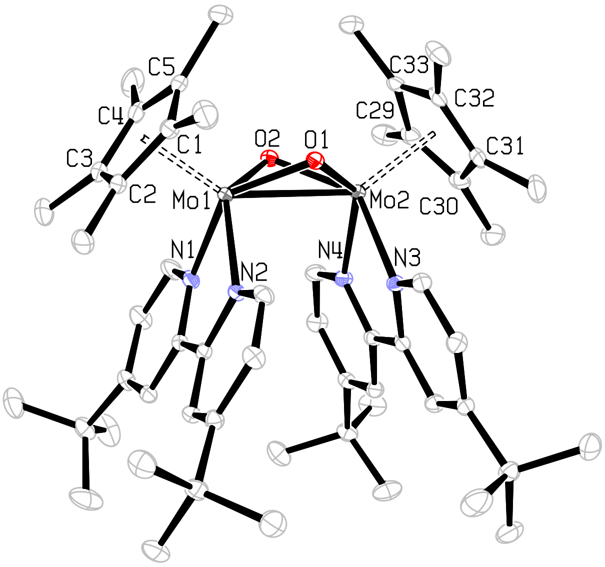

Figure 4.4.: Crystal structure of complex **8-d** (Ortep-representation; 50%). For reasons of clarity, hydrogen atoms and the co-crystallized solvent molecule are not shown.

distances of Mo1-Z1 and MO2-Z2 amount to 2.035 and 2.038 Å respectively.[*] The basal Mo-O distances in **8-d** (1.9325 ~ 1.9401 Å) are significantly shorter than the Mo-O distance in the dpq substituted complex **8-a** (1.964 ~ 1.978 Å). The distance between the two metal centers (2.7187 Å) is 0.0282 Å shorter than the Mo1-Mo2 distance in the dpq substituted complex **8-a**. The bite angles of N1-Mo-N2 (73.26 Å) and N3-Mo2-N4 (73.19 Å) are also smaller than in **8-a**. The bulky ^{t}bu substituents of the bpy ligand in complex **8-d** apparently cause a dramatic increase of the α angle formed by two bipyridine planes to 38.72°, while the torsion angle β between two ^{t}Bu$_2$bpy ligands is just 3.0°, which is comparable to the angles in the ^{t}Bu$_2$bpy substituted tungsten analogue $[(Cp^*W({}^tBu_2bpy)(\mu{-}O))_2][PF_6]_2$.[83]

---

[*] Z1 and Z2 are the centroids of the Cp rings.

Table 4.3.: Selected bond lengths [Å] and -angles [°] of 8-d.[a]

Mo1-Mo2	2.7187(2)		
Mo1-O1	1.9325(13)	Mo2-O1	1.9347(13)
Mo1-O2	1.9386(14)	Mo2-O2	1.9401(13)
Mo1-N1	2.1788(16)	Mo2-N3	2.1768(16)
Mo1-N2	2.1746(16)	Mo2-N4	2.1796(16)
Mo1-C1	2.330(2)	Mo2-C29	2.3222(19)
Mo1-C2	2.410(2)	Mo2-C30	2.3576(19)
Mo1-C3	2.430(2)	Mo2-C31	2.4166(19)
Mo1-C4	2.360(2)	Mo2-C32	2.4038(18)
Mo1-C5	2.319(2)	Mo2-C33	2.3578(19)
Mo1-Z1[b]	2.035	Mo2-Z2[c]	2.038
N1-Mo1-N2	73.26(6)	N3-Mo2-N4	73.19(6)
O1-Mo1-O2	77.93(6)	O1-Mo2-O2	77.85(6)
Mo1-O1-Mo2	89.34(5)	Mo1-O2-Mo2	89.00(6)
N1-Mo1-Mo2	96.81(4)	N3-Mo2-Mo1	95.61(4)
N2-MO1-Mo2	96.25(4)	N4-Mo2-Mo1	95.44(4)
O1-Mo1-Mo2	45.36(4)	O1-Mo2-Mo1	45.30(4)
O2-Mo1-Mo2	45.52(4)	O2-Mo2-Mo1	45.48(4)
O1-Mo1-N1	137.01(6)	O1-Mo2-N3	86.73(6)
O2-Mo1-N1	87.40(6)	O2-Mo2-N3	135.92(6)
O1-Mo1-N2	89.25(6)	O1-Mo2-N4	134.36(6)
O2-Mo1-N2	135.26(6)	O2-Mo2-N4	88.67(6)
Mo2-Mo1-Z1	146.22	Mo1-Mo2-Z2	145.51
N1-Mo1-Z1	110.39	N3-Mo2-Z2	111.34
N2-Mo1-Z1	110.23	N4-Mo2-Z2	112.33
O1-Mo1-Z1	112.50	O1-Mo2-Z2	113.12
O2-Mo1-Z1	114.31	O2-Mo2-Z2	112.71
α[d]	38.72	β[e]	3.0

[a] estimated standard deviations in parentheses

[b] Z1 is the ring centroid of carbon atoms C1-C5.

[c] Z2 is the ring centroid of carbon atoms C29-C33.

[d] α is the angle formed by two bipyridine planes.

[e] β is the torsion angle between two ^{t}Bu$_2$bpy ligands.

4.4. Spectral and Electrochemical Properties of Complex 8-d

4.4.1. Electronic Absorption Spectroscopy

The electronic absorption spectrum was recorded for a 0.71 mM **8-d** solution in acetonitrile in the visible and near IR region. (see Figure 4.5)

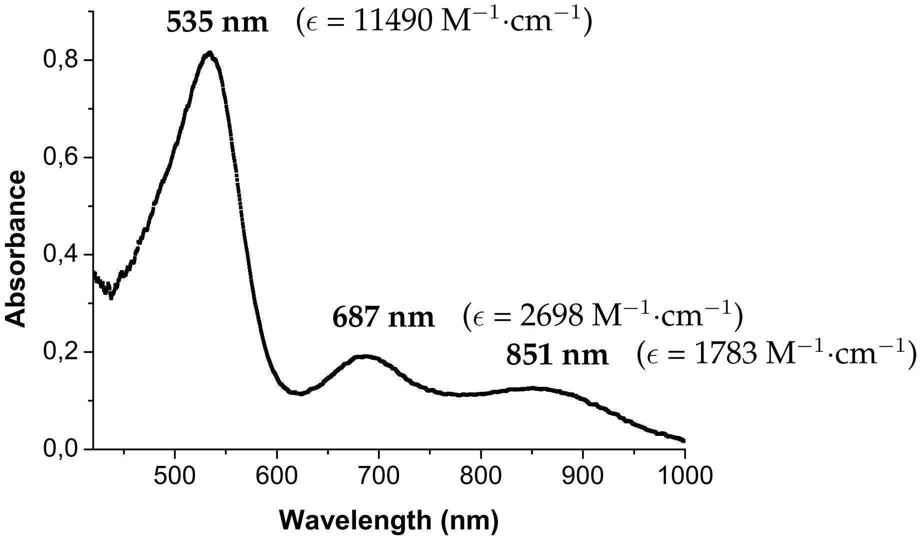

Figure 4.5.: Electronic absorbance spectrum of complex **8-d** in acetonitrile (C = 0.71 mM).

In the absorption spectrum of complex **8-d**, one charge transfer bands at 535 nm with extinction coefficient 11490 $M^{-1}\cdot cm^{-1}$ and two weaker bands at 687 nm (ϵ = 2698 $M^{-1}\cdot cm^{-1}$), 851 nm (ϵ = 1783 $M^{-1}\cdot cm^{-1}$) were observed.

4.4.2. Cyclic Voltammetry

Cyclic voltammetry was applied for complex **8-d** to investigate the electron transfer mechanisms in acetonitrile and THF. The cyclic voltammograms of the $^{t}Bu_2bpy$ substituted molybdenum(*IV,IV*) complex **8-d** in ACN at a scan rate of 100 mVs^{-1} (Figure 4.6) are comparable with the dpphen substituted tungsten(*IV,IV*) half-sandwich complex $[(Cp^*W(dpphen)(\mu{-}O))_2][PF_6]_2$ (**4-b**).

When the CV was acquired before the second reduction wave was reached, two reversible redox waves were observed at + 3 and - 1566 mV for the redox couples $Mo^{V}Mo^{IV}/Mo^{IV}Mo^{IV}$ (ΔE_p = 63 mV, I_{pc}/I_{pa} = 0.98) and $Mo^{IV}Mo^{IV}/Mo^{IV}Mo^{III}$ (ΔE_p = 59 mV, I_{pc}/I_{pa} = 1.15) vs $[Cp_2Fe]^{+/0}$, respectively (see black line in Figure 4.6). The second reduction process is consistent with a EC mechanism, which is a rapid irreversible chemical reaction following the electron transfer. The corresponding anodic peak of the second reduction process is absent because all the reduced form produced near the electrode is instantly removed by fast chemical reaction. Based on the previous results for the dpphen substituted tungsten system, a fast *cis-trans* isomerization process is anticipated. The huge anodic current observed at - 1566 mV vs $[Cp_2Fe]^{+/0}$, which is 5.7 times as the one-electron ca-

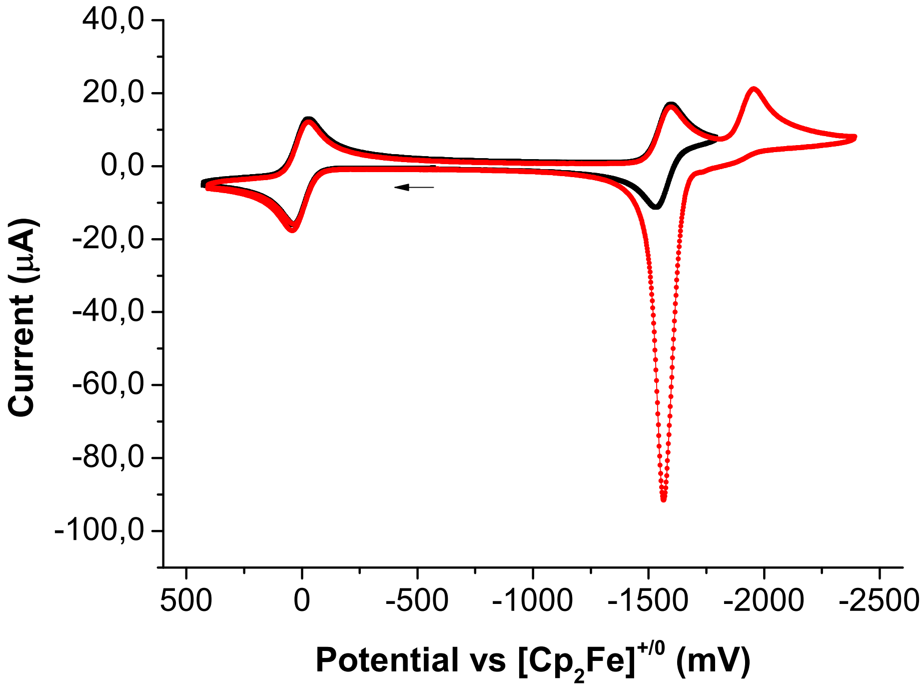

Figure 4.6.: Cyclic voltammograms for complex **8-d** (0.88 mM) in CH_3CN vs $[Cp_2Fe]^{+/0}$ at a scan rate of 100 mVs^{-1}, GC electrode, 0.1 M NBu_4PF_6.

thodic current, is caused by simultaneous two-electron transfer accompanied by *trans-cis* isomerization, which can be described as ECE mechanism (see red line in Figure 4.6).

The HOMO and LUMO energy of complex **8-d** were calculated as - 4.803 eV and - 3.234 eV vs $[Cp_2Fe]^{+/0}$ respectively, which gave a HOMO-LUMO energy gap (E_g) of 1.569 eV. The HOMO-LUMO energy gap for the ${}^{t}Bu_2$bpy substituted dimolybednum(*IV*/*IV*) complex **8-d** is thus 0.202 eV bigger than the dpq substituted analogue **8-a**.

Influence of scan rate

The reversible two redox processes of complex **8-d** in acetonitrile observed in the range of + 440 to - 1840 mV were studied at various scan rates from 20 to 2000 mV/s (see Figure 4.7).

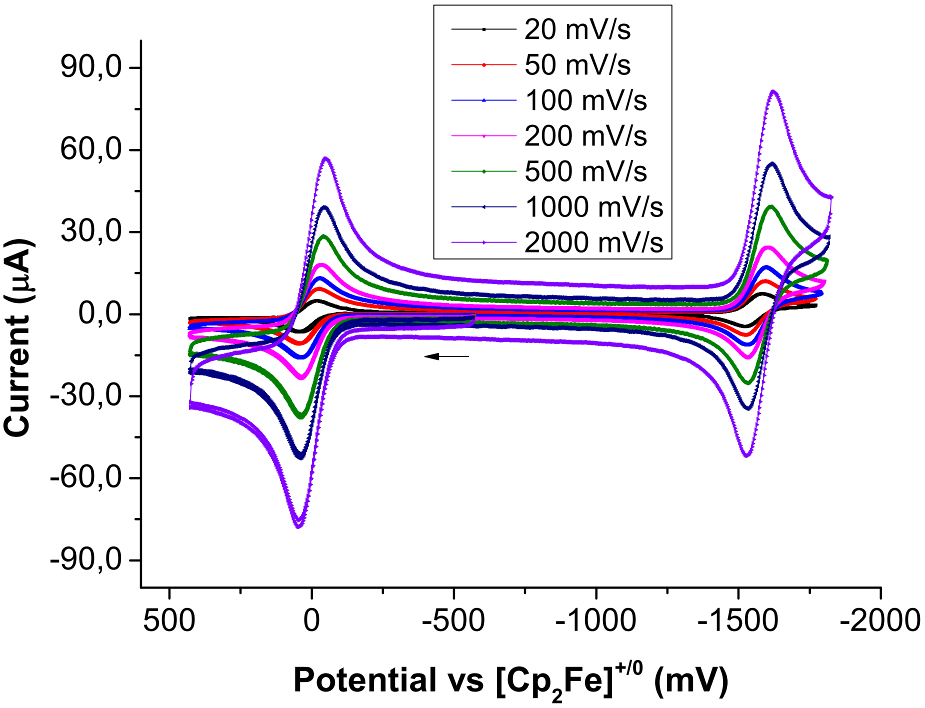

Figure 4.7.: Cyclic voltammograms for complex **8-d** (0.88 mM) in CH_3CN vs $[Cp_2Fe]^{+/0}$ at scan rates from 20 to 2000 mVs^{-1}, GC electrode, 0.1 M NBu_4PF_6.

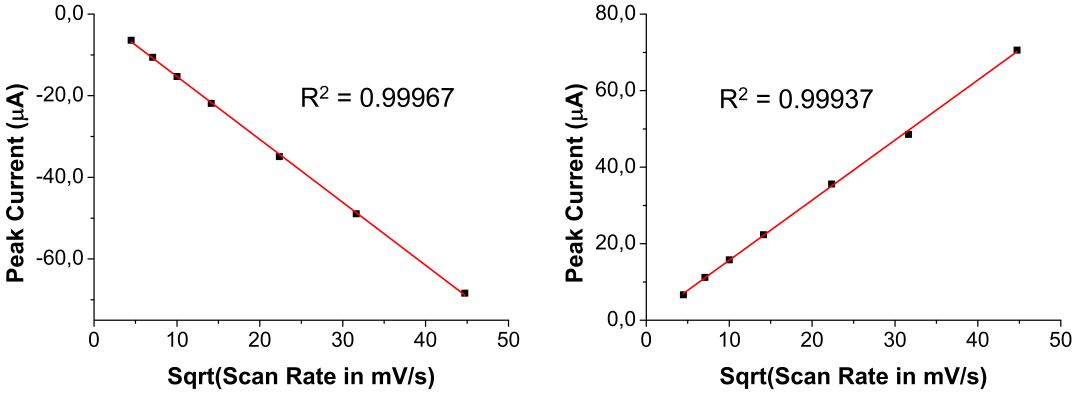

Figure 4.8.: Plots of the peak current for the first oxidation (left) and the first reduction (right) of complex **8-d** in CH_3CN, as a function of the square root of scan rate.

Figure 4.8 shows that the anodic current of one-electron oxidation and the cathodic current of one-electron reduction are increasing linearly with the square root of the scan rate, which means these peaks are diffusion controlled processes.

Scan rate variations on the full potential window of acetonitrile were also investigated from 0.02 to 10 V/s for complex **8-d**. Figure 4.9 shows the currents for scan rates in the range of 20 to 100 mV/s, in which the huge anodic peak is still diffusion controlled owing to the current increase as a function of the square root of the scan rate.

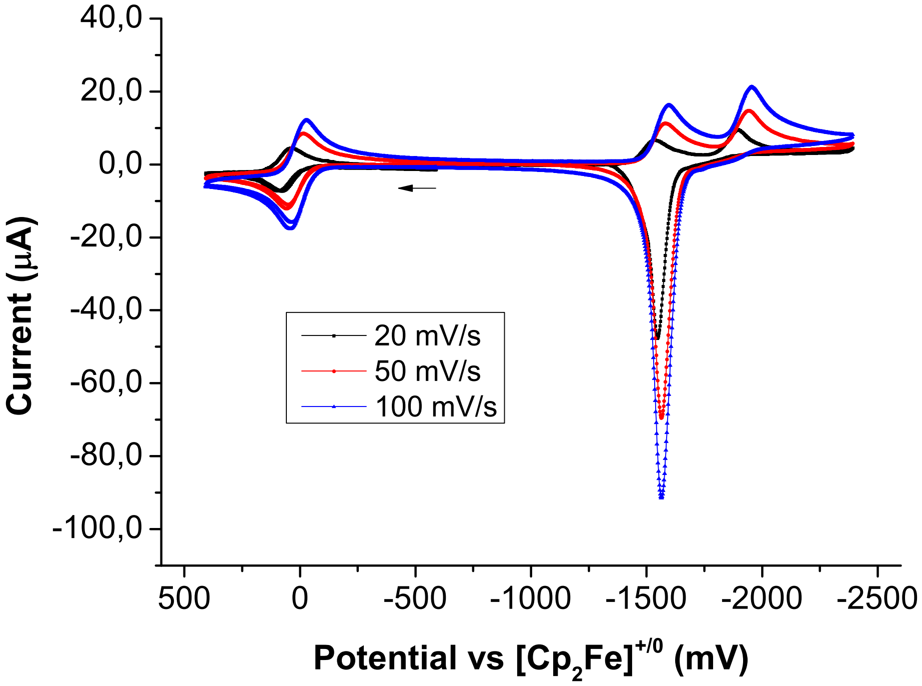

Figure 4.9.: Cyclic voltammograms for complex **8-d** (0.88 mM) in CH_3CN at scan rates from 20 to 100 mVs^{-1}, GC electrode, 0.1 M NBu_4PF_6.

Cyclic voltammograms of complex **8-d** at scan rates from 0.3 to 10 V/s are presented in Figure 4.10. When the scan rate reached 1 V/s, the corresponding anodic peak of the second reduction started to show up. As the scan rate is further increasing, the Gaussian shaped current was decreasing, while the anodic current of second reduction was increasing. Three reversible redox waves were observed at a scan rate of 8 V/s at + 3 mV (ΔE_p = 125 mV, I_{pc}/I_{pa} = 0.91), - 1573 mV (ΔE_p = 141 mV, I_{pc}/I_{pa} = 1.02) and - 1942 mV (ΔE_p = 128 mV, I_{pc}/I_{pa} = 1.04) vs $[Cp_2Fe]^{+/0}$ which can be assigned tp redox couples $Mo^{V}Mo^{IV}/Mo^{IV}Mo^{IV}$, $Mo^{IV}Mo^{IV}/Mo^{IV}Mo^{III}$ and $Mo^{IV}Mo^{III}/Mo^{III}Mo^{III}$ respectively. The electrochemical data for complex **8-d** at a scan rate of 8 V/s are listed in Table 4.4.

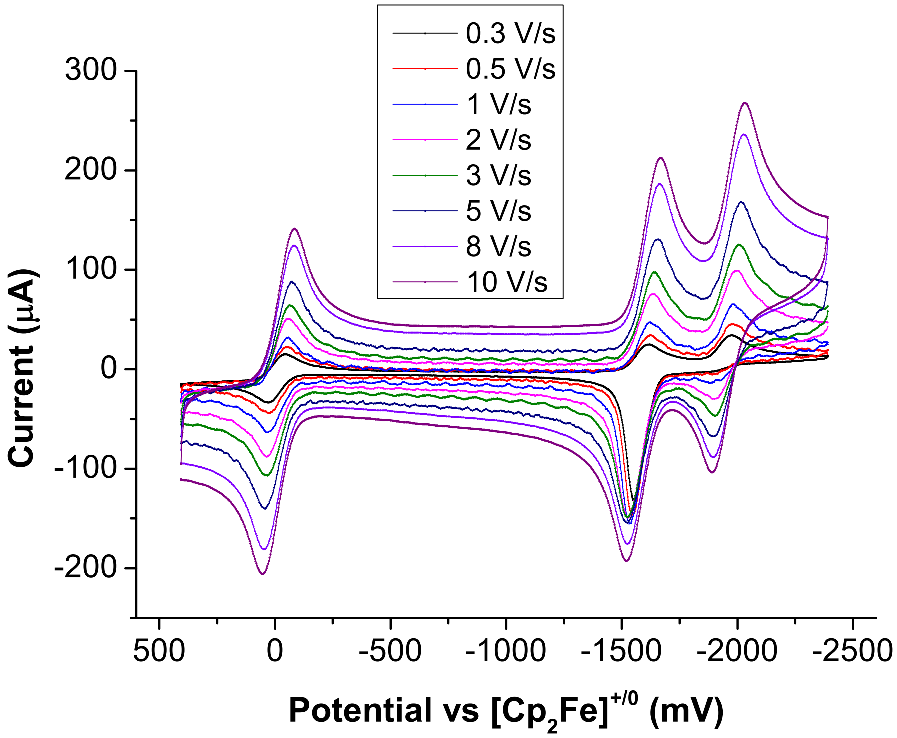

Figure 4.10.: Cyclic voltammograms for complex **8-d** (0.88 mM) in CH_3CN at scan rates from 0.3 to 10 Vs^{-1}, GC electrode, 0.1 M NBu_4PF_6.

Table 4.4.: Results of cyclic voltammetry experiment for complex **8-d** in ACN at a scan rate of 8 V/s.

8-d	$E_{1/2}$ [mV]	ΔE_p [mV]	I_{pc}/I_{pa}
$Mo^{V}Mo^{IV}/Mo^{IV}Mo^{IV}$	+3	125	0.91
$Mo^{IV}Mo^{IV}/Mo^{IV}Mo^{III}$	-1573	141	1.02
$Mo^{IV}Mo^{III}/Mo^{III}Mo^{III}$	-1942	128	1.04

As can be seen from the CV data above, the capacitive current and IR drop becomes significant at high scan rates. With regard to the chemical reaction (isomerization) rate involved in the electrochemical measurements for complex **8-d** and the dpphen substituted tungsten analogue **4-b**, the *cis-trans* isomerization for **8-d** is slower than in **4-b** as the anodic current for the cis-isomer is present for complex **8-d** but absent for complex **4-b** at a scan rate of 2 V/s .

Solvent dependence of reversibility

The solvent dependence of the electrochemical behavior for complex **8-d** was probed by addition of a 0.1 M NBu_4PF_6 THF solution to the ACN solution of the analyte **8-d** at a scan rate of 100 mV/s (see Figure 4.11). The overall concentration of the NBu_4PF_6 electrolyte was kept at 0.1 M for all CV measurements.

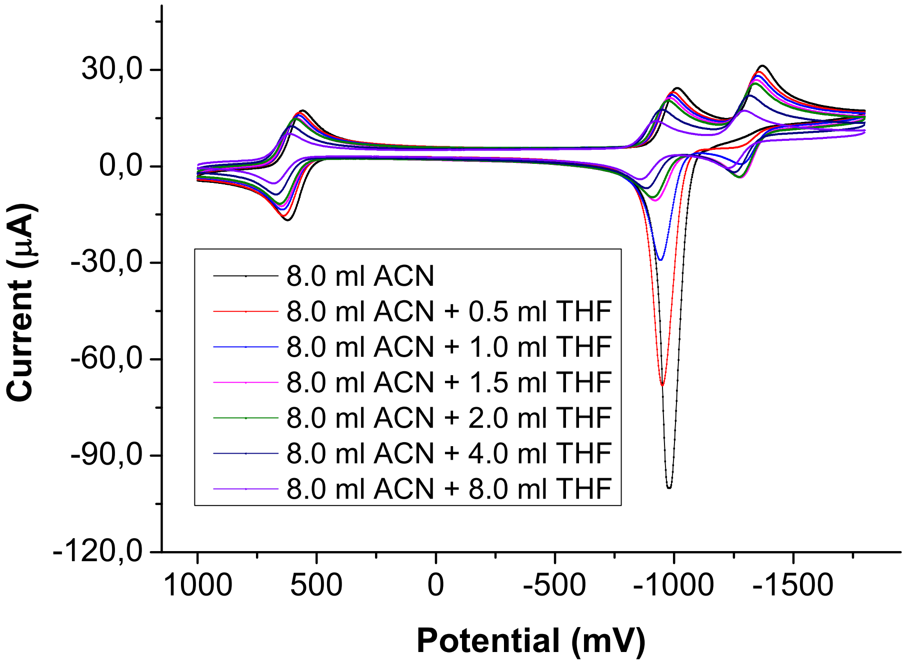

Figure 4.11.: Cyclic voltammograms for complex **8-d** in ACN upon addition of THF at a scan rate of 100 mVs^{-1}, GC electrode, 0.1 M NBu_4PF_6.

Upon addition of THF, the Gaussian shaped anodic current decreased dramatically; the oxidation wave for the second reduction made appearance. Finally three reversible redox waves were observed for a 1:1 solvent mixture of ACN/THF at a scan rate of 100 mVs^{-1}(Figure 4.12).

The reversible redox processes observed at -7 mV (ΔE_p = 68 mV, I_{pc}/I_{pa} = 0.96), -1545 mV (ΔE_p = 64 mV, I_{pc}/I_{pa} = 1.10) and -1915 mV (ΔE_p = 64 mV, I_{pc}/I_{pa} = 0.95) vs $[Cp_2Fe]^{+/0}$ can be safely assigned to redox couples $Mo^{V}Mo^{IV}/Mo^{IV}Mo^{IV}$, $Mo^{IV}Mo^{IV}/Mo^{IV}Mo^{III}$ and $Mo^{IV}Mo^{III}/Mo^{III}Mo^{III}$ respectively. The electrochemical data of complex **8-d** in ACN/THF(1:1) are listed in Table 4.5.

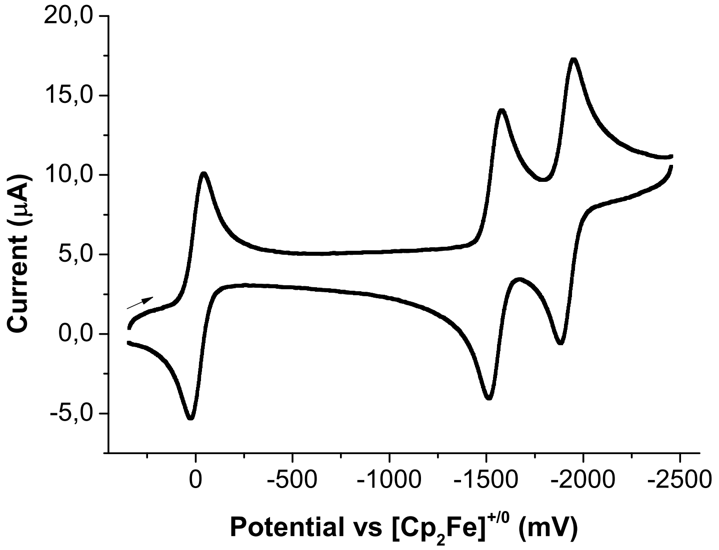

Figure 4.12.: Cyclic voltammograms for complex **8-d** (0.5 mM) in ACN/THF(1:1) vs $[Cp_2Fe]^{+/0}$ at a scan rate of 100 mVs^{-1}, GC electrode, 0.1 M NBu_4PF_6.

Table 4.5.: Results of the cyclic voltammetry experiment for complex **8-d** in ACN/THF(1:1).

8-d	$E_{1/2}$ [mV]	ΔE_p [mV]	I_{pc}/I_{pa}
$Mo^{V}Mo^{IV}/Mo^{IV}Mo^{IV}$	-7	68	0.96
$Mo^{IV}Mo^{IV}/Mo^{IV}Mo^{III}$	-1545	64	1.10
$Mo^{IV}Mo^{III}/Mo^{III}Mo^{III}$	-1915	64	0.95

The $^{t}Bu_2$bpy free ligand was also investigated electrochemically by cyclic voltammetry method. However in the cathodic potential window of acetonitrile, it is not redox active.

The electrochemical properties of the dpq and $^{t}Bu_2$bpy substituted dimolybdenum half-sandwich complexes were compared with the dpq, dpphen and R_2bpy (R = NMe_2, Me, H and Cl)[83] substituted ditungsten analogues in Table 4.6. As Cremer demonstrated, the linear correlation of the Hammett parameters for the substituents R and the measured potentials showed that the more electron donating R substituents led to more negative potentials. The dpq substituted ditungsten(*IV*,*IV*) complex has the comparable HOMO and LUMO energy as complex Cl_2bpy-$W^{IV}W^{IV}$. The oxidation potential for dpq substituted dinuclear complex increases in going from tungsten to molybdenum by roughly 0.29 V while the reduction potentials remains similar.

Table 4.6.: Summary of electrochemical data for the μ-oxo-bridged ditungsten and dimolybdenum complexes (vs $[Cp_2Fe]^{+/0}$).

Complex	$M^VM^{IV}/M^{IV}M^{IV}$ $E_{1/2}$ [mV] (ΔE_p [mV], I_{pc}/I_{pa})	$M^{IV}M^{IV}/M^{IV}M^{III}$ $E_{1/2}$ [mV] (ΔE_p [mV], I_{pc}/I_{pa})	$M^{IV}M^{III}/M^{III}M^{III}$ $E_{1/2}$ [mV] (ΔE_p [mV], I_{pc}/I_{pa})	$(\text{ligand})^{0/-}$ $E_{1/2}$ [mV] (ΔE_p [mV], I_{pc}/I_{pa})	$(\text{ligand})^{0/-}$ $E_{1/2}$ [mV] (ΔE_p [mV], I_{pc}/I_{pa})
$(NMe_2)_2$bpy-WW[a] in ACN	-734 (58, 1.12)	-1999 (70, 1.84)	-2252 (78, 1.00)		
Me_2bpy-WW[a] in ACN	-243 (135, 0.68)	-1387 (142, 1.37)	-1775 (143, 3.71)		
bpy-WW[a] in ACN	-251 (88, 1.00)	-1397 (80, 1.08)	-1765 (90, 1.18)		
Cl_2bpy-WW[a] in ACN	-116 (144, 0.96)	-1232 (72, 1.22)	-1414 (68, 0.97)		
dpq-WW in THF	-129 (68, 1.00)	-1164 (70, 1.16)	-1560 (70, 0.96)	-2116 (70, 1.22)	-2310 (78, 0.72)
dpphen-WW in ACN (100 mV/s)	-208 (63, 0.94)	E_{pc} = -1335.5 mV E_{pa2} = -1236.5 mV	E_{pc} = -1705.5 mV	– –	– –
dpphen-WW in ACN (15 V/s)	-213 (150, 0.92)	-1306 (185, 0.93)	-1696 (172, 1.10)	-2304 (166, 1.22)	-2654 (189, 1.26)
dpphen-WW in ACN/THF (1:1)	-217 (64, 0.94)	-1292 (66, 1.11)	-1668 (66, 0.95)	-2321 (68, 1.09)	– –
dpq-MoMo in ACN	+166 (62, 0.88)	-1201 (58, 0.96)	-1574 (70, 1.08)	-2096 (70, 1.10)	-2359 (68, 1.01)
$^tBu_2$bpy-MoMo in ACN (100 mV/s)	+3 (63, 0.95)	E_{pc} = -1596 mV E_{pa2} = -1566 mV	E_{pc} = -1954 mV	– –	– –
$^tBu_2$bpy-MoMo in ACN (8 V/s)	+3 (125, 0.91)	-1573 (141, 1.02)	-1941.5 (128, 1.04)	– –	– –
$^tBu_2$bpy-MoMo in ACN/THF(1:1)	-7 (68, 0.96)	-1545 (64, 1.10)	-1915 (64, 0.96)	– –	– –

[a] data cited from Cremer's paper.[83]

5. Summary

The development of synthetic molecular water splitting catalysts is an urgent task facing the world's energy supply. Among many approaches, the dinuclear tungsten systems described herein are also potential photocatalysts towards solar water splitting. The chemistry of half-sandwich complexes of tungsten in medium oxidation states was previously established by Cremer.[82–84] In this research work, several efforts were made to synthesize and characterize dinuclear group 6 transition metal complexes with improved photochemical and electrochemical properties.

First of all, several novel mononuclear and dinuclear group 6 organometallic complexes were synthesized and fully characterized. This includes mononuclear dipyrido[3,2-*f*:2′,3′-*h*]quinoxoline (dpq) substituted half-sandwich tungsten(*IV*) and molybdenum(*IV*) complex (**2-a** and **3-a**), 4,7-diphenyl-1,10-phenanthroline (dpphen) substituted tungsten analogue (**2-b**), the 4,4′-di-tert-butyl-2,2′-dipyridyl (^{t}Bu$_2$bpy) substituted molybdenum analogue (**3-d**) as well as further dinuclear oxo-bridged tungsten and molybdenum compounds $[(Cp^*W(dpq)(\mu{-}O))_2][PF_6]_2$ (**4-a**), $[(Cp^*Mo(dpq)(\mu{-}O))_2][PF_6]_2$ (**8-a**), $[(Cp^*W(dpphen)(\mu{-}O))_2][PF_6]_2$ (**4-b**) and $[(Cp^*Mo(^tBu_2bpy)(\mu{-}O))_2][PF_6]_2$ (**8-d**).

Strong absorption arising from MLCT and LMCT transition were observed in the UV/vis and NIR region for all ditungsten and dimolybdenum compound described here. The extinction coefficients are in the order of 10^4 $M^{-1}\cdot cm^{-1}$. Among them, complex **4-b** absorbs the strongest and has a molar extinction coefficient of 17469 $M^{-1}\cdot cm^{-1}$ at wavelength of 590 nm. The molybdenum complexes absorb weaker and at lower wavelengths compared to the tungsten complexes. TD-DFT calculations were carried out to interpret the observed absorption bands for the μ-oxo-bridged ditungsten(*IV*,*IV*) complex **4-a**. According to the TD-DFT calculations, the absorption band at 535 nm has contributions from both LMCT and MLCT transitions while the absorption at 790 nm results purely from MLCT transition. The interligand transition of $Cp^* \rightarrow$ dpq is mainly located in the near UV region. Here, LMCT attributes to charge transfer from the Cp^* π donor ligand to the W^{IV} metal centers, while MLCT bands correspond to the electron transfer from the metal based orbital to the empty low lying π^* orbital of the dpq ligand. Further evidence for the bands assignments was provided by resonant Raman spectroscopy. When the incident laser frequency was chosen to be coincident with the charge transfer band at 535 nm, the intensities of some of the Raman active vibrational modes are enhanced. Based on the results of DFT calculations (PBE functional), the enhanced vibrations incorporate vibrations of the dpq ligand and the Cp* ligand. This result confirms that the absorption at 535 nm of complex **4-a** involves both Cp* and dpq ligands, i.e. the contribution of both LMCT and MLCT transitions.

The potential-controlled electrochemical method CV was used to study the electron transfer properties of these dinuclear tungsten and molybdenum complexes. The dpq substituted ditungsten and dimolybdenum complexes exhibit both three reversible metal based redox processes as well as two reversible ligand based reductions. The oxidation potential for the dpq substituted dinuclear complexes increases in going from tungsten to molybdenum by roughly 0.29 V while the reduction potentials remain similar. With regard to complex dpphen-$W^{IV}W^{IV}$ (**4-b**) and complex $^{t}Bu_2$bpy-$Mo^{IV}Mo^{IV}$ (**8-d**), irreversible redox behaviour were observed at lower scan rate (from 10 mV/s up to 6 V/s) and the Gaussian shaped anodic current attribute to simultaneous two-electron transfer step coupled with *trans-cis* isomerization. In oxidation state of $M^{III}M^{III}$ (M = W, Mo), complex dpphen-$W^{III}W^{III}$ and complex $^{t}Bu_2$bpy-$Mo^{III}Mo^{III}$ favor *trans* orientation of the Cp* ligands in acetonitrile (ACN) due to steric repulsion between the bulky phenyl and ^{t}Bu substituents. At very high scan rate (15 V/s for dpphen-WW and 8 V/s for $^{t}Bu_2$bpy-MoMo), the electrode reaction becomes much faster than the chemical reaction therefore reversible redox waves were observed. In addition, solvent dependence was also noticed for the electrochemical reversibility of complexes **4-b** and **8-d**. THF solvent is preventing the *cis-trans* isomerization process of neutral complex $M^{III}M^{III}$, in other words, the *cis-trans* isomerization is much faster in ACN than in THF. According to transition-state theory, solvents can modify the Gibbs energy of activation by different solvation of the reactants and the activated complex. The transition state of isomerization involves a rotation around W-W bond which will rupture the W-O bond and π-bond of W-W to give a more polar activated complex. This polar transition state compound is preferentially solvated in the more polar solvent ACN. Therefore, it is anticipated that the activation barrier for isomerization is lower in ACN than in THF. Accordingly, the reaction rate of isomerization is assumed to be significantly slower in THF due to its higher activation barrier. This explains the retardation of isomerization upon addition of THF solvent. The dpphen ligand based redox waves were also observed for the dpphen substituted ditungsten complex in ACN, while the pure

^{t}Bu$_2$bpy ligand based redox waves are not present in the potential window of the utilized electrochemical solvent ACN.

The dinuclear tungsten and molybdenum (IV/IV) μ-oxo-bridged complexes offer several advantages as homogeneous photocatalysts:
1. Strong light absorption with high molecular absorption coefficients (ϵ up to 1.75×10^4 $M^{-1} \cdot cm^{-1}$) were observed due to the presence of MLCT and LMCT transition in the visible and NIR region.
2. They are highly redox-active. These complexes can undergo 3 to 5 reversible one-electron transfer making the application of the complexes as a multi-electron catalyst possible.
3. These complexes can combine the role of an photosensitizer and a redox catalyst. The redox power is enhanced from the ground state to the excited state under radiation, which is thermodynamically capable of water oxidation and hydrogen reduction.

The photocatalysis experiments showed no evidence for hydrogen production or oxygen evolution under radiation yet. The measurements of emission spectra of complex **4-a** revealed no light emission in the region of 600 - 1200 nm. It is likely that the emission lines are in the near infrared region, which are hard to detect. Therefore, it is unclear whether the lifetime of the excited state species is too short for water splitting. The measurements of the excited state absorption spectra will shed a light on this issue.

Zusammenfassung

Die Entwicklung von Katalysatoren zur molekularen Wasserspaltung ist eine wichtige Aufgabe im Hinblick auf die weltweite Energieversorgung. Neben vielen anderen Ansätzen ist das hier beschriebene dinukleare Wolfram-System ein potentieller Katalysator zur photochemischen Wasserspaltung. Die Chemie von Wolfram-Halbsandwich-Komplexen in mittleren Oxidationsstufen wurde bereits von Cremer beschrieben. Im Zuge dieser Arbeit wurden zahlreiche Versuche unternommen, dinukleare Übergangsmetallkomplexe der Gruppe 6 mit verbesserten photo- und elektrochemischen Eigenschaften zu synthetisieren und charakterisieren.

Zunächst wurden zahlreiche neue mono- und dinukleare Organometallkomplexe der Gruppe 6 synthetisiert und vollständig charakterisiert, darunter dipyrido[3,2-*f*:2′,3′-*h*]quinoxolin (dpq)-substituierte Halbsandwich Wolfram(IV)- und Molybdän(*IV*)-Komplexe (**2-a** und **3-a**), das 4,7-diphenyl-1,10-phenanthrolin (dpphen)-substituierte Wolfram-Analogon (**2-b**), das 4,4′-di-tert-butyl-2,2′-dipyridyl (^{t}Bu$_2$-bpy)-substituierte Molybdän-Analogon (**3-d**) sowie weitere dinukleare, sauerstoffverbrückte Wolfram- und Molybdän-Verbindungen $[(Cp^*W(dpq)(\mu{-}O))_2][PF_6]_2$ (**4-a**), $[(Cp^*Mo(dpq)(\mu{-}O))_2][PF_6]_2$ (**8-a**), $[(Cp^*W(dpphen)(\mu{-}O))_2][PF_6]_2$ (**4-b**) und $[(Cp^*Mo(^tBu_2bpy)(\mu{-}O))_2][PF_6]_2$ (**8-d**).

Starke Absorption infolge von MLCT- und LMCT-Übergängen wurden im UV/vis- und NIR-Bereich für alle hier beschriebenen Di-Wolfram- und Di-Molybdän-Verbindungen beobachtet. Die Extinktionskoeffizienten liegen in der Größenordnung von 10^4 $M^{-1}{\cdot}cm^{-1}$. Die stärkste Absorption zeigt Komplex **4-b**, der einen molaren Extinktionskoeffizienten von 17469 $M^{-1}{\cdot}cm^{-1}$ bei einer Wellenlänge von 590 nm aufweist. Die Molybdän-Komplexe zeigen im Vergleich zu den Wolfram-Komplexen schwächere Absorptionen bei kleineren Wellenlängen. Zur Interpretation der beobachteten Absorptionsbanden des μ-Oxo-verbrückten Di-Wolfram-(*IV*,*IV*)-Komplexes **4-a** wurden TD-DFT-Rechnungen herangezogen. Denen zufolge tragen sowohl die LMCT- als auch die MLCT-Übergänge zu der Absorptionsbande bei 535 nm bei, während die Absorption bei 790 nm lediglich aus MLCT-Übergängen resultiert. Der Ligand-Ligand-Übergang von $Cp^* \rightarrow$ dpq ist hauptsächlich in der nahen UV-Region zu beobachten. Hierbei ist der LMCT-Übergang dem Ladungstransfer vom Cp^*-π-Donor-Liganden zum Wolfram(IV)-Metallzentrum zuzuordnen, während die MLCT-Banden dem Elektronenübergang von den Orbitalen des Metalls zu den leeren, energetisch niedriger liegenden π^*-Orbitalen des dpq-Liganden entsprechen. Weitere Bestätigung für die Bandenzuordnung liefert die Resonanz-Raman-Spektroskopie. Wenn die Einstrahlfrequenz entsprechend der Frequenz der Charge-Transfer-Bande bei 535 nm gewählt wurde, wurden die Intensitäten einiger Raman-aktiver Schwingungsmoden verstärkt. Ausgehend von den Ergebnissen der DFT-Rechnungen (PBE-Funktional) beinhalten die verstärkten Schwingungen Beiträge von Schwingungen des dpq- und des Cp*-Liganden. Dieses Ergebnis bestätigt, dass an der Absorption des Komplexes **4-a** bei 535 nm sowohl der Cp*- als auch der dpq-Ligand beteiligt sind, folglich also sowohl LMCT- als auch MLCT-Übergänge.

Die potentialkontrollierte elektrochemische Methode CV wurde zur Untersuchung der Elektronenübertragungseigenschaften der dinuklearen Wolfram- und Molybdän-Komplexe verwendet. Die dpq-substituierten Di-Molybdän und Wolfram-Komplexe zeigen jeweils drei reversible, metallbasierte Redox-Vorgänge, ebenso wie zwei ligandenbasierte Reduktionen. Das Oxidationspotential für die dpq-substituierten dinuklearen Komplexe nimmt von Wolfram zu Molybdän um etwa 0.29 V zu, während die Reduktionspotentiale gleichbleiben. Im Falle der Komplexe dpphen-W^{IV}W^{IV} (**4-b**) und ^{t}Bu$_2$bpy-Mo^{IV}Mo^{IV} (**8-d**) wurde ein irreversibles Redoxverhalten bei niedriger Scanrate (von 10 mV/s bis 6 V/s) beobachtet. Der Gauss-förmige Anodenstrom lässt auf einen simultanen Zwei-Elektronentransfer gekoppelt mit einer *trans-cis*-Isomerisierung schließen. In den Oxidationsstufen $M^{III}M^{III}$ (M = Mo, W) bevorzugen die Komplexe dpphen-W^{III}W^{III} und ^{t}Bu$_2$bpy-Mo^{III}Mo^{III} in Acetonitril (ACN) aufgrund sterischer Abstoßung der raumgreifenden Phenyl- und ^{t}Bu-Substituenten *trans*-Orientierung der Cp*-Liganden. Bei hohen Scanraten (15V/s für dpphen-WW und 8 V/s für ^{t}Bu$_2$bpy-MoMo) wird die Reaktion an der Elektrode signifikant schneller als die chemische Reaktion, so dass reversible Redoxwellen beobachtet werden. Darüber hinaus wurde für die elektrochemische Reversibilität der Komplexe **4-b** und **8-d** eine Lösungsmittelabhängigkeit festgestellt. THF als Lösungsmittel verhindert den *cis-trans*-Isomerisierungsvorgang neutraler Komplexe des Typs $M^{III}M^{III}$. Das bedeutet, dass die *cis-trans*-Isomerisierung in ACN erheblich schneller abläuft als in THF. Der Theorie des Übergangszustands (TST) zufolge sind Lösungsmittel in der Lage die Aktivierungsenergie durch verschiedenartige Solvatisierung der Reaktanden und des aktivierten Komplexes zu beeinflussen. Der Übergangszustand der Isomerisierung beinhaltet eine Rotation um die W-W-Bindung, die einen Bindungsbruch der W-O-Bindung und W-W-π-Bindung zur

Folge hat, wodurch ein stärker polarer aktivierter Komplex gebildet wird. Dieser Komplex wird in dem stärker polaren Lösungsmittel ACN bevorzugt gelöst. Daher wird angenommen, dass die Aktivierungsbarriere der Isomerisierung in ACN niedriger ist als in THF. Daraus lässt sich schließen, dass die Reaktionsgeschwindigkeit der Isomerisierung aufgrund der höheren Aktivierungsbarriere in THF kleiner ist. Dies erklärt die Verzögerung der Isomerisierung bei Zugabe von THF. Die auf dem dpphen-Liganden basierenden Redoxwellen wurden ebenfalls für den dpphen-substituierten Wolfram-Komplex in ACN beobachtet, wogegen die auf reinen ^{t}Bu$_2$bpy-Liganden basierenden Redoxwellen im Potentialfenster des verwendeten elektrochemischen Lösungsmittel ACN nicht auftreten.

Dinukleare μ-Oxo-verbrückte Wolfram- und Molybdän- Komplexe (IV/IV) bieten diverse Vorteile als homogene Photokatalysatoren:
1. Aufgrund der MLCT- und LMCT-Übergänge wurden starke Lichtabsorptionen mit hohen molekularen Absorptionskoeffizienten (mit ϵ bis zu 1.75×10^4 $M^{-1}\cdot cm^{-1}$) im sichtbaren und NIR-Bereich beobachtet.
2. Diese Verbindungen sind hoch redoxaktiv, können drei bis fünf reversible Ein-Elektronentransfers durchlaufen und eignen sich somit als Multielektronen-Katalysatoren.
3. Jene Verbindungen können die Funktionen eines Photosensibilisators und Redox-Katalysators kombinieren. Die Redoxaktivität wird durch Promotion der Elektronen vom Grundzustand in den angeregten Zustand mittels Strahlung erhöht, wodurch Wasser-Oxidation und Wasserstoff-Reduktion thermodynamisch möglich werden.

Bis jetzt zeigten die photokatalytischen Experimente keine Beweise für die strahlungsinduzierte Entstehung von Wasserstoff oder Sauerstoff-Freisetzung. Die gemessenen Emissionsspektren von Komplex **4-a** zeigten keine Lichtemission im Bereich von 600 bis 1200 nm. Wahrscheinlich liegen die Emissionsbanden im NIR-Bereich, was die Detektion erschwert. Deswegen ist unklar, ob die Lebensdauer der angeregten Spezies zu kurz für die Wasserspaltung ist. Zeitaufgelöste Ultrakurzzeit-Absorptionsmessungen des angeregten Zustands könnten diese Frage klären.

6. Experiment Section

6.1. General Methods

Unless otherwise stated, all operations were carried out under an inert atmosphere of nitrogen using standard Schlenk techniques, or performed in a dry and oxygen free glove box.

THF, pentane, benzene, toluene and Et_2O were distilled from sodium benzophenone ketyl under nitrogen. Acetonitrile was dried through alumina super I. CH_2Cl_2 was dried first over P_2O_5, then with CaH_2. Butyronitrile was distilled from CaH_2.

The following chemicals are commercially available products from the following suppliers, which were used as received unless otherwise noted:
$W(CO)_6$ (Fluka); Cp^*H (Merck, distilled under nitrogen and protected from light before use); PCl_5 (Merck); $Mo(CO)_6$ (Aldrich); 1,10-phenanthroline (Alfa Aesar); ethylene diamine (Merck); 4,4′-dimethyl-2,2′-bipyridine (Fluka); TDAE (Aldrich); PPNCl (Aldrich, recrystallized several times from Et_2O/DCM to remove trace of water); $[NH_4][PF_6]$ (Aldrich); naphthalene (Fluka); $[NO][PF_6]$ (Acros); $Ag[PF_6]$ (Alfa Aesar); $[Cp_2Fe][PF_6]$ (Aldrich).

6.2. Characterization Methods

NMR-spectroscopy

^1H-NMR	Bruker Avance 400, measurement frequency 400 MHz Bruker Fourier 300, measurement frequency 300 MHz Varian Gemini 2000 BB, measurement frequency 200 MHz
$^{13}C\{^1H\}$-NMR	Bruker Avance 400, measurement frequency 100 MHz
^{19}F-NMR	Varian Gemini 2000 BB, measurement frequency 188 MHz
^{31}P-NMR	Varian Gemini 2000 BB, measurement frequency 81 MHz

Chemical shifts are given in ppm and ^1H-NMR spectra were referenced to the resonances of residual protons of the deuterated solvent (CD_2Cl_2, δ 5.32; CD_3CN, δ 1.94; C_6D_6, δ 7.15; CD_3OD, δ 3.31; THF-d_8, δ 3.58; CD_3Cl, δ 7.26; D_2O, δ 4.79).

If necessary, the assignment of the ^{1}H-NMR was confirmed by two-dimensional H,H-COSY-NMR spectra. The assignment of the ^{13}C-NMR signals was interpreted by two-dimensional NMR techniques (HSQC and HMBC). Unless otherwise indicated, the ^{13}C{^{1}H}-NMR signals are singlets.

All air sensitive samples were prepared in the glove box. For the description of the multiplets, the following abbreviations are used: **s**: Singlet, **d**: Doublet, **dd**: Doublet of doublet, **t**: Triplet, **q**: Quartet, **sept**: Septet, **m**: Multiplet. For paramagnetic NMR spectra, br stands for broad peak and vbr corresponds to very broad peak.

The numbering scheme used for the ^{1}H- and ^{13}C-NMR signals is shown in Figure 6.1.

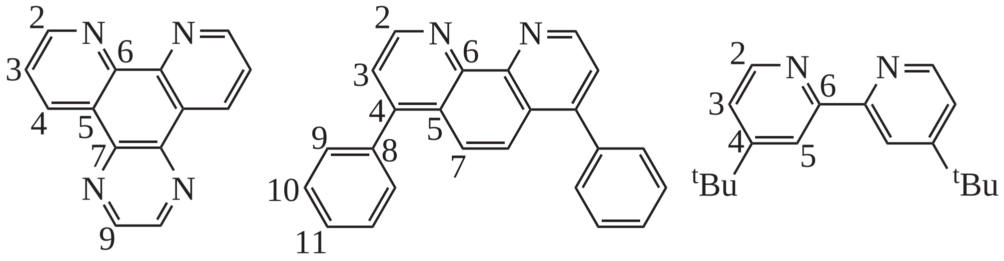

dpq **dpphen** **^{t}Bu$_2$bpy**

Figure 6.1.: Numbering scheme applied for the NMR signals.

Elemental analysis

Heraeus CHN Rapid Analyzer

IR spectroscopy

Bruker VERTEX 70 FT-IR-Spectrometer

The samples were measured as KBr pellets or in solution. Sample preparation was carried out in a glove box. The pellet preperation and the measurements were performed in the atmosphere.

The intensities of the vibrational bands are indicated as follows: **vs**: very strong,

s: strong, **m**: medium, **w**: weak.

EI mass spectrometry

VG 70S EI double focusing sector field device

FAB mass spectrometry

VG Analytical VG/70-250-S-Spectrometer

m-nitrobenzyl alcohol was used as matrix. The sample sample handling was carried out in the atmosphere.

MALDI-TOF mass spectrometry

Matrix assisted laser desorption/ionisation time-of-flight (MALDI-TOF) mass spectrometry was performed on a Bruker UltrafleXtreme mass spectrometer operated in positive ion mode with a Smartbeam *II* Laser. Laser power was used at the threshold level required to generate signal. For measurements in solution, DHB was used as the matrix and prepared as a solution in 30% ACN/0.1% TFA/H_2O. Allotments of matrix and sample were thoroughly mixed together, spotted on the target plate, and allowed to dry. For measurements in the solid state, 0.1 mg of AgTFA, 0.1 mg of analyte and 20 to 80 mg of the DHB matrix (powder) was mixed in a glass vial, vortex for 2 min. Press the powder onto the MALDI target and remove all free grains or crystals.

UV-vis spectroscopy

Varian CARY 50 Scan UV-VIS-NIR-spectrophotometer

StellarNet BLUE-Wave spectrometer

Electrochemical methods

Electrochemical measurements were performed using a BAS 100BW potentiostat with a three-electrode configuration in a single cell. The working electrode was either a glassy carbon disk (diameter = 3.0 mm) or platinum disk (diameter = 1.6 mm), the auxiliary electrode was a Pt wire, and the reference electrode was an Ag wire pseudo-reference, which was referenced externally vs. the $[Cp_2Fe]^{+/0}$ couple. All measurements were performed at room temperature under a nitrogen atmosphere with 0.1 M Bu_4NPF_6 supporting electrolyte in acetonitrile or THF. The working electrode was polished between runs with an alumina slurry to achieve a mirror finish, then thoroughly rinsed with purified water and left to dry in a 40 °C oven. The Pt and Ag wires were polished with fine sandpaper.

For the electrochemical solvents, acetonitrile (Chromasolv®, Fluka) was purified on alumina (Woelm, acidic, super I), THF (Chromasolv®, Fluka) was distilled from sodium/benzophenone. All solvents were degassed before taking into a golvebox and kept in a Young solvent vessel. Water for cleaning was purified using a LaboStar^{TM} Range of UltraPure Water System. NBu_4PF_6 was crystallized twice from methanol, dried at 100 °C under vacuum and used as supporting electrolyte.

X-ray single crystal structure analysis

Bruker AXS smart APEX 3-circle single-crystal diffractometer
- APEX I CCD detector
- Molybdenum source Incoatec Microfocus Source IμS^{TM} (30 watts, air cooling)
- Cryostream nitrogen-flow cooling, 100-300 K (Oxford Cryosystems)

SuperNova 4-circle single-crystal diffractometer from Oxford Diffraction
- Molybdenum and copper source (dual unit), Microfocus tubes
- Cryostream-700 plus-nitrogen flow cooling, 100 - 500 K (Oxford Cryosystems)

The crystal structures were analyzed with the aid of WinGX and SHELX-97 programs, solved by direct methods and expanded using Fourier techniques. All nonhydrogen atoms were refined anisotropically and the hydrogen atoms were treated as riding model in idealized positions (HFIX 137 for $-CH_3$ groups, HFIX

13 for tertiary CH, HFIX 23 for secondary CH_2, HFIX 43 for aromatic CH).

TD-DFT calculations

TD-DFT calculations were performed with Turbomole;[130] Functional:B-P86;[131,132] Basis sets: def2-TZVP for W, def-SV(P) for O, N, C, H.

6.3. Synthetic Details

6.3.1. Synthesis According to Literature

The following compounds and reagents were prepared according to published procedures:

$W(CO)_3(NCPr)_3$[107]

A mixture of $W(CO)_6$ (14.0 g, 0.040 mol) and NCPr (140 ml) was refluxed for 4 days. The volume of the cooled reaction mixture was reduced to 25 ml, and 120 ml of diethyl ether was added to the solution. Fine yellow needles was precipitated from the solution on cooling in the fridge for 2 days. The pure product was seperated by filtration, washing with diethyl ether, and drying in vacuo.
Yield: $\geq$ 17.7 g, 0.036 mol, 90%.

^{1}H-NMR (200 MHz, CD_2Cl_2), δ[ppm]:

2.58	(t, $^3J_{H,H}$ = 7.0 Hz, 6 H, $NCC\boldsymbol{H}_2CH_2CH_3$)
1.75	(m, 6 H, $NCCH_2C\boldsymbol{H}_2CH_3$)
1.09	(t, $^3J_{H,H}$ = 7.3 Hz, 9 H, $NCCH_2CH_2C\boldsymbol{H}_3$)

IR: ν_{CO} [cm^{-1}] = 1913 (**vs**), 1796 (**vs**) [in CH_2Cl_2]

$Cp^*W(CO)_3H$[108]

A solution of Cp^*H (4.3 g, 5 ml, 31 mmol) in 130 ml toluene was added to 7.6 g of $W(CO)_3(NCPr)_3$ (16 mmol). The mixture was stirred for 2 h and then warmed

to 50 - 60 °C until all solid dissolved. The resulting solution was stripped of all liquid volatiles by pumping in vacuo, then dried at 70 - 80 °C. The residue was purified by sublimation at 75 °C under high vacuum.
Yield: $\geq$ 4.7 g, 11.7 mmol, 73%.

^{1}H-NMR (200 MHz, C_6D_6), δ[ppm]: 1.74 (Cp*); -6.50 (hydride)

IR: ν_{CO} [cm^{-1}] = 2014 (**vs**), 1925 (**vs**) [in pentane]

Cp*WCl$_4$[109]

PCl_5 (6.6 g, 31.6 mmol) was slowly added to a solution of Cp*W(CO)$_3$H (5.0 g, 12.4 mmol) in 50 ml toluene and the mixture was stirred at 70 °C for 17 h to give an orange solid which was filtered, washed with methylene chloride, then dried under vacuum.

Cp*Mo(CO)$_3$H[108]

Mo(CO)$_6$ (6.0 g, 22.7 mmol) and 60 mL of butyronitrile were refluxed overnight in a 250 ml flask to give MO(CO)$_3$(NCPr)$_3$. The solvent was removed in vacuo, and Cp*H (5 g, 36.7 mmol) in 200 mL toluene was added to the residue. The mixture was stirred for 2 h and then warmed to 50 - 60 °C until all solid dissolved. The resulting solution was stripped of all liquid volatiles by pumping in vacuo at 70 - 80 °C. The residue, consisting primarily of Cp*Mo(CO)$_3$H, was sublimed at 55 °C under high vacuum.

Cp*MoCl$_4$[99]

Instead of Cp*Mo(CO)$_3$Me, a solution of Cp*Mo(CO)$_3$H dissolved in dichloromethane was added dropwisely to 2.5 equivalents of PCl_5 partially dissolved in dichloromethane. After the mixture was refluxed overnight, an purple solution yielded from which microcrystalline purple Cp*MoCl$_4$ can be isolated.

phd[144]

1,10-phenantroline-5,6-dione was prepared according to a slightly modified method reported by Che.[144] 1,10-phenanthroline (10 g, 50.5 mmol) was added slowly into cold concentrated sulfuric acid (100 ml, 98%) at 0 °C in a three-necked, round-bottomed flask with reflux condenser. Potassium bromide (15 g, 0.126 mol) was added below 5 °C. Fuming nitric acid (68%, w/w, 10 ml) was added drop wise with stirring under 30 °C. When fuming nitric acid drop over, the mixture was heated to 40 °C for 3 h and then heated to 80 - 90 °C for 1 h. Under the same temperature, the Br_2 was blew by N_2 and absorbed by NaOH for 4 h. The orange mixture was cooled and poured onto a mixture of ice and water, the pH was adjusted to 6 - 7 with aqueous saturated sodium hydroxide solution, and the solution was extracted with dichloromethane. The dichloromethane layer was dried with anhydrous magnesium sulfate, and the solvent was removed under vacuum. The residue was recrystallized from methanol to afford yellow needles of 1,10-phenanthroline-5,6-dione, mp 258 °C.
Yield: $\geq$ 4.9 g, 23 mmol, 46%.

^{1}H-NMR (400 MHz, $CDCl_3$), δ[ppm]: 9.09 (dd, 2H); 8.48 (dd, 2H); 7.56 (dd, 2H)

dpq[145]

Ethane-1,2-diamine (0.5 ml) was added to a suspension of 1,10-phenanthroline-5,6-dione (0.50 g, 2.38 mmol) in MeOH (25 ml). A red solution formed, which was stirred overnight at room temperature. The solid formed was filtered off and washed with small amounts of methanol. Recrystallization from toluene gave yellowish white crystals of dipyrido[3,2-a:2′,3′-h]quinoxoline.
Yield: $\geq$ 0.245 g, 1.05 mmol, 44%.

^{1}H-NMR (400 MHz, CD_2Cl_2), δ[ppm]:

9.49	(dd, $^4J_{H[4],H[2]}$ = 1.82 Hz, $^3J_{H[4],H[3]}$ = 8.17 Hz, 2 $H_{[4]}$)
9.22	(dd, $^4J_{H[2],H[4]}$ = 1.81 Hz, $^3J_{H[2],H[3]}$ = 4.38 Hz, 2 $H_{[2]}$)
8.99	(s, 2 $H_{[9]}$)
7.79	(dd, $^3J_{H[3],H[2]}$ = 4.39 Hz, $^3J_{H[3],H[4]}$ = 8.17 Hz, 2 $H_{[3]}$)

bpy(COOH)$_2$[146]

4,4′-dimethyl-2,2′-bipyridine (5.4 g, 30 mmol) was dissolved in concentrated sulfuric acid (140 ml). At 0 °C potassium dichromate (35.2 g, 120 mmol) was added in small portions. Thereafter the reaction mixture was heated to 60 °C for 2 h. The green solution was poured into ice water (600 ml); the resulting precipitate was collected on a filter and washed with water until the filtrate became colorless. The pale greenish yellow solid was refluxed in nitric acid (70 ml; 50% aq.) for 4 h, poured into 300 ml ice, filtered and washed with water and acetone. The resulting white solid was dried in vacuo.
Yield: 5.96 g, 24.4 mmol, 81.4 %.

^{1}H-NMR (400 MHz, $D_2O[Na^+]$), δ[ppm]:

8.64	(d, $^3J_{H[2],H[3]}$ = 5.1 Hz, 2 H$_{[2]}$, bpy)
8.23	(s, 2 H$_{[5]}$, bpy)
7.74	(dd, $^4J_{H[3],H[5]}$ = 1.5 Hz, $^3J_{H[3],H[2]}$ = 5.1 Hz, 2 H$_{[3]}$, bpy)

bpy(COOMe)$_2$[147]

To 4.1 g (16.8 mmol) of 4,4′-dicarboxy-2,2′-bipyridine in 60 ml methanol was added 8.5 ml of concentrated sulfuric acid. After refluxing overnight, the solution was poured onto 180 ml water forming a white slurry. The pH of the slurry was adjusted to 8 with 25% (w/v) sodium hydroxide. The product was then extracted with dichloromethane, dried over sodium sulfate and evaporated to form a white crystalline product. Melting point: 211 °C.
Yield: $\geq$ 3.6 g, 13.2 mmol, 78.7%.

^{1}H-NMR (400 MHz, CD_2Cl_2), δ[ppm]:

8.94	(s, 2 H$_{[5]}$, bpy)
8.84	(d, $^3J_{H[2],H[3]}$ = 4.9 Hz, 2 H$_{[2]}$, bpy)
7.88	(dd, $^4J_{H[3],H[5]}$ = 1.6 Hz, $^3J_{H[3],H[2]}$ = 4.9 Hz, 2 H$_{[3]}$, bpy)
3.98	(s, 6 H, COO*Me*)

6.3.2. Synthesis for Chapter 2

6.3.2.1. [Cp*MoCl$_3$]$_2$ (1-1)

A similar strategy by Poli[94] was applied for the synthesis of complex [Cp*MoCl$_3$]$_2$. 0.96 g (2.57 mmol) of Cp*MoCl$_4$ was added to 12.43 g 0.5%(w/w) of NaHg (62.2 mg Na, 2.7 mmol) in 40 ml toluene. The dark green solution was stirred for 6 hours at room temperature, then the solvent was removed under vacuum. The residue was extracted with 60 ml of dichloromethane, filtered and dried under vacuum. A olive green solid was obtained.
Yield: $\geq$ 0.69 g, 1.02 mmol, 79%.

^{1}H-NMR (400 MHz, CD$_2$Cl$_2$), δ[ppm]:

1.99	(s, $C_5(CH_3)_5$ by-product)
1.36	(br, $\omega_{1/2} = 16.4Hz$ could not be assigned)
-4.19	(br, $C_5(CH_3)_5$ product)

6.3.2.2. PPN[Cp*WCl$_4$] (1-2)

A solution of TDAE (38.6 mg, 0.193 mmol) in 5 ml CH$_2$Cl$_2$ was added into a solution of Cp*WCl$_4$ (159.0 mg, 0.346 mmol), PPNCl (221.8 mg, ca. 0.350 mmol) in 15 ml CH$_2$Cl$_2$ under stirring. After 40 min, the colorless precipitate was filtered off through a glass fabric filter. The filtrate was concentrated to 20 ml and 40 ml of diethyl ether was added to the solution. The next day, brownish black crystals were separated from the solution, washed with diethyl ether and dried under vacuum.
Yield: $\geq$ 286 mg, 0.286 mmol, 83%.

^{1}H-NMR (200 MHz, CD$_2$Cl$_2$), δ[ppm]:

7.53	(m, 30 H, PPN)
6.84	(vbr. s, 15 H, $\omega_{1/2} = 18Hz$, $C_5(CH_3)_5$)

6.3.2.3. PPN[Cp*MoCl$_4$] (1-3)

Complex PPN[Cp*MoCl$_4$] was synthesized as described by Poli.[94] [Cp*MoCl$_3$]$_2$ (295 mg, 0.437 mmol) and PPNCl (554.0 mg, ca. 0.874 mmol) was mixed in 40 ml CH$_2$Cl$_2$ and stirred overnight. The resulting green solution was concentrated to 15 ml under reduced pressure and 25 ml of Et$_2$O was added. The green micro crystalline precipitate was collected by filtration, washed with Et$_2$O and dried under vacuum.
Yield: $\geq$ 682 mg, 0.748 mmol, 86%.

^{1}H-NMR (300 MHz, CD$_2$Cl$_2$), δ[ppm]:

7.58	(br. m, 30 H, PPN)
-13.96	(vbr. s, 15 H, $\omega_{1/2} = 135 Hz$, C$_5$(CH$_3$)$_5$)

6.3.2.4. Cp*W(dpq)Cl$_3$ (2-a)

A solution of the dpq ligand (307.0 mg, 1.322 mmol) in 60 ml CH$_2$Cl$_2$ was slowly added through a dropping funnel to a solution of PPN[Cp*WCl$_4$] (1323.0 mg, 1.324 mmol) in 20 ml CH$_2$Cl$_2$ under vigorous stirring. After 2 days, stirring was switched off and the suspension was allowed to settle down. The green supernatant was decanted with pipette and the black/purple precipitate was washed with CH$_2$Cl$_2$ and pentane, dried under vacuum.
Yield: $\geq$ 777.0 mg, 1.181 mmol, 89.4%.

^{1}H-NMR (300 MHz, CD$_2$Cl$_2$), δ[ppm]:

9.67	(dd, $^4J_{H[4],H[2]}$ = 1.5 Hz, $^3J_{H[4],H[3]}$ = 8.4 Hz, 2 H$_{[4]}$, dpq)
9.36	(dd, $^4J_{H[2],H[4]}$ = 1.4 Hz, $^3J_{H[2],H[3]}$ = 5.4 Hz, 2 H$_{[2]}$, dpq)
9.16	(s, 2 H$_{[9]}$, dpq)
8.08	(dd, $^3J_{H[3],H[2]}$ = 5.3 Hz, $^3J_{H[3],H[4]}$ = 8.3 Hz, 2 H$_{[3]}$, dpq)
1.69	(s, 15 H, C$_5$(CH$_3$)$_5$)

MS(EI): m/z: 656 [M$^+$]

Elemental analysis (C$_{24}$H$_{23}$N$_4$Cl$_3$W)

calcd:	C 43.83 %,	H 3.53 %,	N 8.52 %
found:	C 43.59 %,	H 3.65 %,	N 8.61 %

6.3.2.5. Cp*W(dpphen)Cl$_3$ (2-b)

A solution of the dpphen ligand (234.5 mg, 0.705 mmol) in 50 ml CH_2Cl_2 was slowly added through a dropping funnel to a solution of PPN[Cp*WCl_4] (703.0 mg, 0.703 mmol) in 10 ml CH_2Cl_2 under vigorous stirring. After 2 days, stirring was discontinued. The green supernatant was taken out with glass pipette and the green precipitate was washed with diethyl ether, pumped dry. Further product was obtained from the filtrate, which was concentrated and then diethyl ether was added to the solution. The next day, green crystals was separated and washed with diethyl ether, then dried under vacuum.
Yield: $\geq$ 448.1 mg, 0.591 mmol, 84.1%.

^{1}H-NMR (200 MHz, CD_2Cl_2), δ[ppm]:

9.31	(d, $^3J_{H[2],H[3]}$ = 5.17 Hz, 2 $H_{[2]}$, dpphen)
8.08	(s, 2 $H_{[7]}$, dpphen)
7.88	(d, $^3J_{H[3],H[2]}$ = 4.97 Hz, 2 $H_{[3]}$, dpphen)
7.61	(m, 10 H_{ph}, dpphen)
1.69	(s, 15 H, $C_5(CH_3)_5$)

MS(EI): m/z: 756.2 [M^+]

Elemental analysis ($C_{34}H_{31}N_2Cl_3W + CH_2Cl_2$)

calcd:	C 49.88 %,	H 3.95 %,	N 3.32 %
found:	C 50.22 %,	H 4.20 %,	N 2.96 %

6.3.2.6. Cp*W(COOMe$_2$bpy)Cl$_3$ (2-c)

A colorless suspension of the $(COOMe)_2$bpy ligand (22.0 mg, 0.081 mmol) in 12 ml CH_3CN was added to a brown solution of PPN[Cp*WCl_4] (73.7 mg, 0.074 mmol) in 6 ml CH_2Cl_2. The resulting black solution was stirred at 100 °C for 5 days to yield a dark purple solution. Single crystals suitable for X-ray diffraction were obtained from a diluted filtrate solution at room temperature.

6.3.2.7. Cp*Mo(dpq)Cl$_3$ (3-a)

A solution of the dpq ligand (28.7 mg, 0.123 mmol) in 30 ml CH_2Cl_2 was slowly added through a dropping funnel into a solution of PPN[Cp*MoCl$_4$] (110.0 mg, 0.121 mmol) in 10 ml CH_2Cl_2 under vigorous stirring. A blueish purple solid precipitated from the reaction suspension. The precipitate was washed with CH_2Cl_2, then dried under vacuum.
Yield: $\geq$ 61.3 mg, 0.108 mmol, 89%.

^{1}H-NMR (300 MHz, CD_3CN), δ[ppm]:

9.77	(m, 1 $\mathrm{H}_{[4]}$ + 1 $\mathrm{H}_{[4]}'$, dpq)
9.22	(s, 2 $\mathrm{H}_{[9]}$, dpq)
9.10	(d, $^3J_{H[2],H[3]}$ = 5.5 Hz, 1 $\mathrm{H}_{[2]}$, dpq)
8.80	(d, $^3J_{H[2],H[3]}$ = 5.2 Hz, 1 $\mathrm{H}_{[2]}'$, dpq)
8.20	(m, 1 $\mathrm{H}_{[3]}$ + 1 $\mathrm{H}_{[3]}'$, dpq)
1.51	(s, 15 H, $C_5(CH_3)_5$)

6.3.2.8. Cp*Mo(^{t}Bu$_2$bpy)Cl$_3$ (3-d)

To a solution of 193 mg (0.286 mmol) [Cp*MoCl$_3$]$_2$ in 25 ml methylenechloride, 157 mg (0,586 mmol) of the ligand ^{t}Bu$_2$bpy in 7 ml of methylene chloride was added dropwisely. The resulting dark brown solution was stirred for 16 hours at room temperature and then filtered. The product Cp*Mo(^{t}Bu$_2$bpy)Cl$_3$ was precipitated from the filtrate by addition of diethyl ether. The black precipitate was filtered and washed several times with diethyl ether, and n-hexane to yield 263 mg (0.434 mmol, 76%) light brown solid.

^{1}H-NMR (400 MHz, CD_2Cl_2), δ[ppm]:

8.93	(br s, $\omega_{1/2} = 8Hz$, 2 H, ^{t}Bu$_2$bpy)
8.73	(br s, $\omega_{1/2} = 12Hz$, 2 H, ^{t}Bu$_2$bpy)
7.67	(br s, $\omega_{1/2} = 10Hz$, 2 H, ^{t}Bu$_2$bpy)
2.24	(vbr s, $\omega_{1/2} = 183.8Hz$, $C_5(CH_3)_5$)
1.47	(s, 15 H, $C(CH_3)_3$)

6.3.3. Sythesis for Chapter 3

6.3.3.1. $[(Cp^{*}W(dpq)(\mu-O))_2][PF_6]_2$ (4-a)

400mg of $Cp^{*}W(dpq)Cl_3$ (0.608 mmol) was mixed with 20 ml degassed water to give a dark purple acidic solution. After neutralization by addition of solid $NaHCO_3$, a solution of NH_4PF_6 (100.4 mg, 0.616 mmol) in water (5 ml) was added slowly and a dark purple solid precipitated from the solution. The solvent was removed under reduced pressure and the remaining solid was extracted with CH_2Cl_2. The filtrate was concentrated under vacuum. The analytically pure product was precipitated through addition of diethyl ether. The solid was collected by filtration, washed with ether, dried under high vacuum. Yield: $\geq$ 289.0 mg, 0.203 mmol, 66.7%.

^{1}H-NMR (400 MHz, CD_2Cl_2), δ[ppm]:

8.93	(dd, $^{4}J_{H[4],H[2]}$ = 1.25 Hz, $^{3}J_{H[4],H[3]}$ = 8.14 Hz, 4 $H_{[4]}$, dpq)
8.85	(s, 4 $H_{[9]}$, dpq)
8.83	(dd, $^{4}J_{H[2],H[4]}$ = 1.24 Hz, $^{3}J_{H[2],H[3]}$ = 5.47 Hz, 4 $H_{[2]}$, dpq)
7.94	(dd, $^{3}J_{H[3],H[2]}$ = 5.47 Hz, $^{3}J_{H[3],H[4]}$ = 8.14 Hz, 4 $H_{[3]}$, dpq)
1.63	(s, 30 H, $C_5(CH_3)_5$)

^{1}H-NMR (400 MHz, CD_3OD), δ[ppm]:

9.04	(d, $^{3}J_{H[4],H[3]}$ = 8.2 Hz, $H_{[4]}$, dpq)
8.92	(s, 4 $H_{[9]}$, dpq)
8.81	(d, $^{3}J_{H[2],H[3]}$ = 5.3 Hz, 4 $H_{[2]}$, dpq)
7.86	(dd, $^{3}J_{H[3],H[4]}$ = 8.2 Hz, $^{3}J_{H[3],H[2]}$ = 5.5 Hz, 4 $H_{[3]}$, dpq)
1.69	(s, 30 H, $C_5(CH_3)_5$)

^{1}H-NMR (300 MHz, CD_3CN), δ[ppm]:

8.90	(dd, $^{4}J_{H[4],H[2]}$ = 1.30 Hz, $^{3}J_{H[4],H[3]}$ = 8.16 Hz, 4 $H_{[4]}$, dpq)
8.87	(s, 4 $H_{[9]}$, dpq)
8.67	(dd, $^{4}J_{H[2],H[4]}$ = 1.30 Hz, $^{3}J_{H[2],H[3]}$ = 5.48 Hz, 4 $H_{[2]}$, dpq)
7.77	(dd, $^{3}J_{H[3],H[2]}$ = 5.50 Hz, $^{3}J_{H[3],H[4]}$ = 8.19 Hz, 4 $H_{[3]}$, dpq)
1.61	(s, 30 H, $C_5(CH_3)_5$)

^{13}C{^{1}H}-NMR (75 MHz, CD_3CN), δ[ppm]:

152.70	(s, $\mathbf{C}_{[2]}$H, dpq)
146.99	(s, $\mathbf{C}_{[9]}$H, dpq)
135.70	(s, $\mathbf{C}_{[4]}$H, dpq)
126.44	(s, $\mathbf{C}_{[3]}$H, dpq)
8.91	(s, CH_3, $C_5(CH_3)_5$)

^{19}F-NMR (188 MHz, CD_2Cl_2), δ[ppm]: -72.31 (d, $^1J_{FP}$ = 712 Hz, PF_6^-)

^{19}F-NMR (188 MHz, CD_3CN)), δ[ppm]: -73.03 (d, $^1J_{FP}$ = 704 Hz, PF_6^-)

^{31}P-NMR (81 MHz, CD_2Cl_2), δ[ppm]: -144.17 (m, $^1J_{PF}$ = 712 Hz, PF_6^-)

^{31}P-NMR (81 MHz, CD_3CN)), δ[ppm]: -144.61 (hept, $^1J_{PF}$ = 706 Hz, PF_6^-)

MS(FAB$^+$): m/z: 567.1 [M^{2+}]

Elemental analysis ($C_{48}H_{46}N_8F_{12}O_2P_2W_2$)

calcd:	C 40.47 %,	H 3.25 %,	N 7.87 %
found:	C 40.75 %,	H 3.52 %,	N 8.03 %

6.3.3.2. [(Cp*W(dpq)(μ–O))$_2$][PF$_6$][Al(pftb)$_4$] (4-a1)

A mixture of 90.2 mg [(Cp*W(dpq)(μ–O))$_2$][PF$_6$]$_2$ (0.063 mmol) and 61.7 mg Li[Al(pftb)$_4$] (0.063 mmol) in 10 ml THF was stirred for 150 min. The solvent was removed under reduced pressure and the remaining solid was extracted with CH_2Cl_2. The analytically pure product was recrystallized from CH_2Cl_2 and diethyl ether.

^{1}H-NMR (400 MHz, CD_2Cl_2), δ[ppm]:

8.96	(dd, $^4J_{H[4],H[2]}$ = 1.28 Hz, $^3J_{H[4],H[3]}$ = 8.12 Hz, 4 $H_{[4]}$, dpq)
8.87	(s, 4 $H_{[9]}$, dpq)
8.70	(dd, $^4J_{H[2],H[4]}$ = 1.28 Hz, $^3J_{H[2],H[3]}$ = 5.48 Hz, 4 $H_{[2]}$, dpq)
7.83	(dd, $^3J_{H[3],H[2]}$ = 5.47 Hz, $^3J_{H[3],H[4]}$ = 8.13 Hz, 4 $H_{[3]}$, dpq)
1.63	(s, 30 H, $C_5(CH_3)_5$)

^{1}H-NMR (400 MHz, CD$_3$CN), δ[ppm]:

8.89	(dd, $^{4}J_{H[4],H[2]}$ = 1.26 Hz, $^{3}J_{H[4],H[3]}$ = 8.15 Hz, 4 H$_{[4]}$, dpq)
8.87	(s, 4 H$_{[9]}$, dpq)
8.65	(dd, $^{4}J_{H[2],H[4]}$ = 1.25 Hz, $^{3}J_{H[2],H[3]}$ = 5.46 Hz, 4 H$_{[2]}$, dpq)
7.76	(dd, $^{3}J_{H[3],H[2]}$ = 5.46 Hz, $^{3}J_{H[3],H[4]}$ = 8.15 Hz, 4 H$_{[3]}$, dpq)
1.61	(s, 30 H, $C_5(CH_3)_5$)

^{13}C{^{1}H}-NMR (100 MHz, CD$_3$CN), δ[ppm]:

154.04	(s, ***C***$_{[2]}$H, dpq)
148.37	(s, ***C***$_{[9]}$H, dpq)
143.70	(s, quart. ***C***$_{[6]}$, dpq)
139.19	(s, quart. ***C***$_{[7]}$, dpq)
137.06	(s, ***C***$_{[4]}$H, dpq)
128.70	(s, quart. ***C***$_{[5]}$, dpq)
127.77	(s, ***C***$_{[3]}$H, dpq)
116.05	(s, quart. C, $\boldsymbol{C}_5(CH_3)_5$)
10.28	(s, CH$_3$, $C_5(\boldsymbol{C}H_3)_5$)

^{19}F-NMR (188 MHz, CD$_3$CN)), δ[ppm]:

-72.87	(d, $^{1}J_{FP}$ = 707 Hz, PF_6^-)
-75.98	(s, $Al(pftb)_4^-$)

6.3.3.3. [(Cp*W(dpq)($\mu-$O))$_2$][Al(pftb)$_4$]$_2$ (4-a2)

A mixture of 39.0 mg [(Cp*W(dpq)($\mu-$O))$_2$][PF$_6$]$_2$ (0.027 mmol) and 65.0 mg Li[Al(pftb)$_4$] (0.067 mmol) in 12 ml solvent mixture of THF and acetonitrile (2:1) was stirred for 24 h. The solvent was removed under reduced pressure and the remaining solid was extracted with THF.

^{1}H-NMR (300 MHz, THF-d_8), δ[ppm]:

9.02	(dd, $^{4}J_{H[4],H[2]}$ = 1.3 Hz, $^{3}J_{H[4],H[3]}$ = 8.1 Hz, 4 H$_{[4]}$, dpq)
8.91	(s, 4 H$_{[9]}$, dpq)
8.83	(dd, $^{4}J_{H[2],H[4]}$ = 1.3 Hz, $^{3}J_{H[2],H[3]}$ = 5.5 Hz, 4 H$_{[2]}$, dpq)
7.90	(dd, $^{3}J_{H[3],H[2]}$ = 5.5 Hz, $^{3}J_{H[3],H[4]}$ = 8.2 Hz, 4 H$_{[3]}$, dpq)
1.68	(s, 30 H, $C_5(CH_3)_5$)

^{1}H-NMR (300 MHz, CD_2Cl_2), δ[ppm]:

8.98	(dd, $^4J_{H[4],H[2]}$ = 1.3 Hz, $^3J_{H[4],H[3]}$ = 8.1 Hz, 4 $H_{[4]}$, dpq)
8.89	(s, 4 $H_{[9]}$, dpq)
8.61	(dd, $^4J_{H[2],H[4]}$ = 1.4 Hz, $^3J_{H[2],H[3]}$ = 5.5 Hz, 4 $H_{[2]}$, dpq)
7.76	(dd, $^3J_{H[3],H[2]}$ = 5.5 Hz, $^3J_{H[3],H[4]}$ = 8.1 Hz, 4 $H_{[3]}$, dpq)
1.63	(s, 30 H, $C_5(CH_3)_5$)

^{19}F-NMR (188 MHz, CD_2Cl_2), δ[ppm]: -77.77 (s, $Al(pftb)_4^-$)

6.3.3.4. [Cp*W(dpq)($NCCH_3$)$_2$(OH)][PF_6]$_2$ (5-a)

A solution of [NO][PF_6] (20.5 mg, 95%, 0.111 mmol) in 6 ml CH_3CN was added to a solution of [(Cp*W(dpq)(μ−O))$_2$][PF_6]$_2$ (77 mg, 0.054 mmol) in 10 ml CH_3CN under stirring. The purple solution turned to brown. The reaction solution was filtered and concentrated to 4 ml. 10 ml Et_2O was added into the solution to give brown crystals.

^{1}H-NMR (400 MHz, CD_3CN), δ[ppm]:

9.92	(dd, $^4J_{H[4],H[2]}$ = 0.93 Hz, $^3J_{H[4],H[3]}$ = 8.31 Hz, 2 $H_{[4]}$, dpq)
9.27	(s, 2 $H_{[9]}$, dpq)
8.99	(d, $^3J_{H[2],H[3]}$ = 5.22 Hz, 2 $H_{[2]}$, dpq)
8.30	(dd, $^3J_{H[3],H[2]}$ = 5.35 Hz, $^3J_{H[3],H[4]}$ = 8.33 Hz, 2 $H_{[3]}$, dpq)
1.92	(s, 15 H, $C_5(CH_3)_5$)

6.3.3.5. [(Cp*W(dpq)(μ−O))$_2$] (6-a)

Complex [(Cp*W(dpq)(μ−O))$_2$][PF_6]$_2$ (**4-a**) was dissolved 3 times in acetonitrile and pumped dry, then treated with THF for 3 times in order to remove residual co-crystallized CH_2Cl_2 and acetonitrile. A solution of sodium naphthalenide prepared in situ by stirring naphthalene (27.3 mg, 0.212 mmol) with an excess amount of freshly cut sodium in 3 ml THF. The green solution was filtered into a suspension of **4-a** (144.0 mg, 0.101 mmol) in 4 ml THF under vigorous stirring. The solvent was removed from the resulting dark violet solution under reduced pressure and the residue was treated three times with pentane to remove residual

THF. The solid residue was extracted with pentane and the violet pentane solution was filtered over a glass fiber filter and dried in vacuo. The crude product was redissolved several times in pentane and dried under high vacuum to remove residual naphthalene to yield a dark violet powder. Yield: $\geq$ 88.0 mg, 0.078 mmol, 76.8%.

^{1}H-NMR (400 MHz, C_6D_6), δ[ppm]:

7.84	(s, 4 $H_{[9]}$, dpq)
7.35	(d, $^3J_{H[4],H[3]}$ = 7.70 Hz, 4 $H_{[4]}$, dpq)
6.31	(d, $^3J_{H[2],H[3]}$ = 4.67 Hz, 4 $H_{[2]}$, dpq)
5.62	(t, $^3J_{H[3],H[2,4]}$ = 6.47 Hz,4 $H_{[3]}$, dpq)
1.63	(s, 30 H, $C_5(CH_3)_5$)

MS(MALDI-TOF): m/z: 1134.291 [M^+]

6.3.3.6. [(Cp*W(dpphen)($\mu-$O))$_2$][PF$_6$]$_2$ (4-b)

442.5 mg of Cp*W(dpphen)Cl_3 (0.584 mmol) was mixed with 30 ml degassed water and stirred overnight to give a dark blue acidic solution. After neutralization by addition of solid $NaHCO_3$, a solution of NH_4PF_6 (105.0 mg, 0.644 mmol) in water (10 ml) was added slowly and a dark blue solid precipitated from the solution. The solvent was removed under reduced pressure and the remaining solid was extracted with 40 ml CH_2Cl_2. The analytically pure product was precipitated through addition of 60 ml diethyl ether. The solid was collected by filtration, washed with ether, dried under high vacuum. Yield: $\geq$ 360.0 mg, 0.222 mmol, 75.8%.

^{1}H-NMR (200 MHz, CD_2Cl_2), δ[ppm]:

8.86	(d, $^3J_{H[2],H[3]}$ = 5.69 Hz, 4 $H_{[2]}$, dpphen)
7.77	(d, $^3J_{H[3],H[2]}$ = 5.68 Hz, 4 $H_{[3]}$, dpphen)
7.70	(s, 4 $H_{[7]}$, dpphen)
7.40, 7.09	(m, 20 H_{ph}, dpphen)
1.63	(s, 30 H, $C_5(CH_3)_5$)

^{1}H-NMR (300 MHz, CD_3CN), δ[ppm]:

8.74	(d, $^3J_{H[2],H[3]}$ = 5.7 Hz, 4 $H_{[2]}$, dpphen)
7.74	(s, 4 $H_{[7]}$, dpphen)
7.67	(d, $^3J_{H[3],H[2]}$ = 5.7 Hz, 4 $H_{[3]}$, dpphen)
7.48	(m, 4 $H_{[11]}$, dpphen)
7.39	(m, 8 $H_{[9]}$, dpphen)
7.16	(dt, $^3J_{H[10],(H[11],H[9])}$ = 7.1, 1.4 Hz, 8 $H_{[10]}$, dpphen)
1.62	(s, 30 H, $C_5(CH_3)_5$)

$^{13}C\{^1H\}$-NMR (75 MHz, CD_3CN), δ[ppm]:

151.30	(s, $\boldsymbol{C}_{[2]}$H, dpphen)
130.09	(s, $\boldsymbol{C}_{[11]}$H, dpphen)
130.05	(s, $\boldsymbol{C}_{[9]}$H, dpphen)
128.89	(s, $\boldsymbol{C}_{[10]}$H, dpphen)
125.07	(s, $\boldsymbol{C}_{[7]}$H, dpphen)
124.52	(s, $\boldsymbol{C}_{[3]}$H, dpphen)
8.95	(s, CH_3, $C_5(\boldsymbol{C}H_3)_5$)

MS(FAB$^+$): m/z: 667.2 [M^{2+}]

Elemental analysis ($C_{68}H_{62}N_4F_{12}O_2P_2W_2$)

calcd:	C 50.26 %,	H 3.85 %,	N 3.45 %
found:	C 49.03 %,	H 3.91 %,	N 3.22 %

6.3.4. Synthesis for Chapter 4

6.3.4.1. [(Cp*Mo(dpq)(μ–O))$_2$][PF$_6$]$_2$ (8-a)

308 mg of Cp*Mo(dpq)Cl_3 (0.541 mmol) was mixed with 25 ml degassed water to give a dark red acidic solution. After neutralization by addition of solid $NaHCO_3$, a solution of NH_4PF_6 (98 mg, 0.601 mmol) in water (10 ml) was added slowly and a dark reddish purple solid precipitated from the solution. The solvent was removed under reduced pressure and the remaining solid was extracted with CH_2Cl_2. The filtrate was concentrated under vacuum. The analytically pure product was precipitated through addition of diethyl ether. The solid was collected by filtration, washed with ether, dried under high vacuum. Yield: $\geq$ 258.8 mg, 0.207 mmol, 76.6%.

^{1}H-NMR (300 MHz, CD_3CN), δ[ppm]:

9.07	(d, $^3J_{H[4],H[3]}$ = 8.2 Hz, 4 $H_{[4]}$, dpq)
8.88	(s, 4 $H_{[9]}$, dpq)
8.76	(d, $^3J_{H[2],H[3]}$ = 4.6 Hz, 4 $H_{[2]}$, dpq)
7.77	(m, 4 $H_{[3]}$, dpq)
1.49	(s, 30 H, $C_5(CH_3)_5$)

^{1}H-NMR (300 MHz, CD_2Cl_2), δ[ppm]:

9.12	(dd, $^3J_{H[4],H[3]}$ = 8.2 Hz, $^4J_{H[4],H[2]}$ = 1.4 Hz, 4 $H_{[4]}$, dpq)
8.95	(dd, $^3J_{H[2],H[3]}$ = 5.3 Hz, $^4J_{H[2],H[4]}$ = 1.4 Hz, 4 $H_{[2]}$, dpq)
8.86	(s, 4 $H_{[9]}$, dpq)
7.96	(dd, $^3J_{H[3],H[4]}$ = 8.2 Hz, $^3J_{H[3],H[2]}$ = 5.3 Hz, 4 $H_{[3]}$, dpq)
1.51	(s, 30 H, $C_5(CH_3)_5$)

^{13}C{^{1}H}-NMR (100 MHz, CD_3CN), δ[ppm]:

154.72	(s, $\boldsymbol{C}_{[2]}$H, dpq)
147.88	(s, $\boldsymbol{C}_{[9]}$H, dpq)
143.00	(s, quart. $\boldsymbol{C}_{[6]}$, dpq)
138.74	(s, quart. $\boldsymbol{C}_{[7]}$, dpq)
137.05	(s, $\boldsymbol{C}_{[4]}$H, dpq)
128.66	(s, quart. $\boldsymbol{C}_{[5]}$, dpq)
127.63	(s, $\boldsymbol{C}_{[3]}$H, dpq)
117.80	(s, quart. C, $\boldsymbol{C}_5(CH_3)_5$)
10.02	(s, CH_3, $C_5(\boldsymbol{C}H_3)_5$)

MS(MALDI-TOF): m/z: 481.1 [M^{2+}]

Elemental analysis ($C_{48}H_{46}N_8F_{12}Mo_2O_2P_2$)

calcd:	C 46.17 %,	H 3.71 %,	N 8.97 %
found:	C 45.85 %,	H 3.64 %,	N 9.03 %

6.3.4.2. $[(Cp^*Mo(^t Bu_2bpy)(\mu-O))_2][PF_6]_2$ (8-d)

176 mg of $Cp^*Mo(^t Bu_2bpy)Cl_3$ (0.291 mmol) was hydrolyzed with 15 ml degassed water to give a red acidic solution. After neutralization by addition of solid

$NaHCO_3$, a solution of NH_4PF_6 (65.0 mg, 0.400 mmol) in water (3 ml) was added slowly and a dark red solid precipitated from the solution. The solvent was removed under reduced pressure and the remaining solid was extracted with 15 ml CH_2Cl_2. The analytically pure product was precipitated through addition of 20 ml diethyl ether. The solid was collected by filtration, washed with ether, dried under high vacuum. Yield: $\geq$ 124 mg, 0.094 mmol, 65%.

^{1}H-NMR (400 MHz, CD_2Cl_2), δ[ppm]:

8.48 (d, $^3J_{H[2],H[3]}$ = 5.95 Hz, 4 $H_{[2]}$, ^{t}Bu$_2$bpy)
7.90 (s, 4 $H_{[5]}$, ^{t}Bu$_2$bpy)
7.42 (d, $^3J_{H[3],H[2]}$ = 5.98 Hz, 4 $H_{[3]}$, ^{t}Bu$_2$bpy)
1.37 (s, 30 H, $C_5(CH_3)_5$)
1.29 (s, 36 H, $C(CH_3)_3$bpy)

^{1}H-NMR (300 MHz, CD_2Cl_2), δ[ppm]:

8.47 (d, $^3J_{H[2],H[3]}$ = 6.04 Hz, 4 $H_{[2]}$, ^{t}Bu$_2$bpy)
7.91 (d, $^4J_{H[5],H[3]}$ = 1.97 Hz, 4 $H_{[5]}$, ^{t}Bu$_2$bpy)
7.42 (dd, $^4J_{H[3],H[5]}$ = 1.92 Hz, $^3J_{H[3],H[2]}$ = 6.05 Hz, 4 $H_{[3]}$, ^{t}Bu$_2$bpy)
1.37 (s, 30 H, $C_5(CH_3)_5$)
1.29 (s, 36 H, $C(CH_3)_3$bpy)

^{13}C{^{1}H}-NMR (100 MHz, CD_2Cl_2), δ[ppm]:

166.99 (s, quart. C, ($\boldsymbol{C}(CH_3)_3)_2$bpy)
152.44 (s, $\boldsymbol{C}_{[2]}$H, ^{t}Bu$_2$bpy)
151.20 (s, quart. $\boldsymbol{C}_{[6]}$, ^{t}Bu$_2$bpy)
123.01 (s, $\boldsymbol{C}_{[3]}$H, ^{t}Bu$_2$bpy)
120.61 (s, $\boldsymbol{C}_{[5]}$H, ^{t}Bu$_2$bpy)
116.24 (s, quart. C, $\boldsymbol{C}_5(CH_3)_5$)
36.60 (s, quart. $\boldsymbol{C}_{[4]}$, ^{t}Bu$_2$bpy)
30.44 (s, CH_3, $(C(\boldsymbol{C}H_3)_3)_2$bpy)
9.86 (s, CH_3, $C_5(\boldsymbol{C}H_3)_5$)

MS(FAB$^+$): m/z: 517.1 [M^{2+}]

Elemental analysis ($C_{56}H_{78}N_4F_{12}Mo_2O_2P_2$)

calcd:	C 50.91 %,	H 5.95 %,	N 4.24 %
found:	C 51.16 %,	H 6.06 %,	N 3.97 %

Bibliography

[1] Barber, J. *Chem. Soc. Rev.* **2009**, *38*, 185–196.

[2] Eisenberg, R.; Nocera, D. G. *Inorg. Chem.* **2005**, *44*, 6799–6801.

[3] Lewis, N. S.; Nocera, D. G. *Proc. Nati. Acad. Sci. USA* **2006**, *103*, 15729–15735.

[4] Service, R. F. *Science* **2007**, *315*, 789.

[5] Esswein, A. J.; Nocera, D. G. *Chem. Rev.* **2007**, *107*, 4022–4047.

[6] Hammarström, L.; Hammes-Schiffer, S. *Acc. Chem. Res.* **2009**, *42*, 1859–1860.

[7] Bolton, J. R.; Hall, D. O., M. B. *Photochem. Photobiol.* **1991**, *53*, 545–548.

[8] Taiz, L.; Zeiger, E. *Plant Physiology*; Sinauer Associates. Sunderland, MA, **2006**.

[9] Yachandra, V. K.; Sauer, K.; Klein, M. P. *Chem. Rev.* **1996**, *96*, 2927–2950.

[10] Riggs-Gelasco, P. J.; Mei, R.; Ghanotakis, D. F.; Yocum, C. F.; Penner-Hahn, J. E. *J. Am. Chem. Soc.* **1996**, *118*, 2400–2410.

[11] Tommos, C.; Babcock, G. T. *Acc. Chem. Res.* **1998**, *31*, 18–25.

[12] Ferreira, K. N.; Iverson, T. M.; Maghlaoui, K.; Barber, J.; Iwata, S. *Science* **2004**, *303*, 1831–1838.

[13] Haumann, M.; Liebisch, P.; MÃ¼ller, C.; Barra, M.; Grabolle, M.; Dau, H. *Science* **2005**, *310*, 1019–1021.

[14] Sjöholm, J.; Styring, S.; Havelius, K. G. V.; Ho, F. M. *Biochemistry* **2012**, *51*, 2054–2064.

[15] Kok, B.; Forbush, B.; Mcgloin, M. *Photochem. Photobiol.* **1970**, *11*, 457–475.

[16] Styring, S.; Sjöholm, J.; Mamedov, F. *Biochim. Biophys. Acta* **2012**, *1817*, 76–87.

[17] Vrettos, J. S.; Limburg, J.; Brudvig, G. W. *Biochim. Biophys. Acta* **2001**, *1503*, 229–245.

[18] Siegbahn, P. E. *Curr. Opin. Chem. Biol.* **2002**, *6*, 227–235.

[19] Loll, B.; Kern, J.; Saenger, W.; Zouni, A.; Biesiadka, J. *Nature* **2005**, *438*, 1040–1044.

[20] Meyer, T. J. *Acc. Chem. Res.* **1989**, *22*, 163–170.

[21] Gust, D.; Moore, T. A.; Moore, A. L. *Acc. Chem. Res.* **2001**, *34*, 40–48.

[22] Wasielewski, M. R. *Chem. Rev.* **1992**, *92*, 435–461.

[23] Gust, D.; Moore, T. A.; Moore, A. L. *Acc. Chem. Res.* **1993**, *26*, 198–205.

[24] Arakawa, H.; et al. *Chem. Rev.* **2001**, *101*, 953–996.

[25] Zhang, M.-T.; Hammarström, L. *J. Am. Chem. Soc.* **2011**, *133*, 8806–8809.

[26] Gagliardi, C. J.; Vannucci, A. K.; Concepcion, J. J.; Chen, Z.; Meyer, T. J. *Energy Environ. Sci.* **2012**, *5*, 7704–7717.

[27] Hetterscheid, D. G. H.; van der Vlugt, J. I.; de Bruin, B.; Reek, J. N. H. *Angew. Chem. Int. Ed.* **2009**, *48*, 8178–8181.

[28] Alstrum-Acevedo, J. H.; Brennaman, M. K.; Meyer, T. J. *Inorg. Chem.* **2005**, *44*, 6802–6827.

[29] Moore, T. A.; Gust, D.; Mathis, P.; Mialocq, J.-C.; Chachaty, C.; Bensasson, R. V.; Land, E. J.; Doizi, D.; Liddell, P. A.; Lehman, W. R.; Nemeth, G. A.; Moore, A. L. *Nature* **1984**, *307*, 630–632.

[30] Wasielewski, M. R.; Niemczyk, M. P.; Svec, W. A.; Pewitt, E. B. *J. Am. Chem. Soc.* **1985**, *107*, 5562–5563.

[31] Wasielewski, M. R. *Acc. Chem. Res.* **2009**, *42*, 1910–1921.

[32] Meyer, G. J. *Inorg. Chem.* **2005**, *44*, 6852–6864.

[33] Yagi, M.; Kaneko, M. *Chem. Rev.* **2001**, *101*, 21–36.

[34] Chakraborty, S.; Wadas, T. J.; Hester, H.; Schmehl, R.; Eisenberg, R. *Inorg. Chem.* **2005**, *44*, 6865–6878.

[35] Meyer, T. J. *Pure Appl. Chem.* **1986**, *58*, 1193–1206.

[36] Maestri, M.; Armaroli, N.; Balzani, V.; Constable, E. C.; Thompson, A. M. W. C. *Inorg. Chem.* **1995**, *34*, 2759–2767.

[37] Hicks, C.; Ye, G.; Levi, C.; Gonzales, M.; Rutenburg, I.; Fan, J.; Helmy, R.; Kassis, A.; Gafney, H. D. *Coord. Chem. Rev.* **2001**, *211*, 207–222.

[38] Gersten, S. W.; Samuels, G. J.; Meyer, T. J. *J. Am. Chem. Soc.* **1982**, *104*, 4029–4030.

[39] Rüttinger, W.; Dismukes, G. C. *Chem. Rev.* **1997**, *97*, 1–24.

[40] Cady, C. W.; Crabtree, R. H.; Brudvig, G. W. *Coord. Chem. Rev.* **2008**, *252*, 444–455.

[41] Piers, W. E. *Organometallics* **2011**, *30*, 13–16.

[42] Danielson, E.; Elliott, C. M.; Merkert, J. W.; Meyer, T. J. *J. Am. Chem. Soc.* **1987**, *109*, 2519–2520.

[43] Ashford, D. L.; Stewart, D. J.; Glasson, C. R.; Binstead, R. A.; Harrison, D. P.; Norris, M. R.; Concepcion, J. J.; Fang, Z.; Templeton, J. L.; Meyer, T. J. *Inorg. Chem.* **2012**, *51*, 6428–6430.

[44] Concepcion, J. J.; Jurss, J. W.; Brennaman, M. K.; Hoertz, P. G.; Patrocinio, A. O. T.; Murakami Iha, N. Y.; Templeton, J. L.; Meyer, T. J. *Acc. Chem. Res.* **2009**, *42*, 1954–1965.

[45] Wasylenko, D. J.; Ganesamoorthy, C.; Koivisto, B. D.; Henderson, M. A.; Berlinguette, C. P. *Inorg. Chem.* **2010**, *49*, 2202–2209.

[46] Robson, K. C. D.; Koivisto, B. D.; Yella, A.; Sporinova, B.; Nazeeruddin, M. K.; Baumgartner, T.; Grätzel, M.; Berlinguette, C. P. *Inorg. Chem.* **2011**, *50*, 5494–5508.

[47] McDaniel, N. D.; Coughlin, F. J.; Tinker, L. L.; Bernhard, S. *J. Am. Chem. Soc.* **2008**, *130*, 210–217.

[48] DiSalle, B. F.; Bernhard, S. *J. Am. Chem. Soc.* **2011**, *133*, 11819–11821.

[49] Lalrempuia, R.; McDaniel, N. D.; Müller-Bunz, H.; Bernhard, S.; Albrecht, M. *Angew. Chem. Int. Ed.* **2010**, *49*, 9765–9768.

[50] Du, P.; Schneider, J.; Jarosz, P.; Eisenberg, R. *J. Am. Chem. Soc.* **2006**, *128*, 7726–7727.

[51] Kanan, M. W.; Nocera, D. G. *Science* **2008**, *321*, 1072–1075.

[52] Kanan, M. W.; Surendranath, Y.; Nocera, D. G. *Chem. Soc. Rev.* **2009**, *38*, 109–114.

[53] Symes, M. D.; Surendranath, Y.; Lutterman, D. A.; Nocera, D. G. *J. Am. Chem. Soc.* **2011**, *133*, 5174–5177.

[54] Hetterscheid, D. G. H.; Reek, J. N. H. *Angew. Chem. Int. Ed.* **2012**, *51*, 9740–9747.

[55] Zong, R.; Thummel, R. P. *J. Am. Chem. Soc.* **2005**, *127*, 12802–12803.

[56] Concepcion, J. J.; Jurss, J. W.; Templeton, J. L.; Meyer, T. J. *J. Am. Chem. Soc.* **2008**, *130*, 16462–16463.

[57] Concepcion, J. J.; Jurss, J. W.; Norris, M. R.; Chen, Z.; Templeton, J. L.; Meyer, T. J. *Inorg. Chem.* **2010**, *49*, 1277–1279.

[58] Yagi, M.; Tajima, S.; Komi, M.; Yamazaki, H. *Dalton Trans.* **2011**, *40*, 3802–3804.

[59] Maeda, K.; Domen, K. *J. Phys. Chem. C* **2007**, *111*, 7851–7861.

[60] Osterloh, F. E. *Chem. Mater.* **2008**, *20*, 35–54.

[61] Kudo, A.; Miseki, Y. *Chem. Soc. Rev.* **2009**, *38*, 253–278.

[62] Maeda, K.; Higashi, M.; Lu, D.; Abe, R.; Domen, K. *J. Am. Chem. Soc.* **2010**, *132*, 5858–5868.

[63] Iwase, A.; Ng, Y. H.; Ishiguro, Y.; Kudo, A.; Amal, R. *J. Am. Chem. Soc.* **2011**, *133*, 11054–11057.

[64] Kohl, S. W.; Weiner, L.; Schwartsburd, L.; Konstantinovski, L.; Shimon, L. J. W.; Ben-David, Y.; Iron, M. A.; Milstein, D. *Science* **2009**, *324*, 74–77.

[65] Kubas, G. J. *J. Organomet. Chem.* **2009**, *694*, 2648–2653.

[66] Eisenberg, R. *Science* **2009**, *324*, 44–45.

[67] Li, J.; Shiota, Y.; Yoshizawa, K. *J. Am. Chem. Soc.* **2009**, *131*, 13584–13585.

[68] Yang, X.; Hall, M. B. *J. Am. Chem. Soc.* **2010**, *132*, 120–130.

[69] Chen, Y.; Fang, W. H. *J. Phys. Chem. A* **2010**, *114*, 10334–10338.

[70] Brown, G. M.; Chan, S. F.; Creutz, C.; Schwarz, H. A.; Sutin, N. *J. Am. Chem. Soc.* **1979**, *101*, 7638–7640.

[71] Kirch, M.; Lehn, J.-M.; Sauvage, J.-P. *Helv. Chim. Acta* **1979**, *62*, 1345–1384.

[72] Chan, S.-F.; Chou, M.; Creutz, C.; Matsubara, T.; Sutin, N. *J. Am. Chem. Soc.* **1981**, *103*, 369–379.

[73] Cline, E. D.; Adamson, S. E.; Bernhard, S. *Inorg. Chem.* **2008**, *47*, 10378–10388.

[74] Du, P.; Knowles, K.; Eisenberg, R. *J. Am. Chem. Soc.* **2008**, *130*, 12576–12577.

[75] Du, P.; Schneider, J.; Luo, G.; Brennessel, W. W.; Eisenberg, R. *Inorg. Chem.* **2009**, *48*, 4952–4962.

[76] Ozawa, H.; Haga, M.-a.; Sakai, K. *J. Am. Chem. Soc.* **2006**, *128*, 4926–4927.

[77] Fihri, A.; Artero, V.; Razavet, M.; Baffert, C.; Leibl, W.; Fontecave, M. *Angew. Chem. Int. Ed.* **2008**, *47*, 564–567.

[78] Fihri, A.; Artero, V.; Pereira, A.; Fontecave, M. *Dalton Trans.* **2008**, 5567–5569.

[79] White, T. A.; Whitaker, B. N.; Brewer, K. J. *J. Am. Chem. Soc.* **2011**, *133*, 15332–15334.

[80] White, T. A.; Higgins, S. L. H.; Arachchige, S. M.; Brewer, K. J. *Angew. Chem. Int. Ed.* **2011**, *50*, 12209–12213.

[81] Heyduk, A. F.; Nocera, D. G. *Science* **2001**, *293*, 1639–1641.

[82] Cremer, C.; Burger, P. *J. Chem. Soc., Dalton Trans.* **1999**, 1967–1974.

[83] Cremer, C.; Burger, P. *Chem. Eur. J.* **2003**, *9*, 3583–3596.

[84] Cremer, C.; Burger, P. *J. Am. Chem. Soc.* **2003**, *125*, 7664–7677.

[85] Farus, O.; Balashev, K.; Ivanov, M.; Tkacheva, T.; Panova, A. *Russ. J. Gen. Chem.* **2006**, *76*, 311–316.

[86] Balashev, K.; Ivanov, M.; Taraskina, T.; Cherezova, E. *Russ. J. Gen. Chem.* **2006**, *76*, 781–790.

[87] Adams, C. J.; Bartlett, I. M.; Carlton, S.; Connelly, N. G.; Harding, D. J.; Hayward, O. D.; Orpen, A. G.; Patron, E.; Ray, C. D.; Rieger, P. H. *Dalton Trans.* **2007**, *0*, 62–72.

[88] Poli, R. *Chem. Rev.* **1991**, *91*, 509–551.

[89] Poli, R.; Krueger, S. T.; Abugideiri, F.; Haggerty, B. S.; Rheingold, A. L. *Organometallics* **1991**, *10*, 3041–3046.

[90] Abugideiri, F.; Kelland, M. A.; Poli, R.; Rheingold, A. L. *Organometallics* **1992**, *11*, 1303–1311.

[91] Wang, L.-S.; Fettinger, J. C.; Poli, R. *J. Am. Chem. Soc.* **1997**, *119*, 4453–4464.

[92] Fettinger, J. C.; Keogh, D. W.; Poli, R. *J. Am. Chem. Soc.* **1996**, *118*, 3617–3625.

[93] Abugideiri, F.; Gordon, J. C.; Poli, R.; Owens-Waltermire, B. E.; Rheingold, A. L. *Organometallics* **1993**, *12*, 1575–1582.

[94] Abugideiri, F.; Brewer, G. A.; Desai, J. U.; Gordon, J. C.; Poli, R. *Inorg. Chem.* **1994**, *33*, 3745–3751.

[95] Desai, J. U.; Gordon, J. C.; Kraatz, H.-B.; Lee, V. T.; Owens-Waltermire, B. E.; Poli, R.; Rheingold, A. L.; White, C. B. *Inorg. Chem.* **1994**, *33*, 3752–3769.

[96] Fettinger, J. C.; Pleune, B. A.; Poli, R. *J. Am. Chem. Soc.* **1996**, *118*, 4906–4907.

[97] Pleune, B.; Poli, R.; Fettinger, J. C. *Organometallics* **1997**, *16*, 1581–1594.

[98] Blackburn, H.; Kraatz, H.-B.; Poli, R.; Torralba, R. C. *Polyhedron* **1995**, *14*, 2225–2230.

[99] Murray, R. C.; Blum, L.; Liu, A. H.; Schrock, R. R. *Organometallics* **1985**, *4*, 953–954.

[100] Schrock, R. R.; Liu, A. H.; O'Regan, M. B.; Finch, W. C.; Payack, J. F. *Inorg. Chem.* **1988**, *27*, 3574–3583.

[101] Green, M. L. H.; Hubert, J. D.; Mountford, P. *J. Chem. Soc., Dalton Trans.* **1990**, 3793–3800.

[102] Schrock, R. R.; Glassman, T. E.; Vale, M. G.; Kol, M. *J. Am. Chem. Soc.* **1993**, *115*, 1760–1772.

[103] Morise, X.; Green, M. L. H.; McGowan, P. C.; Simpson, S. J. *J. Chem. Soc., Dalton Trans.* **1994**, 871–878.

[104] Pleune, B.; Morales, D.; Meunier-Prest, R.; Richard, P.; Collange, E.; Fettinger, J. C.; Poli, R. *J. Am. Chem. Soc.* **1999**, *121*, 2209–2225.

[105] Liu, A. H.; Murray, R. C.; Dewan, J. C.; Santarsiero, B. D.; Schrock, R. R. *J. Am. Chem. Soc.* **1987**, *109*, 4282–4291.

[106] Bayse, C. A.; Hall, M. B.; Pleune, B.; Poli, R. *Organometallics* **1998**, *17*, 4309–4315.

[107] Kubas, G. J. *Inorg. Chem.* **1983**, *22*, 692–694.

[108] Kubas, G. J.; Kiss, G.; Hoff, C. D. *Organometallics* **1991**, *10*, 2870–2876.

[109] de la Mata, F. J.; Gómez, J.; Royo, P. *J. Organomet. Chem.* **1998**, *564*, 277–281.

[110] Smith, R. A.; Stokes, E. C.; Langdon-Jones, E. E.; Platts, J. A.; Kariuki, B. M.; Hallett, A. J.; Pope, S. J. A. *Dalton Trans.* **2013**, *42*, 10347–10357.

[111] Anfuso, C. L.; Snoeberger, R. C.; Ricks, A. M.; Liu, W.; Xiao, D.; Batista, V. S.; Lian, T. *J. Am. Chem. Soc.* **2011**, *133*, 6922–6925.

[112] Haines, R. J.; Nyholm, R. S.; Stiddard, M. H. B. *J. Chem. Soc. A* **1966**, 1606–1607.

[113] Connelly, N. G.; Geiger, W. E. *Chem. Rev.* **1996**, *96*, 877–910.

[114] Legzdins, P.; Phillips, E. C.; Rettig, S. J.; Trotter, J.; Veltheer, J. E.; Yee, V. C. *Organometallics* **1992**, *11*, 3104–3110.

[115] Ohki, Y.; Matsuura, N.; Marumoto, T.; Kawaguchi, H.; Tatsumi, K. *J. Am.*

Chem. Soc. **2003**, *125*, 7978–7988.

[116] Legzdins, P.; Lumb, S. A. *Organometallics* **1997**, *16*, 1825–1827.

[117] Legzdins, P.; Lumb, S. A.; Young, V. G. *Organometallics* **1998**, *17*, 854–871.

[118] Bendix, J.; Bøgevig, A. *Inorg. Chem.* **1998**, *37*, 5992–6001.

[119] Kober, E. M.; Sullivan, B. P.; Meyer, T. J. *Inorg. Chem.* **1984**, *23*, 2098–2104.

[120] Chen, P.; Meyer, T. J. *Chem. Rev.* **1998**, *98*, 1439–1478.

[121] Hush, N. S.; Reimers, J. R. *Chem. Rev.* **2000**, *100*, 775–786.

[122] Fantacci, S.; Angelis, F. d.; Selloni, A. *J. Am. Chem. Soc.* **2003**, *125*, 4381–4387.

[123] Pourtois, G.; Beljonne, D.; Moucheron, C.; Schumm, S.; Kirsch-De Mesmaeker, A.; Lazzaroni, R.; Brédas, J.-L. *J. Am. Chem. Soc.* **2004**, *126*, 683–692.

[124] Charlot, M.-F.; Pellegrin, Y.; Quaranta, A.; Leibl, W.; Aukauloo, A. *Chem. Eur. J.* **2006**, *12*, 796–812.

[125] Yang, L.; Ren, A.-M.; Feng, J.-K.; Liu, X.-D.; Ma, Y.-G.; Zhang, H.-X. *Inorg. Chem.* **2004**, *43*, 5961–5972.

[126] Nahhas, A. E.; Cannizzo, A.; van Mourik, F.; Blanco-Rodríguez, A. M.; Záliš, S.; Vlček, J. A.; Chergui, M. *J. Phys. Chem. A* **2010**, *114*, 6361–6369.

[127] Nahhas, A. E.; Consani, C.; Blanco-Rodríguez, A. M.; Lancaster, K. M.; Braem, O.; Cannizzo, A.; Towrie, M.; Clark, I. P.; Záliš, S.; Chergui, M.; Vlček, J. A. *Inorg. Chem.* **2011**, *50*, 2932–2943.

[128] Záliš, S.; Consani, C.; Nahhas, A. E.; Cannizzo, A.; Chergui, M.; Hartl, F.; Vlček Jr., A. *Inorg. Chim. Acta* **2011**, *374*, 578–585.

[129] Hay, P. J. *J. Phys. Chem. A* **2002**, *106*, 1634–1641.

[130] Ahlrichs, R.; Bär, M.; Häser, M.; Horn, H.; Kölmel, C. *Chem. Phys. Lett.* **1989**, *162*, 165–169.

[131] Perdew, J. P. *Phys. Rev. B* **1986**, *33*, 8822–8824.

[132] Becke, A. D. *Phys. Rev. A* **1988**, *38*, 3098–3100.

[133] Davis, W. B.; Svec, W. A.; Ratner, M. A.; Wasielewski, M. R. *Nature* **1998**, *396*, 60–63.

[134] Davis, W. B.; Ratner, M. A.; Wasielewski, M. R. *J. Am. Chem. Soc.* **2001**, *123*, 7877–7886.

[135] Ricks, A. B.; Brown, K. E.; Wenninger, M.; Karlen, S. D.; Berlin, Y. A.; Co, D. T.; Wasielewski, M. R. *J. Am. Chem. Soc.* **2012**, *134*, 4581–4588.

[136] Gosser, D. K. *Cyclic Voltammetry: Simulation and Analysis of Reaction Mechanisms*; VCH Publishers, Inc.. New York, **1993**.

[137] Robin, M. B.; Day, P. *Adv. Inorg. Chem. Radiochem.* **1967**, *10*, 247–422.

[138] Tan, G.; Chen, S.; Sun, N.; Li, Y.; Fortin, D.; Wong, W.-Y.; Kwok, H.-S.; Ma, D.; Wu, H.; Wang, L.; Harvey, P. D. *J. Mater. Chem. C* **2013**, *1*, 808–821.

[139] Zanello, P. *Inorganic Electrochemistry: Theory, Practice and Application*; The Royal Society of Chemistry. Cambridge, UK, **2003**.

[140] Bélanger, G.; Sauvageau, P.; Sandorfy, C. *Chem. Phys. Lett.* **1969**, *3*, 649–651.

[141] Reichardt, C. *Solvents and Solvent Effects in Organic Chemistry*; WILEY-VCH Verlag GmbH & Co. KGaA. Weinheim, **1993**.

[142] Rehm, D.; Weller, A. *Isr. J. Chem.* **1970**, *8*, 259– 271.

[143] Vlcek, A. A.; Dodsworth, E. S.; Pietro, W. J.; Lever, A. B. P. *Inorg. Chem.* **1995**, *34*, 1906–1913.

[144] Che, G.; Li, W.; Kong, Z.; Su, Z.; Chu, B.; Li, B.; Zhang, Z.; Hu, Z.; Chi, H. *Synth. Commun.* **2006**, *36*, 2519–2524.

[145] Delgadillo, A.; Romo, P.; Leiva, A. M.; Loeb, B. *Helv. Chim. Acta* **2003**, *86*, 2110–2120.

[146] Schwalbe, M.; Schäfer, B.; Görls, H.; Rau, S.; Tschierlei, S.; Schmitt, M.; Popp, J.; Vaughan, G.; Henry, W.; Vos, J. G. *Eur. J. Inorg. Chem.* **2008**, *2008*, 3310–3319.

[147] Wiederholt, K.; Mclaughlin, L. W. *Nucleic Acids Res.* **1999**, *27*, 2487–2493.

[148] Bruker *SADABS*; Bruker AXS Inc., Madison.Wisconsin, USA, **2008**.

[149] Sheldrick, G. M. *Acta Crystallogr., Sect. A: Found. of Crystallogr.* **2008**, *64*, 112–122.

I. Appendix

I.I. Synthetic compounds directory

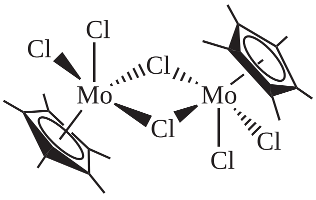

1-1

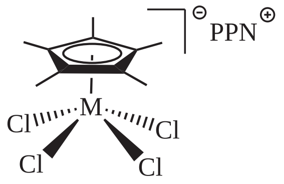

1-1, M = W
1-2, M = Mo

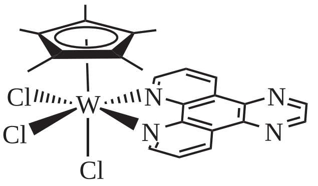

2-a

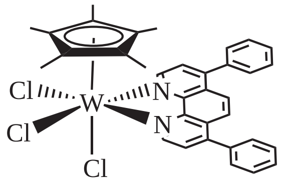

2-b

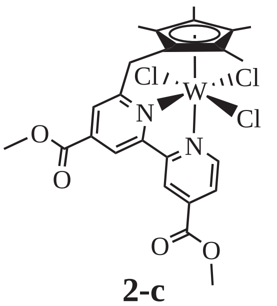

2-c

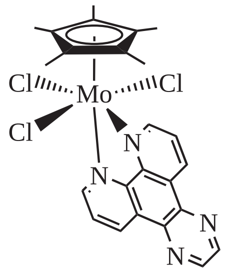

3-a

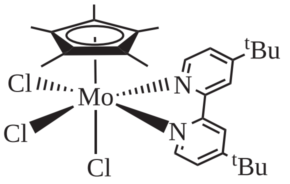

3-d

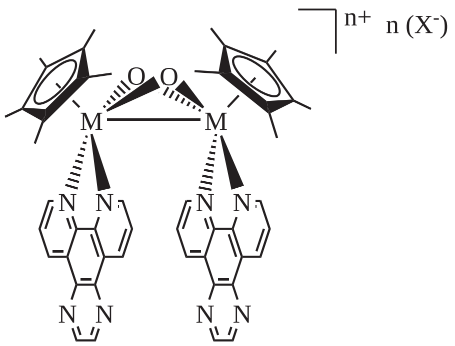

4-a, M = W, n =2, X = PF_6
4-a1, M = W, n = 2, X = $Al(pftb)_4$, PF_6
4-a2, M = W, n = 2, X = $Al(pftb)_4$
6-a, M = W, n = 0
7-a, M = W, n = 1, X = $Al(pftb)_4$
7-a1, M = W, n = 1, X = PF_6
8-a, M = Mo, n =2, X = PF_6

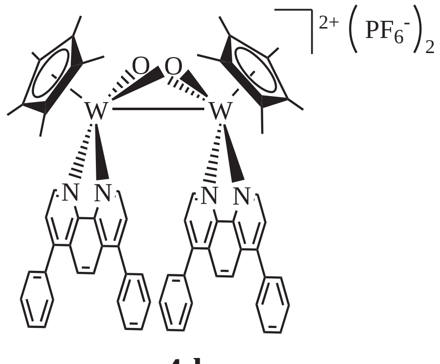

4-b

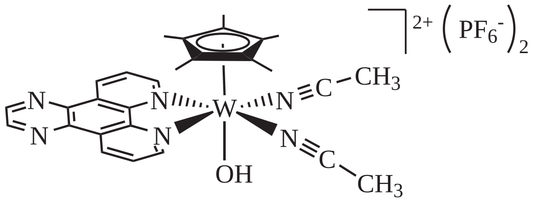

5-a

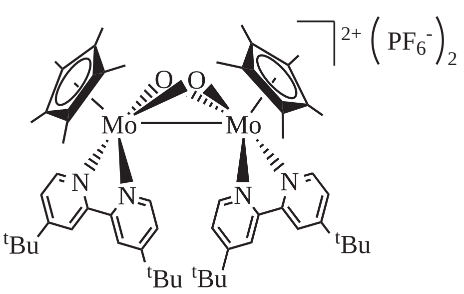

8-d

I.II. X-ray structural data

The measurement of single crystals was carried out on a Bruker APEX single crystal diffractometer with graphite monochromated Mo-K_α-rays (λ = 0.71073 Å) at low temperatures. Suitable crystals were grown in a highly viscous polybutylene oil mounted on a glass fiber on the goniometer head. The empirical absorption correction was carried out with the program SADABS[148] or numerically for indexed faces. The program SHELXS-97[149] was used for the solution of the structure (direct method). The refinement was performed with the program SHELXL-97 and the program package WinGX v1.70.01 considering all independent reflections. If not otherwise specified below, all non-hydrogen atoms were refined anisotropically. If not specified, the hydrogen atoms were refined isotropically using a riding model.

I.II.I. Cp*W(dpphen)Cl_3 (2-b)

The asymmetric unit of the structure of the complex [Cp*W(dpphen)Cl_3] contains a cocrystallized dichloromethane molecule, the non-hydrogen atoms were refined anisotropically.

Identification code	**2-b** Cp*W(dpphen)Cl_3×DCM
Empirical formula	$C_{35}H_{33}Cl_5N_2W$
Formula weight [g/mol]	842.73
Color of crystal	green
Crystal system, Space group	monoclinic, Cc
a [Å]	9.0763(3)
b [Å]	24.3755(8)
c [Å]	14.5457(5)
α [°]	
β [°]	94.2400(10)
γ [°]	
Volume [Å^3]	3209.27(19)
Z	4
Density (calculated) [g/cm^3]	1.744
Absorption coefficient [mm^{-1}]	4.045
Crystal size [mm^3]	0.50×0.31×0.03
Θ range for data collection [°]	2.18 - 32.50
Index ranges	$-13 \leftarrow h \leftarrow 13$ $-36 \leftarrow k \leftarrow 36$ $-21 \leftarrow l \leftarrow 21$
Reflections collected	40930
Independent reflections	11289 [R(int) = 0.0318]
Completeness to theta = 30.00° [%]	99.9
Absorption correction	semi-empirical
Data / restraints / parameters	11289 / 2 / 393
Goodness-of-fit on F^2	1.022
Final R indices ($F^2>2\sigma F^2$)	$R_1 = 0.0254$, $wR_2 = 0.0609$
R indices (all data)	$R_1 = 0.0268$, $wR_2 = 0.0614$
Largest diff. peak and hole [e$^-$Å^3]	3.260, -2.778

I.II.II. Cp*W(bpy−COOMe)Cl$_3$ (2-c)

The ester group of the complex [Cp*W(bpy−COOMe)Cl$_3$] is rotationally disordered and was splitted into two positions. The non-hydrogen atoms were refined anisotropically.

Identification code	**2-c** Cp*W(bpy−COOMe)Cl$_3$
Empirical formula	$C_{24}H_{25}Cl_3N_2O_4W$
Formula weight [g/mol]	695.66
Color of crystal	brown
Crystal system, Space group	monoclinic, P2$_1$/c
a [Å]	12.2887(2)
b [Å]	12.0503(2)
c [Å]	15.9903(3)
α [°]	
β [°]	98.4880(10)
γ [°]	
Volume [Å^3]	2341.95(7)
Z	4
Density (calculated) [g/cm^3]	1.973
Absorption coefficient [mm^{-1}]	5.311
Crystal size [mm^3]	0.35×0.26×0.04
Θ range for data collection [°]	2.12 - 30.00
Index ranges	-17 ← h ← 17 -16 ← k ← 16 -22 ← l ← 22
Reflections collected	55290
Independent reflections	6793 [R(int) = 0.0217]
Completeness to theta = 30.00° [%]	99.4
Absorption correction	semi-empirical
Data / restraints / parameters	6793 / 3 / 324
Goodness-of-fit on F^2	1.074
Final R indices ($F^2>2\sigma F^2$)	R_1 = 0.0143, wR_2 = 0.0356
R indices (all data)	R_1 = 0.0151, wR_2 = 0.0359
Largest diff. peak and hole [e$^-$Å^3]	0.955, -0.505

I.II.III. $[(Cp^{*}W(dpq)(\mu{-}O))_2][PF_6]_2$ (4-a)

The non-hydrogen atoms were refined anisotropically.

Identification code	**4-a** $[(Cp^{*}W(dpq)(\mu{-}O))_2][PF_6]_2$
Empirical formula	$C_{48}H_{46}F_{12}N_8O_2P_2W_2$
Formula weight [g/mol]	1424.57
Color of crystal	purple
Crystal system, Space group	monoclinic, C2/c
a [Å]	12.8777(2)
b [Å]	21.8770(4)
c [Å]	16.9369(3)
α [°]	
β [°]	95.8210(10)
γ [°]	
Volume [$Å^3$]	4746.95(14)
Z	4
Density (calculated) [g/cm^3]	1.993
Absorption coefficient [mm^{-1}]	5.009
Crystal size [mm^3]	0.22×0.12×0.03
Θ range for data collection [°]	1.84 - 30.00
Index ranges	$-18 \leftarrow h \leftarrow 18$ $-30 \leftarrow k \leftarrow 30$ $-23 \leftarrow l \leftarrow 23$
Reflections collected	55950
Independent reflections	6918 [R(int) = 0.0321]
Completeness to theta = 30.00° [%]	99.9
Absorption correction	numerical
Data / restraints / parameters	6918 / 0 / 339
Goodness-of-fit on F^2	1.043
Final R indices ($F^2>2\sigma F^2$)	R_1 = 0.0192, wR_2 = 0.0401
R indices (all data)	R_1 = 0.0263, wR_2 = 0.0425
Largest diff. peak and hole [$e^{-}Å^3$]	1.232, -0.546

Identification code	**4-a1** $[(Cp^*W(dpq)(\mu{-}O))_2][PF_6][Al(pftb)_4]$ $\times$DCM$\times Et_2O$
Empirical formula	$C_{69}H_{56}AlCl_2F_{42}N_8O_7PW_2$
Formula weight [g/mol]	2405.78
Color of crystal	purple
Temperature [K]	100(2)
Crystal system, Space group	monoclinic, $P2_1/c$
a [Å]	16.2552(4)
b [Å]	23.4608(5)
c [Å]	21.9032(5)
α [°]	
β [°]	97.4780(10)
γ [°]	
Volume [$Å^3$]	8282.0(3)
Z	4
Density (calculated) [g/cm^3]	1.929
Absorption coefficient [mm^{-1}]	3.022
F(000)	4688
Crystal size [mm^3]	0.22×0.22×0.14
Θ range for data collection [°]	1.88 - 32.50
Index ranges	$-24 \leftarrow h \leftarrow 24$ $-35 \leftarrow k \leftarrow 35$ $-33 \leftarrow l \leftarrow 33$
Reflections collected	212314
Independent reflections	29720 [R(int) = 0.0482]
Completeness to theta = 30.00° [%]	99.1
Absorption correction	numerical
Max. and min. transmission	0.6770, 0.5561
Data / restraints / parameters	29720 / 0 / 1201
Goodness-of-fit on F^2	1.083
Final R indices ($F^2 > 2\sigma F^2$)	$R_1 = 0.0438$, $wR_2 = 0.0978$
R indices (all data)	$R_1 = 0.0268$, $wR_2 = 0.1228$
Largest diff. peak and hole [$e^- Å^3$]	2.426, -2.239

I.II.IV. $[(Cp^*W(dpq)(NCCH_3)_2(OH)][PF_6]_2$ (5-a)

The asymmetric unit of the structure of the complex $[(Cp^*W(dpq)(NCCH_3)_2(OH)][PF_6]_2$ contains several cocrystallized acetonitrile molecules. The $[PF_6]^-$ anions were split into two positions and the non-hydrogen atoms were refined anisotropically.

Identification code	**5-a** $[(Cp^*W(dpq)(NCCH_3)_2(OH)][PF_6]_2$
Empirical formula	$C_{28}H_{30}F_{12}N_6OP_2W$
Formula weight [g/mol]	940.35
Color of crystal	brown
Crystal system, Space group	triclinic, P-1
a [Å]	9.3680(6)
b [Å]	14.7525(4)
c [Å]	15.3540(6)
α [°]	80.545(3)
β [°]	77.360(4)
γ [°]	73.724(4)
Volume [Å^3]	1975.50(16)
Z	2
Density (calculated) [g/cm^3]	1.671
Absorption coefficient [mm^{-1}]	3.097
Crystal size [mm^3]	0.4×0.25×0.2
Θ range for data collection [°]	2.89 - 34.36
Index ranges	$-14 \leftarrow h \leftarrow 14$ $-22 \leftarrow k \leftarrow 23$ $-23 \leftarrow l \leftarrow 23$
Reflections collected	43219
Independent reflections	15492 [R(int) = 0.0425]
Completeness to theta = 34.36° [%]	93.6
Absorption correction	numerical
Data / restraints / parameters	15492 / 122 / 634
Goodness-of-fit on F^2	0.779
Final R indices ($F^2 > 2\sigma F^2$)	$R_1 = 0.0592$, $wR_2 = 0.1598$
R indices (all data)	$R_1 = 0.0834$, $wR_2 = 0.2052$
Largest diff. peak and hole [e$^-$Å^3]	5.228, -2.522

I.II.V. $[(\mathrm{Cp}^{*}\mathrm{W}(\mathrm{dpq})(\mu{-}\mathrm{O}))_2]$ (6-a)

The asymmetric unit of the structure of the complex $[(\mathrm{Cp}^{*}\mathrm{W}(\mathrm{dpq})(\mu{-}\mathrm{O}))_2]$ contains a cocrystallized THF molecule, the non-hydrogen atoms were refined anisotropically.

Identification code	**6-a** $[(\mathrm{Cp}^{*}\mathrm{W}(\mathrm{dpq})(\mu{-}\mathrm{O}))_2]\times\mathrm{THF}$
Empirical formula	$C_{52}H_{54}N_8O_3W_2$
Formula weight [g/mol]	1206.73
Color of crystal	purple
Crystal system, Space group	monoclinic, Pn
a [Å]	11.6116(2)
b [Å]	10.8992(2)
c [Å]	18.0299(3)
α [°]	
β [°]	106.18
γ [°]	
Volume [$Å^3$]	2191.42(7)
Z	2
Density (calculated) [g/cm^3]	1.829
Absorption coefficient [mm^{-1}]	5.301
Crystal size [mm^3]	0.20×0.05×0.05
Θ range for data collection [°]	1.87 - 32.50
Index ranges	$-17 \leftarrow h \leftarrow 17$ $-16 \leftarrow k \leftarrow 16$ $-27 \leftarrow l \leftarrow 26$
Reflections collected	56159
Independent reflections	15207 [R(int) = 0.0256]
Completeness to theta = 30.00° [%]	98.8
Absorption correction	semi-empirical
Data / restraints / parameters	15207 / 2 / 596
Goodness-of-fit on F^2	0.938
Final R indices ($F^2>2\sigma F^2$)	$R_1 = 0.0168$, $wR_2 = 0.0310$
R indices (all data)	$R_1 = 0.0179$, $wR_2 = 0.0314$
Largest diff. peak and hole [$e^{-}Å^3$]	0.950, -0.368

I.II.VI. $[(Cp^{*}W(dpq)(\mu{-}O))_2][PF_6]$ (7-a1)

The asymmetric unit of the structure of the complex $[(Cp^{*}W(dpq)(\mu{-}O))_2][PF_6]$ contains a cocrystallized ACN molecule, the non-hydrogen atoms were refined anisotropically. The PF_6^- anion was disordered and was not split.

Identification code	**7-a1** $[(Cp^{*}W(dpq)(\mu{-}O))_2][PF_6]$ ×ACN
Empirical formula	$C_{50}H_{49}F_6N_9O_2PW_2$
Formula weight [g/mol]	1320.65
Color of crystal	purple
Crystal system, Space group	monoclinic, $P2_1/c$
a [Å]	14.2834(3)
b [Å]	17.7629(4)
c [Å]	18.7069(4)
α [°]	
β [°]	101.2180(10)
γ [°]	
Volume [Å^3]	4655.33(17)
Z	4
Density (calculated) [g/cm^3]	1.884
Absorption coefficient [mm^{-1}]	5.049
Crystal size [mm^3]	0.50×0.14×0.12
Θ range for data collection [°]	1.85 - 27.50
Index ranges	$-20 \leftarrow h \leftarrow 18$ $-24 \leftarrow k \leftarrow 24$ $-26 \leftarrow l \leftarrow 22$
Reflections collected	75402
Independent reflections	13400 [R(int) = 0.0237]
Completeness to theta = 30.00° [%]	98.7
Absorption correction	semi-empirical
Refinement method	full-matrix least-squares on F^2
Data / restraints / parameters	13400 / 0 / 636
Goodness-of-fit on F^2	1.150
Final R indices ($F^2>2\sigma F^2$)	R_1 = 0.0294, wR_2 = 0.0722
R indices (all data)	R_1 = 0.0313, wR_2 = 0.0729
Largest diff. peak and hole [e$^-$Å^3]	3.207, -1.209

I.II.VII. $[(Cp^{*}W(dpphen)(\mu{-}O))_2][PF_6]_2$ (4-b)

The asymmetric unit of the structure of the complex $[(Cp^{*}W(dpphen)(\mu{-}O))_2][PF_6]_2$ contains cocrystallized dichloromethane and diethyl ether molecules, which were refined as 0.33 DCM, 0.45 and 0.22 of two independent Et_2O. The non-hydrogen atoms were refined anisotropically.

Identification code	**4-b** $[(Cp^{*}W(dpphen)(\mu{-}O))_2][PF_6]_2$ $\times 0.33DCM \times 0.45Et_2O \times 0.22Et_2O$
Empirical formula	$C_{71.01}H_{69.36}Cl_{0.66}F_{12}N_4O_{2.67}P_2W_2$
Formula weight [g/mol]	1702.62
Color of crystal	blue
Crystal system, Space group	monoclinic, $P2_1/c$
a [Å]	11.1558(3)
b [Å]	24.6290(7)
c [Å]	23.8428(7)
α [°]	
β [°]	99.0250(10)
γ [°]	
Volume [Å^3]	6469.9(3)
Z	4
Density (calculated) [g/cm^3]	1.748
Absorption coefficient [mm^{-1}]	3.717
Crystal size [mm^3]	0.43×0.24×0.10
Θ range for data collection [°]	1.87 - 32.50
Index ranges	$-16 \leftarrow h \leftarrow 16$ $-37 \leftarrow k \leftarrow 37$ $-36 \leftarrow l \leftarrow 36$
Reflections collected	168508
Independent reflections	23377 [R(int) = 0.0301]
Completeness to theta = 30.00° [%]	99.9
Absorption correction	semi-empirical
Data / restraints / parameters	23377 / 10 / 942
Goodness-of-fit on F^2	1.096
Final R indices ($F^2 > 2\sigma F^2$)	$R_1 = 0.0253$, $wR_2 = 0.0497$
R indices (all data)	$R_1 = 0.0351$, $wR_2 = 0.0537$
Largest diff. peak and hole [e^{-}Å^3]	1.588, -1.068

I.II.VIII. $[(Cp^*Mo(dpq)(\mu{-}O))_2][PF_6]_2$ (8-a)

The asymmetric unit of the structure of the complex $[(Cp^*Mo(dpq)(\mu{-}O))_2][PF_6]_2$ contains no solvent molecule, the non-hydrogen atoms were refined anisotropically.

Identification code	**8-a** $[(Cp^*Mo(dpq)(\mu{-}O))_2][PF_6]_2$
Empirical formula	$C_{48}H_{46}F_{12}Mo_2N_8O_2P_2$
Formula weight [g/mol]	1248.75
Color of crystal	red
Crystal system, Space group	monoclinic, C2/c
a [Å]	12.8912(7)
b [Å]	21.9565(12)
c [Å]	16.9736(9)
α [°]	
β [°]	95.448(2)
γ [°]	
Volume [$Å^3$]	4782.6(4)
Z	4
Density (calculated) [g/cm^3]	1.734
Absorption coefficient [mm^{-1}]	0.689
Crystal size [mm^3]	$0.296 \times 0.122 \times 0.089$
Θ range for data collection [°]	1.84 - 30.00
Index ranges	$-17 \leftarrow h \leftarrow 17$ $-30 \leftarrow k \leftarrow 30$ $-23 \leftarrow l \leftarrow 23$
Reflections collected	38498
Independent reflections	6845 [R(int) = 0.0411]
Completeness to theta = 30.00° [%]	98.1
Absorption correction	numerical
Refinement method	full-matrix least-squares on F^2
Data / restraints / parameters	6845 / 0 / 339
Goodness-of-fit on F^2	1.048
Final R indices ($F^2 > 2\sigma F^2$)	$R_1 = 0.0532$, $wR_2 = 0.1351$
R indices (all data)	$R_1 = 0.0634$, $wR_2 = 0.1422$
Largest diff. peak and hole [$e^-Å^3$]	2.779, -0.949

I.II.IX. $[(Cp^{*}Mo({}^{t}bu_2bpy)(\mu{-}O))_2][PF_6]_2$ (8-d)

The asymmetric unit of the structure of the complex $[(Cp^{*}Mo({}^{t}bu_2bpy)(\mu{-}O))_2][PF_6]_2$ contains two independent halves of cocrystallized DCM molecule, the non-hydrogen atoms were refined anisotropically.

Identification code	**8-d** $[(Cp^{*}Mo({}^{t}bu_2bpy)(\mu{-}O))_2][PF_6]_2$ ×DCM
Empirical formula	$C_{57}H_{71}Cl_2F_{12}Mo_2N_4O_2P_2$
Formula weight [g/mol]	1396.90
Color of crystal	red
Crystal system, Space group	monoclinic, $P2_1/n$
a [Å]	13.19540(10)
b [Å]	12.82850(10)
c [Å]	37.1844(4)
α [°]	
β [°]	94.1450(10)
γ [°]	
Volume [Å^3]	6278.01(10)
Z	4
Density (calculated) [g/cm^3]	1.478
Absorption coefficient [mm^{-1}]	0.614
Crystal size [mm^3]	0.40×0.09×0.06
Θ range for data collection [°]	3.04 - 28.94
Index ranges	$-17 \leftarrow h \leftarrow 16$ $-17 \leftarrow k \leftarrow 17$ $-48 \leftarrow l \leftarrow 50$
Reflections collected	80780
Independent reflections	15405 [R(int) = 0.0340]
Completeness to theta = 30.00° [%]	92.9
Absorption correction	numerical
Refinement method	full-matrix least-squares on F^2
Data / restraints / parameters	15405 / 6 / 776
Goodness-of-fit on F^2	1.074
Final R indices ($F^2 > 2\sigma F^2$)	$R_1 = 0.0314$, $wR_2 = 0.0745$
R indices (all data)	$R_1 = 0.0387$, $wR_2 = 0.0780$
Largest diff. peak and hole [e$^-$Å^3]	0.833, -0.517

I.III. NMR spectroscopic data

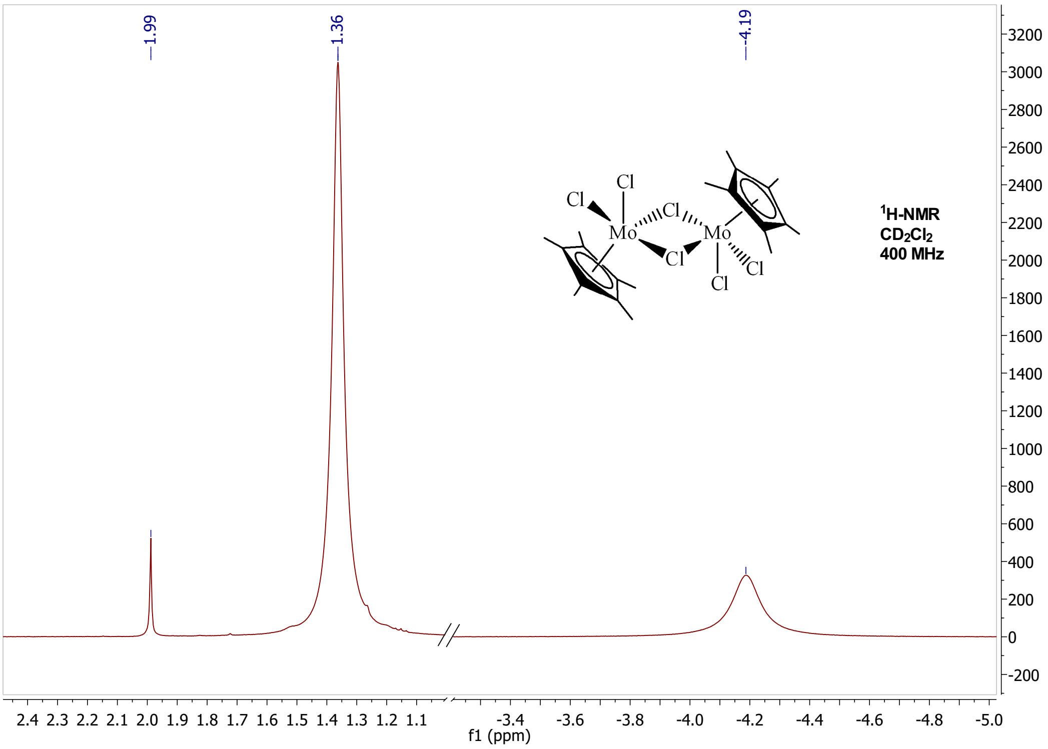

Figure III.I.: ^{1}H-NMR Spectrum of complex [Cp*MoCl$_3$]$_2$ (**1-1**) in CD$_2$Cl$_2$.

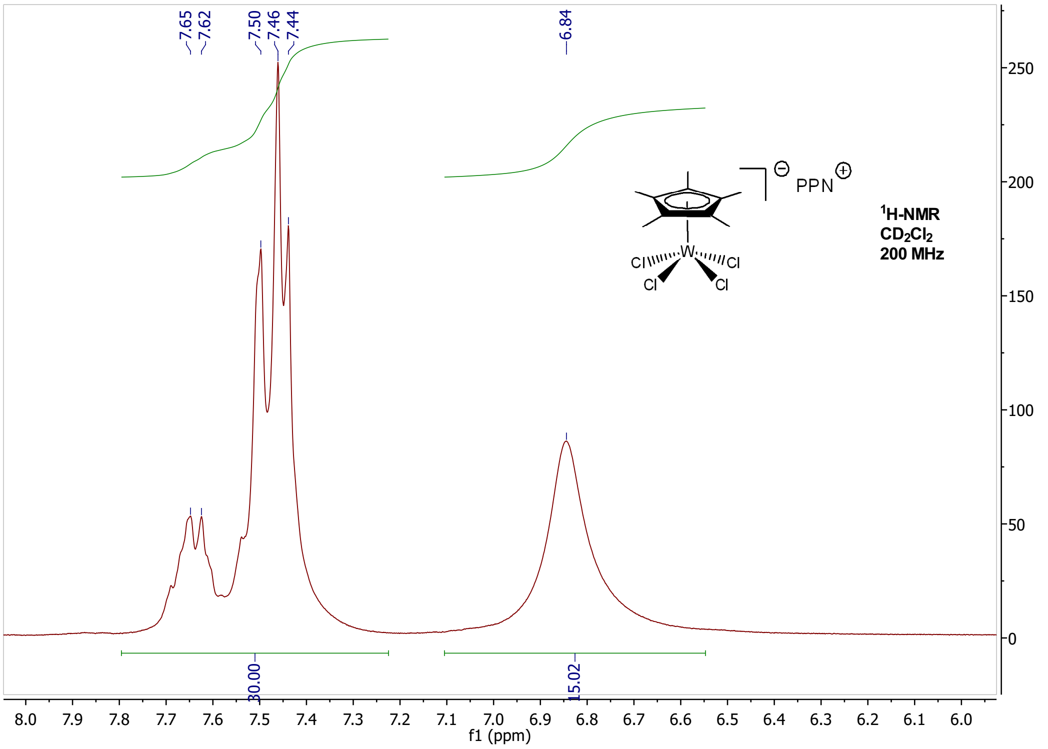

Figure III.II.: ^{1}H-NMR Spectrum of complex PPN[Cp*WCl$_4$] (**1-2**) in CD$_2$Cl$_2$.

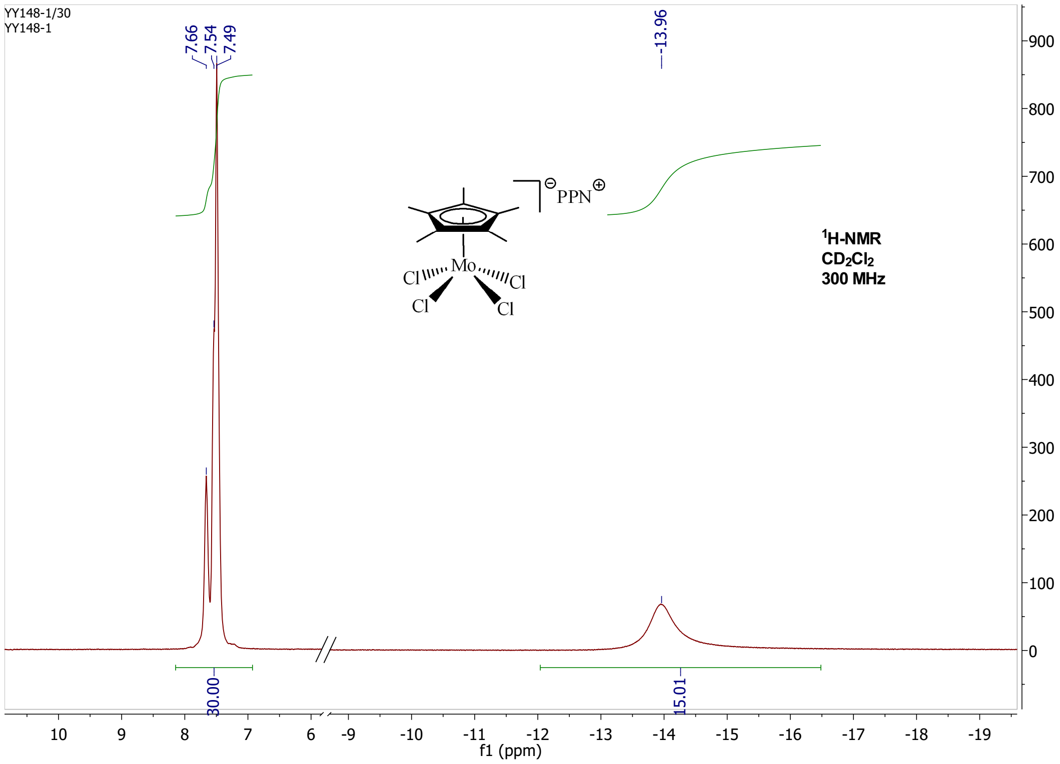

Figure III.III.: ^{1}H-NMR Spectrum of complex PPN[Cp*MoCl$_4$] (**1-3**) in CD$_2$Cl$_2$.

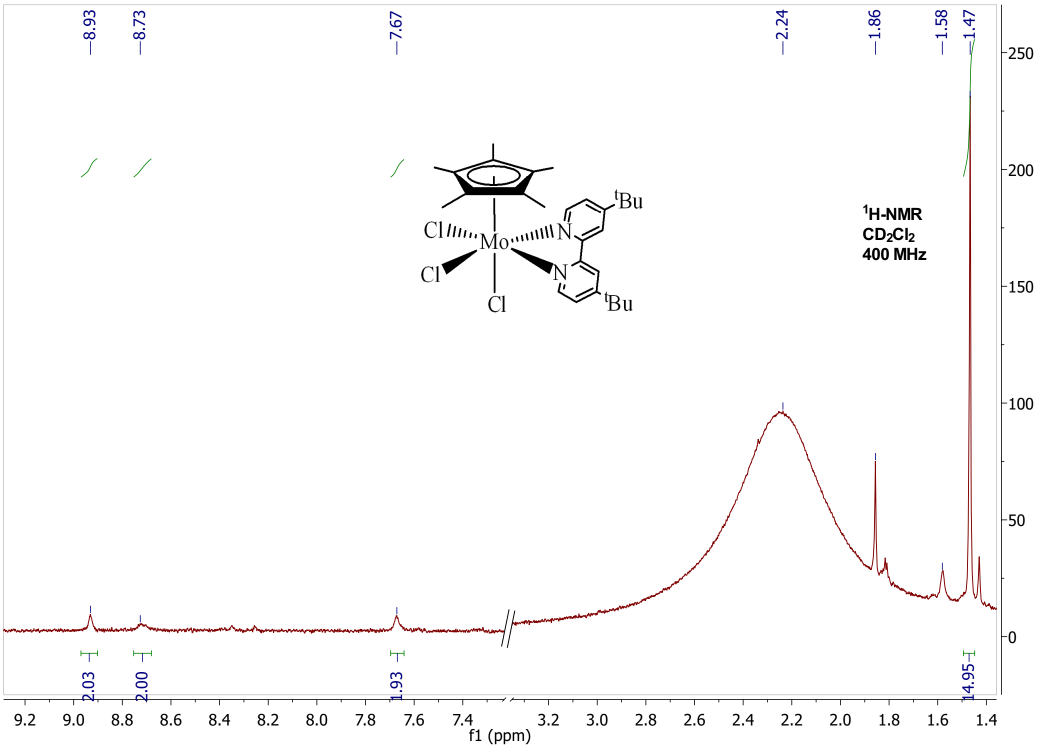

Figure III.IV.: ^{1}H-NMR Spectrum of complex [Cp*Mo(^{t}Bu$_2$bpy)Cl$_3$] (**3-d**) in CD$_2$Cl$_2$.

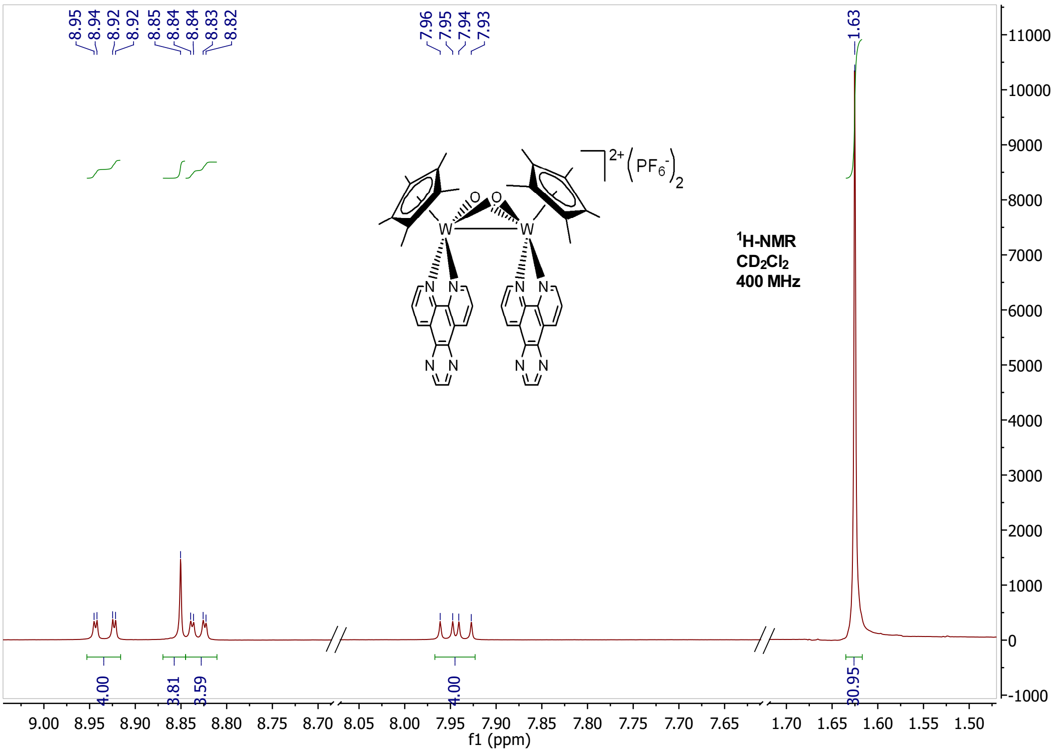

Figure III.V.: ^{1}H-NMR Spectrum of complex $[(Cp^*W(dpq)(\mu{-}O))_2][PF_6]_2$ (**4-a**) in CD_2Cl_2.

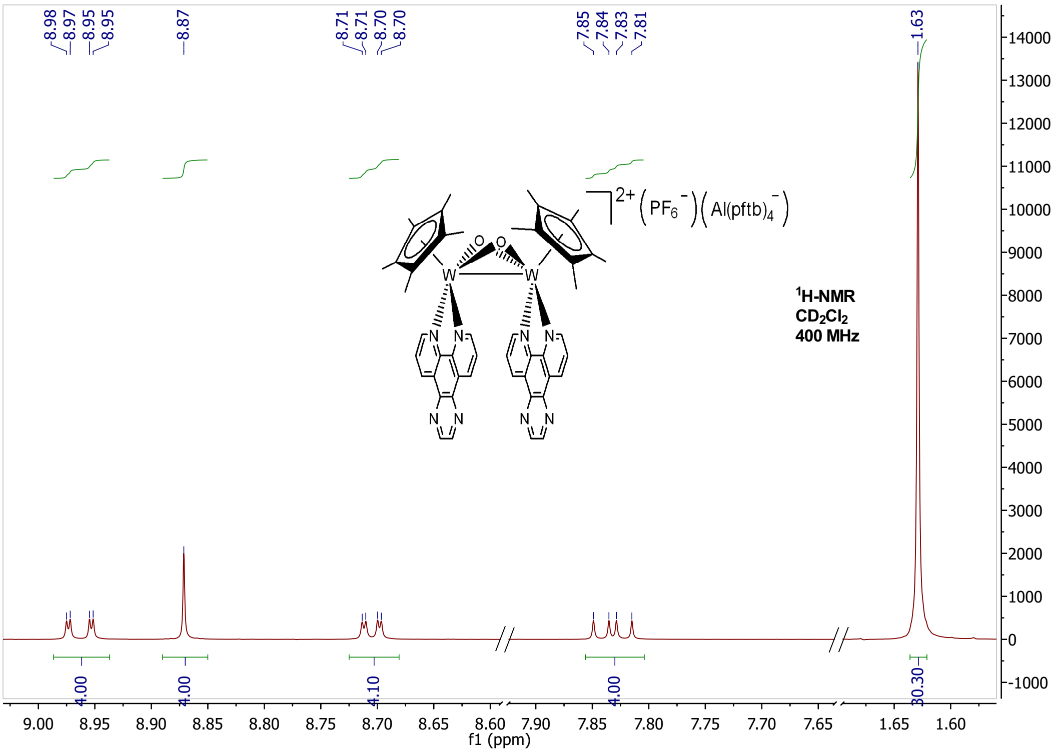

Figure III.VI.: ^{1}H-NMR Spectrum of complex $[(Cp^*W(dpq)(\mu{-}O))_2][PF_6][Al(pftb)_4]$ (**4-a1**) in CD_2Cl_2.

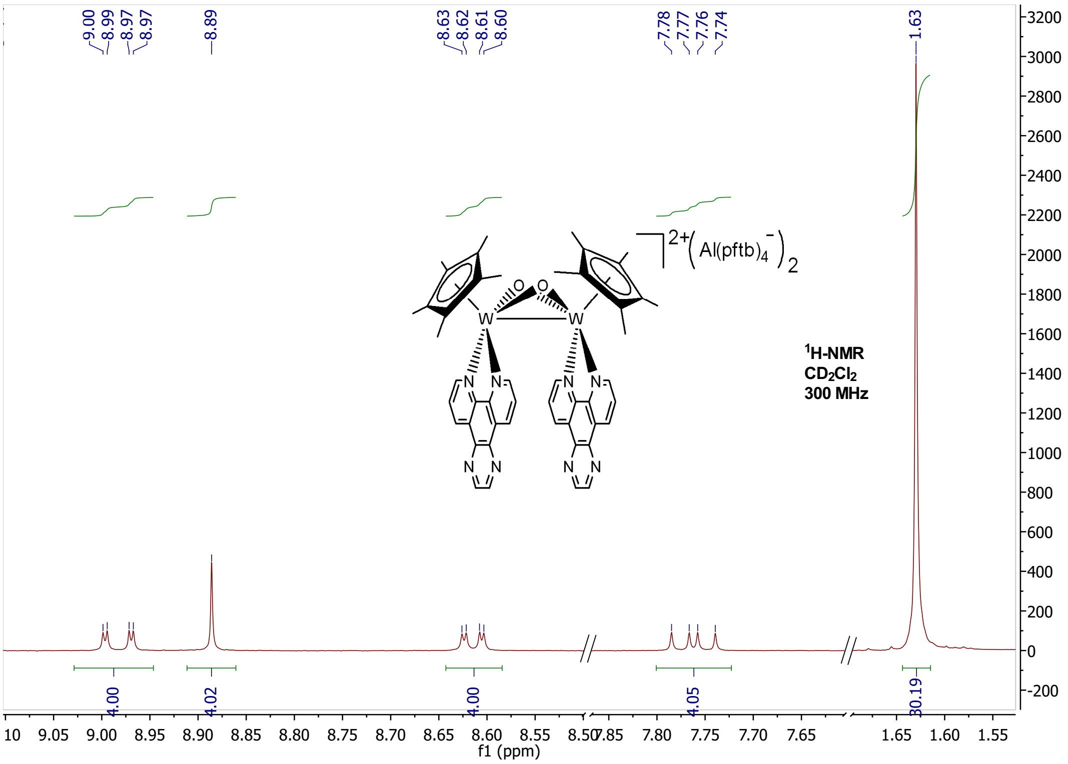

Figure III.VII.: ^{1}H-NMR Spectrum of complex $[(Cp^*W(dpq)(\mu{-}O))_2][Al(pftb)_4]_2$ (**4-a2**) in CD_2Cl_2.

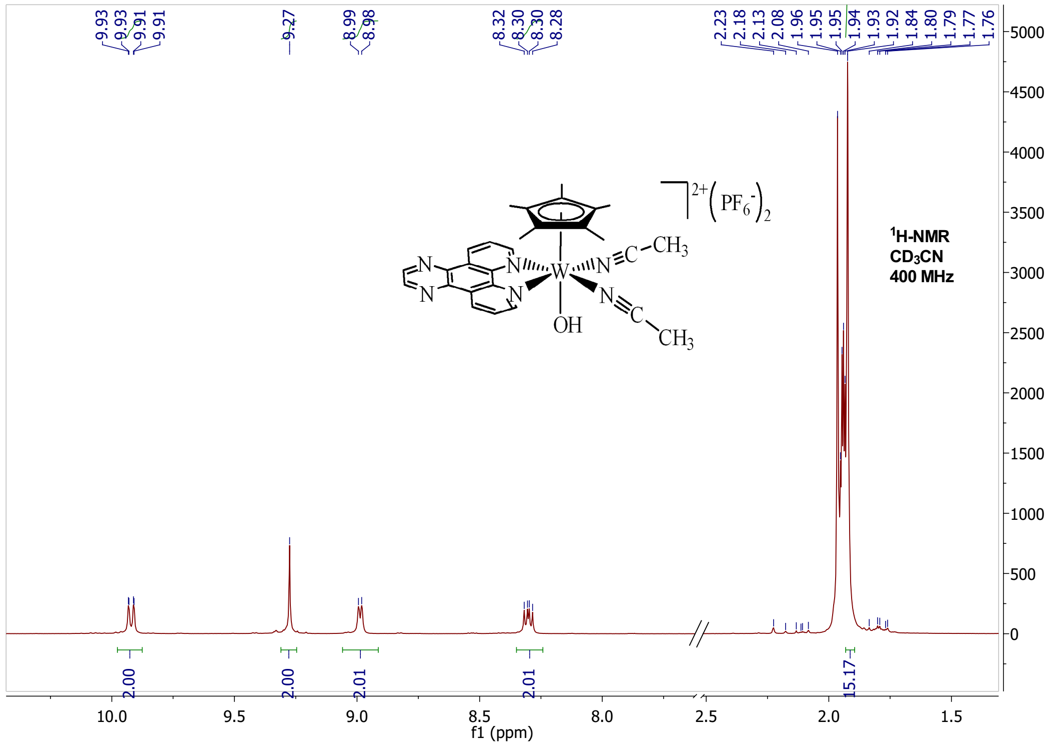

Figure III.VIII.: ^{1}H-NMR Spectrum of complex $[Cp^*W(dpq)(NCCH_3)_2(OH)][PF_6]_2$ (**5-a**) in CD_3CN.

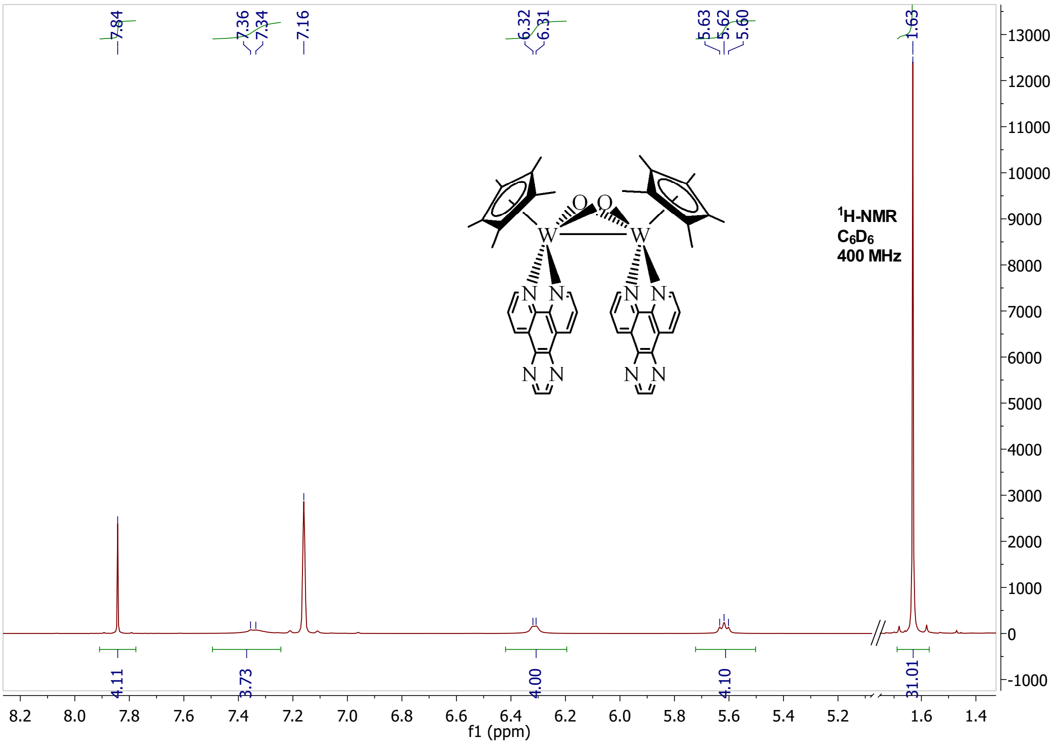

Figure III.IX.: ^{1}H-NMR Spectrum of complex [(Cp*W(dpq)(μ−O))$_2$] (**6-a**) in C_6D_6.

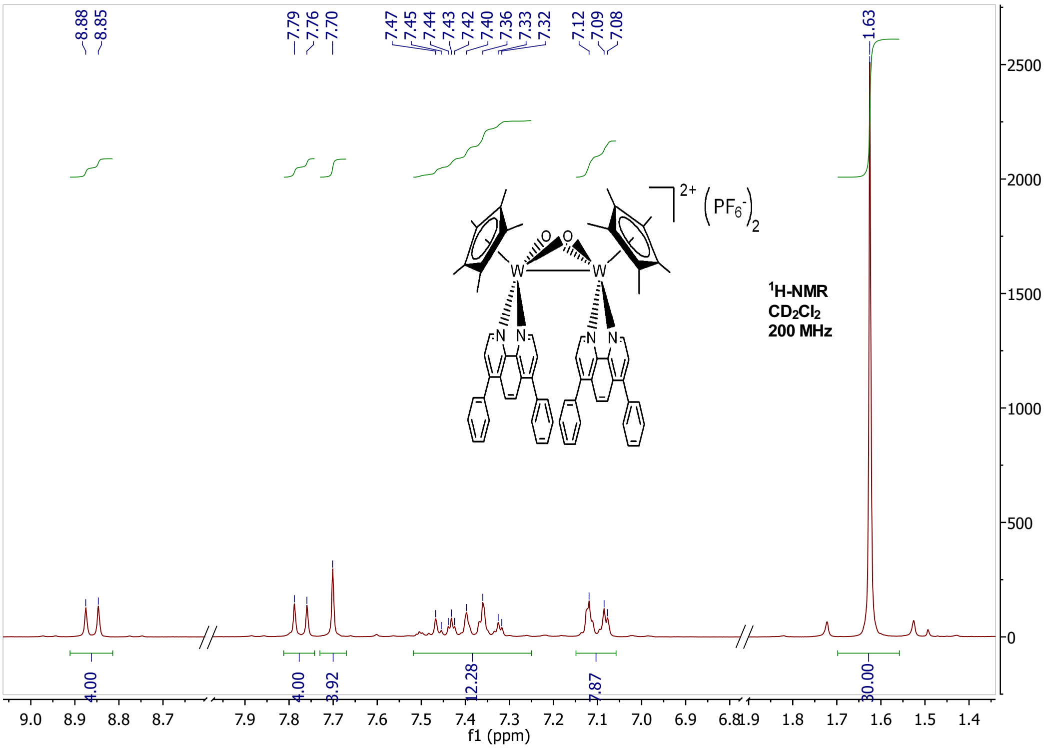

Figure III.X.: ^{1}H-NMR Spectrum of complex [(Cp*W(dpphen)(μ−O))$_2$][PF$_6$]$_2$ (**4-b**) in CD_2Cl_2.

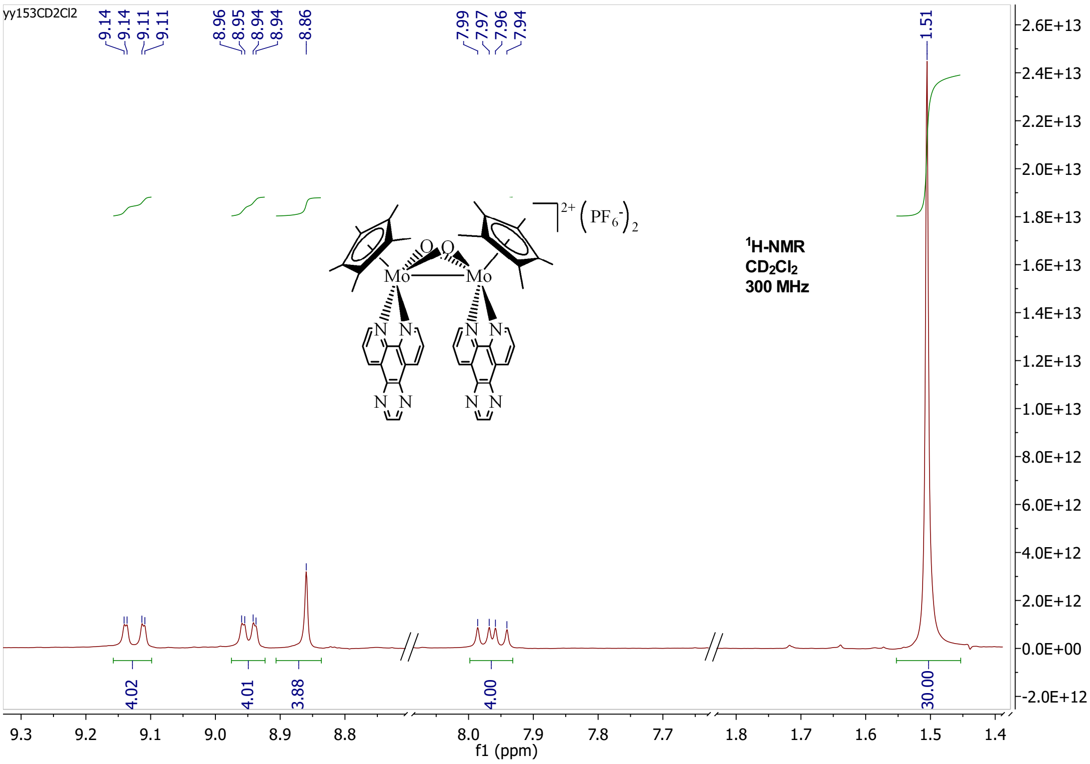

Figure III.XI.: ^{1}H-NMR Spectrum of complex $[(Cp^*Mo(dpq)(\mu{-}O))_2][PF_6]_2$ (**8-a**) in CD_2Cl_2.

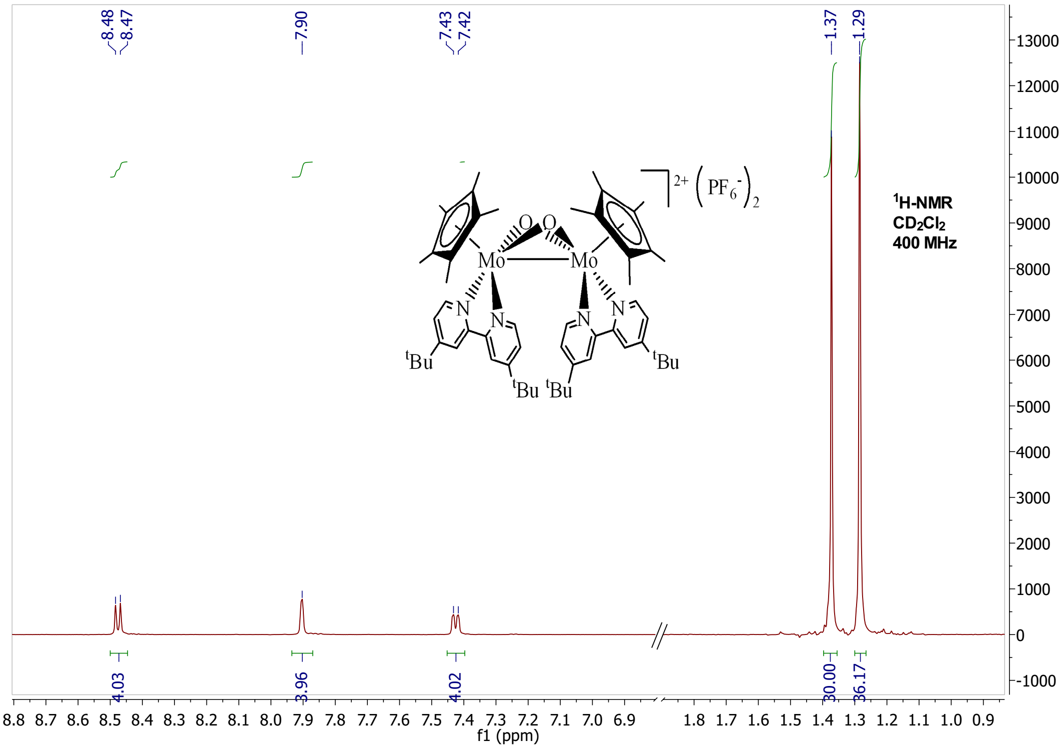

Figure III.XII.: ^{1}H-NMR Spectrum of complex $[(Cp^*Mo(tBu_2bpy)(\mu{-}O))_2][PF_6]_2$ (**8-d**) in CD_2Cl_2.

I.IV. Chemicals categorized according to GHS

Substance	**GHS symbols**	**Hazard statements**	**Precautionary statements**
Acetonitrile		H225, H302 + H312 + H332, H319	P210, P280, P305 + P351 + P338
Ammonium hexafluorophosphate		H314	P280, P305 + P351 + P338, P310
Benzene		H225, H304, H315, H319, H340, H350, H372	P201, P210, P301 + P310, P305 + P351 + P338, P308 + P313, P331
Bis(triphenyl-phosphoranylidene)-ammonium chloride		H315, H319, H332, H335	P261, P305 + P351 + P338
Butyronitrile		H225, H301, H311, H331	P210, P261, P280, P301 + P310, P311
Dichlormethane		H315, H319, H335, H336, H351, H373	P261, P281, P305 + P351 + P338
Diethyl ether		H224, H302, H336	P210, P261
4,4′-Dimethyl-2,2′-dipyridyl		H315, H319, H335	P261, P305 + P351 + P338
Ethylendiamine		H226, H302, H312, H314, H317, H334	P261, P280, P305 + P351 + P338, P310

Ferrocenium hexafluorophosphate		H315, H319, H335	P261, P305 + P351 + P338
Hexane		H225, H304, H315, H336, H361f, H373, H411	P210, P261, P273, P281, P301 + P310, P331
Methanol		H225, H301 + H311 + H331, H370	P210, P260, P280, P301 + P310, P311
Molybdenum hexacarbonyl		H300, H310, H330	P260, P264, P280, P284
Naphthalene		H228, H302, H351, H410	P210, P273, P281, P501
Nitric acid		H272, H314	P220, P280, P305 + P351 + P338, P310
Nitrosonium hexafluorophosphate		H314	P301 + P330 + P331, P280, P305 + P351 + P338, P310
1,10-Phenanthroline		H301, H410	P273, P301 + P310, P501
1,2,3,4,5-Pentamethyl-cyclopentadiene		H226	–
Phosphorus pentachloride		H302, H314, H330, H373	P260, P280, P284, P305 + P351 + P338, P310

Potassium bromide		H315, H319, H335	P261, P305 + P351 + P338
Potassium dichromate		H272, H301, H312, H314, H317, H330, H334, H340, H350, H360, H372, H410	P201, P220, P260, P273, P280, P284
Silver hexafluorophosphate		H314	P280, P305 + P351 + P338, P310
Sodium		H260, H314	P223, P231 + P232, P280, P305 + P251 + P338, P370 + P378, P422
Sodium hydroxide		H314	P280, P280, P305 + P351 + P338, P310
Sodium mercury amalgam		H260, H314, H330, H360, H372, H410	P201, P223, P231 + P232, P206, P370 + P378, P422
Sulfuric acid		H314, H412	P273, P280, P305 + P351 + P338, P310
Tetrahydrofuran		H225, H319, H335, H351	P210, P261, P281, P305 + P351 + P338

Tetrakis(dimethylamino)ethylene	 	H226, H314	P280, P305 + P351 + P338, P310
Toluene	  	H225, H304, H315, H336, H361d, H373	P210, P261, P281, P301 + P310, P331
Tungsten hexacarbonyl		H301 + H311 + H331	P261, P280, P301 + P310, P311

Erklärung über frühere Promotionsversuche

Hiermit erkläre ich, ,dass vorher keine weiteren Promotionsversuche unternommen worden sind, oder an einer anderen Stelle vorgelegt wurden.

Hamburg, den 06.01.2014

....
- Unterschrift -

Eidesstattliche Versicherung

Hiermit erkläre ich an Eides Statt, dass die vorliegende Dissertationsschrift selbstständig und allein von mir unter den angegebenen Hilfsmitteln angefertigt wurde.

Hamburg, 06.01.2014

....
- Unterschrift -